3-20-2017

A Numerical Model Investigation of the Role of the Glacier Bed in Regulating Grounding Line Retreat of Thwaites Glacier, West Antarctica

Michael Scott Waibel
Portland State University

10.15760/etd.3343

A Numerical Model Investigation of the Role of the Glacier Bed in Regulating Grounding Line Retreat of Thwaites Glacier, West Antarctica

by

Michael Scott Waibel

A dissertation submitted in partial fulfillment of the
requirements for the degree of

Doctor of Philosophy
in
Environmental Sciences and Resources: Geology

Dissertation Committee:
Scott F. Burns, Chair
Christina L. Hulbe
Charles S. Jackson
Andrew G. Fountain
Brittany A. Erickson

Portland State University
2017

ABSTRACT

I examine how two different realizations of bed morphology affect Thwaites Glacier response to ocean warming through the initiation of marine ice sheet instability and associated grounding line retreat. A state of the art numerical ice sheet model is used for this purpose. The bed configurations used are the 1-km resolution interpolated BEDMAP2 bed and a higher-resolution conditional simulation produced by John Goff at the University of Texas using the same underlying data. The model is forced using a slow ramp approach, where melt of ice on the floating side of the grounding line is increased over time, which gently nudges the glacier toward instability. Once an instability is initiated, the anomalous forcing is turned off, and further grounding line retreat is tracked.

Two model experiments are conducted. The first experiment examines the effect of different anomalous forcing magnitudes over the same bed. The second experiment compares the generation and progress of instabilities over different beds. Two fundamental conclusions emerge from these experiments. First, different bed geometries require different ocean forcings to generate a genuine instability, where ice dynamics lead to a positive feedback and grounding line retreat becomes unstable. Second, slightly different forcings produce different retreat rates, even after the anomalous forcing is shut off, because different forcing magnitudes produce different driving stresses at the time the instability is initiated. While variability in the retreat rate over time depends on bed topography, the rate itself is set by the magnitude of the forcing. This signals the importance of correct knowledge of both bed shape and ocean circulation under floating

portions of Antarctic ice sheets. The experiments also imply that different ocean warming rates delivered by different global warming scenarios directly affects the rate of Antarctic contribution to sea level rise.

ACKNOWLEDGEMENTS

Writing a dissertation is a long, difficult endeavor. Fortunately, I had help and support from individuals and organizations along the way. This is where I acknowledge the assistance and support provided to me. However, I want to be clear that the following paragraphs do not form a comprehensive list. There are many people and conversations that have been influential to my studies over the years, and I'm grateful to have had the opportunity of being in an environment that encourages scholarly discourse as well as achievement. Thank you Portland State and the community that is Portland. No matter what the future holds, I will always have fond memories of my time here.

I'm going to begin my list of specific acknowledgements with funding and supporting organizations that enabled me to conduct this research. NASA award number NNX11AH89 to the University of Texas and Portland State funded this work while additional support was provided SciDac's PISCEES project. A profuse thanks to both NASA and PISCEES is in order, and I laud these organizations' efforts contributing to our increasing understanding of the past and future evolution of ice sheets as well as their influence on climate and sea level.

Next, I would like to collectively thank my dissertation committee: Dr. Scott Burns, Dr. Christina Hulbe, Dr. Charles Jackson, Dr. Andrew G. Fountain, and Dr. Brittany Erickson. I appreciate all members' questions and guidance throughout this process. Additionally, I appreciate the thoughtful edits provided to improve the dissertation.

A special thank you goes to Dr. Scott Burns, the chair of my dissertation committee. Scott is a knowledgeable, dedicated geologist and emeritus professor at PSU who is frequently consulted even in his retirement. There is no one quite like Dr. Burns when it comes to navigating PSU's bureaucracy. Furthermore, Scott is an incredibly kind and compassionate human being. If there were more people in this world like Dr. Burns, the world would be a happier, kinder place.

A special thank you goes to Dr. Charles Jackson as well. Dr. Jackson was essentially a co-advisor (along with Dr. Christina Hulbe) for me and ultimately this research would not have been possible without his guidance. I appreciate the opportunity he provided me for travelling to the University of Texas so that I could learn how to use the computing resources provided by the Texas Advanced Computing Center. Moreover, my other trips to UTIG for research were invaluable, and I was pleased to meet so many knowledgeable and gifted scholars there.

I'd like to acknowledge Dr. John Goff at the University of Texas Institute for Geophysics. Dr. Goff created a topographic bed model that is an integral part of this research. The conclusions reached by this research certainly validate his effort.

I would like to thank Nancy Eriksson, PSU Geology Department's former office coordinator. Like Dr. Burns, Nancy was adept at navigating the bureaucracy and cutting through red tape, and I am indebted to her. Another fact about Nancy is that she is an excellent cook. The newer geology students at PSU don't know what they are missing.

I owe a debt of gratitude to Dr. Dan Martin at Lawrence Berkeley National Laboratory. As a model developer, Dan provided invaluable guidance for the numerical

model used in this research. I learned much from Dan, and he was an integral part of the effort.

I would like to thank my family for their support. Erin, my wife, and Pat, my mother, are both strong women; and they probably deserve a medal for putting up with me. Erin has often been a sounding board for my ideas, and I hold her insights in high esteem. In response to my wishes, my mother began teaching me to read when I was four years old and has always been extremely supportive of my academic endeavors ever since. Additionally, I would like to say that I consider Erin's family as my own, and I sincerely appreciate their encouragement.

I would also like to thank Alisa Humphrey, the current office coordinator at PSU's Geology Department, and Paul Brooks, a computer systems analyst. I judge Alisa to be a fine addition to the office staff as she undertakes administrative tasks allowing students to focus on their work. Paul was a tremendous help as I transitioned to Unix-like systems.

I've saved my most profuse and heartfelt thanks for last. Thank you, Dr. Christina Hulbe, for everything that you have done to further my career. There really are no words that can amply express my gratitude. Christina was my original advisor and the one who set me on the path to this academic achievement. Christina's faith in me gave me the confidence to carry on and overcome obstacles along the way (and there were some big ones). I feel very privileged and humbled to have had the opportunity to work with one of the most highly respected minds in ice dynamics.

TABLE OF CONTENTS

LIST OF FIGURES

LIST OF ABBREVIATIONS

AMR	adaptive mesh refinement
AS	Amundsen Sector
ASE	Amundsen Sea Embayment
B260	Simulation over Bedmap2 in which the anomalous forcing (slow ramp) was turned off at model year 260.
B270	Simulation over Bedmap2 in which the anomalous forcing (slow ramp) was turned off at model year 270.
BEDMAP	bed topography of the Antarctic
BISICLES	Berkeley Ice Sheet Initiative for Climate at Extreme Scales
EAIS	East Antarctic Ice Sheet
FDM	Finite Difference Method
FEM	Finite Element Method
FVM	Finite Volume Method
G425	Simulation over the Goff bed in which the anomalous forcing (slow ramp) was turned off at model year 425.
MCDW	Modified Circumpolar Deep Water
PLF	piecewise linear form (or piecewise linear function)
ROI	region of interest
SLE	sea level equivalent
SSA	Shallow Shelf Approximation aka Shelfy-Stream Approximation
SSA*	modified Shallow Shelf Approximation
TAM	Transantarctic Mountains
T1 – T5	Transects that are flow paths
UTIG	University of Texas Institute for Geophysics
VAF	volume above floatation
WAIS	West Antarctic Ice Sheet

LIST OF SYMBOLS

$\dot{a}$	accumulation or ablation rate at the ice surface
$a^{\perp}$	ice volume flux perpendicular to the ice surface
$\dot{b}$	melting or freezing rate at the ice base
$b^{\perp}$	ice volume flux perpendicular to the ice base
c_i	expansion coefficients
$\mathbf{f}$	body force acting on ice
$\mathbf{g}, g$	gravitational acceleration (= 9.81 ms^{-2})
h	z-coordinate of the ice surface
k	ice thermal conductivity
l	exponent taken to be 1
$\mathbf{n}$	unit normal vector
n	exponent usually taken to be 3
p	1) pressure 2) exponent for e
q	exponent for e
r	bedrock elevation below sea level
s	ice surface elevation
t	time
$\mathbf{u}$	velocity vector in three Cartesian dimensions
u_i, u_j	horizontal components of velocity (index notation)
u_x, u_y, u_z	Cartesian components of velocity
$\mathbf{u}_s$	ice surface velocity vector
$\mathbf{w}$	velocity vector of free surface
$\mathbf{x}$	position vector
x_i, x_j	horizontal Cartesian coordinates (index notation)
x, y	horizontal Cartesian coordinates

z	vertical Cartesian coordinate
A	rate factor
B_b	free surface boundary at ice base
B_s	free surface boundary at ice surface
C	coefficient representing basal properties
J	cost function
J'	cost function with outside constraint
J_m	misfit function
J_p	Tikhonov penalty function
H	ice thickness
T	temperature
$\alpha_u^2(x, y)$	coefficient equal to 1 where velocity data is available and zero otherwise in misfit function, J_m
α_C^2	coefficient in basal traction term of Tikhonov penalty function, J_p
α_ϕ^2	coefficient in stiffening term of Tikhonov penalty function, J_p
$\beta(x, y)$	spatially variable basal traction field
$\dot{\varepsilon}_{ij}$	component of strain rate tensor
$\dot{\varepsilon}_{II}$	effective strain
η	effective viscosity
λ, μ	components of Lagrange-multiplier vector
ρ, ρ_i	density of ice (= 918 kgm^{-3})
ρ_w	density of water (= 1028 kgm^{-3})
$\rho\mathbf{g}$	effective force of gravity
$\boldsymbol{\sigma}$	Cauchy stress tensor
$\boldsymbol{\tau}$	deviatoric stress tensor

τ_{ij}		component of deviatoric stress tensor
	τ_{xz}, τ_{yz}	vertical shear components in the horizontal plane
	τ_{II}	effective stress
τ_b		basal drag (traction)
	τ_b^x, τ_b^y	basal drag in the superscripted direction
τ_d		driving stress
ϕ		coefficient representing ice stiffness
Λ		Lagrange-multiplier vector
Φ		heat source term
Φ_i		basis functions
Ω		model domain
	Ω_V	model domain where ice volume above floatation is present

1.0 INTRODUCTION

Recently, much Antarctic research has been focused on the marine terminating glaciers of the West Antarctic Ice Sheet (WAIS) (e.g. Anandakrishnan et al., 2007; Bindschadler et al., 2001; Gudmundsson, 2006; Joughin and Tulaczyk, 2002; Pollard and DeConto, 2009; Ross et al., 2012). The glaciers of the Amundsen Sea Embayment (ASE) have been of particular interest due to their physical setting that includes beds on a regional reverse slope (e.g. Holt et al., 2006; Joughin et al., 2014; Parizek et al., 2013; Rignot, 2001; Rignot et al., 2014; Shepherd et al., 2002). The presence of a reverse slope means the bedrock on which the glaciers lie dips landward such that it becomes deeper inland. This creates the potential for rapid, unstable ice mass loss and grounding line retreat according to the Marine Ice Sheet Instability Hypothesis (Mercer, 1978). In flowline models, no steady state grounding line positions can be obtained over reverse bed slopes (Schoof, 2007; Weertman, 1974).

Two (horizontal) dimensional grounding lines are more complicated than the 1-dimensional case examined in flowline models. This is because the plan-view shape of the ice shelf generates resistive stresses that balance part of the gravitational driving stress, reducing longitudinal stresses at the grounding line. If the longitudinal stresses are sufficiently reduced, a steady state grounding line may be found on a reverse slope (Dupont and Alley, 2005; Goldberg et al., 2009; Gudmundsson et al., 2012). This is often called ice shelf buttressing although the analogy to an engineering buttress is inappropriate as a compressional term opposing longitudinal stretching is not involved. Whether or not a steady state configuration exists depends on the width of the floating ice

shelf, traction at the base of the grounded ice, and of course environmental boundary conditions such as the surface accumulation rate. This current work examines the generation and propagation of an ice sheet instability over a reverse slope using a two-dimensional depth integrated numerical model.

1.1 Physical Setting

The WAIS is one of three distinct regions of Antarctic ice, along with the ice caps, mountain glaciers, and ice shelves of the Antarctic Peninsula and the very large East Antarctic Ice Sheet (King and Turner, 2007). The WAIS covers about 15% of the continent (King and Turner, 2007), has a volume of approximately 2 million km^3, and is estimated raise the global sea level by about 4.3 meters if converted entirely to water (Fretwell et al., 2013). The WAIS is separated from the East Antarctic Ice Sheet (EAIS) by the Transantarctic Mountains (TAM) and adjoined to the Antarctic Peninsula (Figure 1).

These three glaciated regions are distinguished by the tectonic history of the underlying continent and sea floor (Anderson, 1999). East Antarctica is comprised of thick Precambrian to Ordovician basement of igneous and sedimentary rocks, locally overlain by younger sedimentary rocks, and intruded by igneous and volcanic rocks of various ages. Together, these form the East Antarctic Shield except near its western edge where it is underlain by a Paleozoic mobile belt terminating at the TAM (Anderson, 1999). West Antarctica is underlain by four microplates (Dalziel and Lawver, 2001; Mukasa and Dalziel, 2000). These crustal blocks have moved relative to each other and

East Antarctica since the breakup of Gondawana in the early Jurassic to their present day configuration (Anderson, 1999; Cande et al., 2000; Mukasa and Dalziel, 2000). The mountainous Antarctic Peninsula is underlain by a single block that has experienced

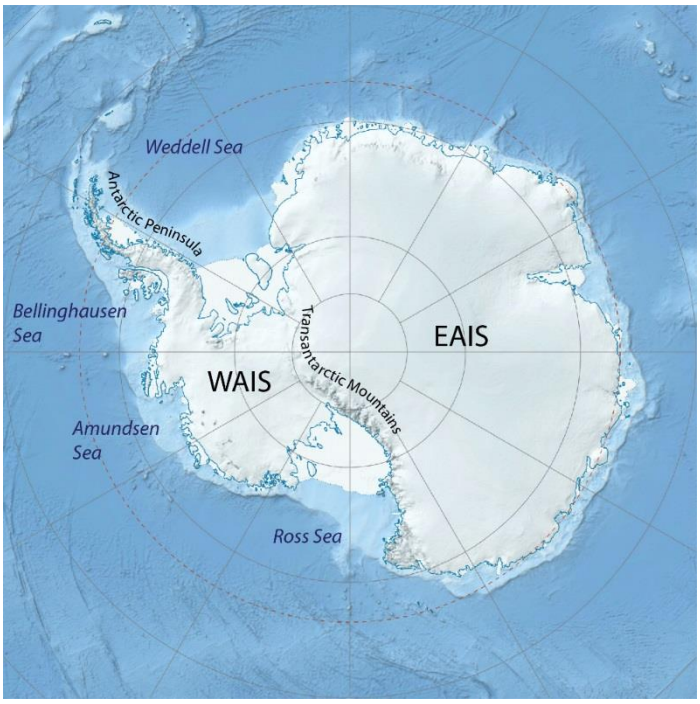

Figure 1. The West Antarctic Ice Sheet is adjoined to the Antarctic Peninsula and separated from the larger EAIS by the Transantarctic Mountains. The continental shelf is seen in light blue surrounding the continent. Adapted from a University of Texas Institute for Geophysics figure.

phases of subduction due to a convergent margin near its western edge since the middle Jurassic (Anderson, 1999). Outlet, valley, and piedmont glaciers are prevalent in this region (Anderson, 1999). The remainder of West Antarctica has been in an extensional tectonic regime forming a rift system as the blocks moved relative to each other with some rifts active into the Cenozoic (Anderson, 1999; Behrendt, 1999; Cande et al., 2000).

The former rift system underlying the WAIS has implications for ice dynamics. Continental crust is thinner here than in East Antarctica. In fact, the majority of the EAIS except near the coast is a high plateau that is grounded well above sea level due to the thick crust on which it lies (Anderson, 1999). This is not the case for the WAIS which is termed a marine ice sheet because the majority of the bed on which it rests is well below sea level. Prior to glaciation, most of the region was below sea level and as a result, is blanketed by poorly consolidated marine sediments. The sediments can contribute to fast ice flow rates due either to the high basal water pressure it supports or to deformation within the sediment itself (Cuffey and Paterson, 2010). Another consequence of thinner crust evolved in an extensional setting is relatively high heat flux into the base of the WAIS. One research team found that heat fluxes increase from 51 mW/m^2 in East Antarctica to 68 mW/m^2 near the coast in West Antarctica (Llubes et al., 2006). This has implications for flow as it increases the likelihood of melting at the base of the ice sheet and because the deformation rate of ice is strongly dependent on temperature (Cuffey and Paterson, 2010). Complicated subglacial hydrologic networks have been observed in many parts of the WAIS (Carter et al., 2011; Carter et al., 2013; Rémy and Legresy, 2004). Finally, the generally lower surface elevations of the WAIS as compared to the other Antarctic ice regions allow higher snow accumulation rates farther inland, as the lack of topographic barriers can allow cyclones to more readily move toward the interior of the WAIS (King and Turner, 2007).

Ice flow within the WAIS is generally convergent to ice streams (Bindschadler et al., 2001). Ice divides form three distinct regional catchments that are named after the

seas into which the ice flows: the Weddell Sea sector, the Amundsen Sea sector, and the Ross Sea sector. The focus here is on the Amundsen Sea (AS) sector (Figure 2).

Figure 2. The location of the Amundsen Sea sector catchment area is shown in red. Note that the areas of white between the red region and ocean are showing small ice shelves and the Thwaites Glacier Tongue.

The geography and mass balance of the AS region are two factors that distinguish it from the other WAIS sectors. The subglacial topography of the AS region includes deep channels that connect coastal outlets to the interior of the ice sheet (Goff et al., 2014; Holt et al., 2006). This suggests ice flow in these areas may more resemble isbrae in Greenland than the ice streams in the Ross Sea sector of West Antarctica (Truffer and Echelmeyer, 2003). Also, the AS is much less embayed than the margins on the Ross and Weddell Seas (Figure 1). This geometry suggests that the formation of very large ice shelves, which affect stress balance at the grounding line, are not likely here (Parizek et

al., 2013). However, small ice shelves and the Thwaites ice tongue exist today at the marine margin in the ASE (Figure 2). The continental shelf near the ASE narrows from over 400 km north of Pine Island Bay to between 100 and 200 km west of Siple Island (Nitsche et al., 2007). This is important because relatively warm Modified Circumpolar Deep Water (MCDW) is found near continental shelf breaks around the majority of the continent (Dinniman et al., 2012).

The snow accumulation rate is higher over the AS sector than elsewhere in West Antarctica because it is at the end of a major storm track that begins in the mid-latitudes and directs relatively moist air to the region (King and Turner, 2007). However, the rate of new mass accumulation over much of the AS sector has not kept pace with increasing ice discharge. The net effect of the imbalance is thinning of glaciers and grounding line retreat (Rignot et al., 2014; Shepherd et al., 2002). Today, the AS sector is one of the most rapidly changing regions in Antarctica (Parizek et al., 2013; Rignot, 2008; Rignot et al., 2002; Shepherd et al., 2012; Shepherd and Wingham, 2007; Thomas et al., 2004; Wåhlin et al., 2010).

The physical setting of the AS sector must influence the recent mass loss. The lack of a large ice shelf and the proximity of MCDW exposes the ice front to climate forcings such as ocean variability and ocean warming (Gille, 2014; Pritchard et al., 2009) and indeed, the intrusion of relatively warm MCDW beneath the small ice shelves is thought to be driving present changes in the ASE (Shepherd et al., 2004). The geomorphology of the bed beneath the grounded ice will determine how the interior responds to that forcing.

1.2 Climate Context

The expected future high atmospheric CO_2 world is one in which the WAIS will be smaller than at present and may retreat to isolated ice caps and mountain glaciers (Golledge et al., 2012; Naish et al., 2009; Pollard and DeConto, 2009). According to the physics as it is understood, the change will be driven from the sea, but may also involve warming in the atmosphere above (Mayewski et al., 2009; Nowicki et al., 2013). As deglaciation proceeds, sea level will rise, sea ice extent will change, and the circulation of both the ocean and the atmosphere will be modified. These changes will affect Antarctic ecosystems and will propagate northward through the climate system (Ainley et al., 2005; Smith et al., 1999; Trathan et al., 2007). What is less clear, however, is at what rate key changes will take place. Both direct observation and paleoclimate proxies show that rates in cryosphere systems are not uniform over time, a situation that confounds direct comparison between observations and climate models, and that makes understanding sources of variability in the coupled ice—ocean—atmosphere system of particular scientific and social relevance.

The rate at which the WAIS responds to climate forcing depends on a set of processes and process interactions involving ice, ocean, atmosphere, and the terrestrial subglacial environment. Substantial gaps exist in the scientific understanding of most of these. This is the case because direct observation in the Antarctic is challenging and because time and spatial scales of observation are often mismatched with the fundamental scales of the underlying processes. Nevertheless, model projections of future change are

of critical importance and are routinely produced (Goelzer et al., 2013; Golledge et al., 2015; Nowicki et al., 2013). Here I focus on the subglacial environment of Thwaites Glacier in the AS sector of the West Antartica, and in particular the influence of (estimated) bed morphology on model projections. As the shape of the ice sheet base is inferred from geophysical observations, many realizations are possible and thus, many ice sheet model outcomes are also possible.

1.3 Glaciological Context

The WAIS is thought to be particularly prone to rapid mass loss due to its marine setting. The grounded inland ice sheet rests on an inland-deepening bed and terminates in a deeply embayed floating ice shelf. The marine ice sheet instability hypothesis first put forward in the 1970s holds that a perturbation causing thinning of ice at the transition from grounded to floating ice could yield runaway retreat of that boundary (Mercer, 1978). In brief: when ice upstream of the grounding line thins and goes afloat, it can flow more rapidly than was previously possible, generating additional thinning and additional speedup at the grounding line. The dynamical connection between floating and grounded ice is particularly strong because the ice sheet is drained by fast-flowing ice streams that, due to the unconsolidated, water saturated sediments over which they flow, are only weakly coupled to the bed (Bougamont et al., 2003).

The grounding zone is the gateway through which terrestrial ice must pass before entering the floating ice shelf and contributing to sea level. The geographic setting of the grounding zone influences the rate at which ice flows through this gateway such that any

processes influencing its position must be well understood if credible assessments of ice sheet vulnerability to warming and likely future rates of change are to be made.

In a real-world setting, the transition from grounded to floating ice occurs as ice passes over a strip of bed, hence the term grounding zone. However, it is conceptually simpler to discuss processes related to this zone by expressing it in terms of a line. Models treat the grounding zone as a line, and any reference in this work to a grounding line implies grounding zone.

1.4 Research Question

Accurately modeling marine ice sheet response to environmental forcing requires good fidelity to a variety of physical processes. The importance of grounding line dynamics and downstream processes like ice shelf basal melting are widely addressed. My focus is directed upstream to the influence of bed morphology on ice sheet retreat. This is accomplished using accurate sub-kilometer scale topographic data and a high-resolution ice sheet model with appropriate grounding line physics.

My primary goal is to understand how and why the more realistic bed geometry affects model behavior and projections of future change. I use the same type of forcing as prior work on the Thwaites and Pine Island Glacier systems – parameterized warm water incursion beneath the floating glacier terminus – and compare the resulting ice sheet retreat across simulations using different basal elevation data sets. This allows me to consider how representation of the bed affects the simulation.

2.0 METHODS

The transition from grounded (ice flowing over bedrock) to floating (ice flowing over water) is also a transition in flow regime. On the floating side, basal shear stress is very small, so that vertical shearing does not occur and the stress balance is dominated by horizontal shear and normal stresses. On the grounded side, basal traction ranges from small but non-zero to nearly equal the gravitational driving stress and so vertical shearing ranges from negligible to dominant in the balance of stresses, with horizontal shear and normal stresses making up the rest of the balance (Cuffey and Paterson, 2010). The relative magnitudes of the stresses depend on spatially variable conditions such as properties of the basal material and bed morphology. The physics necessary to reasonably model grounding line retreat must accommodate flow regime on either side of the transition, as well as the transition itself.

The flow of ice can be described by a system of partial differential equations. Such a system is derived from conservation laws (governing equations) and constitutive equations and can be solved, at least through numerical approximations, with the addition of boundary and initial conditions. A very brief description of the governing equations and constitutive relationships that lead to ice flow approximations is provided in this section. In order to provide context, some of the more widely used approximations for fast flowing regimes such as Thwaites Glacier are shown. The hybrid approximation implemented in the model used here is discussed at the beginning of the *2.5 Numerical Model* section.

2.1 Governing Equations

Ice is a viscous, non-Newtonian fluid. Like all fluids it must obey the conservation laws of mass, energy, and momentum. In all cases, ice deformation is treated as an irrotational flow of an incompressible fluid.

The general form of mass conservation is:

$$\frac{\partial \rho}{\partial t} + \nabla \cdot \rho \mathbf{u} = 0 \tag{2.1.1}$$

where ρ represents ice density and $\mathbf{u}$ represents the velocity vector in three Cartesian dimensions. Boldface is used to indicate a vector-valued quantity.

Incompressibility leads to:

$$\nabla \cdot \mathbf{u} = 0 \tag{2.1.2}$$

Equation (2.1.2) can be vertically integrated using the Leibniz integral rule to obtain mass continuity for ice thickness in terms of mass flux divergence and melting & freezing:

$$\frac{\partial H}{\partial t} = -\nabla \cdot \left(\bar{\mathbf{u}} H \right) + \dot{b} - \dot{a} \tag{2.1.3}$$

where H represents ice thickness, $\dot{b}$ represents melting or freezing rate at the base, and $\dot{a}$ represents accumulation or ablation rate at the surface. The overbar indicates a depth-averaged value.

Following Fourier's law of heat conduction, the equation for the conservation of energy can be written as:

$$\rho c \frac{\partial T}{\partial t} = k \frac{\partial^2 T}{\partial z^2} - \rho c \mathbf{u} \cdot \nabla T + \Phi \tag{2.1.4}$$

where T represents temperature, c represents the ice heat capacity, k represents the ice thermal conductivity, and Φ is a heat source term. The first term on the right represents vertical heat diffusion, the second term represents advection, while the third heat source term may include viscous dissipation and latent heat (freezing). The small aspect ratio of ice sheets, about 10^{-3}, means that horizontal diffusion may be neglected (Cuffey and Paterson, 2010). The material properties *c* and *k* are temperature-dependent (Cuffey and Paterson, 2010).

The Navier-Stokes equation for the conservation of linear momentum is:

$$\rho \frac{d\mathbf{u}}{dt} = -\nabla p + \nabla \cdot \boldsymbol{\tau} + \mathbf{f} \tag{2.1.5}$$

where p represents pressure, $\boldsymbol{\tau}$ is the deviatoric stress tensor, and $\mathbf{f}$ represents the body force acting on the ice. The effective force of gravity, $\rho\mathbf{g}$, and the Coriolis force, which is an inertial force, comprise $\mathbf{f}$. However, scaling arguments lead to simplifications of the complete Navier-Stokes equation for conservation of linear momentum using typical values for the horizontal and vertical ice sheet extent, the typical horizontal and vertical flow velocities, typical pressure, and typical time-scale (Greve and Blatter, 2009). The Froude number, a ratio involving acceleration and pressure gradient, is about 10^{-15} in the horizontal direction and about 10^{-21} in the vertical direction. The acceleration term on the left-hand side of equation (2.1.5) is very small compared to the viscous terms on the right so it is neglected. Similarly, a scaling argument is used to estimate the ratio between the Coriolis force and pressure gradient is about 5×10^{-8}, which is still very small compared

to viscous terms. As a result, the Coriolis force inertial term is also neglected and the equation for the conservation of linear momentum for ice is:

$$-\nabla p + \nabla \cdot \boldsymbol{\tau} + \rho \mathbf{g} = 0 \tag{2.1.6}$$

where $\mathbf{g}$ represents the acceleration due to gravity. Equation (2.1.6) describes what is known as Stokes flow (Greve and Blatter, 2009).

2.2 Constitutive Equations

Ice sheets are in static equilibrium even while in motion, as expressed in equation (2.1.6) (Cuffey and Paterson, 2010). This balance is often represented in terms of driving and resisting stresses. The divergence of the stress deviator in equations (2.1.5) and (2.1.6) can be written using the effective fluid viscosity, η.

$$\nabla \cdot \boldsymbol{\tau} = \eta \nabla^2 \mathbf{u} \tag{2.2.1}$$

and the viscosity, then, should be written in terms of the effective strain rate.

A constitutive relation between stress and strain is needed. For an incompressible, isotropic material, each strain rate component must be proportional to its corresponding deviatoric stress component. Treating ice as such a material leads to the power-law relation known as the generalized Glen's Law or the Nye-Glen Isotropic Law:

$$\dot{\varepsilon}_{ij} = A \tau_{II}^{n-1} \tau_{ij} \qquad i, j \in \{x, y, z\} \tag{2.2.2}$$

where $\dot{\varepsilon}_{ij}$ is a component of the strain rate tensor and τ_{ij} is a component of the deviatoric stress tensor. The second invariant of the deviatoric stress tensor is known as the effective deviatoric stress, τ_{II}. The exponent in the flow law, n, is usually 3. The rate factor A is

a spatially variable parameter that is strongly dependent on temperature and fabric of the ice. This temperature dependence is described by an Arrhenius relationship with different constants above and below 263 K (Cuffey and Paterson, 2010). Some of the pioneering work for the flow relation in equation (2.2.2) was accomplished by Nye who proposed that:

$$\dot{\varepsilon}_{II} = A\tau_{II}^{n} \tag{2.2.3}$$

where once again the subscript II denotes the second invariant or effective strain rate and effective deviatoric stress respectively (Cuffey and Paterson, 2010). Considering equations (2.2.2) and (2.2.3), deviatoric stress can be written as:

$$\tau_{ij} = A^{-(1/n)}\dot{\varepsilon}_{II}^{(1-n)/n}\dot{\varepsilon}_{ij} \tag{2.2.4}$$

The flow relation in equation (2.2.2) can be written in the inverse form and expressed in terms of effective viscosity and strain rate as:

$$\tau_{ij} = 2\eta\dot{\varepsilon}_{ij} \tag{2.2.5}$$

Setting the right side of equation (2.2.5) equal to the right side of equation (2.2.4), the effective viscosity of ice may be expressed as:

$$\eta = \frac{1}{2}A^{-(1/n)}\dot{\varepsilon}_{II}^{(1-n)/n} \tag{2.2.6}$$

This shows that viscosity decreases (ice softens) with increasing strain rate, which is analogous to increasing deviatoric stress, and that viscosity is strongly dependent on ice temperature and fabric.

2.3 Ice Flow Approximations

The incompressibility equation (2.1.2) and force balance represented by the conservation of momentum in equation (2.1.6) comprise the field equations that describe ice flow. Using the relation between strain rate and velocity shown here in tensor notation:

$$\dot{\varepsilon}_{ij} = \frac{1}{2}\left(\frac{\partial u_i}{\partial x_j} + \frac{\partial u_j}{\partial x_i} \right) \tag{2.3.1}$$

and the constitutive relationship between stress and strain in Glen's Law leads to the following 3D representation known as the full-Stokes model:

$$\begin{cases} \frac{\partial}{\partial x}\left(2\eta \frac{\partial u_x}{\partial x} \right) + \frac{\partial}{\partial y}\left(\eta \frac{\partial u_x}{\partial y} + \eta \frac{\partial u_y}{\partial x} \right) + \frac{\partial}{\partial z}\left(\eta \frac{\partial u_x}{\partial z} + \eta \frac{\partial u_z}{\partial x} \right) - \frac{\partial p}{\partial x} = 0 \\ \frac{\partial}{\partial x}\left(\eta \frac{\partial u_x}{\partial y} + \eta \frac{\partial u_y}{\partial x} \right) + \frac{\partial}{\partial y}\left(2\eta \frac{\partial u_y}{\partial y} \right) + \frac{\partial}{\partial z}\left(\eta \frac{\partial u_y}{\partial z} + \eta \frac{\partial u_z}{\partial y} \right) - \frac{\partial p}{\partial y} = 0 \\ \frac{\partial}{\partial x}\left(\eta \frac{\partial u_x}{\partial z} + \eta \frac{\partial u_z}{\partial x} \right) + \frac{\partial}{\partial y}\left(\eta \frac{\partial u_y}{\partial z} + \eta \frac{\partial u_z}{\partial y} \right) + \frac{\partial}{\partial z}\left(2\eta \frac{\partial u_z}{\partial z} \right) - \frac{\partial p}{\partial z} - \rho g = 0 \\ \frac{\partial u_x}{\partial x} + \frac{\partial u_y}{\partial y} + \frac{\partial u_z}{\partial z} = 0 \end{cases} \tag{2.3.2}$$

where η is effective viscosity, p is the ice pressure, g is the acceleration due to gravity and u_x, u_y, and u_z are the three Cartesian components of velocity. This system, including the strain-rate dependent viscosity, is computationally challenging. Due to this, glacier and ice sheet modelers take advantage of scaling arguments and boundary conditions to reduce the order of the equations.

Various simplifications have been developed that depend on assumptions about stress boundary conditions and relative magnitudes of stress gradients in the ice (see

Hindmarsh, 2004; Hutter, 1983; MacAyeal, 1989; Morland, 1985). The Blatter-Pattyn first order ice sheet model makes the assumption that the horizontal derivatives of the vertical velocity component are negligible (Blatter, 1995; Pattyn, 2003):

$$\frac{\partial u_z}{\partial x} \approx 0 \quad \text{and} \quad \frac{\partial u_z}{\partial y} \approx 0 \tag{2.3.3}$$

Furthermore, bridging effects are considered negligible so that the vertical momentum balance at a location is independent of horizontal coordinates. This means that the horizontal components of velocity may be uncoupled from the system leading to the following system of equations:

$$\begin{cases} \frac{\partial}{\partial x}\left(2\eta \frac{\partial u_x}{\partial x}\right) + \frac{\partial}{\partial y}\left(\eta \frac{\partial u_x}{\partial y} + \eta \frac{\partial u_y}{\partial x}\right) + \frac{\partial}{\partial z}\left(\eta \frac{\partial u_x}{\partial z}\right) = \rho g \frac{\partial s}{\partial x} \\ \frac{\partial}{\partial x}\left(\eta \frac{\partial u_x}{\partial y} + \eta \frac{\partial u_y}{\partial x}\right) + \frac{\partial}{\partial y}\left(2\eta \frac{\partial u_y}{\partial y}\right) + \frac{\partial}{\partial z}\left(\eta \frac{\partial u_y}{\partial z}\right) = \rho g \frac{\partial s}{\partial y} \end{cases} \tag{2.3.4}$$

where s is the surface elevation and as an input it can be determined by the ice thickness evolution equation (2.1.3). This also simplifies the constitutive relations between stress, strain, and viscosity, equations (2.2.2) through (2.2.6), so that now they only depend on the horizontal velocity components. After solving for the horizontal velocities, the vertical velocity component may be determined by vertical integration of:

$$\frac{\partial u_z}{\partial z} = -\frac{\partial u_x}{\partial x} - \frac{\partial u_y}{\partial y} \tag{2.3.5}$$

The MacAyeal-Morland "shelfy-stream" equations, which are also known as the shallow-shelf approximation (SSA), takes the first order model one step further. For this ice flow approximation, vertical shear is treated as negligible so that:

$$\frac{\partial u_x}{\partial z} \approx 0 \quad \text{and} \quad \frac{\partial u_y}{\partial z} \approx 0 \tag{2.3.6}$$

(MacAyeal, 1989; Morland, 1985). This leads to the following model that when integrated yields the horizontal components of velocity:

$$\begin{cases} \frac{\partial}{\partial x}\left(4H\bar{\eta}\frac{\partial u_x}{\partial x}+2H\bar{\eta}\frac{\partial u_y}{\partial y}\right)+\frac{\partial}{\partial y}\left(H\bar{\eta}\frac{\partial u_x}{\partial y}+H\bar{\eta}\frac{\partial u_y}{\partial x}\right)=\rho gH\frac{\partial s}{\partial x}-\tau_b^x \\ \frac{\partial}{\partial y}\left(4H\bar{\eta}\frac{\partial u_y}{\partial y}+2H\bar{\eta}\frac{\partial u_x}{\partial x}\right)+\frac{\partial}{\partial x}\left(H\bar{\eta}\frac{\partial u_x}{\partial y}+H\bar{\eta}\frac{\partial u_y}{\partial x}\right)=\rho gH\frac{\partial s}{\partial x}-\tau_b^y \end{cases} \tag{2.3.7}$$

where $\bar{\eta}$ is the depth-averaged viscosity, H is ice thickness, and τ_b is the basal drag in the superscripted direction.

2.4 Boundary Conditions

Suitable boundary conditions must be applied in order to solve any system of equations describing ice motion. Kinematic boundary conditions are applied at impermeable boundaries, and define the conditions where fluid flow normal to the boundary must be zero at a stationary boundary or equal to the velocity of a moving boundary normal to itself. The first case essentially describes the situation for a solid/fluid boundary such as that at the bedrock/ice interface while the second case can describe the situation for a fluid/fluid boundary such as that at the atmosphere/ice interface. The derivation and application of kinematic boundary conditions at the ice surface and ice base will now be discussed in greater detail.

If the boundary at the free surface (atmosphere/ice interface) is defined by the implicit equation

$$B_s(\mathbf{x},t) = z - h(x,y,t) = 0 \tag{2.4.1}$$

where z is a vertical coordinate, t is time, and h is the *z*-coordinate of the ice surface (Greve and Blatter, 2009) then, equation (2.4.1) describes a zero-equipotential surface where the unit normal vector pointing toward the atmosphere is defined as

$$\mathbf{n} = \frac{\nabla B_s}{|\nabla B_s|} = \left(\left(\frac{\partial h}{\partial x} \right)^2 + \left(\frac{\partial h}{\partial y} \right)^2 + 1 \right)^{-1/2} \begin{bmatrix} -\frac{\partial h}{\partial x} \\ -\frac{\partial h}{\partial y} \\ 1 \end{bmatrix} \tag{2.4.2}$$

As flow evolves, particles can only remain on B_s if

$$\frac{DB_s}{Dt} = \frac{\partial B_s}{\partial t} + \mathbf{w} \cdot \nabla B_s = 0 \tag{2.4.3}$$

where $\frac{D}{Dt}$ is the notation for the material derivative and $\mathbf{w}$ represents the velocity of the free surface. An ice volume flux perpendicular to the free surface can be specified by letting $\mathbf{u}_s$ equal the surface velocity in the mass balance equation:

$$a^{\perp} = (\mathbf{w} - \mathbf{u}_s) \cdot \mathbf{n} \tag{2.4.4}$$

For this surface mass balance equation, the sign is typically chosen such that accumulation is positive and ablation is negative. Now equation (2.4.3) can be rewritten using equation (2.4.2) and the definition provided by equation (2.4.4) as

$$\frac{\partial B_s}{\partial t} + \nabla B_s \cdot \mathbf{u}_s = -|\nabla B_s| a^{\perp} \tag{2.4.5}$$

which, using $B_s = z - h$ and the definitions in equation (2.4.2) , is equivalent to

$$\frac{\partial h}{\partial t} + u_s^x \frac{\partial h}{\partial x} + u_s^y \frac{\partial h}{\partial y} - u_s^z = a_s^{\perp} \sqrt{\left(\frac{\partial h}{\partial x}\right)^2 + \left(\frac{\partial h}{\partial y}\right)^2 + 1} \tag{2.4.6}$$

in which a superscript on a vector component indicates the Cartesian coordinate direction. This is the kinematic boundary condition for the freely evolving surface of an ice sheet (Greve and Blatter, 2009).

The dynamic boundary condition for the free surface is derived from a momentum jump condition. Since the atmospheric stress is small compared to typical stresses in an ice sheet and ice flow velocities are small, the end result is the stress-free condition

$$\boldsymbol{\sigma} \cdot \mathbf{n} = 0 \tag{2.4.7}$$

for the surface (Greve and Blatter, 2009).

Additionally, thermodynamic boundary conditions are required for the energy equation (2.1.4). This is accomplished by specifying the surface temperature T_s ,

$$T = T_s, \tag{2.4.8}$$

which can be approximated in sub-zero (°C) regions by the mean annual surface temperature (Greve and Blatter, 2009). Similarly, if the basal temperature is at the pressure melting point, the basal temperature can be specified as

$$T = T_m \tag{2.4.9}$$

where the subscript m indicates the pressure melting point.

The kinematic boundary condition for the ice base is derived in a similar manner to that of the free surface. The normal vector points into the bedrock, so that the components of the gradient at the boundary between ice and bedrock ∇B_b have the

opposite sign than in equation (2.4.2). Similarly, the ice volume flux perpendicular to the basal boundary is

$$b^{\perp} = \left(\mathbf{u}_s - \mathbf{w}\right) \cdot \mathbf{n} \tag{2.4.10}$$

so that positive values for $b^{\perp}$ indicate mass loss due to basal melting.

Since the normal component of ice velocity vanishes at the basal boundary in the same manner as the free surface, the end result for the basal kinematic boundary condition is analogous to equations (2.4.5) and (2.4.6) (respectively):

$$\frac{\partial B_b}{\partial t} + \nabla B_b \cdot \mathbf{u}_b = -\left|\nabla B_b\right| b^{\perp} \tag{2.4.11}$$

and

$$\frac{\partial b}{\partial t} + u_b^x \frac{\partial b}{\partial x} + u_b^y \frac{\partial b}{\partial y} - u_b^z = a_b^{\perp} \sqrt{\left(\frac{\partial h}{\partial x}\right)^2 + \left(\frac{\partial h}{\partial y}\right)^2 + 1} \tag{2.4.12}$$

where the subscript b indicates the base and superscripts indicate the Cartesian coordinate direction for *u*-velocity components.

The upper and lower surfaces may have any orientation relative to the fixed coordinate system and the fluxes perpendicular to the free surface and ice base can be written in terms of the vertical coordinate as

$$\dot{a} = \left|\nabla B_s\right| a^{\perp} \tag{2.4.13}$$

for accumulation and ablation rates, and

$$\dot{b} = \left|\nabla B_b\right| b^{\perp} \tag{2.4.14}$$

for basal melt rate. With these fluxes in the vertical direction, these kinematic boundary conditions can be used with the Leibniz integral rule to form the mass continuity equation (2.1.3) as previously mentioned.

The momentum jump condition for the basal interface is simplified once again as the advective ice flow term is small, so that

$$\boldsymbol{\sigma} \cdot \mathbf{n} = \boldsymbol{\sigma}_{\text{lith}} \cdot \mathbf{n}, \tag{2.4.15}$$

where $\boldsymbol{\sigma}_{\text{lith}}$ indicates lithospheric stresses. Equation (2.4.15) shows continuity of the stress vector across the interface, but this is inadequate for a dynamic boundary condition as it provides no information about the stress regime in the underlying material (Greve and Blatter, 2009). Stress state and deformation in the subglacial material is a topic of ongoing research and various parameterizations are used to represent the effect of the material on ice flow (Bougamont et al., 2015; Bougamont et al., 2011). In the model implemented here, sliding creates resistance according to a viscous law (Cornford et al., 2015). The resulting basal traction term, τ_b, is spatially variable according to the motion of the ice and a coefficient *C* that represents basal properties

$$\tau_b = \begin{cases} -C|u|^{l-1}u & \text{if } \dfrac{\rho_i}{\rho_w} H > -r \\ 0 & \text{otherwise} \end{cases} \tag{2.4.16}$$

The coefficients C are determined during model initialization by the adjoint equations. For this equation, $l = 1$ and r represents the bedrock elevation below sea level.

2.5 Numerical Model

The Berkeley Ice Sheet Initiative for Climate at Extreme Scales (BISICLES) ice sheet model is used here. BISICLES applies a block-structured finite volume method with adaptive mesh refinement (AMR) to solve the governing equations for ice sheet dynamics (Cornford et al., 2013). The momentum equations are simplified using the Schoof-Hindmarsh model (Cornford et al., 2013). As this approximation was similar to the SSA at the time the modeling in this paper took place, it is hereafter informally referred to as SSA*. SSA* is like other approaches that make use of the small aspect ratio and near-zero basal traction, but treats the effective viscosity differently. In brief, the deviatoric stress tensor $\boldsymbol{\tau}$ is split into a tensor representing the horizontal and vertical normal components together with the horizontal shear, and a tensor representing the vertical shear components. The first tensor is the usual case of the MacAyeal-Morland SSA. In the case of a near-zero basal shear condition, the second tensor is very small, compared to the first, and may be neglected when computing velocity terms. It is, however, of use in computing the effective viscosity. For that purpose, vertical shear components are computed using the shallow ice approximation of Hutter (1983) and Morland (1984)

$$\begin{cases} \tau_{xz} = -\rho g (h - z) \dfrac{\partial h}{\partial x} \\ \tau_{yz} = -\rho g (h - z) \dfrac{\partial h}{\partial y} \end{cases} \tag{2.5.1}$$

in which τ_{xz} and τ_{yz} represent the vertical shear components in the horizontal plane and z represents the vertical Cartesian coordinate.

Cornford et al. (2013) tested the SSA* model using steady-state grounding line experiment for an ice stream with a simple geometry. Comparison against a full-Stokes solution showed that the modification increased the accuracy of a steady-state grounding line about 10 times over the standard SSA. Although this experiment incorporated simple ice stream and basal geometry with the assumption of isothermal ice, it does provide evidence that the SSA* approximation may be more accurate in determining grounding line position than the shelfy-stream approximation alone.

The finite volume method (FVM) is similar to both the finite difference method (FDM) and finite element methods (FEM). All three methods solve discretized governing equations over discretized domains. In particular, the governing equations of a system are solved over a structured grid for both the FVM and FDM. In contrast to the FDM in which a truncated Taylor series is used to approximate governing equations at each node, the FVM and FEM solve the integral form of the governing equations. the strong formulation is discretized for the FVM while the weak formulation is discretized for the FEM (Patankar, 1980; Price et al., 2007; Versteeg and Malalasekera, 2007).

Discretizing the domain into cells, creating control (or finite) volumes that surround grid points, and evaluating the integral strong form of governing equations over each cell is distinguish the FVM from other approximation methods (Patankar, 1980; Versteeg and Malalasekera, 2007). The numerical scheme implies that the integral conservation of a conserved quantity is exact over any number of control volumes up to and including the entire domain (Patankar, 1980; Versteeg and Malalasekera, 2007).

Furthermore, the exact integral balances apply to a domain consisting of coarse cells or fine cells alike, not just in the limiting case of sufficiently high resolution.

The block structured AMR facilitates efficient modeling of ice sheet regions that include a grounding line. Numerical models always require compromises between resolution (and thus computation time) and convergence. Problems involving a grounding line tend to exhibit decreasing rates of convergence with increasing mesh spacing (Cornford et al., 2013). Therefore, it is desirable to have a mesh with the smallest spacing at the grounding line which quickly coarsens away from it and that is able to evolve over time as the grounding line migrates, and this is exactly what the AMR in BISICLES accomplishes

AMR in BISICLES is hierarchical with the coarsest mesh spacing on the bottom in plan view (Figure 3). The mesh spacing of a level divided by the mesh spacing of the level immediately below it is known as the refinement ratio. The refinement ratio is always an even integer and each level domain is properly nested. The stress balance equations are first solved for the coarsest level mesh and progresses upward where refinement criteria have been applied, using the previous coarser mesh solution as a starting point. Refinement criteria can be based on the Laplacian of the velocity field,

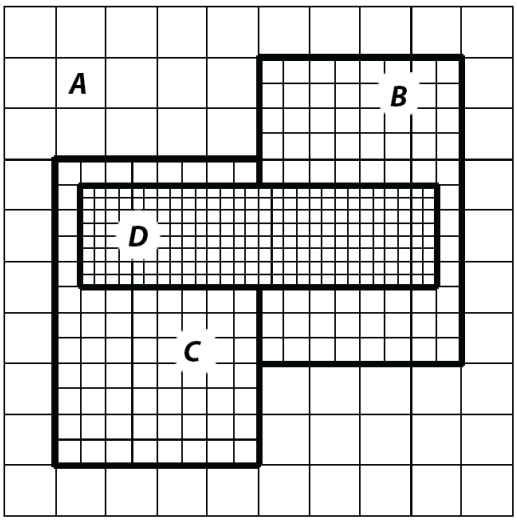

Figure 3. An example of a block-structured mesh. The first discrete level domain is comprised of the coarsest mesh labeled *A*. Overlaying this is the next discrete level domain comprised of meshes in the rectangular blocks labeled *B* and *C*. The finest mesh comprises the discrete level domain in block *D*. The valid domain includes the subsets of discrete levels that are not overlain by other discrete levels. In other words, what one sees in plan view is the valid domain. Figure adapted from Cornford et al., 2013.

by tagging cells adjacent to the grounding line, or both (Cornford et al., 2013). However, modifications to the FVM discretization on meshes must be made to accommodate the coarse-fine boundaries separating valid regions of the domain. The flux of a vector field across a coarse-fine boundary is handled by modifying the following three discrete operators: the flux divergence term in the thickness evolution equation (2.1.3), the driving stresses on the right hand side of SSA*, which can be seen in equation (2.3.7), and the viscous terms on the left hand side of SSA*, equation (2.3.7) (Cornford et al., 2013). These modifications simply partition the flux from a coarse cell correctly into the bordering finer cells.

2.6 Model Domain and Boundaries

The model domain includes the entire ASE sector, both grounded and floating ice. The boundary is the union of ice in contact with the atmosphere, ice in contact with the ocean, and ice in contact with the bed. For our simulations, ice thickness and ice surface elevation come from the standard Bedmap2 dataset (Fretwell et al., 2013). The ice accumulation field (ice equivalent surface snow accumulation), is provided in conjunction with the Bedmap2 data (Arthern et al., 2006).

Thermal boundary conditions at the base and surface derive from an estimation of spatially varying ice temperatures provided by Pattyn (2010). This dataset is used to specify an initial temperature distribution in the ice. No geothermal flux under grounded ice is specified. Instead, the model initialization technique used here accounts for the contribution to ice velocity from basal melt.

Boundary conditions are also needed for the ice shelf and lateral boundaries. For the shelf, the normal stress at the lower surface is equal to the hydrostatic water pressure (Cornford et al., 2013). At ice divides, the flow velocity normal to the divide is zero, a Dirichlet condition, while a Neumann condition is applied to the tangential velocity such that its derivative is zero (Cornford et al., 2013). A Neumann condition is applied at the calving front such that the normal stress across it is equal to the hydrostatic pressure there (Cornford et al., 2013).

2.7 Bed Topography

Two realizations of the Earth surface beneath the ice sheet are used. These include a benchmark data set widely used by ice sheet modelers, and a new data set produced by colleagues associated with this research project (Goff et al., 2014).

The BEDMAP project (Fretwell et al., 2013; Lythe et al., 2001) is the cryosphere community standard suite of boundary condition data sets. The Bedmap2 topography is a 1 km resolution gridded dataset of subglacial topography and seabed elevation for the Antarctic region extending from the South Pole to 60° S (Fretwell et al., 2013). The Bedmap2 collection of gridded datasets also includes ice thickness and surface elevation. Over grounded regions and away from rock outcrops, the bed topography was created by subtracting 5 km gridded ice thickness data from 1 km gridded surface elevation data. In order to fill in detail close to outcrops, a denser 1 km coverage of ice thickness from a thin-ice-model was subtracted from the surface elevation data within 10 km of rock outcrops but not including the rock, which is an expression of surface elevation. These data were combined with ocean and sub-ice-shelf bathymetry and gridded, interpolating where necessary, to produce the final 1 km gridded topography (Fretwell et al., 2013).

The second realization of the subglacial bed was created by project partners at the University of Texas Institute for Geophysics (UTIG) using the same airborne radar observations of the ice surface and thickness as the Bedmap2, but with a novel computational approach. This approach summarizes the along track radar data into 250 m resolved bed geometries. The new 250 m resolution conditional simulation, combines a

stochastic realization with a deterministic surface of the bed beneath Thwaites Glacier and its catchment area (Goff et al., 2014) (Figure 4).

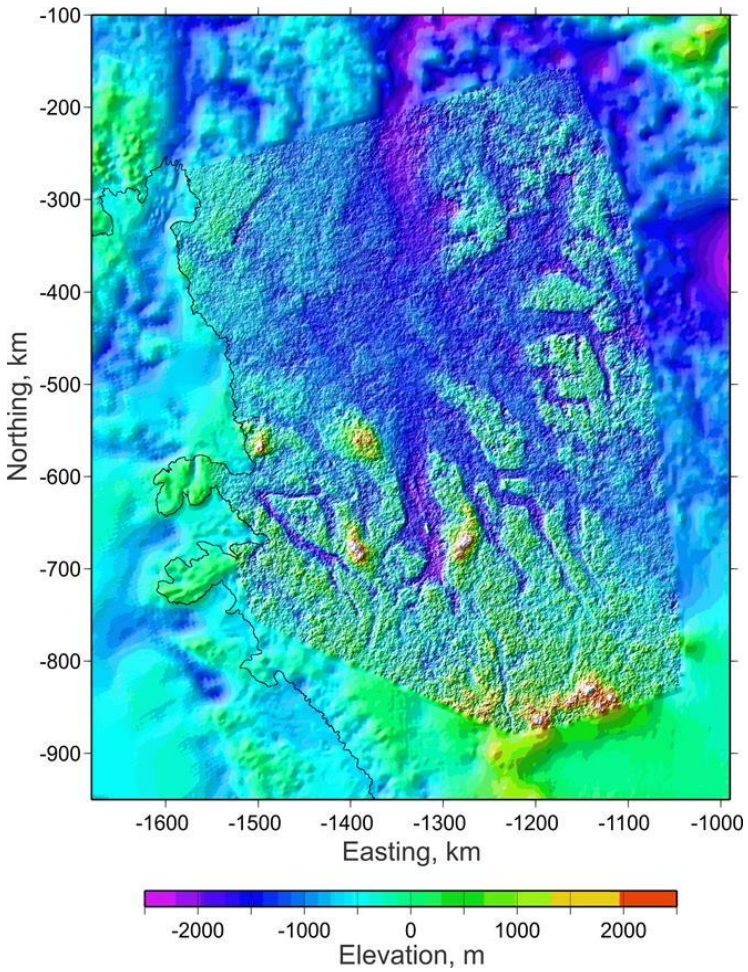

Figure 4. The new 250 m resolution bed of the Thwaites catchment created by UTIG researchers. This bed has been "sewn into" a 250 m interpolation of the Bedmap2 bed for the sake of continuity.

The aerogeophysical observations over the Thwaites catchment were interpolated to the fine grid using inhomogeneous statistics with channelized morphology and a realistic small-scale roughness to create this new bed topography (Goff et al., 2014). A conditional simulation is non-unique. It allows multiple realizations of the features that

could lie between radar flight lines to be generated using the statistics of the features that do lie along the flight lines (Goff et al., 2014). Multiple bed models could be used to quantify uncertainty in ice sheet model projections, however, only one realization is used here. The UTIG conditional simulation will hereafter be referred to as the Goff bed, named after the bed's principal creator.

2.8 Model Initialization

Model initialization is based on optimal control theory, in which unknown values of parameter fields and boundary conditions are estimated using known (observed) fields and the fundamental dynamics of the model (MacAyeal, 1993). The goal is to find, as efficiently as possible, the best fit between the observed and modeled fields. A cost function that quantifies the quality of the fit is minimized by repeated estimation of the unknown parameters, that is, by iterating on those parameters. In this case, basal traction and ice stiffening coefficients, which locally modify ice viscosity, are estimated through minimization of the cost function for the BISICLES control problem (Cornford et al., 2015).

While not fully developed in the present work, a brief example of a control method application is provided here so that both the benefits and the limitations of the approach may be discussed later. In this example, basal traction coefficients are sought.

The spatially variable basal traction field $\beta(x, y)$ can be represented by an infinite two-dimensional Fourier series:

$$\beta(x,y)=\sum_{n=1}^{\infty}c_i\Phi_i(x,y) \tag{2.8.1}$$

in which c_i represents the expansion coefficients and Φ_i represents basis functions that are assumed to span the associated function space (MacAyeal, 1993). In practice, this series is truncated which is both a practical limitation and reflects the fact that distribution of observed surface velocity data may not allow $\beta(x,y)$ to be calculated beyond some spatial resolution. The cost function can be written as:

$$J=\iint_{\Omega}\frac{1}{2}\left(u_x-u_{x,obs}\right)+\frac{1}{2}\left(u_y-u_{y,obs}\right)d\Omega \tag{2.8.2}$$

in which the subscripted *obs* indicates observational data and Ω represents the domain. Considering the SSA system of equations in equation (2.3.7) and recognizing that $-\boldsymbol{\tau}_b=\beta^2\mathbf{u}=\left(\sum_{n=1}^{\infty}c_i\Phi_i\right)^2\mathbf{u}$, where the square is used to enforce the constraint that basal traction is positive,

$$\begin{aligned}f_1(x,y)=&\frac{\partial}{\partial x}\left(4H\bar{\eta}\frac{\partial u_x}{\partial x}+2H\bar{\eta}\frac{\partial u_y}{\partial y}\right)+\frac{\partial}{\partial y}\left(H\bar{\eta}\frac{\partial u_x}{\partial y}+H\bar{\eta}\frac{\partial u_y}{\partial x}\right)\\&-\rho gH\frac{\partial s}{\partial x}-\left(c_i\Phi_i\right)^2u_x\end{aligned} \tag{2.8.3}$$

and

$$\begin{aligned}f_2(x,y)=&\frac{\partial}{\partial y}\left(4H\bar{\eta}\frac{\partial u_y}{\partial y}+2H\bar{\eta}\frac{\partial u_x}{\partial x}\right)+\frac{\partial}{\partial x}\left(H\bar{\eta}\frac{\partial u_x}{\partial y}+H\bar{\eta}\frac{\partial u_y}{\partial x}\right)\\&-\rho gH\frac{\partial s}{\partial y}-\left(c_i\Phi_i\right)^2u_y\end{aligned} \tag{2.8.4}$$

The summation convention is used to drop the summation sign.

The method of Lagrange multipliers can be used to find minima for functions like *J'*, on which there is an outside constraint (see Bryson, 1975; MacAyeal, 1993):

$$J' = \iint_{\Omega} \frac{1}{2}\left[\left(u_x - u_{x,obs}\right) + \left(u_y - u_{y,obs}\right)\right] dxdy + \iint_{\Omega} \lambda(x,y) f_1(x,y)\, dxdy + \iint_{\Phi} \mu(x,y) f_2(x,y)\, dxdy \tag{2.8.5}$$

where a Lagrange-multiplier vector $\Lambda = (\lambda, \mu)$ has been used.

Minimizing J' requires that the variation of J' with respect to velocity components u_x, u_y, expansion coefficients C_i, and the Lagrange-multiplier components λ, μ be zero. A common simplification to achieve this is to ignore the relationship between effective viscosity and velocity (MacAyeal, 1993). When the SSA equations (2.3.7) are satisfied, the variation in λ and μ is zero, and the variation of J' with respect to arbitrary variations in u_x and u_y is zero when the following are satisfied:

$$\begin{cases} \dfrac{\partial}{\partial x}\left(4H\overline{\eta}\dfrac{\partial \lambda}{\partial x} + 2H\overline{\eta}\dfrac{\partial \mu}{\partial y}\right) + \dfrac{\partial}{\partial y}\left(H\overline{\eta}\dfrac{\partial \lambda}{\partial y} + H\overline{\eta}\dfrac{\partial \mu}{\partial x}\right) - \left(C_i \Phi_i\right)^2 \lambda = \left(u_{x,obs} - u_x\right) \\ \dfrac{\partial}{\partial y}\left(4H\overline{\eta}\dfrac{\partial \mu}{\partial y} + 2H\overline{\eta}\dfrac{\partial \lambda}{\partial x}\right) + \dfrac{\partial}{\partial x}\left(H\overline{\eta}\dfrac{\partial \lambda}{\partial y} + H\overline{\eta}\dfrac{\partial \mu}{\partial x}\right) - \left(C_i \Phi_i\right)^2 \mu = \left(u_{y,obs} - u_y\right) \\ \lambda = \mu = 0 \text{ on the boundary of } \Omega \end{cases} \tag{2.8.6}$$

Equations (2.8.6) are known as adjoint equations since they are adjoint to the linear forms of the SSA equations (2.3.7) (MacAyeal, 1993). When the variation of J' with respect to the arbitrary variations in expansion coefficients C_i is zero a solution to the inverse problem is found, and this condition is fulfilled when

$$\nabla J' = 0 \tag{2.8.7}$$

Smooth fields of basal traction coefficients, $C(x, y)$, and ice stiffening coefficients, $\phi(x, y)$, are similarly estimated by the BISICLES control problem using a nonlinear conjugate gradient method to minimize a cost function (Cornford et al., 2015). This cost function is represented as

$$J = J_m + J_p \tag{2.8.8}$$

and consists of a misfit function

$$J_m = \frac{1}{2} \int_{\Omega_V} \alpha_u^2(x, y)\left(|\mathbf{u}| - |\mathbf{u}_{obs}|\right) d\Omega \tag{2.8.9}$$

and a Tikhonov penalty function

$$J_p = \frac{\alpha_C^2}{2} \int_{\Omega_V} \left|\nabla C^2\right| d\Omega + \frac{\alpha_\phi^2}{2} \int_{\Omega_V} \left|\nabla \phi\right|^2 d\Omega \tag{2.8.10}$$

where the subscripted omega symbol, Ω_V, indicates that the calculations are carried out in the domain where ice volume above floatation is present. Importantly, $\alpha_u^2(x, y)$ is a coefficient that is equal to 1 where velocity data is available and zero otherwise (Cornford et al., 2015). Both $\alpha_C^2, \alpha_\phi^2 > 0$ and are chosen such that lower values cause faster growth in J_p than decay in J_m, and conversely that higher values cause a greater decay in J_m and slower growth in J_p (Cornford et al., 2015). Essentially, optimization is achieved by minimizing the cost function based on observed velocity and field smoothness. Where no observational velocity data is available, smoothness is principally being optimized.

To successfully minimize equation (2.8.8) can begin, initial estimates for the fields to be optimized must be provided. These initial estimates for the basal traction and stiffening factors are represented as

$$C_0 = \begin{cases} \dfrac{\rho_i g h |\nabla s|}{|\mathbf{u}_{obs}| + 1} & \text{if } \alpha_u^2 > 0 \\ 10^5 & \text{otherwise} \end{cases} \qquad \text{and } \phi_0 = 1 \tag{2.8.11}$$

while the following representations

$$C = C_0 e^q \quad \text{and} \quad \phi = \phi_0 e^p \tag{2.8.12}$$

guarantee positive definitiveness and equation (2.8.8) can be minimized with respect to q and p (Cornford et al., 2015).

2.8.1 Implementation and Spatial Maps

The BISICLES control problem is run for the entire continent over Bedmap2 topography and then again for the model domain over each bed (Figure 5). The process begins and proceeds using data comprising the geometry of the problem (bed elevation, ice thickness); ice temperature; and control data (ice velocity, initial estimates of the fields in question) to generate basal traction and ice stiffening coefficients (Figure 6, Figure 7, & Figure 8). The sole purpose of the continental run is to establish a realistic velocity field so that the *model* AS catchment may be delineated and used to create the experiment model domain. This is accomplished by first subregioning a rectangular domain that includes the AS catchment. Then the velocity components are used to

identify and exclude areas where ice is not flowing into catchment. Exclusion is accomplished by turning off flow outside the AS catchment and raising basal coefficients to a high value, 1 x 10^5. The necessary input files are then subregioned and the process is repeated to give basal traction and stiffening coefficients corresponding to the Bedmap2 and Goff beds (Figure 5). Differences in basal traction between the beds will be addressed in Section *4.1 Spatial Patterns of Difference in Driving Stress*.

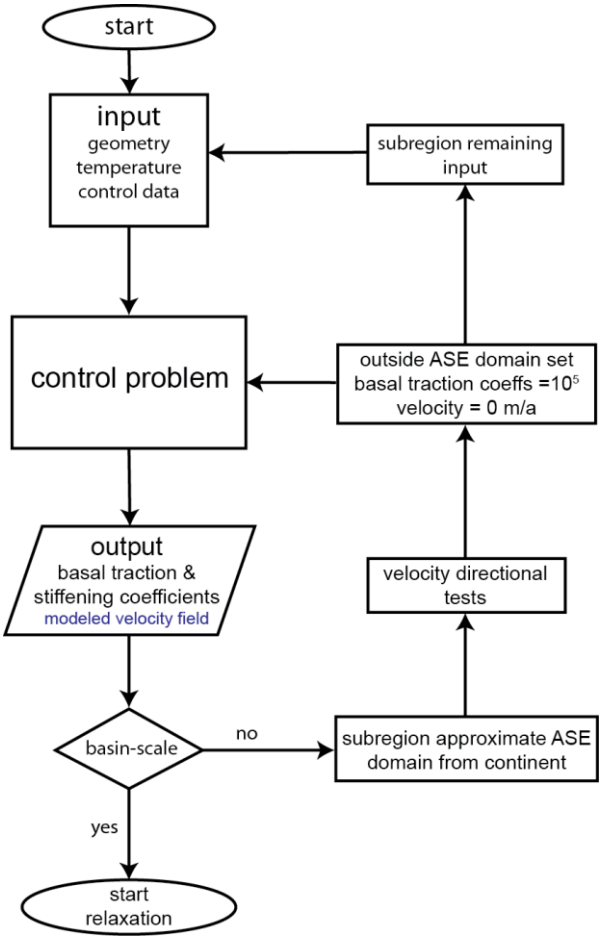

Figure 5. Flowchart showing how model initialization is implemented. The control problem is run twice; first at the continental scale then at the basin-scale. The objective of the continental control run is to obtain a realistic velocity field that can be used to delineate the ASE sector catchment basin. The basin-scale control run finalizes the basal traction and stiffening coefficients over each bed.

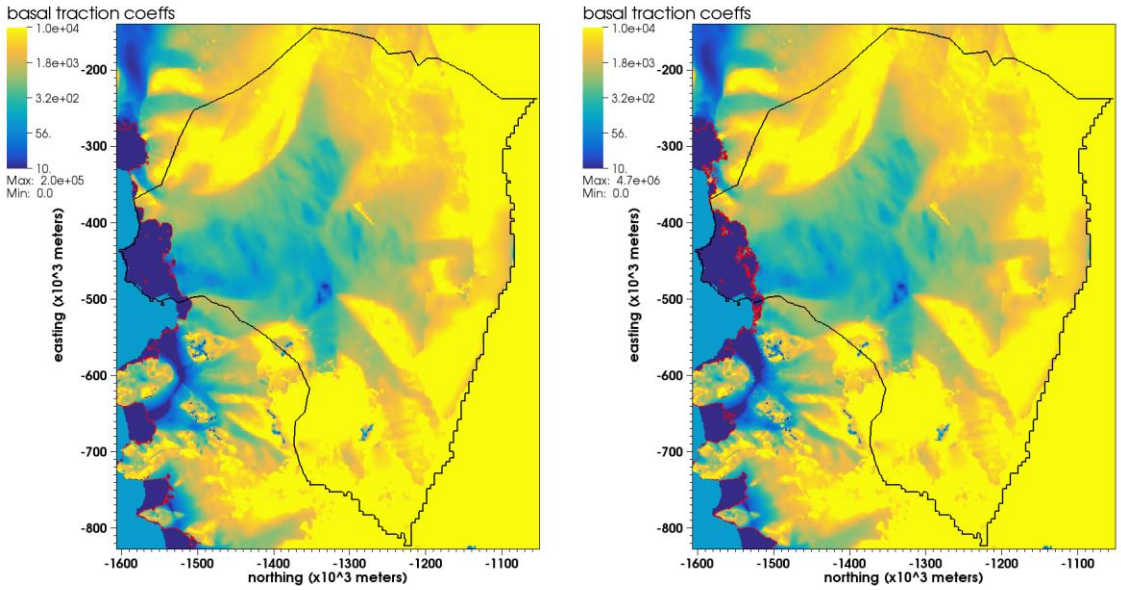

Figure 6. (LEFT) Basal traction coefficients for Bedmap2 with the Thwaites catchment delineated in black. (RIGHT) Basal traction coefficients for the Goff Bed. (BOTH) The red line indicated the grounding line position after relaxation. A log scale for basal traction is used for both panes

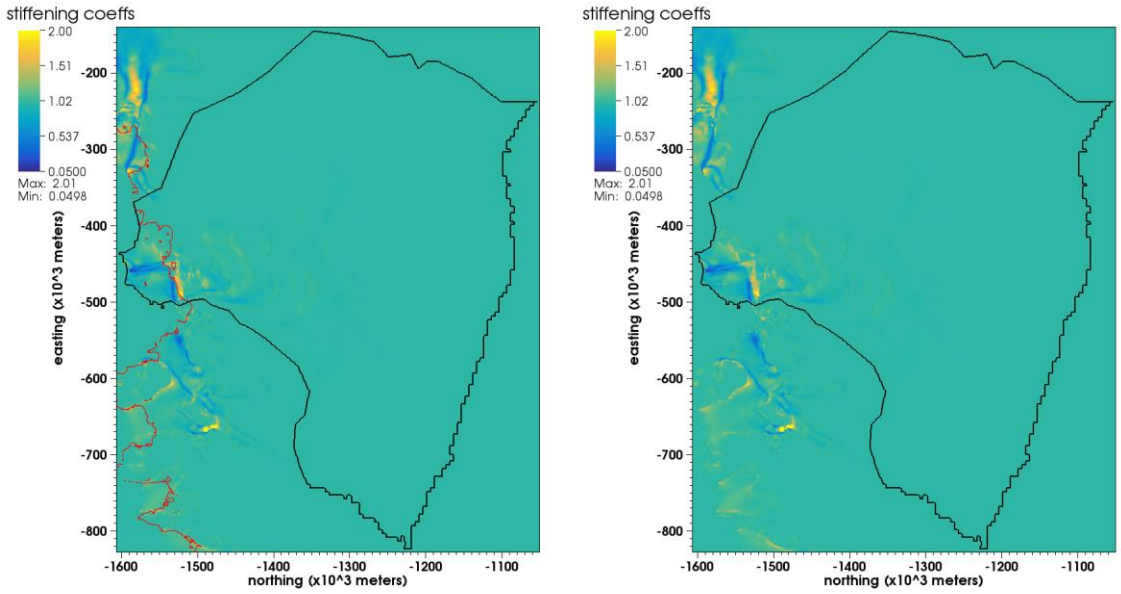

Figure 7. (LEFT) Stiffening coefficients over Bedmap2 in the Thwaites catchment with the grounding line at the end of relaxation shown in red. (RIGHT) Same as left pane but with grounding line removed to provide more detail.

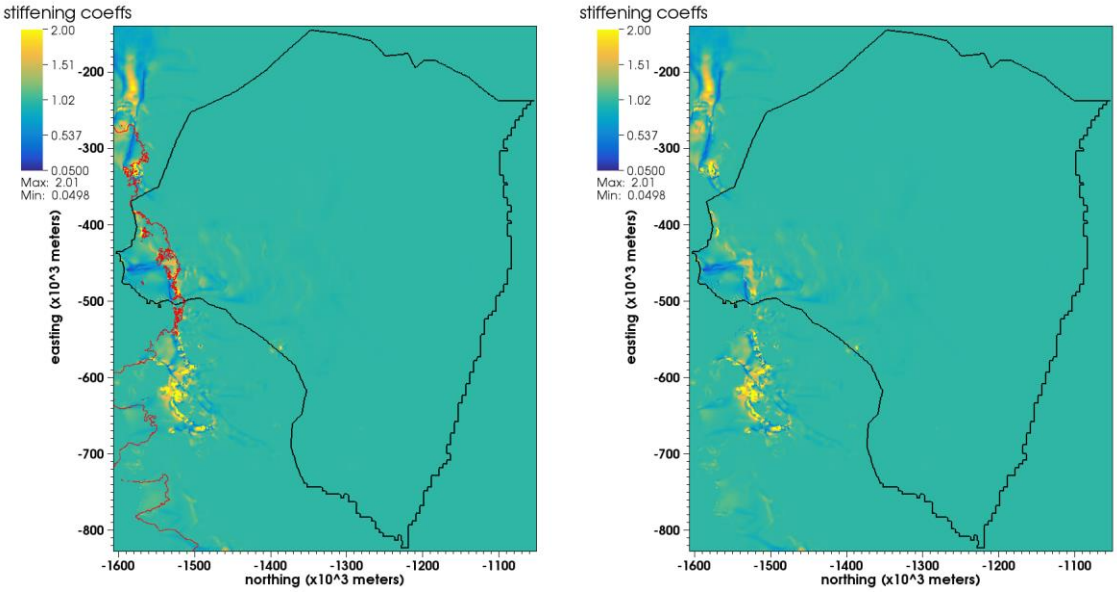

Figure 8. (LEFT) Stiffening coefficients over the Goff bed in the Thwaites catchment with the grounding line at the end of relaxation shown in red. (RIGHT) Same as left pane but with grounding line removed to provide more detail.

2.9 Oceanic Forcing

Parameterized basal melt rates are applied to floating ice in order to simulate an oceanic forcing to which the ice sheet responds. The goal in developing this forcing is to perturb it such that an instability is initiated within the model ice sheet, that is, a sustained retreat that does not depend on the external processes. Thus, while the ocean melting parameterization should be realistic, absolute fidelity to ocean processes is not required. The melting parameterization is only applied to floating ice because the basal traction coefficients for grounded ice, optimized by the control problem, include a basal melt contribution. The surface accumulation field is constant through time, with the result that in model experiments, the ice sheet solely responds to an oceanic forcing.

The parameterization has a piecewise linear form (PLF), with coefficients informed by the work of other authors (e.g. Joughin et al., 2014) and short trials. Using the rationale that melt rates vary in part according to the circulation of water under the shelf, a simple dependence on the thickness of the water layer under the floating ice is

$$\dot{m} = f(wc_{thk}) = \begin{cases} -1 & \text{for } wc_{thk} \leq 100 \text{ m} \\ 0.005wc_{thk} - 1.5 & \text{for } 100 \text{ m} < wc_{thk} \leq 200 \text{ m} \\ 0.004wc_{thk} - 1.3 & \text{for } 200 \text{ m} < wc_{thk} \leq 250 \text{ m} \\ -0.3 & \text{for } wc_{thk} < 250 \text{ m} \end{cases} \quad (2.9.1)$$

used during relaxation where the mean annual melt rate, $\dot{m}$ in ma^{-1}, is a function of water column thickness, wc_{thk} (Figure 9). Following the inverse approximation of other model parameters, the basal melt parameterization is applied during the model relaxation toward steady state.

In order to represent spatial control on heat transport under the shelf, the basal melting parameterization is only applied to floating ice where the bedrock beneath is at least 420 meters below sea level. If the bed is not at least this far below sea level, then no melt is applied to the ice above regardless of the water column depth. In effect, this restriction limits the locations where warm water (which can be thought of as MCDW) interacts with floating ice beneath. As the MCDW flows near the continental slope, submarine channels provide conduits that can allow it to maintain a higher heat content to locally interact with ice (Sergienko, 2013; Thoma et al., 2008). This implies that melting

is not likely to be spatially uniform and that stronger melting is possible over features like the head of a canyon.

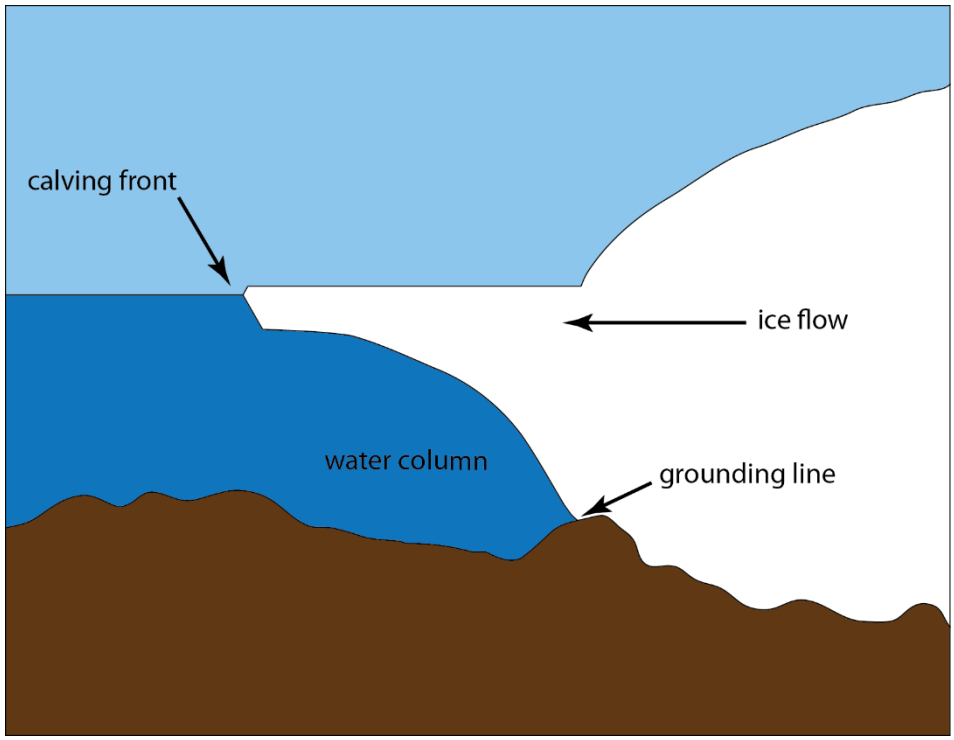

Figure 9. Simplified cartoon depiction of transitional regions of a marine terminating glacier. Grounded ice transitions to floating ice beyond the grounding line. At the calving front, the ice shelf ends with detached icebergs located beyond. The water column beneath the ice shelf tends to narrow as it approaches the grounding line.

Once the ocean parameterization is turned on in the model, a new steady state must be found. Artifacts arising from the inversion may complicate this step because adjustments made to force agreement among present-day boundary conditions may not represent a realistic steady state configuration. An unperturbed simulation with melting applied to achieve steady-state may be used to identify long-lived transients, should they arise.

Localized transients remained after 200 years into the relaxation when the model was run forward in time using the coefficients in equation (2.9.1). This is because the regional effects of ice grounded over an artificial bedrock high on the outer upper portion of the tongue, are long-lived, even though the pinning point ungrounded within the first decade of simulation (Figure 10). The bedrock high was constructed by BISICLES

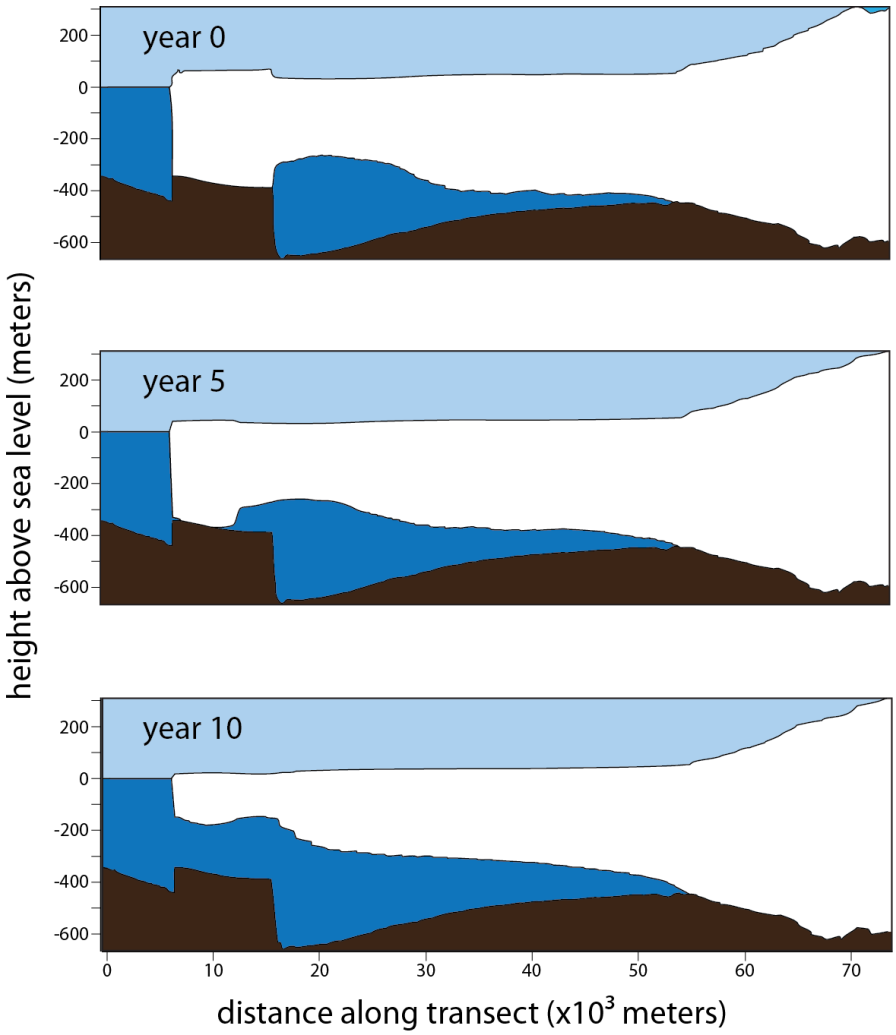

Figure 10. Ice grounded over a bedrock high under Thwaites tongue quickly becomes ungrounded once a simulation begins, even if no forcing is applied. A model steady-state with an ice geometry that conforms to the current observed coastline cannot be achieved with the fields used to run the model.

developers to accommodate initialization (Martin, 2014). In other words, a reasonable model match to observed ice flow velocities on Thwaites tongue via the control problem was not be achieved without it. The initial geometry of the floating ice over this bedrock high and thinner floating ice immediately south, toward the continent, plays a major role once ice advection begins (Figure 10). Advection pushes the thinner ice toward the bedrock high, but as it is thinner the high can no longer act as a pinning location. As the system adjusts to the accumulation field used, the floating ice never gets thick enough to ground on this high again.

As model steady-state is not achieved within a reasonable amount of runtime and ice geometry in this location cannot conform to the current observed coastline, the final stages of model initialization were adapted. A new PLF is used for the first 40 years of relaxation while equation (2.9.1) is used for the last 60 years. Note that both functions

$$\dot{m} = f(wc_{thk}) = \begin{cases} -10 & \text{for } wc_{thk} \leq 100 \text{ m} \\ 0.08wc_{thk} - 18 & \text{for } 100 \text{ m} < wc_{thk} \leq 200 \text{ m} \\ 0.034wc_{thk} - 8.8 & \text{for } 200 \text{ m} < wc_{thk} \leq 250 \text{ m} \\ -0.3 & \text{for } wc_{thk} < 250 \text{ m} \end{cases} \quad (2.9.2)$$

are implemented over the AS in an attempt to bring Thwaites into model steady-state. There does not appear to be a single PLF that optimizes a model steady-state for all glaciers in this region. The effect of using equation (2.9.2) for the first 40 years is to save time and computational expense while bringing the coastline into the configuration that it would achieve with a much longer relaxation run using only equation (2.9.1). Model

steady-state is still not satisfactorily achieved within 100 years using both equations (2.9.1) & (2.9.2). As the experiments are run, however, their steady-state run counterpart, using equation (2.9.1) as the only forcing, is continued so that differences between the two can be accounted for until such time as the transient disappears or becomes negligible.

2.9.1 Perturbation and Experiment Design

The system is perturbed after the 100-year relaxation runs. The perturbation consists of a constant increase of melt rate applied to all floating ice with time, which is applied in addition to the PLF in equation (2.9.1). This slow ramp (aka anomalous forcing) increases melt by 1 meter every 20 years. The objective here is simply to generate a genuine marine ice sheet instability such that grounding line retreat down the reverse slope and thinning of ice in the interior will continue via positive feedback if the ramp is turned off. This is opposed to a situation where the ramp is turned off and the grounding line stalls.

Two model experiments are conducted and each experiment involves two simulations. For experiment 1, both simulations are conducted over Bedmap2 with different picks for the time of instability. This allows us to examine the effect of a small difference in the magnitude of the forcing on grounding line retreat. Once the instability is detected, the anomalous forcing is turned off and the ice sheet is allowed to iterate further with only the steady ocean boundary condition at work. The forcing is turned off a decade later for the second simulation in this experiment. Experiment 2 proceeds in the

same manner as experiment 1 but addresses the effect of bed topography on retreat by comparing the generation of instabilities and resulting retreat rates over different beds. The Bedmap2 simulation with the latter ramp shutoff time is compared to a third simulation conducted over the Goff bed for this experiment.

Unfortunately, after year 200 in the first experiment, the PLF parameterization was overwritten during a migration from one computing cluster to another due to complications with the revision control permissions. A similar event occurred at the start of the anomalous forcing in the Goff Bed simulation. The intended PLF was replaced with a simpler parametrization: constant melt rate of 0.3 ma^{-1} applied to all Thwaites floating ice except at the fringe near the calving front where it increases to a maximum of 1 m melt. This event was not detected until analysis of the model outcomes was underway. That it was not detected sooner is a sign that the effect of the mistake was minor. This is because the anomalous forcing overwhelms the PLF and the smaller melt rate was only applied during the unstable retreat phase, when a small melting rate is desirable (the attention should be on the instability, not the ocean forcing).

Additional experiments were run in order to ensure directly comparable model time series. These experiments are corrected runs that use the slow ramp with the PLF as intended to examine differences in the timing of instability. The results are addressed in Section *3.1 Instabilities*.

3.0 RESULTS

Applying the slow ramp forcing has three main effects relevant to the evolution of the unforced system. In the case of a later (earlier) onset of instability, these are decreased (increased) area of floating ice, a general increase (decrease) in surface gradients near the grounding line, and thicker (thinner) grounded ice at the grounding line when the instability initiates. Thwaites' geographic setting does not include a large embayment to provide large lateral resistive stresses via contact with the coastline so the loss of floating ice here (i.e., initially Thwaites Tongue) is not as important to flow and retreat rates as it might be otherwise. This leaves driving stress, offset by basal resistive stresses, as the principal control on retreat rate.

3.1 Instabilities

The slow ramp produced instabilities over both beds. Three spatial scales are used when discussing instabilities and unforced retreat: *basin-scale*, the entire Thwaites catchment; *regional*, involving thousands of square kilometers of the basin or a significant portion of the length of the grounding line within Thwaites catchment; and *local*, which involves hundreds of square kilometers down to sub-kilometer scale. It is important to note that in this basin-scale study, regional retreat trends and effects may vary at any given time. That is, each location on the grounding line is affected by adjacent regions and different regions may be experiencing different trends. Regional instability is identified as the time when the magnitude of glacier response exceeds the magnitude of the forcing and leads to basin-scale retreat. This can be visualized by

comparing the change in grounded ice area vs the anomalous melt rate (Figure 11). Local instabilities, for example near year 170 over Bedmap2, support unforced retreat for decades in some cases but retreat eventually stalls (Figure 11 & Figure 12). Turning off the slow ramp prior to the initiation of any scale of instability leads to rapid grounding line stall (Figure 13).

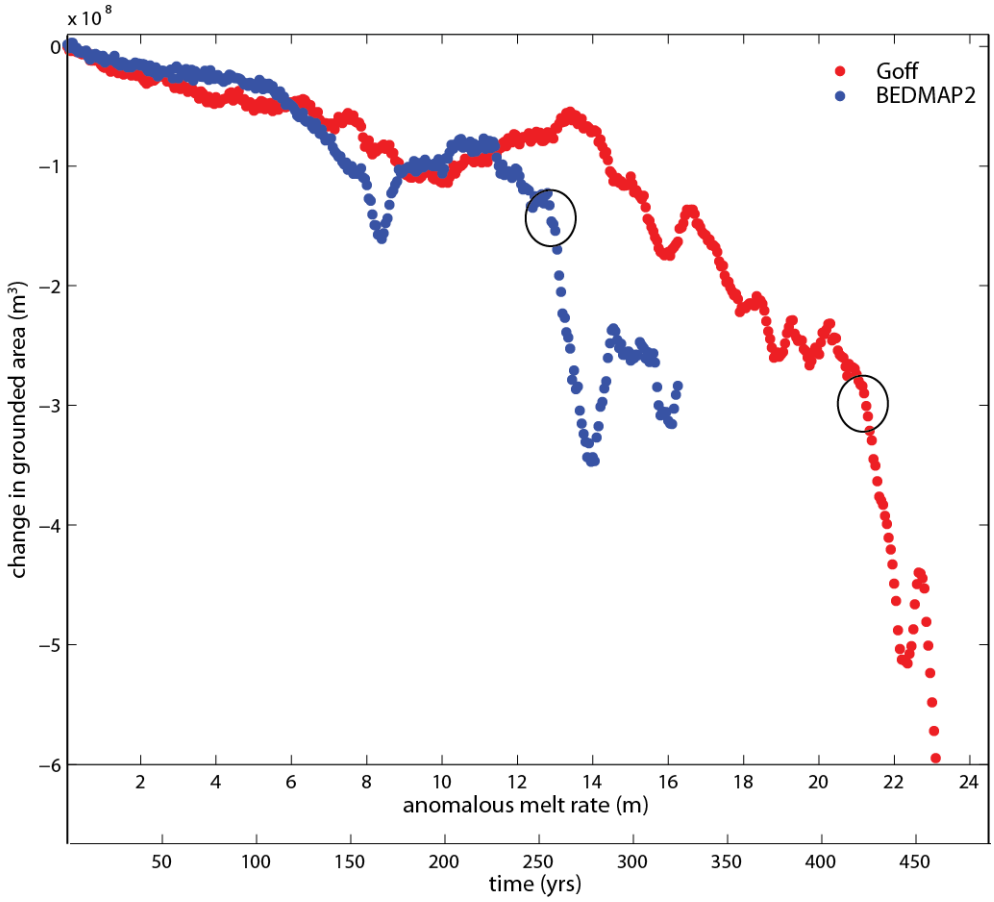

Figure 11. Change in smoothed grounded ice area vs anomalous melt rate / time. The ellipses indicate the approximate rate / time where basin-scale instabilities were detected. Therefore, slow ramp shutoff times for all simulations in the model experiments are demarcated by these ellipses.

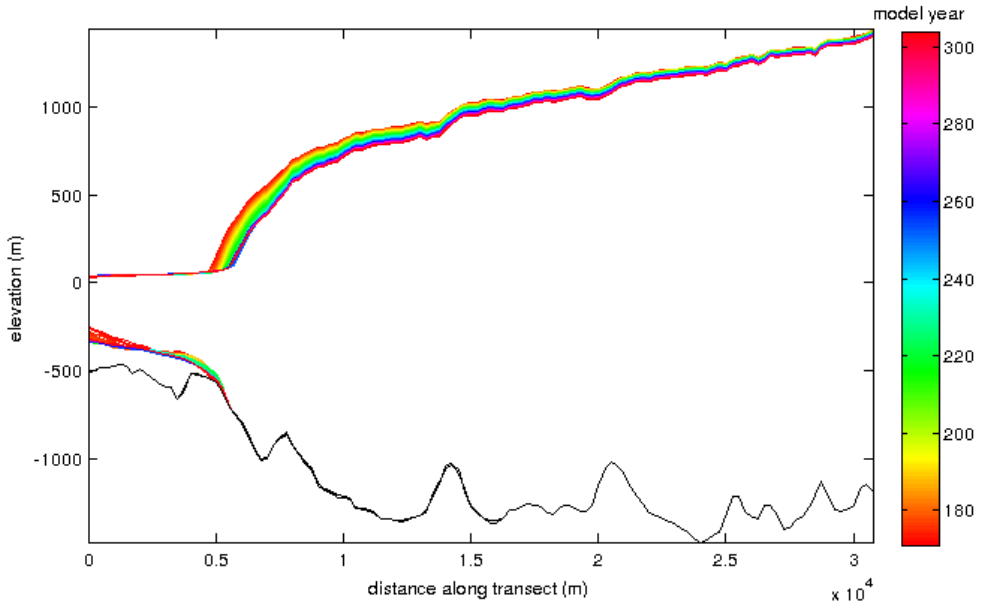

Figure 12. Example of grounding line stall along the approximate centerline after a local instability. The slow ramp was turned off at the initiation of the local instability over Bedmap2 at year 170. Although difficult to discern at the bed, the grounding line ultimately retreated about 750 m along this transect. Time interval is 1 year.

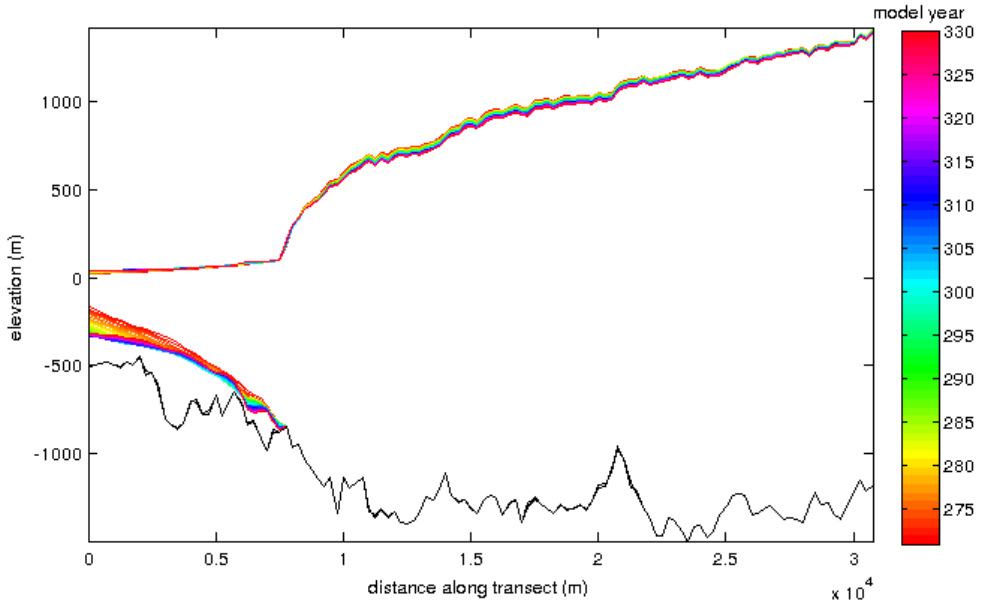

Figure 13. Example of grounding line stall along the approximate centerline when there is no instability. The slow ramp was turned off at year 270 over the Goff and retreat quickly stalled. Time interval is 1 year.

The simulations comprising the experiments are termed B260, B270, and G425, respectively, in which the number indicates the model year in which the anomalous ocean forcing is shut off (Figure 11). Hereafter, the results for experiment 1: B260 vs B270 and experiment 2: B270 vs G425 will be presented independently.

The corrected runs, used to ensure comparability of the series in experiments 1 and 2, show that the timing of instability does not greatly change over either bed when the slow ramp is used with the intended PLF (Figure 14 & Figure 15). Over Bedmap2,

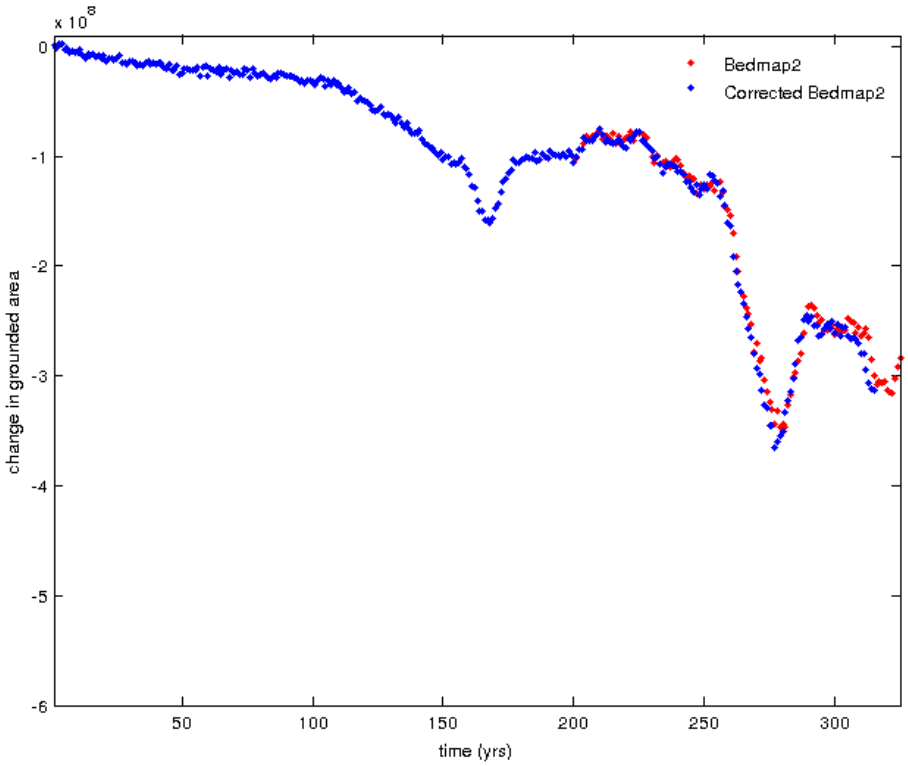

Figure 14. Instability timing difference over Bedmap2. The model run consisting of the slow ramp plus constant rate is shown in red, and the corrected slow ramp plus PLF shown in blue. There is a maximum of three years difference in the timing of regional instability.

The correction shows that regional instability occurs closer to year 257, a difference of three years from the pick for instability. Over the Goff bed, the correction shows instability occurring about year 417, eight years difference from the Goff simulation pick used in experiment 2. As the differences in instability timing between the corrected model runs are minor compared with those incorporating the constant melt rate, the blunder will not have a significant impact on experiment outcomes.

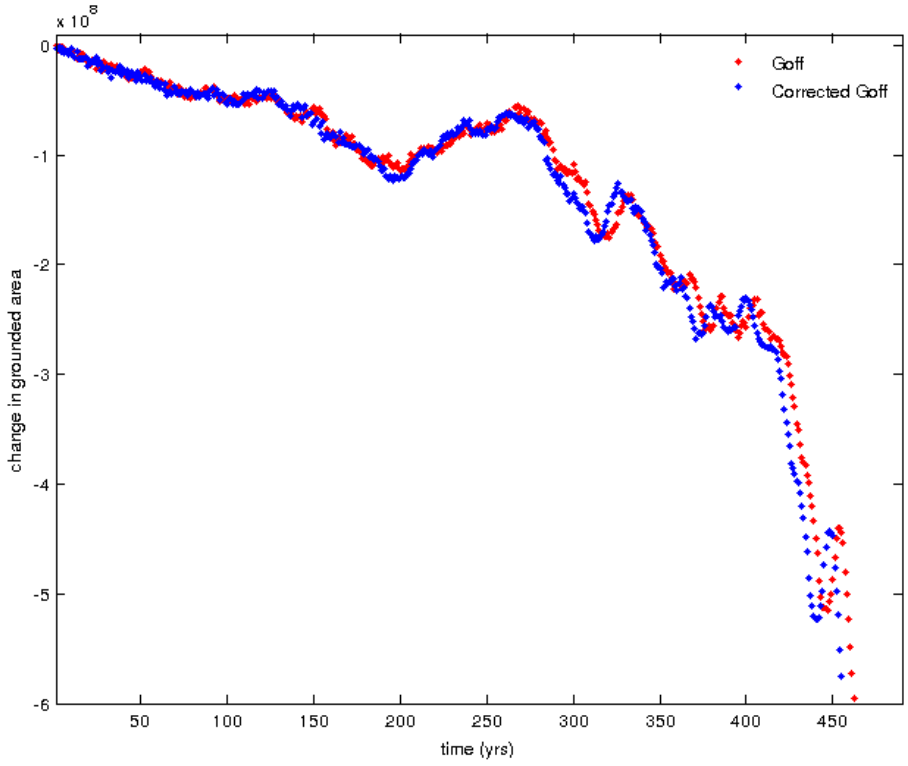

Figure 15. Instability timing difference over the Goff bed. The model run consisting of the slow ramp plus constant rate is shown in red, and the corrected slow ramp plus PLF shown in blue. There is a maximum of eight years difference in the timing of regional instability over this bed.

3.2 Analysis tools

Comparisons across the two simulations are presented both as maps and as summary statistics plotted against grounding line position during the retreat. The latter is accomplished by co-locating the grounding line across along fixed transects in the model domain. The transects were created following particle flowpaths (Childs et al., 2012) although one path, uppermost in the figures, was altered in the interior of the basin to follow the centerline of a deep channel (Figure 20). While the map view is comprehensive, the transects allow comparisons to be made across many intervals of time. Additionally, animations of fields of interest and ice profiles along transects aid in interpretations (Appendices C - M).

Retreat is presented and discussed in terms of driving stress and ice flux (discharge) across the grounding line. The reasons for this are twofold. First, driving stress encapsulates several related state variables. Ice flow is the result of surface slope, ice thickness, and basal sliding, all of which both depend on driving stress. Second, discharge of ice across the grounding line causes the center of the ice sheet to thin, which drives further retreat.

In order to focus the analysis, spatially-varying and summary statistics are restricted to a region of interest (ROI) around Thwaites glacier (Figure 16) The ROI includes the glacier and its tributaries but excludes areas where flow is less than 10 ma^{-1}. This removes effects arising in the low-flow boundary regions from the calculation. The ROI boundary is not fixed through time or across simulations although differences are

small and by definition occur well away from areas subject to rapid change (Appendices L & M).

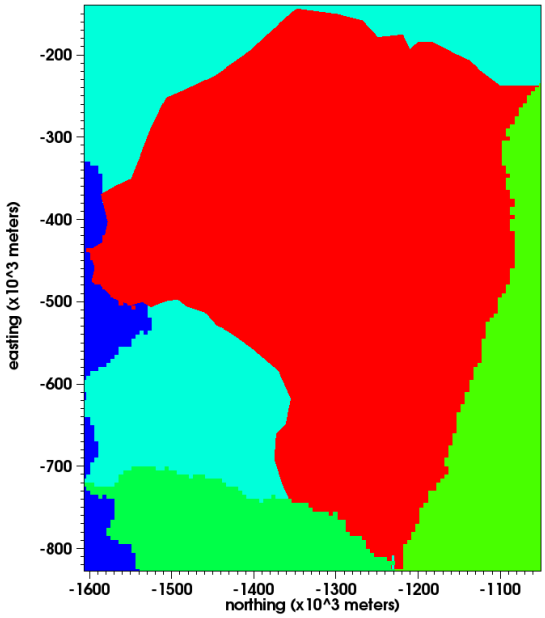

Figure 16. The region of interest (ROI) for calculating driving stress is within the Thwaites catchment shown in red. Note, however, that Driving stress is only calculated only over grounded ice where the flow velocity exceeds 10 ma^{-1}. Thwaites glacier is a part of the partially shown AS sector (light blue). Other portions of regional drainage catchments are shown in shades of green.

Driving stress τ_d is calculated as

$$\tau_d = \rho g H \left|\nabla s\right| \tag{3.2.1}$$

Ice flux across the grounding line is calculated for the entire Thwaites basin and where each of five transects cross the grounding line.

Differences in grounding line position across the experiments will be evident in a side-by-side comparison of the plan view maps but a quantitative assessment of the associated model fields is less simple. Differencing model fields at equivalent times would be complicated and possibly misleading because some ice that is grounded in one

case is floating in the other. A better approach is to compare times of equivalent grounding line position. Co-location in time identifies genuine differences in the state of the ice sheet that are due solely to the slightly different conditions at the time the unstable retreat begins.

Perfect co-location between simulations along the entire length of the grounding line is impossible because spatial patterns of retreat are complicated (Appendices L & M). For comparisons over the same bed, the criterion for co-location is that the two grounding lines are separated by less than 250 meters along the transect that represents the approximate centerline, T3. Note that the five curvilinear transects throughout the Thwaites catchment are referred to and labeled as T1 (uppermost) through T5 (lowermost) (see Figure 20) When the overall grounding line configurations do not match well using T3, another transect can often be substituted (Appendix A). The general shapes with both retreats over Bedmap2 along the entire lengths of the grounding lines are most similar when points along this transect are compared. The total number of co-located grounding line positions is limited by the differences in retreat rates such that if rapid retreat occurs in one simulation but not the other the distance criterion won't always be met. Also, the lobate patterns of retreat and differences therein between the simulations can eliminate instances of co-location. As a result, there are occasional discontinuities in time (forward jumps) for co-located grounding line positions (Appendices A & B).

3.3 Experiment 1: Retreats over Bedmap2

The progress of an unforced retreat depends on the state of the system at the end of the forced retreat. The position of the grounding line in the basin is important because it dictates ice thickness at that boundary, and the surface gradient induced by the forced response is important because it dictates basin-scale driving stress at shutoff. Since the instability is generated over a reverse slope, ice thickness generally increases in the retreat direction (upstream), tending to maintain the driving stress. However, the presence of bumps on the bed locally modulates the surface gradient and this can either promote or retard retreat. As the grounding line moves up toward the crest of a bump, the flux through the grounding zone is reduced, temporarily slowing retreat and leading to a locally larger surface gradient (Figure 17). The opposite is true as the grounding line crests a bump and moves in the direction leeward to the direction of retreat. Furthermore, large bumps and linear features on the bed tend to have been assigned higher basal traction coefficients in the model initialization, which also tends to cause a steepening in the gradient while temporarily slowing retreat (Figure 17). All together, bumps may locally or regionally increase or decrease surface gradients, flow velocity, and discharge in ways that generate considerable spatial and temporal variability in the overall retreat.

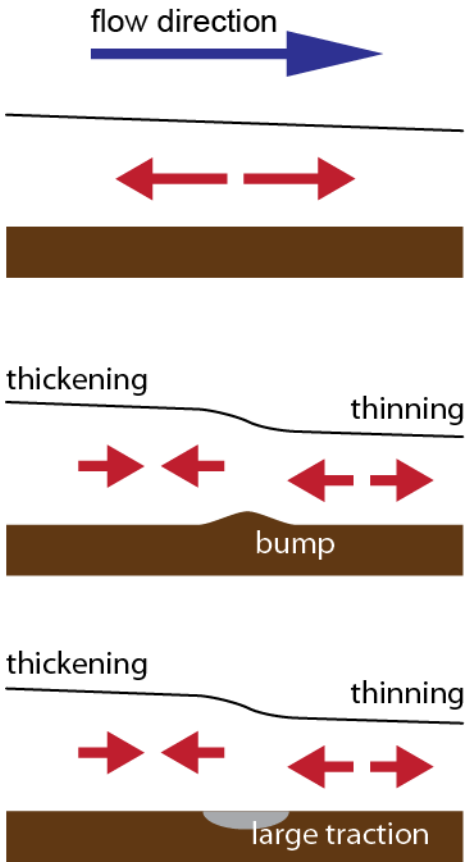

Figure 17. A cartoon demonstrating the effect of bumps and large basal tractions on ice geometry. Ice flows in the direction dictated by the surface gradient (blue arrow), and if flow is unimpeded and the ice supply is finite this leads to thinning as shown by the diverging red arrows (TOP). A bump in the bed causes thickening and a local increase in the surface gradient on the "windward" side and thinning on the leeward side. Should the grounding line retreat through a geometry like this, a local decrease and then increase in retreat rate would result (MIDDLE). A large basal traction has a similar effect to a basal high (BOTTOM).

An instability is first detected at year 260 and this is when the first retreat simulation, B260, begins (Figure 11). The anomalous forcing at that time is 13 ma^{-1}. Ten years later, when the B270 simulation begins, the anomalous melting rate is 13.5 ma^{-1}. Despite the closeness in time and similarity in the anomalous forcing ice sheet

configurations have important differences at the start of the two retreat simulations. As a result, the unforced retreats over the Bedmap2 bed also have significant differences.

Both grounding lines have an arcuate shape at the start of the two retreat simulations, though this shape is more pronounced in B270. Near the centerline of the glacier, (ordinate 2.645 x 10^6 meters on the model grid), the B260 grounding line has retreated about 57.5 km while the B270 grounding line has retreated about 66 km (Figure 18). The maximum horizontal distance between the two grounding line positions is about

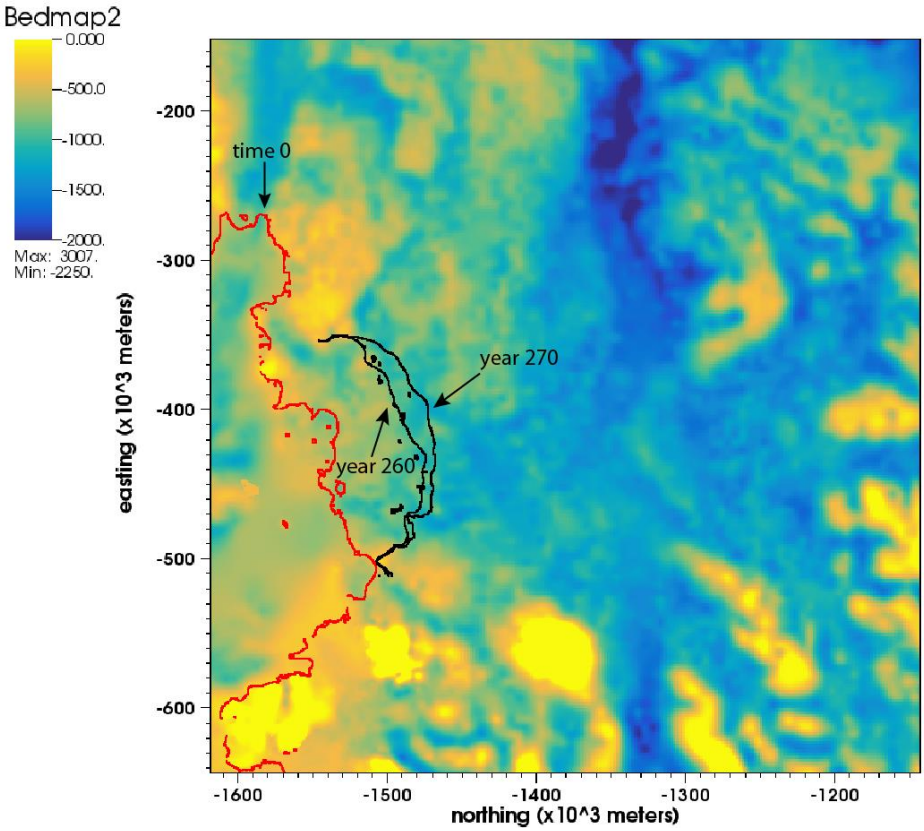

Figure 18. The grounding line positions at the years of slow ramp shutoff over the Bedmap2 bed elevation. The grounding line positions are shown as black lines. The red line shows the grounding line position at the initiation of the slow ramp in anomalous forcing.

22 km. The average ice thickness at the grounding line is 858 m at the start of B260 and 930 m when the shutoff is at year 270. Small ice rises tend to confound examination of surface gradients in the vicinity of the grounding line but in general, the surface gradient near the grounding line is lower at the start of B260 than at the start of B270. Grounded ice volumes at the start of B260 and B270 are 4.657×10^5 km^3 with a volume of flotation (VAF) of 2.442×10^5 km^3 and 4.623×10^5 km^3 and 2.425×10^5 km^3, respectively.

The longer forcing period leads to a larger mean driving stress at the start of the B270 scenario relative to B260, 90.2 kPa and 88.0 kPa, over the respective ROIs. Viewed spatially, the driving stress is larger near the grounding line for B270 (Figure 19). This is because thinner, lower slope ice has already been lost that was still present at B260. Put another way, the B270 grounding line has moved back into thicker, steeper ice at the start of the instability.

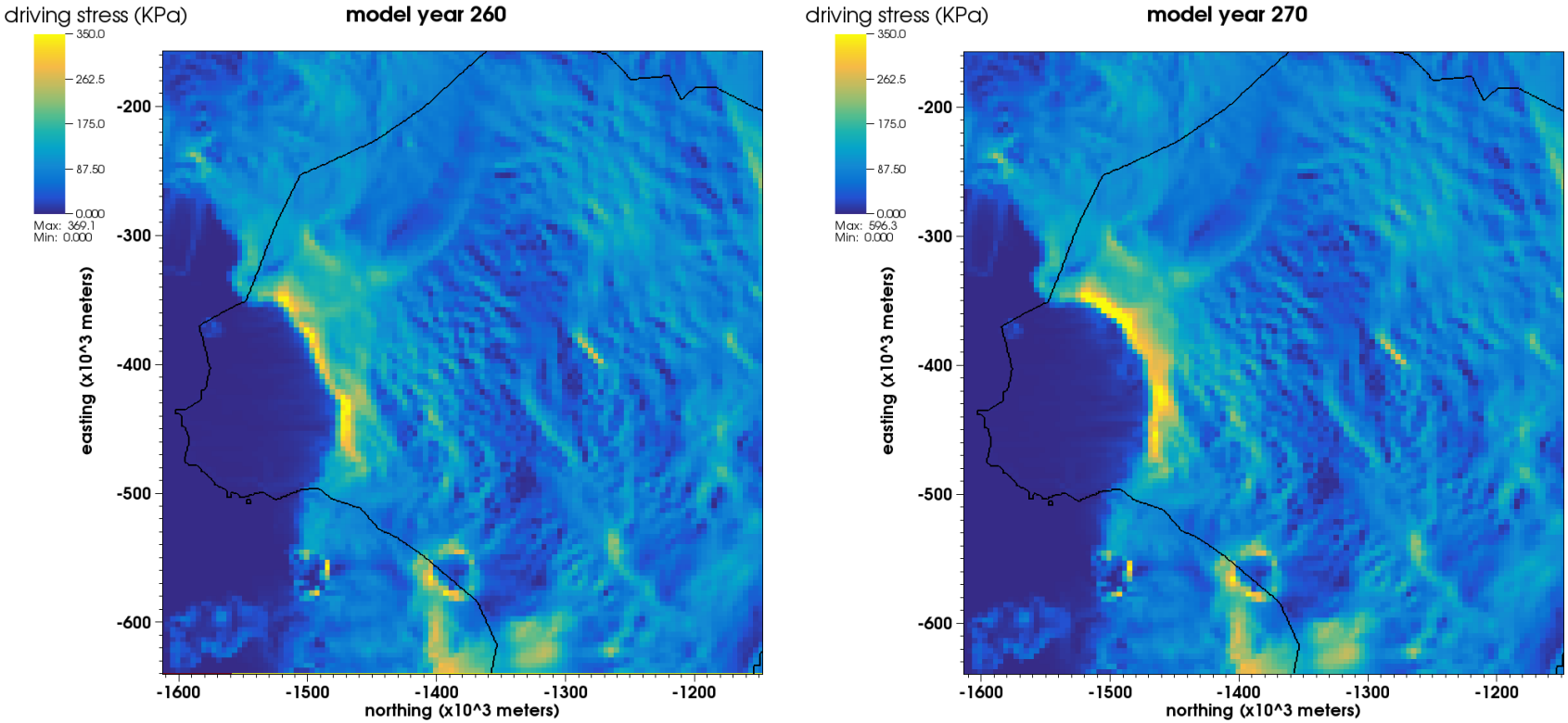

Figure 19. Driving stress at 4km resolution in the ROI and surrounding areas at year 260 (RIGHT) and year 270 (LEFT). Higher intensity colors represent larger stress. Driving stress near the grounding line is higher at year 270 than at year 260 due to a longer period of forcing increasing surface gradients and thicker ice down the reverse slope (toward interior of basin).

The unforced retreat progresses more rapidly in the B270 simulation than in B260. The difference between the two simulations grows until the ice supply begins to dwindle and the faster retreat starts to slow down (Figure 20 & Figure 21). Spatial details in the time co-located grounding line position vary across the two simulations, even though the retreats play out over the same bed geometry. These differences are both causes and effects of differences in the driving stress.

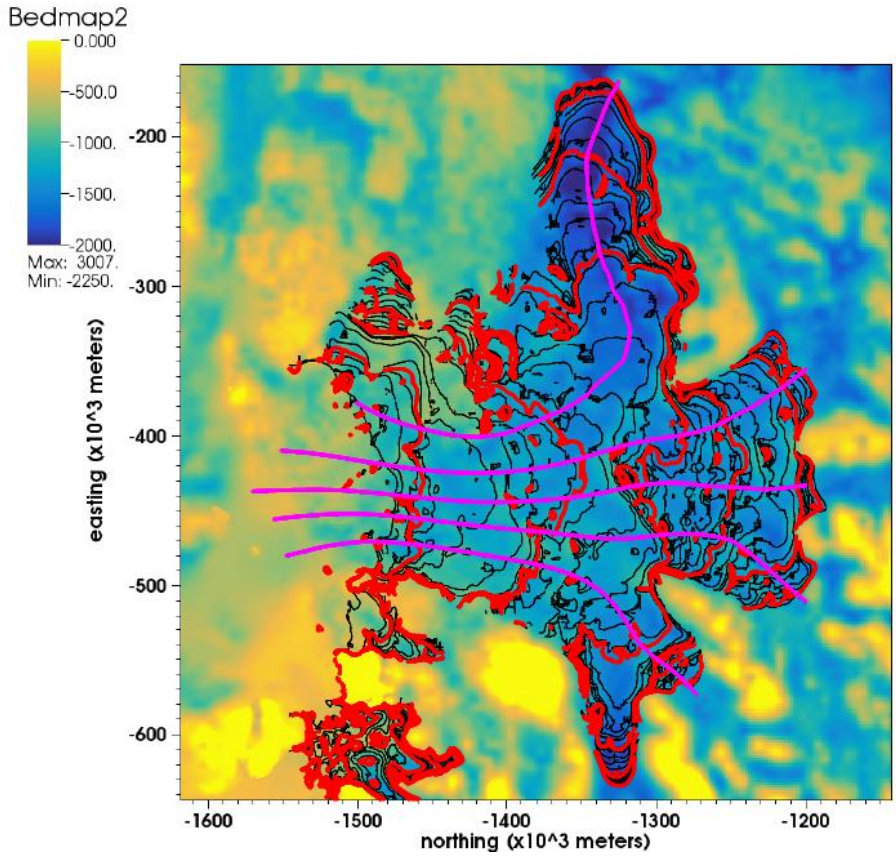

Figure 20. Contours of grounding line retreat for B260. The contour interval for black lines is 100 years starting the year 261. The contour interval for red lines is 500 years starting at year 500. The magenta lines indicate the location of transects with T1 being the uppermost and T5 the lowermost.

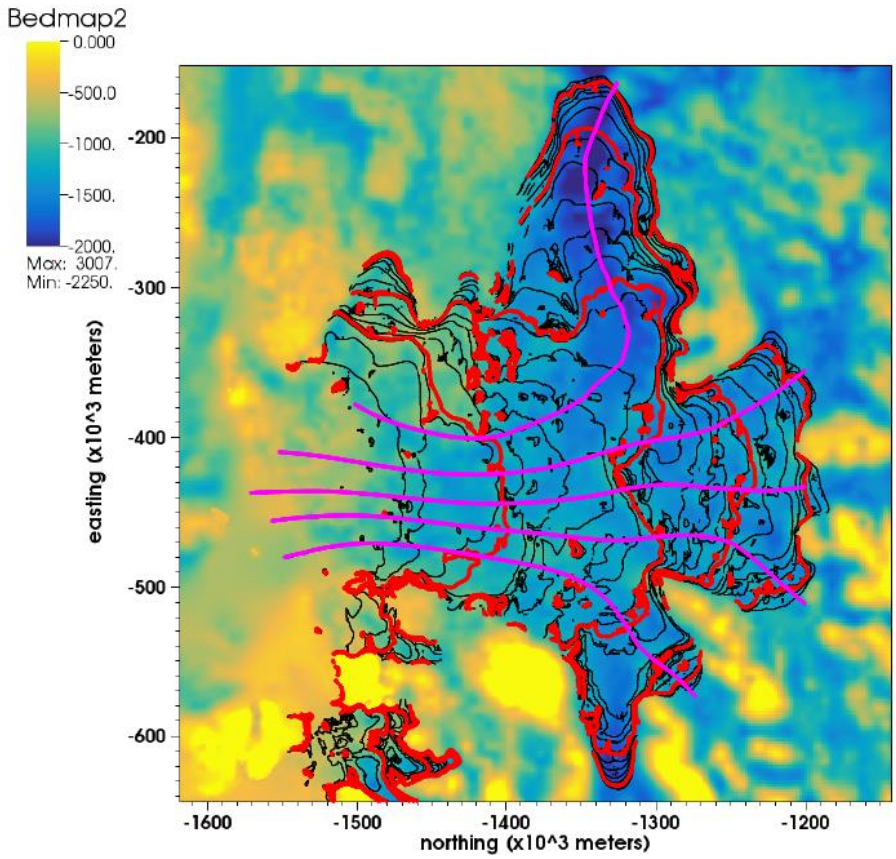

Figure 21. Contours of grounding line retreat for B270. The contour interval for black lines is 100 years starting at year 271. The contour interval for red lines is 500 years starting at year 500. The magenta lines indicate the location of transects.

Overall, the mean driving stress over the ROIs is larger in the B270 simulation than in B260 and the difference increases over time (Figure 22). However, there are important details in the driving stress difference and these must be interpreted with care. From the 1st observation until the 17th, the difference in model years decreases. This is because the grounding line for B270 advances locally (below about -425 E) between model years 273, (observation 3) and 287 (observation 17). Grounding line advance does not happen everywhere, but instead is associated with highs on the sea floor, where re-grounding is possible, and where basal traction may be locally large. After the 17th observation, the

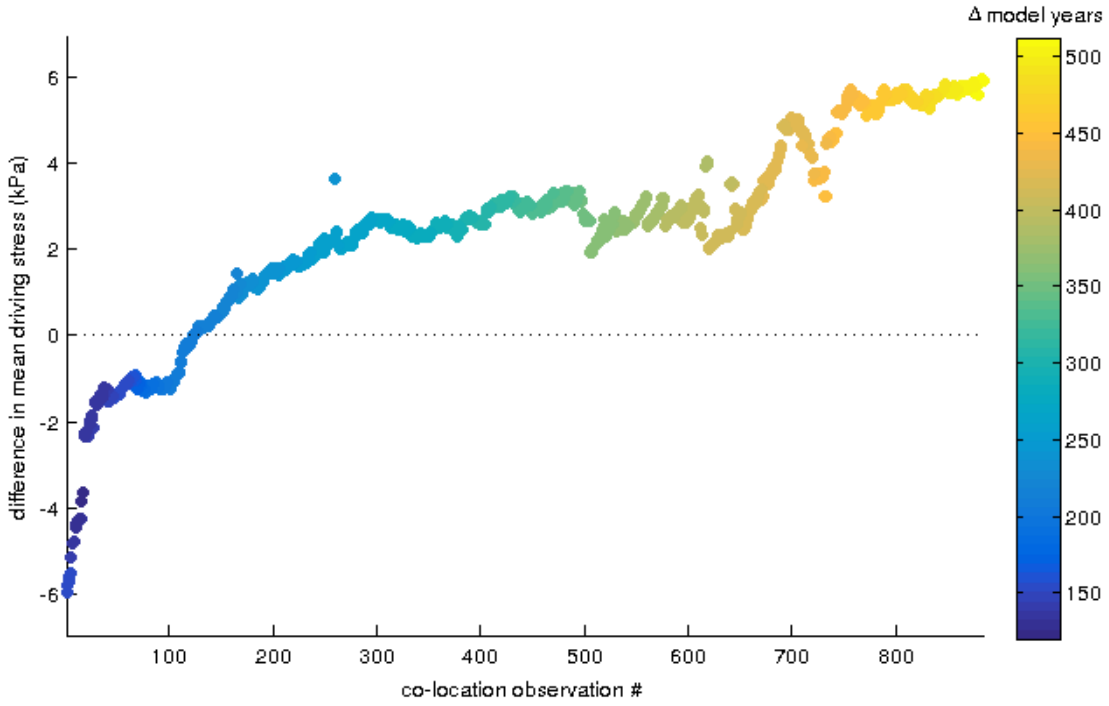

Figure 22. The difference in mean driving stress over Bedmap2 (B270 - B260). The colorbar indicates the difference in model years as B260 minus B270. Initially there is an approximate 150-year difference between co-located positions that decreases to a minimum of 120-years difference associated with local grounding line advance in B270 before increasing again as the grounding lines retreat over the basin.

difference in model years generally tends to increase as the observation numbers increase (Figure 22).

Another important detail emerges during the first 17 co-located observations. While the western portion of the grounding line for B270 advances below about -425 E, there is an unrelated grounding line configuration mismatch in the eastern region, between approximately -350 km E and -400 km E, with the grounding line for B260 retreated farther into the basin here (Figure 23). The grounding lines are retreating into a region of relatively high basal traction here so surface gradients, hence driving stress, will

be relatively high also. The effect on driving stress is brief, and as the overall grounding line retreat proceeds, the difference between B270 and B260 grows increasingly positive (Figure 24).

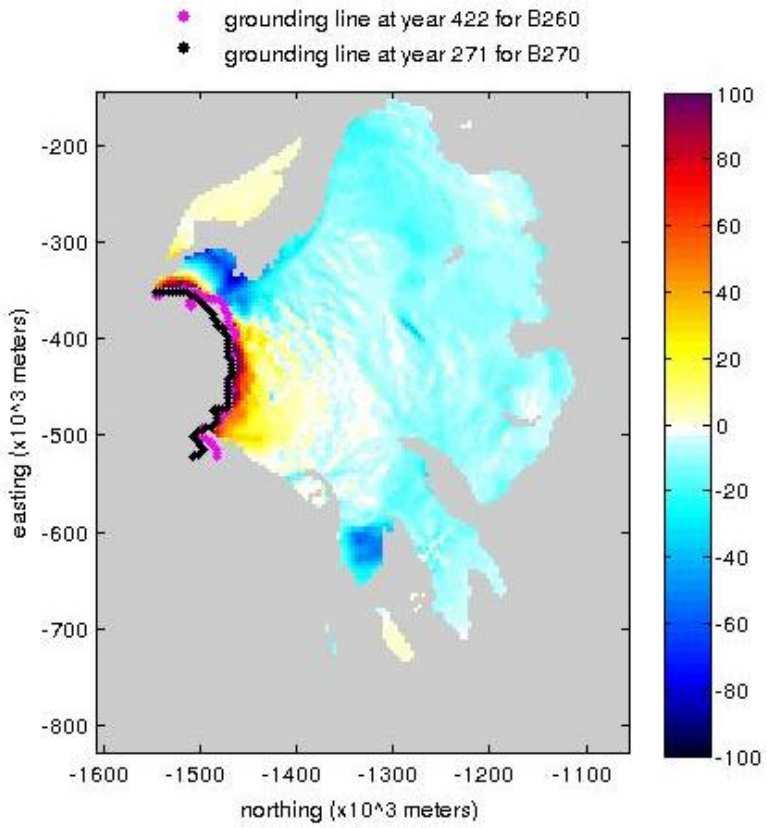

Figure 23. The spatial difference in driving stress B270 minus B260 (only where ROIs overlap) for the first co-located observation for both retreats over Bedmap2. This observation corresponds to model year 422 for B260 and model year 271 for B270. Between about -350 km E and -400 km E, the grounding line of B260 is in an advanced position relative to B270.

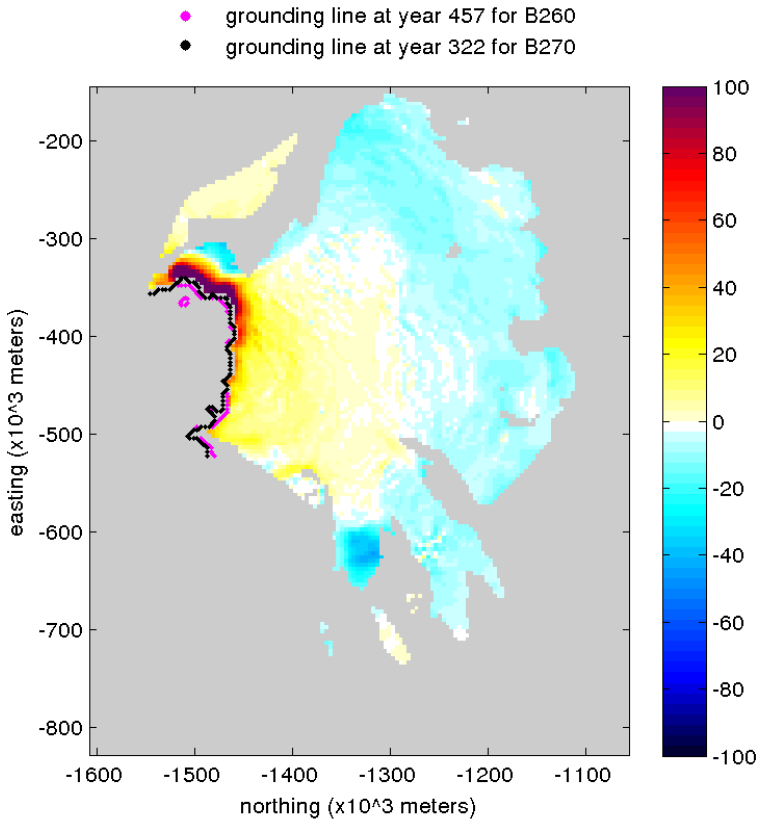

Figure 24. Spatial differences in driving stress for the 18th co-located observation of retreats over Bedmap2. The grounding line of B270 has caught up to that of B260 between about -300 km E and -400 km E by model year 457 for B260 and model year 322 for B270.

The summary driving stress comparison reflects different total elapsed times and thus different basin-wide thickness and surface slope when the grounding line arrives at any particular location (Figure 22). Therefore, care must be taken when interpreting the result. The negative differences for the initial comparisons seem to imply that the B270 grounding line retreats more slowly than B260 grounding line over a particular region of the bed. However, this is not the case. Even for the first 17 co-located observations, the driving stress near the grounding line is generally higher for B270 than it is for B260 (for

example see Figure 23). This is indicative of faster movement of the grounding line though the magnitude of the difference in driving stress indicates nothing of the direction of movement. However, starting with the 18th co-located observation there is no longer any advance occurring. So another issue dominates at the other

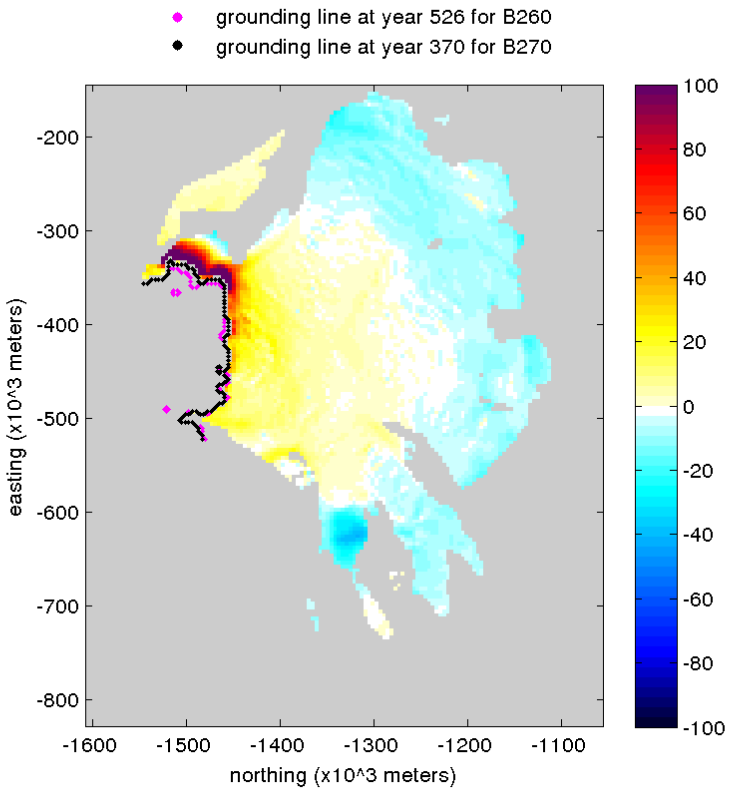

Figure 25. Spatial difference of overlapping ROIs in driving stress for co-location observation number 60, an arbitrarily chosen example of the limitation of using regional mean driving stresses for comparison purposes. This observation (co-located position) corresponds to year 526 of B260 and year 370 of B270. Although the difference in mean driving stress is -1.3 kPa, it is apparent that there is higher driving stress near the grounding line for B270. Note that the area shown is only the overlapping ROIs for the two simulations. The difference in mean driving stress for the overlapping region shown is about -0.3 kPa.

co-located positions. For these observations, higher surface gradients in the interior of the basin for B260 have created higher driving stresses away from the grounding line (for example Figure 25). The B260 grounding line retreats more slowly such that the B260 ice sheet has been thinning for 151 years longer than the B270 ice sheet when grounding line co-location begins (Appendix A). The discharge causes a surface deflation signal which propagates toward the interior of the B260 basin that hasn't happened in the B270 retreat. While the faster B270 retreat maintains a higher driving stress near the grounding line than does the slower B260 retreat, it is possible for the difference in driving stress ROI means to be negative (Figure 22 & Figure 25). Spatially, it is observed that at the beginning of grounding line co-location, the driving stress at the grounding line is greater for B270, the ice in the basin is thicker for B270; and the surface gradient in the interior is higher for B260 due to the earlier downstream thinning. These patterns persist through the simulation, via the increasing difference between model years, and the interior surface gradient signal of B260 propagates farther back into the interior of the basin as grounding line retreat continues. The continuing retreat increases the length of the grounding line and decreases the area of the ROIs (for example Figure 26). This increasing length, with greater driving stress at the grounding line for B270, along with the interior surface deflation signal being pushed farther toward the basin margins causes the apparent increasing trend in difference of mean driving stress (Figure 22).

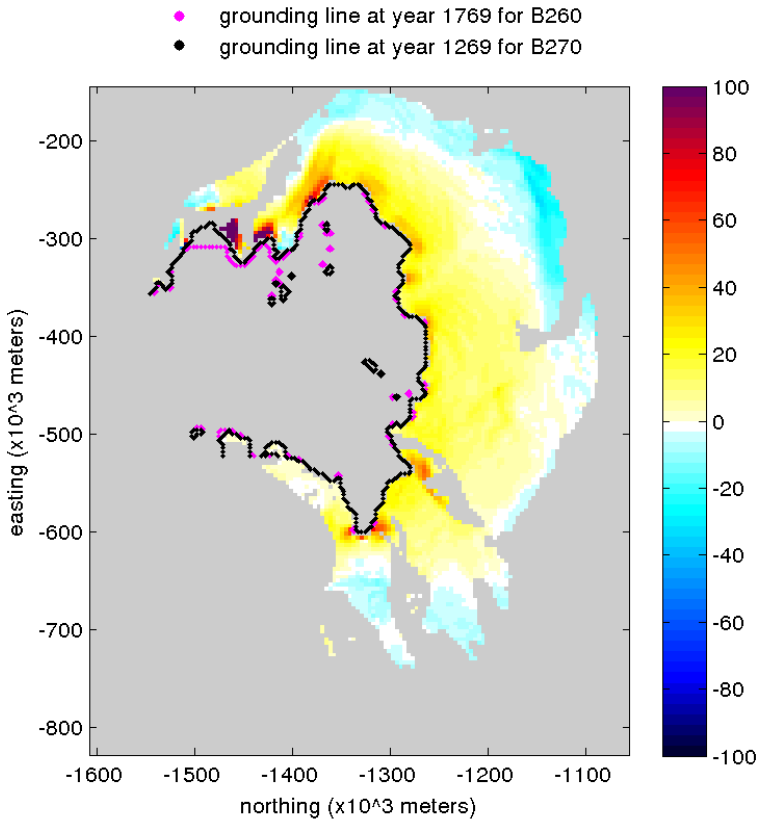

Figure 26. Spatial difference of overlapping ROIs in driving stress for co-location observation number 861. The length of the grounding line has increased with retreat and the area of the ROIs where driving stress is calculated has decreased. The surface deflation signal of B260, causing a greater surface gradient in the interior of the basin and a negative difference in mean driving stress, has been pushed back toward the margins of the catchment.

The short-lived grounding line advance at some locations at the start of the B270 unforced retreat is interesting in its own right. To understand the effect, we must recognize that the anomalous melting yields anomalous local steepening, and so when the anomalous melting is shut off, so too is the steepening. Re-advance along the eastern section of the grounding line is due to local details of the bed shape relative to the location of the grounding line when the anomalous melting stops. Without the extra

melting, ice that is close to the floatation limit may re-ground. If the grounding line is located on the leeward (relative to the direction of retreat) side of a subglacial high, it advances upslope and accommodates reduced ice flux through the grounding line via lowering of the surface gradient (Figure 27). This is the reverse of the

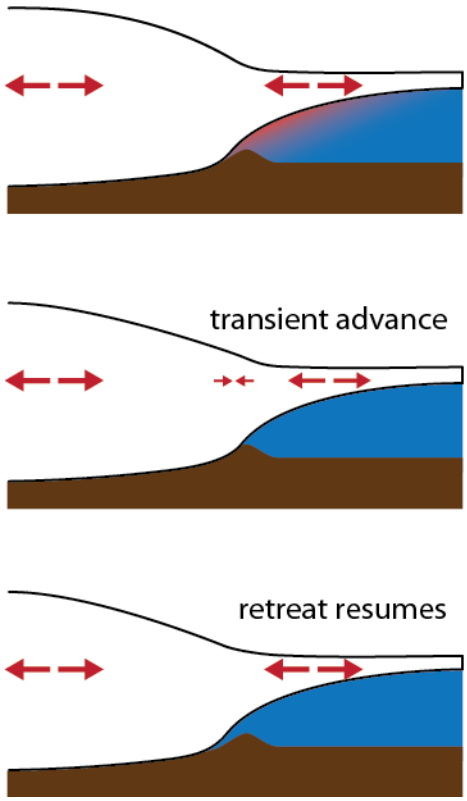

Figure 27. A cartoon depicting the transient advance observed after ramp shutoff in some locations of the B270 simulation. The grounding line is located on the leeward side of a bump in direction of retreat (TOP). As the surface gradient adjusts (lowers) to the lack of forcing after the slow ramp is turned off, the grounding line is able to advance a distance back up the bump (MIDDLE). After the system has adjusted to the new condition, retreat resumes (BOTTOM).

process in the direction of retreat, in which movement of the grounding line upslope on a bump is associated with reduced flux and an increase in the surface gradient.

Driving stress and ice flux are coupled attributes of the system, yet they reveal different aspects of the instability as it progresses. While the difference in mean driving stress diverges over time, this is not the case for ice flux through the grounding line (Figure 20). Flux across the B270 grounding line initially decreases, when the larger anomalous melting rate is turned off and the grounding line advances, but after that, the primary difference is B270's overall larger rate.

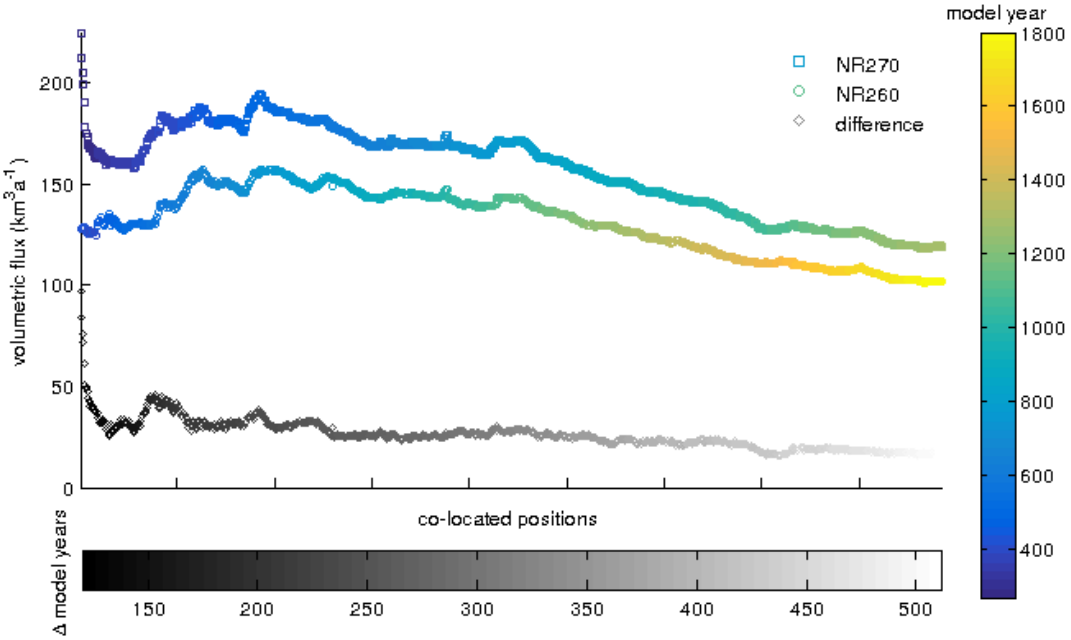

Figure 28. Volumetric flux across the grounding line for B260 and B270 over Bedmap2.

Through most of the simulation, the temporal patterns of change in ice flux across the co-located grounding line are very similar, with a Pearson correlation coefficient of 0.96 (Figure 28). In a general sense, then, the largest fluxes are associated with the same regions of the bed in both cases, irrespective of differences in driving stress. There is no

simple relationship between grounding line location, relative to the bed shape, and overall peak discharge. Instead, the grounding line positions at this time highlight the complicated 3-D nature of retreat as at some locations they are located near crests of bed features while at others they are passing through troughs (Figure 29).

Peak discharge is followed by a slow, steady decline in flux showing that the effect of grounding line retreat is dwindling over time (Figure 28), However, this is complicated by the competing fact that the length of the grounding line is increasing with time which increases the total volumetric flux. Additionally, the flux rates tend to converge over time. There is a statistically significant negative linear trend in the flux difference when the first 17 observations are not included in the trend analysis (Figure 28). This makes sense, as the ice supply is relatively more depleted in the B270

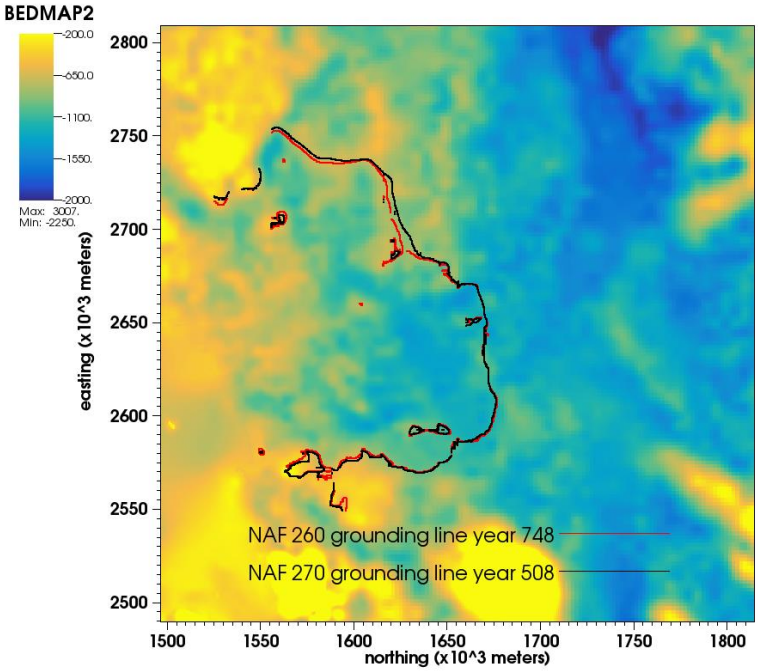

Figure 29. The grounding line positions for both simulations over Bedmap2 at the maximum volumetric flux across the grounding line for B270.

simulation compared to the B260 simulation. Overall, the instability initiated with slightly larger melting yields a larger flux response but it also has a more complicated history, with an initial decrease and a more rapid slow-down once peak discharge is achieved.

3.4 Experiment 2: Comparison to Retreat over Goff Bed

A regional instability was detected over the Goff bed at year 425 (21.25 m/a melt) of the anomalous forcing (Figure 11). This is an additional 155 years (165 years) and 7.75 m/a additional melt (8.25 m/a) relative to the B270 (B260) scenario. Consequently, the grounding is approaching the center of the basin by the time a true instability is initiated (Figure 30). The arcuate shape of the retreating grounding line is even more pronounced than it was in the other simulations (Figure 18 & Figure 30) and the grounding line has retreated to a much deeper part of the reverse slope. The G425 grounding line does not experience re-advance when the anomalous forcing is shut off. It might be expected, then, that the retreat rate over the Goff bed is greater than the retreat rate over Bedmap2 (Figure 31). However, the higher resolution, rougher Goff bed supports more complicated grounding line geometry and retreat pattern than the lower resolution, smoother bed (Figure 31).

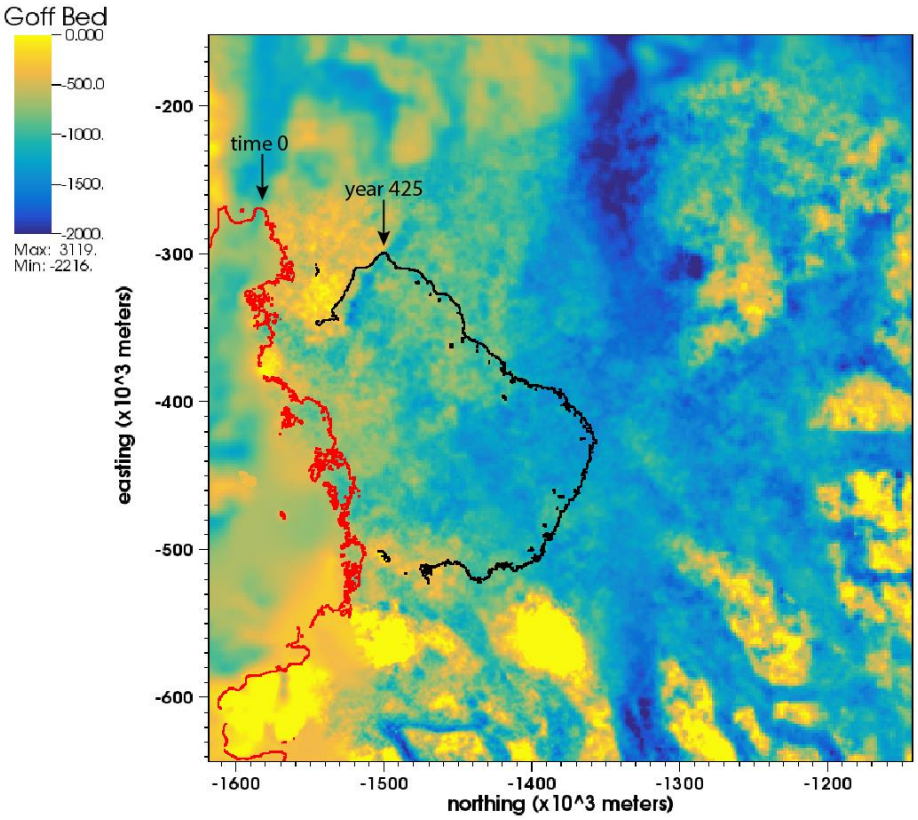

Figure 30. Grounding line position at the start of the anomalous forcing (red line) and at the year an instability is detected (black line) over the Goff bed.

As B270 is the faster of the two unforced retreats over Bedmap2, it will be used for comparison to G425. Results of this comparison are presented in a similar manner as the first experiment, focusing on driving stress and discharge. but co-location of the grounding line is more challenging. For retreats over Bedmap2, co-location by matching grounding line positions along a single transect through the basin generally provided a reasonable result. When the first transect did not produce a good match over a number of model years, another transect usually did and could be substituted in the comparison. Different sub-basins experienced similar retreat rates and while the timing differed, the spatial pattern of retreat was similar for B270 and B260. This does not hold for

comparisons across different bed geometries, meaning that a more complicated approach is required to co-locate grounding lines between B270 and G425.

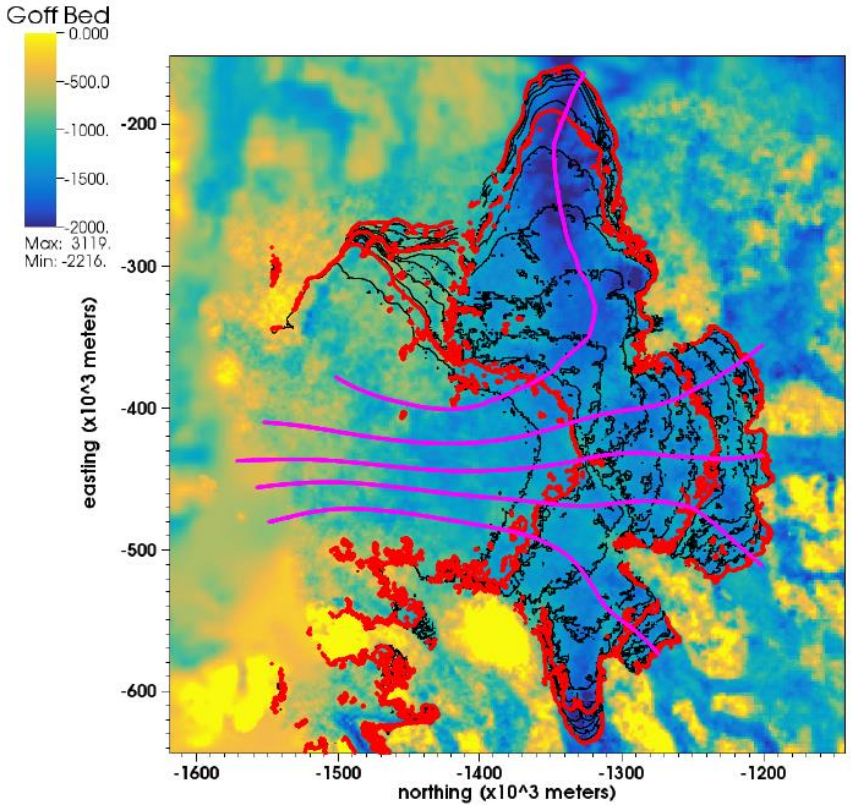

Figure 31. Contours of unforced grounding line retreat for G425. The contour interval for black lines is 100 years starting at year 425. The contour interval for red lines is 500 years starting at year 500. The magenta lines indicate transect locations used for the co-location procedure and in other figures. The final contours are at model year 1500.

Initial attempts at grounding line co-location for retreats over different beds showed that poor grounding line configuration matches result in greater thickness differences between the ROIs. This is due to the lobate shape of the grounding line during retreat and the fact that usually when there is a mismatch it is because the grounding line is co-located at the transect but the slower scenario is in an advanced retreat position

elsewhere. This exaggerates the positive differences in ice thickness between ROIs. On the other hand, in the fewer instances where the faster simulation's grounding line is in an advanced position, negative thickness differences tend to be localized near the grounding line and do not cause the mean difference to be negative at any position determined to be co-located.

The following approach was developed to find the best possible co-located grounding line positons between B270 and G425. Transects T1, T2, and T4 were used, while T3 and T5 proved to have very limited grounding line position matches between the two simulations (Appendix B).

1. For any given year in the G425 simulation, the grounding line matches, if any available, were collected and the one with the lowest positive difference in thickness between G425 minus B270 was selected. Note that this is using the 10 m/a velocity cutoff in the ROIs.
2. Overall, thickness differences should decline as time and spatial positions advance from the relatively high starting values along the transects. Therefore, any records that had a higher value than the initial difference along T1 were discarded. The initial thickness difference for the grounding line position match at T1 is the median of the three transects used.
3. Any records where the thickness difference increases more than 20 m, an arbitrarily selected value, from the previous record are discarded.
4. Since more than one transect is involved in providing grounding line position matches, thus far it is possible that an increase in model year for G425 from the

previous observation may be accompanied by a decrease in model year for the B270 simulation when switching transects for successive observations. For example, if the grounding line match was best using T1 for model year 450 (G425) and model year 680 (B270), and T2 provided best grounding line position match for next observation at year 451 (G425) the co-located position along this transect may be model year 679 (B270). Therefore, any records where B270 moves back in time are removed so that co-location always involves increasing model year for G425 and B270.

5. Eight records were removed by visual inspection due to a lack of continuity concerning matching positions.

This procedure improves continuity in time above what could be achieved along any single transect though the co-locations are not as precise as in the B270 to B260 comparison. Inspection of many outcomes gives some confidence that the co-location is suitable to make comparisons (Appendix M).

The initial G425 grounding line is co-located with the year 659 grounding line in the B270 scenario. The G425 retreat proceeds more quickly over the same region of the bed (Figure 18, increasing difference in model year at co-location) and as in the B270 to B260 comparison, the difference in mean driving stress is higher for the simulation in which the anomalous forcing is shut off at a later time (Figure 32; using the same 10 m/a velocity cutoff as in the first experiment). This is primarily a result of the larger of driving stress difference near the grounding line (for example Figure 33). The driving

stress difference grows for the first 571 years of the G425 simulation (to observation 106) but then begins to decline as the model ice sheet experiences surface lowering in its interior. Short-lived variations in the driving stress difference, as between observations 10 and 50, are due to local across-flow differences in grounding line order (in some locations, at some times, the B270 grounding line leads the G425 grounding line).

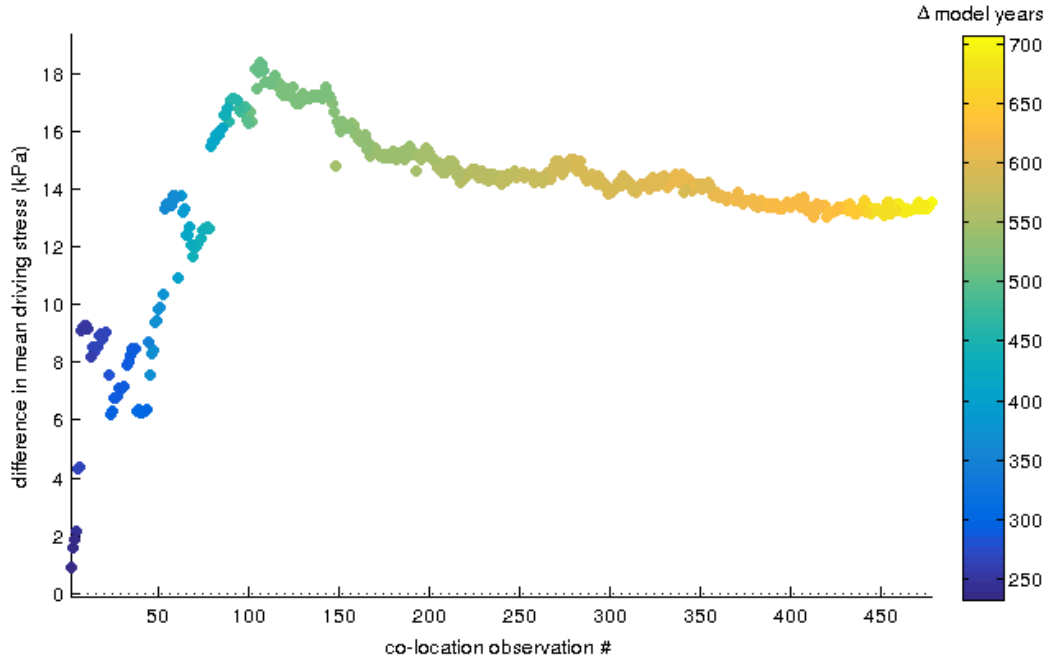

Figure 32. The differences in mean driving stress for B270 vs G425 (G425 – B270).

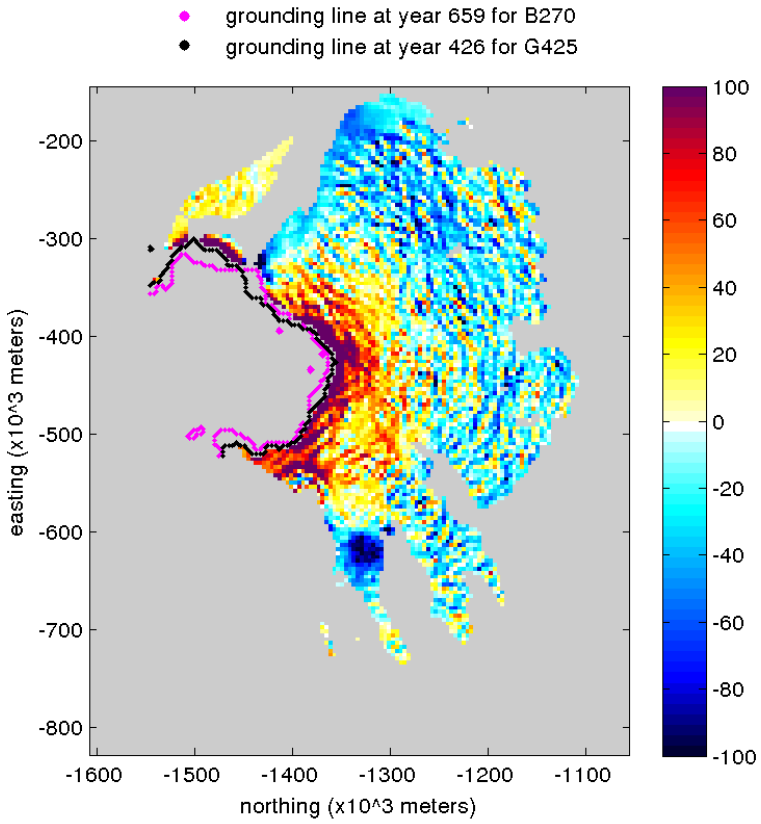

Figure 33. The first spatial observation (4 km resolution) of difference in driving stress (kPa) in overlapping ROIs for co-located grounding lines in the second experiment (G425 minus B270). The magnitude of the difference is generally greater than the B270 - B260 comparison.

Different bed geometries yield different spatial patterns of grounding line retreat. For example, at the first co-location (Figure 33), the B425 grounding line leads (in the upstream sense) in some locations while it lags in others. Switches in the lead/lag relationship also occur (Figure 34 & Figure 35). Leads and lags sometimes generate gaps in the comparison series during which the grounding line geometries are so different that co-location is not possible.,

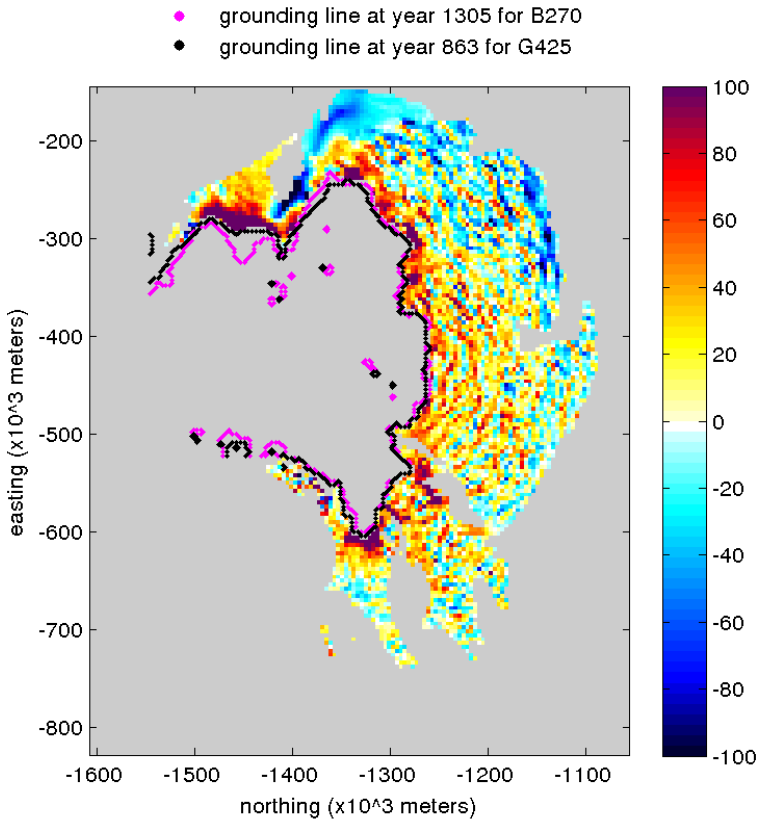

Figure 34. Observation 78 of the difference in mean driving stress for overlapping ROIs (4 km resolution). The grounding line of B270 is leading that of G425 in most of the locations in the lobe above -300 m E. In the lobe near -600 m E, the grounding line of G425 leads.

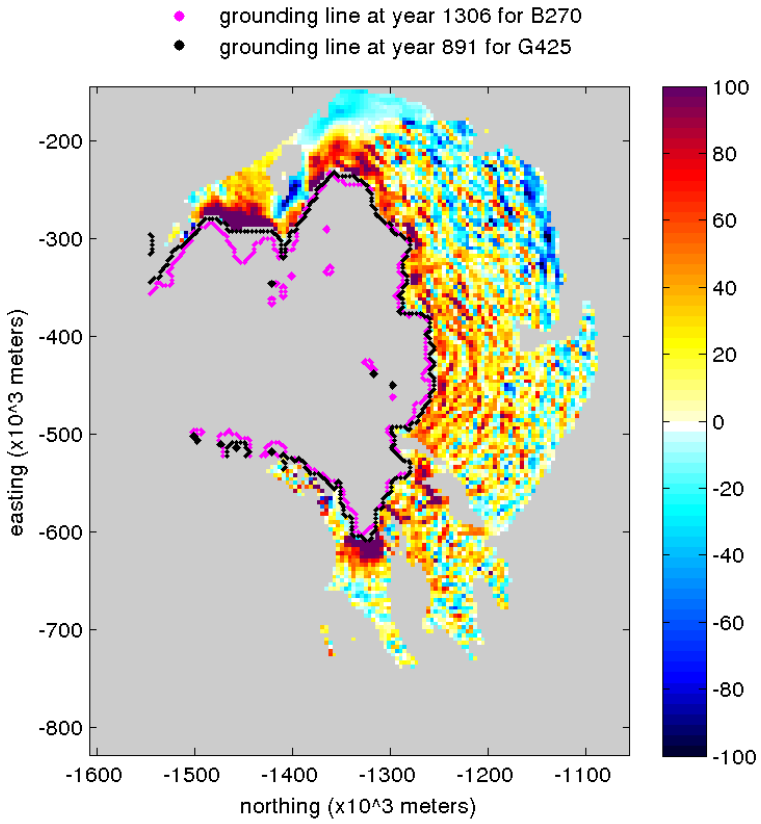

Figure 35. Observation 79 of the difference in mean driving stress for overlapping ROIs (4 km resolution). The grounding line of G425 is either co-located in an advanced position of retreat relative to that of B270 in the lobe above -300 m E. This results in greater positive differences and a lessening in the magnitude of negative differences in this location. Furthermore, the grounding line of G425 has retreated farther than B270 at the lobe near -600 m E causing greater positive differences in driving stress here.

Gaps are not characteristic of the entire simulation comparison. Instead, they are a feature of the time when the model grounding line is retreating over the widest part of the catchment basin. The largest co-location gap, between observations 43 and 44, is 215 years for B270 and 166 years for B425 (Figure 36). The maximum difference in mean driving stress of 14.8 kPa is reached at observation 106 corresponding to model year

1498 for B270 and model year 997 for G425 (Figure 32). After this, the difference in means decreases slowly toward a minimum of 13.1 kPa is at observation 403, beyond which, the difference in mean driving stress holds relatively steady (Figure 32). This is an interval during which the grounding line is retreating up different tributary subbasins.

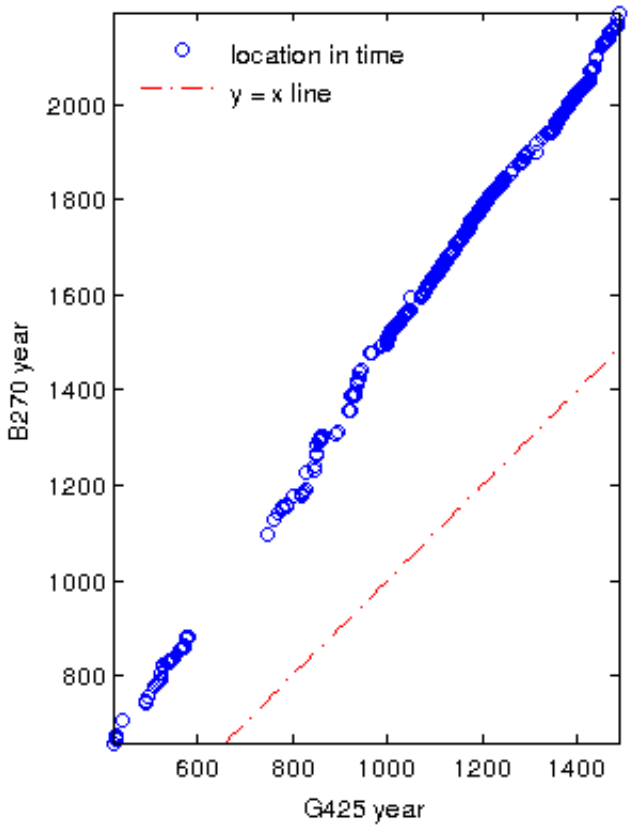

Figure 36. Year of co-located position in the B270 and G425 simulations. The largest gap, between observations 43 and 44, spans 215 years of B270 model time and 166 years of G425 model time. The trend for locations in time is nearly linear with a slope greater than 1.

The volume flux rate is relatively high when the G425 instability is triggered and declines from that time forward. Meanwhile, the B270 ice sheet is well past peak discharge (Figure 28) when the co-located flux comparison begins (Figure 28 & Figure

37). The G425 flux rate is larger than the B270 rate but the difference between the two declines toward a nearly constant, and relatively small, offset as the grounding line retreats into the upper reaches of the basin (Figure 37).

All three simulations are characterized by different rates of grounding line retreat and the spatial patterns of retreat are more similar for simulations over the same bed than for simulations over different bed geometries. Nevertheless, important similarities also exist. While the flux rate difference is more variable for the B270 to B260 comparison, the pattern of change is overall more similar than for the G425 to B270 comparison (Pearson correlation coefficient of 0.90 for G425 vs B270 and 0.97 for B270 vs B260). Yet both correlation coefficients are relatively large and this yields important insight into the role of the bed. Local and regional scale relief determine the timing of instability onset, and thereby set the time trajectory for each scenario, but the basin scale geometry appears to set the longer time scale response of the system. Were this not the case, the flux rate *patterns* of all three scenarios would not be so similar.

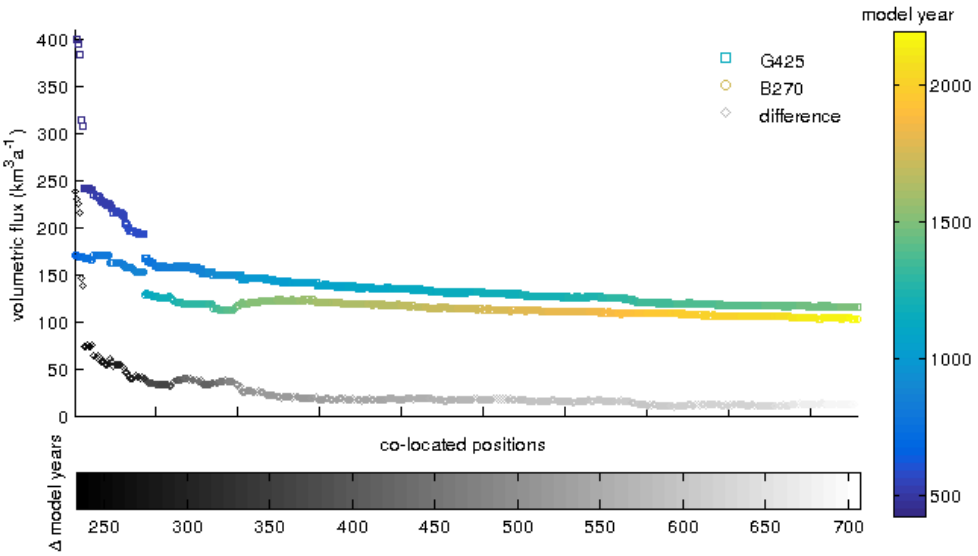

Figure 37. Spatial series of volumetric flux across Thwaites grounding line for B270 over Bedmap2 and G425 over the Goff Bed.

3.5 Summary of Mass Loss for all Simulations

The three scenarios yield different contributions to global mean sea level in both amplitude and timing. Using 918 kg m^{-3} as the density of glacier ice, the global sea level equivalent (SLE) is calculated from the VAF (Figure 38 & Figure 39). In order to examine the total contribution to sea level, year 0 is set to be when the anomalous forcing begins. Thus, these figures are time series rather than co-located spatial series. Dashed lines indicate when the ramp was turned off for each simulation (Figure 38 & Figure 39). These are not forecasts of sea level rise but rather a means to compare the loss of ice across all simulations.

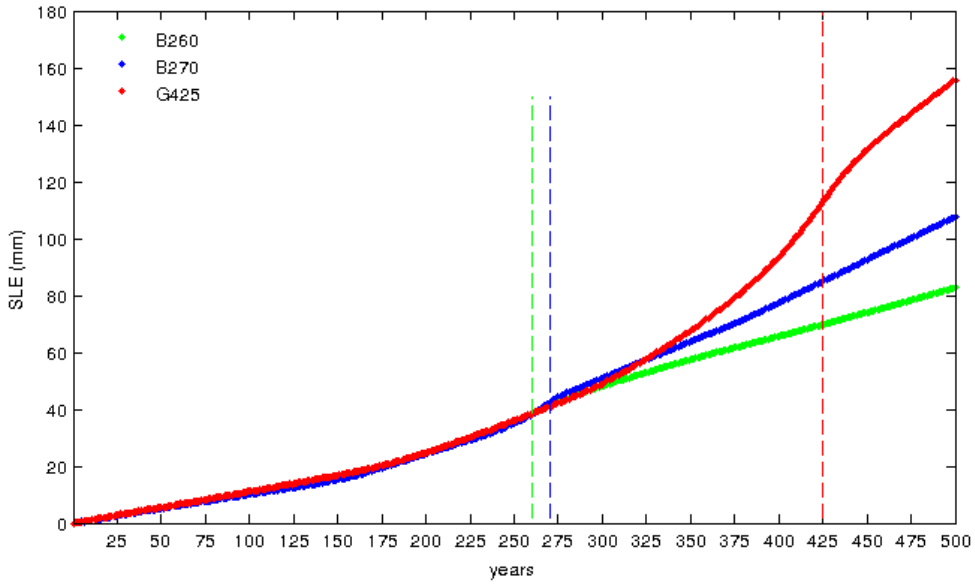

Figure 38. Ice mass loss in terms of SLE over the first 500 years for all simulations. Year 0 is when the slow ramp in anomalous forcing begins. Dashed vertical lines show when the ramp was shut off for each simulation and the unforced system was allowed to evolve.

The total mass loss for all simulations over both beds is similar until year 300 (Figure 38). The three models experienced similar anomalous forcing for most of that time. After year 300, mass loss for both B270 and G425 exceeds mass loss for B260. At year 323, mass loss for G425 begins to exceed that of B270. However, the anomalous forcing was still applied to G425 at this time. In all three cases, turning off the anomalous forcing is associated with an inflection in the time trajectory—from an increasing to a decreasing flux rate (Figure 39). Unstable retreat contributes less, overall, to sea level than forced retreat. Although a steady state is not achieved in any of the simulations, the total mass loss in terms of sea level rise are within 7.5% of each other at the end of the model runs (Figure 39). This end is where the final grounding line contours are most co-located in the catchment.

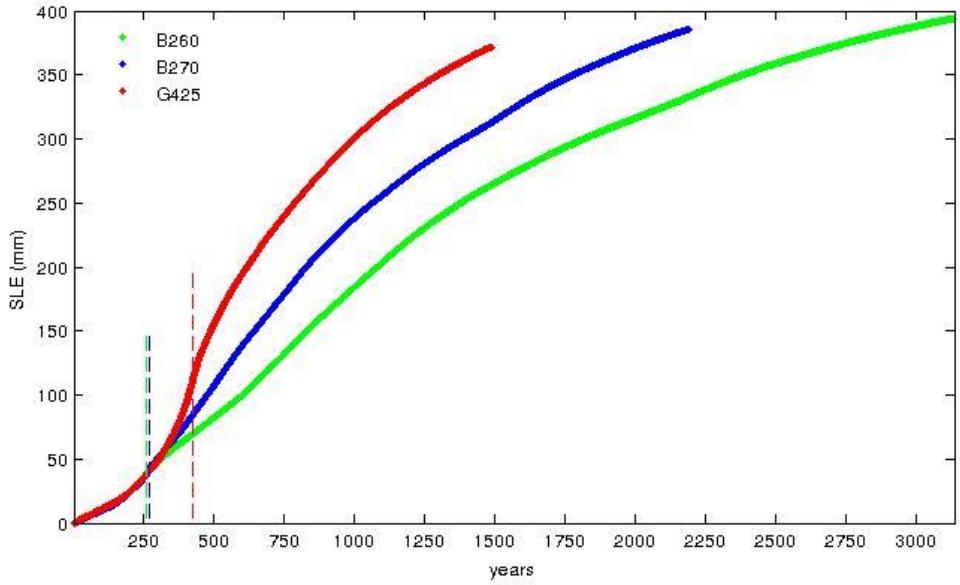

Figure 39. Ice mass loss in terms of SLE over the course of all simulations. Year 0 is when the slow ramp in anomalous forcing begins. Dashed vertical lines show when the ramp was shut off for each simulation and the unforced system was allowed to evolve. Note the inflection points for all series between years 250 and 500.

4.0 DISCUSSION

Change initiated at its marine margins has the potential to drive rapid change in the West Antarctic Ice Sheet. Rapid retreat may arise via an instability associated with the inland-deepening bed beneath the ice. It may also be driven simply by large melting at the grounding line, without ever triggering an instability. Either situation may apply to a given grounding line, but the two are not the same and the distinction is important. A genuine instability will sustain itself if the initial forcing is removed while a melt-driven retreat will not. Here, the focus is on finding and understanding a genuine instability, and in particular the role of the bed in both the onset and progress of unstable grounding line retreat.

The choice of bed for modeling a system like Thwaites Glacier and its role in ice sheet evolution is important for several reasons. Contact with the land surface, both at the base and along the sidewalls of outlet glaciers, provides resistance to the driving stress. Bed topography strongly influences the basal traction field, both in the actual system and as obtained in model initialization. Large-scale bed features also play a role in guiding the flow path (e.g. Sun et al., 2014). As discussed in Section *4.1 Spatial Patterns of Difference in Driving Stress* for Thwaites Glacier and in detail for general cases by several other authors, bed features also influence the surface topography of the ice sheet, and therefore the driving stress, because surface undulations are formed by ice flowing over bed features (Gudmundsson, 2003; Rydt et al., 2013; Schoof, 2002; Sergienko et al., 2014). Now, this study shows that bed resolution is important to the initiation of an instability and the resulting retreat rate as the ice evolves.

A key finding of this study is that bed resolution appears to set the threshold for the initiation of an instability. This is shown by the second experiment, in which 8.25 m more anomalous melt, which led to a grounding line configuration extending far into the basin was required to generate an instability over the higher resolution Goff bed compared to what was required over the Bedmap2 bed. When the retreat response is not dominated by a very large forcing, the grounding line retreat rate is paced by the shape of the bed. Retreat slows as the grounding line approaches the crest of a local topographic high and in some cases pauses at the crest before rapidly continuing the retreat. This is due to induced changes in ice flux across the grounding line (Figure 40 & Appendices G - K). It appears that this spatial variation in retreat rate along the length of a grounding line has a net effect influencing the forcing magnitude necessary to generate an instability.

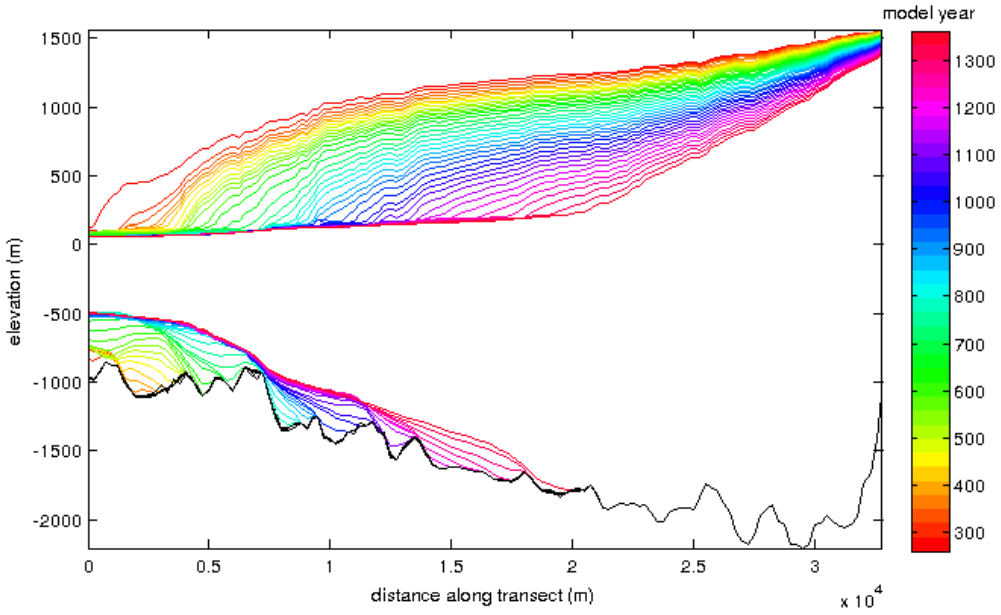

Figure 40. The first 1,360 years of unforced grounding line retreat along T1 for B260. Time interval is 30 years. Note that the grounding line slows or appears to hang near the crest of a bedrock bump before rapidly descending.

The magnitude of anomalous forcing required and the location in the basin of the grounding line at the time the instability initiates together effect the ensuing rate of retreat. It seems reasonable to suppose that when summed together, the local rate changes around highs on the bed (slower on the forward slope, faster on the reverse, inland-deepening, slope) would produce the same overall rates over the higher and lower resolution beds. This is not the case. The location of the grounding line on an inland-deepening bed generally means thicker ice toward the interior of the basin. A larger surface gradient caused by larger anomalous forcing at shutoff means the surface gradient during unforced retreat is higher than it would otherwise. My model experiment results show that both greater thickness and a larger surface gradient near the grounding line create greater driving stress here, hence a faster retreat rate, for an instability generated over the higher resolution bed, or when anomalous forcing beyond that required to generate an instability is applied.

Faster unforced retreat for a higher resolution and more realistic bed has implications for basins in similar settings. Projections of future contributions to sea level will be much less accurate if they are not made over higher resolution beds. Furthermore, correct representation of the marine forcing is clearly important in conditioning the unstable retreat. Overall, it is the combination of the bed shape and the anomalous forcing that set both the transition to unstable retreat and overall rate at which the retreat progresses.

An interesting outcome of the experiments using a slow ramp forcing approach is that slight changes to the duration and magnitude of the forcing send the system along different trajectories. This emphasizes the importance of improved knowledge of the real world forcing for models intended to make high temporal resolution projections of future sea level change. It also indicates that even in the case that an instability is initiated, the magnitude of the climate change that led to the retreat matters. Ongoing retreat may be inevitable, even in the case that the ocean forcing is removed, but the rate of the retreat is not locked in. Perhaps models such as this can be used to help global communities understand the importance of carbon emissions policy settings.

The melting parameterization used here takes a particular point of view on the ocean that comes into contact with the grounding line. By setting a water layer thickness limit on the maximum melt rate, we envision a seawater wedge moving inland, modified by mixing with cold meltwater as the ice lifts off the bed. This approach places the maximum melting rate where the slope of the ice base is relatively large, and away from the point where the ice lifts off from the bed. As the slow ramp grows, the geometric effect of the piecewise function decreases and the anomalous forcing comes to dominate the melting pattern. Although simplified as compared to the real-world setting, the melting parameterization is meant to capture the basin-scale retreat effect. As no forecasts or focus on the timing of retreat over particular subbasins are involved, there is no reason to include a more complicated parameterization. Moreover, a more complicated melt parameterization such as a plume model, would deliver warm water differently over different beds, confounding our aim of comparing the effect of the bed

on ice sheet evolution and grounding line retreat. It is worth noting that a simplified melt-forced retreat assumes that warm water will continually reach the grounding line. However, as retreat proceeds and the fetch to the ocean increases, there is no guarantee that this would occur.

The surface accumulation rate is fixed in the model. This means that the increase in snow accumulation that is in general associated with lower elevations is not accounted for as the grounding line retreats and the model ice sheet lowers. The result may be a slightly faster retreat than would otherwise be the case.

As with all numerical models, the ice sheet model used here has limitations. Three related issues should be considered here. First, the inverse initialization generates a fixed basal traction field and no processes that might modify the traction are represented in the model. Yet certainly, as ice thickness and surface slope change, the properties governing basal traction will change as well. Second, SSA* is used everywhere, yet clearly vertical shearing drives ice flow in the thinner, frozen bed areas of the Thwaites basin. Third, the model assumes a viscous till rheology.

Problems with the fixed basal traction involve both is initial setting and the fact that it does not change in response to changing ice conditions. The largest blunders associated with assigning the initial basal traction are probably close to the grounding line, where slope and thickness change the most. In fact, zero and first order ice flow approximations assume bridging forces are negligible which lead to a higher, compensating basal traction near the grounding line (Morlighem et al., 2010). Inland of the grounding line, basal traction may vary as the hydraulic gradient and basal thermal

condition change but this cannot be accounted for in the present model. The situation is no different than for other models initialized using an adjoint approach. Fortunately, this is a comparative study and no projections are being made so issues associated with a fixed basal traction field are not as important as they might be otherwise.

The model could be improved by inclusion of a parameterization that routes ice sheet basal meltwater and connects that water with basal properties (Creyts and Schoof, 2009; Flowers, 2015; Flowers and Clarke, 2002; Hiester et al., 2016). However, such an addition would add poorly constrained parameters to the initialization and would require thorough investigation. Well constrained parameters lead to a straightforward interpretation of results. However, a parameter space investigation using a Bayesian approach may enable the addition of processes and parameters to improve the model fidelity with a real-world system.

Vertical shearing occurs where the ice sheet flows over a bed that provides significant resistance to ice flow, for example where sliding ice is in direct contact with bedrock or where the ice is frozen to the bed (Cuffey and Paterson, 2010; Greve and Blatter, 2009; Schoof, 2007). Another model study showed that vertical shear can be important for initiating the transition from ice sheet to ice stream flow (Hulbe et al., 2003). Many marine terminating glaciers display fast flow principally via the effects of very weak subglacial material, in which case vertical shearing is small and longitudinal stresses are large (Cuffey and Paterson, 2010; Greve and Blatter, 2009; Pattyn et al., 2012). In the present situation, the focus is on wide, deep, and fast-flowing coastal outlet glacier flow, where the SSA approximation is suitable. Slow-flowing regions of the

basin, where vertical shearing dominates, are peripheral to the experiments conducted here. Furthermore, the results of the Marine Ice Sheet Intercomparison Project suggest that assumptions about material properties may introduce larger errors than the ice flow approximation used, particularly in regard to sliding behavior (Pattyn et al., 2012). Nevertheless, the lack of vertical shear for the BISISCLES model used in this project is a limitation that could not be overcome at the time the simulations were run. Since this time, model developers have more fully established an ice flow approximation for BISICLES known as L1L2 that does account for vertical shearing.

Accurate resolution of the momentum balance around the grounding zone is essential for correct representation of grounding line motion (Pattyn et al., 2012). This can be accomplished by implementing high model grid resolution near the grounding line or a moving grid that focusses high resolution and computational effort around the grounding zone (Pattyn et al., 2012; Vieli and Payne, 2005). The AMR of the BISICLES model down to 250 meter resolution is beneficial in this regard.

Ideally, the subglacial till should be parameterized by considering its rheology and subglacial transport of sediments, as well as the timescales involved with transport, in a numerical model used for predictive purposes. The basal traction approach used here assumes a viscous rheology. However, most laboratory experiments have shown plastic rheology for till (Hindmarsh, 1997; Iverson et al., 1998; Tulaczyk, 2006). Some researchers have suggested that the aggregate of plastic failures at the fine scale lead to an apparent viscous behavior at the ice stream scale justifying the viscous model of till deformation (Hindmarsh, 1997). Alternatively, field observations of Whillans Ice Stream

in West Antarctica are consistent with plastic rheology determined from laboratory tests (Tulaczyk, 2006). If the model is incorrect, the bed might provide either more or less resistance to flow than is appropriate for the real-world system.

The notion of till, and hence till rheology, only matters to the basal traction field if it includes time varying properties of the bed. Otherwise, the role of the till is to provide a basal boundary condition for the ice. However, there are currently no constraints for the inversion of a time varying process in the adjoint model that comprises the BISICLES control problem. By design, the singular focus here is how the shape of the bed affects model projections. It is thus advantageous to hold model parameters constant through time.

4.1 Spatial Patterns of Difference in Driving Stress

Driving stress in the vicinity of the grounding line is clearly important to the initiation and progression of the ice sheet instability but this is not the only difference apparent across the model simulations. The driving stress difference field for experiment 1, in which both simulations are over Bedmap2, tends to vary smoothly away from the grounding line (Figure 41) while the Bedmap2 to Goff bed comparison in experiment 2 yields driving stress variations over shorter wavelengths that are locally-organized into distinct bands of highs and lows (Figure 42). Comparing the two difference fields, it is clear that higher resolution spatial variability is present in the G425 simulation than in the B260 and B270 simulations. This difference must arise from the influence of the bed shape during model initialization and grounding line retreat.

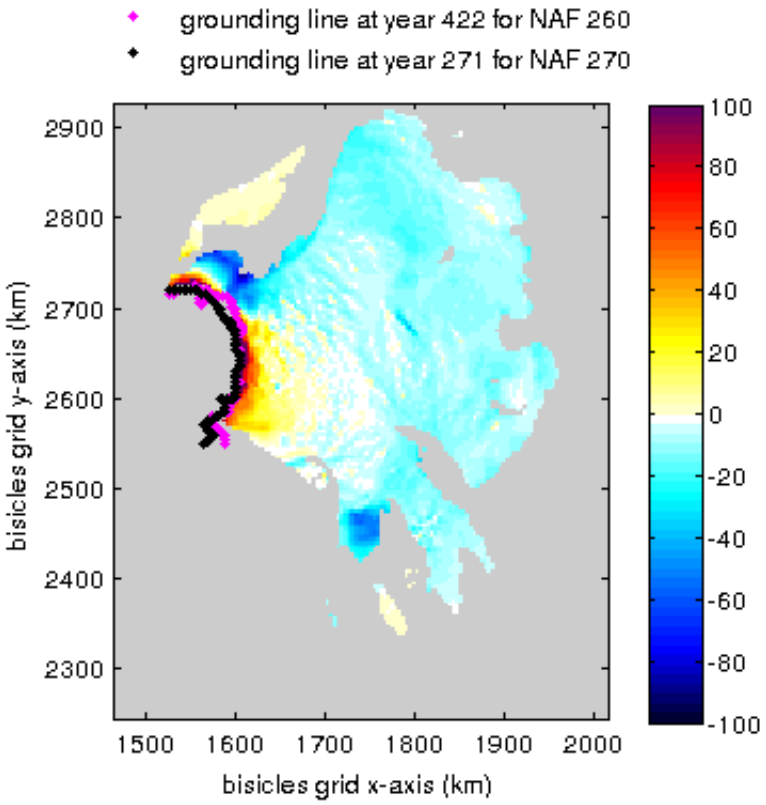

Figure 41. The first 4 km resolution co-located grounding line position difference in driving stress spatial field (kPa) for experiment 1. The driving stress varies smoothly away from the grounding line. Only the intersection of ROIs is shown and ROIs are constrained by the 10 m/a cutoff value.

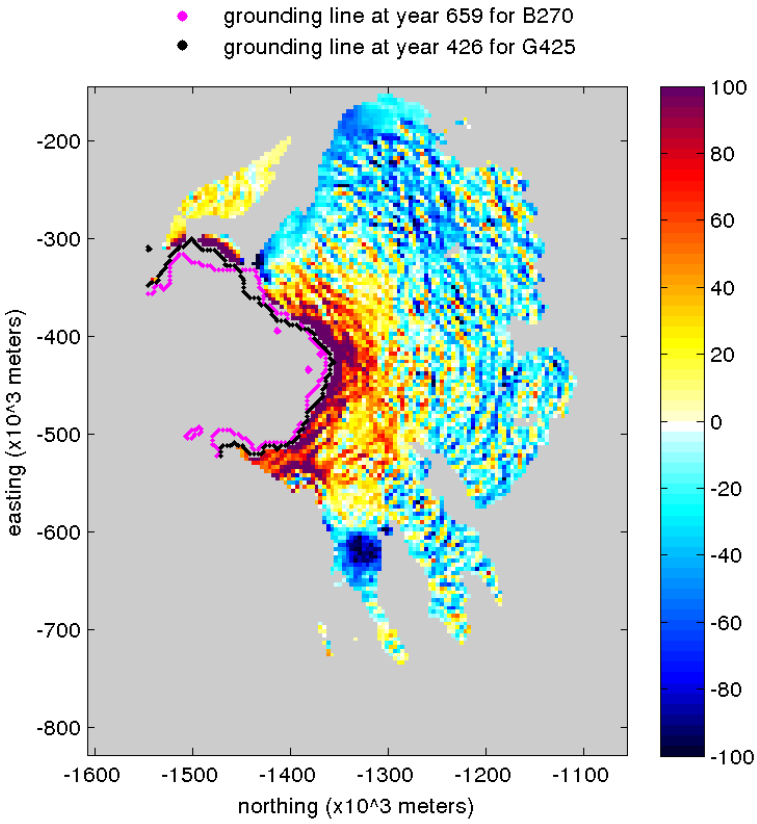

Figure 42. The first 4 km resolution co-located grounding line position driving stress difference spatial field (kPa) for experiment 2. The driving stress field appears rough in many locations with bands of high and low values apparent. Only the intersection of ROIs is shown and ROIs are constrained by the 10 m/a cutoff value

The fundamental difference between experiment 1 and experiment 2 is that the shapes of the subglacial beds differ in experiment 2. The two bed realizations capture the same broad features but they differ in detail and this is apparent even after the two data sets, which have different fundamental resolutions (1 km and 250 m respectively) are coarsened to a 4 km grid. This is primarily noticeable as steeper horizontal gradients on the Goff bed, giving it a more detailed appearance relative to Bedmap2 (e.g. Figure 43).

This difference has implications for ice thickness and basal drag, and through these, the evolution of the ice surface slope and driving stress over time.

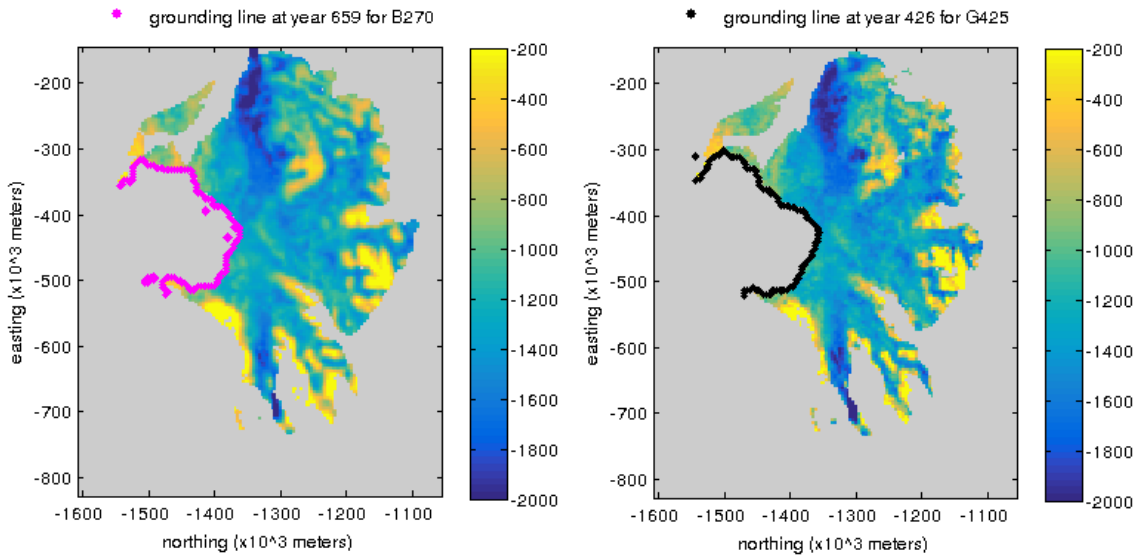

Figure 43. (LEFT) The 4 km resolution bed elevations (m) at the first co-located observation for Bedmap2 and (RIGHT) the Goff Bed. Only the ROIs with the 10 m/a velocity cutoff are shown.

Different bed elevations yield different ice thickness fields under the fixed initial surface elevation. Therefore the ice thickness field is less smooth and more detailed over the Goff bed (Figure 44). As driving stress is proportional to ice thickness, which can be seen by examination of equation (3.2.1), the differences in thickness between the two beds contribute to large local variation in the driving stress in experiment 2 (Figure 42 & Figure 45).

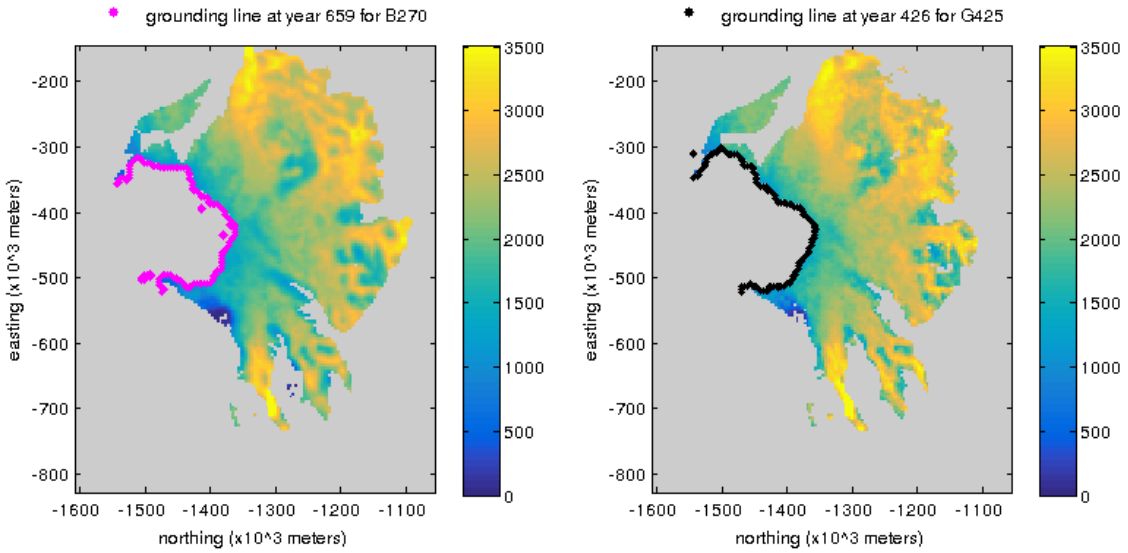

Figure 44. (LEFT) The 4 km resolution ice thickness (m) at the first co-located observation for Bedmap2 and (RIGHT) the Goff Bed in the second experiment. Only the ROIs with the 10 m/a velocity cutoff are shown.

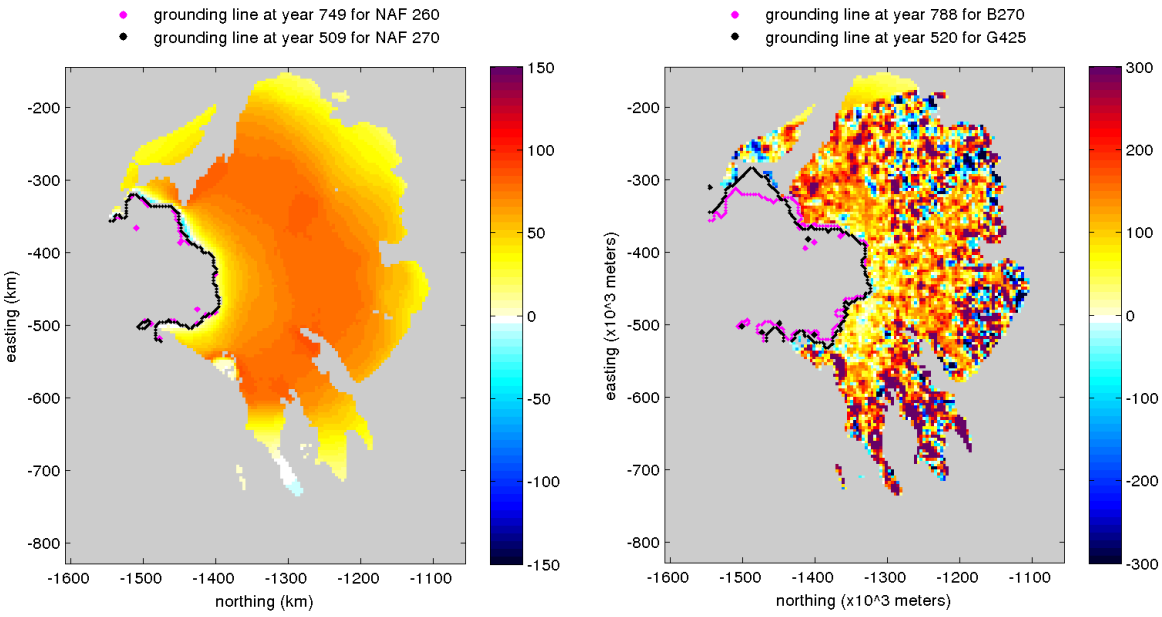

Figure 45. (LEFT) The 4 km resolution thickness difference (m) at the 186th observation of grounding line co-location for experiment 1, B260 vs B270. (RIGHT) The 4 km resolution thickness difference (m) at the 17th observation of grounding line co-location for experiment 2, B270 vs G425. The magnitude of differences tends to increase with grounding line mismatch so the observations were only selected to show differences in the general spatial patterns. Only the ROIs with the 10 m/a velocity cutoff are shown.

Differences in bed shape also yield differences in the basal traction field. Basal traction is, overall, lower in the downstream reach and higher in the upstream reach of B260 and B270 than in the G425 simulation (Figure 46). Basal traction differences are apparent even at the coarse 4km resolution (Figure 47). These are the result of differences in the bed shapes and ice thicknesses with which the basal traction field was found by inverting these together with the surface velocity. When the model relaxes to a steady state during the next phase of initialization, the more detailed bed, thickness, and basal drag together tend to preserve a more detailed surface shape. The surface undulations and thickness then generate the higher resolution and spatial detail in the driving stress over

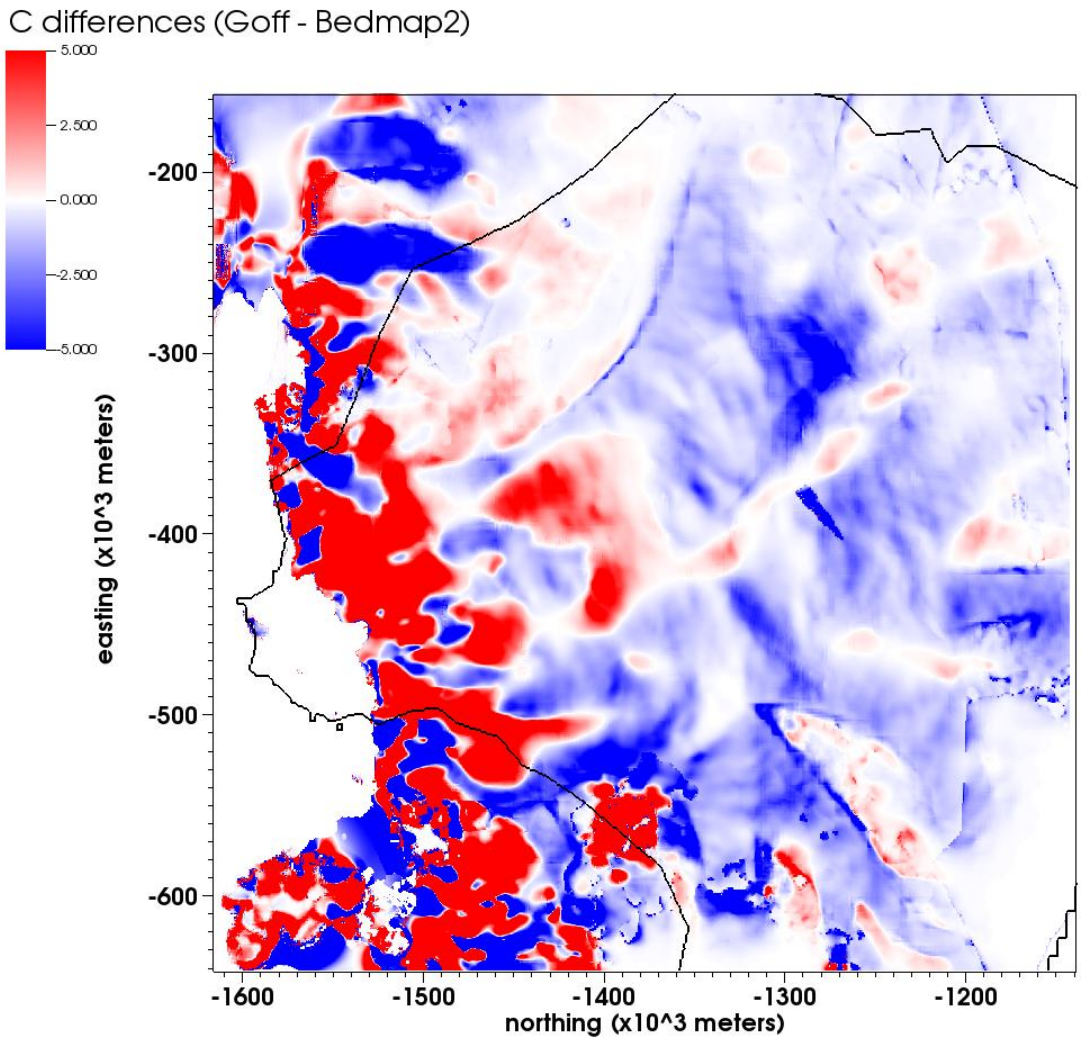

Figure 46. Difference in basal traction coefficients for Goff minus Bedmap2. Basal traction coefficients are generally higher for Bedmap2 in the lower reaches and higher for Goff in the upper reaches. The color scale limits shown here are -5 to 5 although higher and lower values are present. The greatest differences in basal traction occur where relatively high surface gradients are present at the start of the simulations.

the more detailed Goff bed. This outcome mimics the effect investigated by Sergeinko et al. (2014), in which varying topography and basal traction produces undulations on the surface which in turn produce spatial variation in the driving stress. However, without

incorporating a transient basal traction field via parameterized physical processes, the effect in these simulations is static.

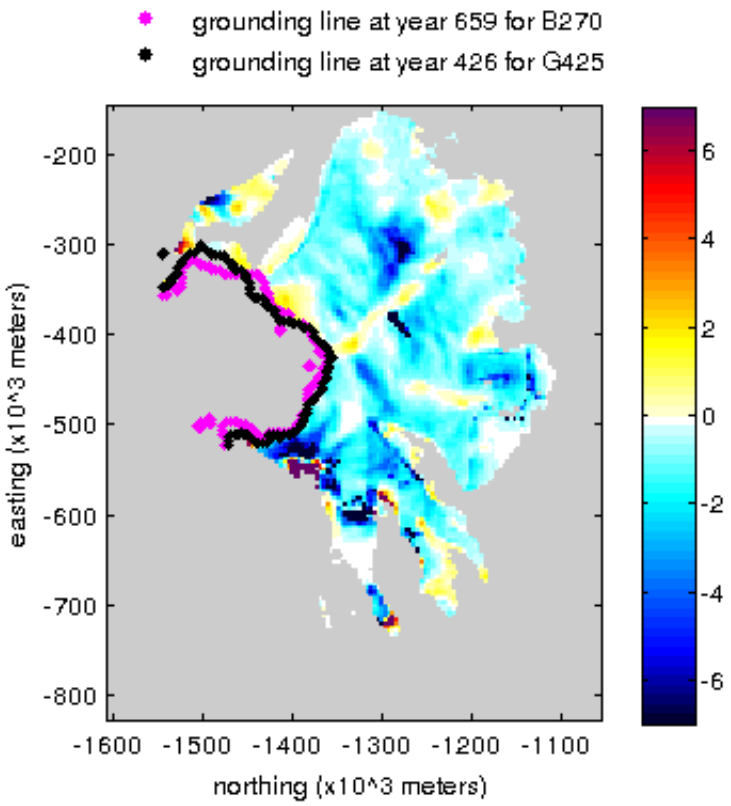

Figure 47. 4km resolution Goff bed minus Bedmap2 difference in basal traction in areas over the 10 m/a velocity threshold for the first co-located grounding line position in experiment 2. Note that by the time the instability is initiated on the Goff bed, the grounding line has retreated to a region where basal drag is lower than for the Bedmap2 case.

All together, these effects produce the band-like alternating highs and lows in the spatial difference of mean driving stress field for experiment 2 (Figure 42). Examination of the surface gradients through time does show stationary spatial patterns of surface gradients over Bedmap2 and the Goff bed that differ somewhat from each other (Figure 48). The primary difference between the two is that the surface gradient for G425 appears

sharper and more resolved with more and narrower bands that tend to follow distribution of the bands in B270 (Figure 48). The magnitude of the differences along these features change as the location of the grounding line changes, placement is stationary (Figure 49).

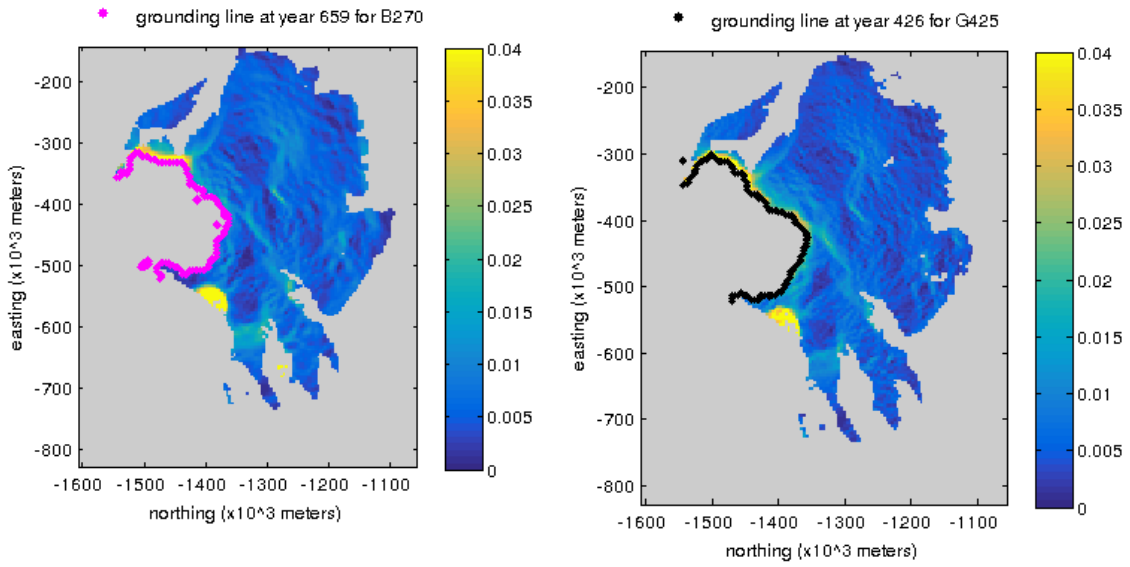

Figure 48. (LEFT) Surface gradient at 4 km resolution for B270 at the first instance of grounding line co-location in experiment 2. (RIGHT) Surface gradient at 4km resolution for G425 at the first instance of grounding line co-location in experiment 2. Gradients are only shown over ROIs (where velocities are greater than 10 m/a). There are differences with the G425 gradient appearing more resolved.

In summary, the difference in driving stress field through time for the first experiment, B260 vs B270, appears smoother spatially than that for the second experiment, B270 vs G425, for two reasons. First, the difference in thickness fields through time are smoother with differences in the first experiment being controlled solely by flux rates across the grounding line as opposed to any topographical differences. Second and most importantly, surface gradient patterns are the same for both simulations

over the same bed in the first experiment. These two reasons are directly related to the differences between Bedmap2 and the Goff Bed.

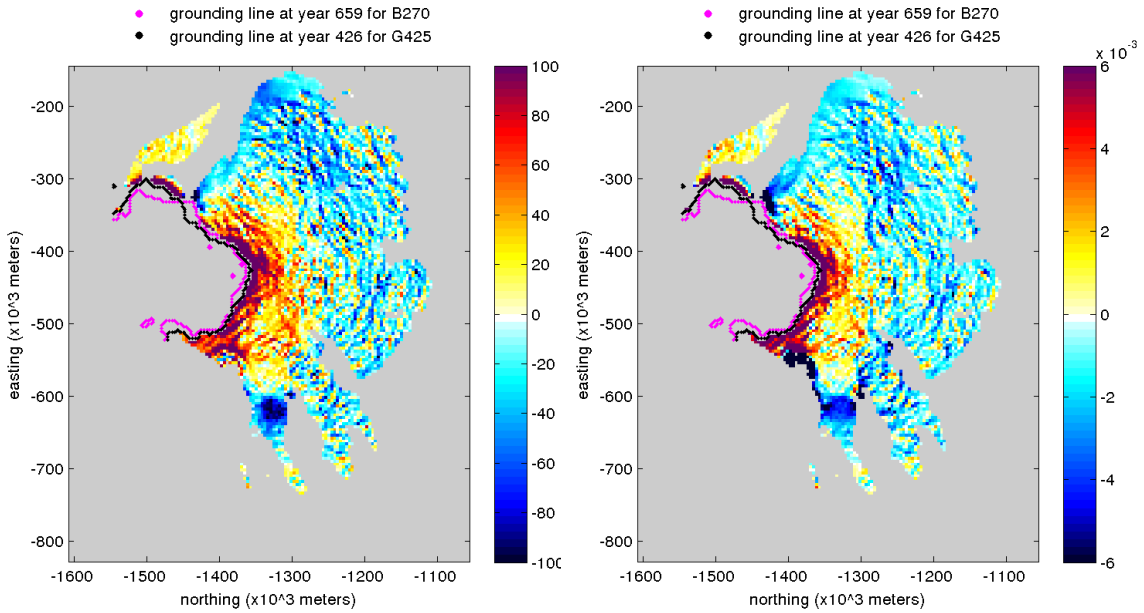

Figure 49. (LEFT) Driving stress difference (kPa) at the first observation of grounding line co-location for the second experiment, B270 vs G425. (RIGHT) Surface gradient difference at the first observation of grounding line co-location for the second experiment. Alternating bands of highs and lows appear well correlated for these fields.

5.0 CONCLUSIONS

The marine ice sheet instability is topic of a long-standing interest and concern in glaciology. This phenomenon is often investigated along two-dimensional flowlines but transverse-direction effects can be important. Here, the problem has been expanded to three dimensions, so that the influence of bedrock geometry in initiating and propagating unstable grounding line retreat can be explored. An instability is defined as a situation in which the dynamics of the system responding to an external forcing experiences a positive feedback such that external forcing is no longer required to sustain the mode of response. To find this transition in the ice sheet model, a slowly increasing anomaly (melt), is superimposed over a steady-state ocean forcing. The slow ramp, an increase of 0.05 m a^{-1} melt, is turned off once an instability is identified, after which the retreat continues. Different forcing rates would trigger instability at different grounding line locations but the conclusions drawn here would remain largely the same.

Two model experiments were designed to investigate the role of the bedrock geometry in the initiation and propagation of a marine instability in the Thwaites Glacier system. The experiments also provide insight into how instabilities arise. The first experiment compares the effects of different magnitudes of anomalous forcing over the same bed. The second experiment compares instabilities invoked over different beds. Small changes in forcing duration and magnitude lead to grounding line retreats that diverge in time. Different beds require different forcings in order to generate a genuine instability.

Three-dimensional basin morphology sets the stage for unstable grounding line retreat. The first model experiment shows generally the same spatial pattern of retreat over the same bed, but with rates that vary with the magnitude of the anomalous forcing, even after the forcing is turned off. This has two important implications. First, the reverse slope alone does not dictate unstable retreat. Even though the spatial pattern of retreat over the Goff bed in the second experiment is less similar to retreat over Bedmap2 than the two Bedmap2 retreats are to each other, it is nevertheless apparent that large-scale three-dimensional bed features shape the spatial pattern of both the forced and unforced retreat. Second, the state of the system at the end of forced retreat, namely the specific location of the grounding line and the surface gradient of ice near the grounding line, determine the rate of retreat.

Fine-scale features on the bed determine where and when the instability is initiated. A significantly larger anomalous forcing is required to generate an instability over the rougher Goff bed than over the smoother Bedmap2. Put another way, the bed morphology is a primary factor for establishing the ice sheet's sensitivity to the ocean forcing. Correct knowledge of the bed shape is thus essential to projection of future change. This result supports the conclusions of Parizek et al. (2013) in this regard, and we show that morphology matters because the rougher bed is associated with overall steeper surface slope near the grounding line, which produces larger ice flux. However, when surface slope is anomalously steepened by a large marine forcing, the bed features become less influential. When the anomalous forcing ends, bed features become more important again.

Local apparent instabilities arise as the grounding line retreats in response to the anomalous forcing. These are not the same as the basin-scale effects associated with a genuine instability but might be mistaken for such effects in the natural world. Local instabilities tend to involve relatively short distances of grounding line retreat within subbasins. They have the excess mass flux characteristic of unstable retreat but begin to slow soon after initiation. Local instabilities play out over decades to 200 hundred years. This implies that care must be taken in the attribution of modern observed retreat. Neither retreat nor its pace over short time scales is sufficient to indicate an actual instability. And if an instability has not been invoked by the marine forcing, then the grounding line may quickly come to a new equilibrium position if the anomalous forcing halts.

This new steady state shape is obtained because the ice now experiences different boundary conditions in association with its new extent. Flowline models generally do not consider transverse effects of flow and resistance beyond the inclusion of a width parameter. On the other hand, a plan view model does such that deflating interior surface of an ice sheet with a mass accumulation field that is spatially variable but constant through time creates the potential for new steady-states when shutoff prior to an instability occurs.

The shape of the bed influences ice sheet configuration at the start of the transient simulation. The adjoint initialization requires agreement between known and unknown variables and parameters. Changing the bed shape under a fixed surface elevation changes the ice thickness, which in turn changes the basal drag required to support the observed surface velocity. Once the basal traction is set, relaxation occurs and bed

features propagate upward through the ice flow to modify the initial surface elevation. The end result is an undulating pattern like the patterns identified in Sergienko et al. (2014). This happens on both the Bedmap2 bed and the Goff bed but is more pronounced in the latter due to its finer resolution topographic features.

The magnitude of the anomalous forcing also affects model outcome. As the larger of the two forcings in experiment 1 results in a more inland (down reverse slope) location for the grounding line when the instability is left to run on its own, the driving stress near the grounding line is larger and the ensuing retreat proceeds more rapidly than for the smaller forcing case. This implies that accurate knowledge of the marine forcing is critical to correctly projecting unstable retreat. Very different future scenarios can be invoked by small differences in anomalous forcings, as shown by the 0.5 ma^{-1} melt difference at the time of ramp shutoffs in experiment 1. It also implies that decisions about carbon emission pathways and ensuing ocean warming can have meaningful influence on ice sheet retreat, even after marine ice sheet retreat is invoked. Retreat may be inevitable past a certain dynamical threshold, but the rate at which the retreat proceeds is not. Moreover, this research suggests that the threshold for instability is not a specific boundary on the sea floor, but is instead a synthesis of sea floor shape and forcing magnitude.

Projection of future change in the Thwaites Glacier region, and presumably other outlets of the Antarctic ice sheet, is clearly connected to the realism and the resolution of the of the glacier bed geometry. The two bed realizations used here generate different rates of retreat in the forced phases of the experiments unforced phases of the simulations

and the difference is larger when the anomalous forcing is larger. This is the case even though our parameterization of bed processes is simple and the effect of time-varying bed properties should also be investigated.

The experiments conducted here also demonstrate the difference between a purely *marine forcing* and a *marine-triggered instability*. Overall, the rate of mass loss is larger during the forced phase of a retreat than during the purely unstable retreat phase. If an instability is not triggered, grounding line retreat ceases when the forcing is removed and the ice sheet relaxes to a new steady state shape associated with that grounding line position, even if it is locally on a reverse slope. Large melting during the forced part of the retreat maintains (or enhances) a large surface slope near the grounding line and thus large flux across it. When the anomalous forcing is reduced, so is that effect. In the case that an instability has been triggered, the two effects proceed together. This is why the ice flux declines during the unstable, committed retreat phase of our experiments. The positive feedback is controlled by the floatation criterion as the grounding line retreats into deeper water.

Strictly, no ice shelf melting is required to sustain the instability. Retreats continue in our experiments when the background marine forcing is very small; a value of 0.30 ma-1 is applied after the slow ramp ended.

The increased grounding line fluxes associated with retreat in the model simulations are the result of surface steepening near the grounding line. That is, there is no requirement for changes in ice-shelf "buttressing" to generate rapid retreat. As the grounding line retreats upstream into the very wide Thwaites catchment, the distance to

lateral margins of the ice shelf increases and thus their effect on the budget of forces at the grounding line decreases.

6.0 FUTURE WORK

Coupling an ocean warming model to the BISICLES model could provide additional insights. These would likely pertain to distinguishing the areas of the Thwaites catchment that are most vulnerable to unstable retreat initiation, with all other factors being the same, on local as well as regional scales. This would be accomplished by a spatially variable melt parameterization. The slow ramp could be implemented as a boundary condition on the ocean circulation model or spatial variations of melt could be incorporated in the PLF.

Similarly, other processes could be incorporated such as isostatic rebound, spatially variable geothermal heat flow, and water routing. These, including spatially variable ocean warming, are a collection of processes that are important, but they won't change the conclusions about bed shape. Rather, they should provide additional details about instability initiation and unstable retreat.

REFERENCES

Ainley, D. G., Clarke, E. D., Arrigo, K., Fraser, W. R., Kato, A., Barton, K. J., and Wilson, P. R., 2005, Decadal-scale changes in the climate and biota of the Pacific sector of the Southern Ocean, 1950s to the 1990s: Antarctic Science, v. 17, no. 02, p. 171-182.

Anandakrishnan, S., Catania, G. A., Alley, R. B., and Horgan, H. J., 2007, Discovery of till deposition at the grounding line of Whillans Ice Stream: Science, v. 315, no. 5820, p. 1835-1838.

Anderson, J. B., 1999, Antarctic Marine Geology, Cambridge University Press.

Arthern, R. J., Winebrenner, D. P., and Vaughan, D. G., 2006, Antarctic snow accumulation mapped using polarization of 4.3-cm wavelength microwave emission: Journal of Geophysical Research: Atmospheres (1984–2012), v. 111, no. D6.

Behrendt, J. C., 1999, Crustal and lithospheric structure of the West Antarctic Rift System from geophysical investigations—a review: Global and Planetary Change, v. 23, no. 1, p. 25-44.

Bindschadler, R., Bamber, J., and Anandakrishnan, S., 2001, Onset of streaming flow in the Siple Coast region, West Antarctica, The West Antarctic Ice Sheet: Behavior and Environment, Volume 77, American Geophysical Union, p. 123-136.

Blatter, H., 1995, Velocity and stress fields in grounded glaciers: a simple algorithm for including deviatoric stress gradients: Journal of Glaciology, v. 41, no. 138, p. 333-344.

Bougamont, M., Christoffersen, P., Price, S., Fricker, H., Tulaczyk, S., and Carter, S., 2015, Reactivation of Kamb Ice Stream tributaries triggers century-scale reorganization of Siple Coast ice flow in West Antarctica: Geophysical Research Letters, v. 42, no. 20, p. 8471-8480.

Bougamont, M., Price, S., Christoffersen, P., and Payne, A., 2011, Dynamic patterns of ice stream flow in a 3-D higher-order ice sheet model with plastic bed and simplified hydrology: Journal of Geophysical Research: Earth Surface, v. 116, no. F4.

Bougamont, M., Tulaczyk, S., and Joughin, I., 2003, Response of subglacial sediments to basal freeze-on 2. Application in numerical modeling of the recent stoppage of Ice Stream C, West Antarctica: JGRB Journal of Geophysical Research: Solid Earth, v. 108, no. B4.

Bryson, A. E., 1975, Applied optimal control: optimization, estimation and control, CRC Press.

Cande, S. C., Stock, J. M., Müller, R. D., and Ishihara, T., 2000, Cenozoic motion between east and west Antarctica: Nature, v. 404, no. 6774, p. 145-150.

Carter, S. P., Fricker, H. A., Blankenship, D. D., Johnson, J. V., Lipscomb, W. H., Price, S. F., and Young, D. A., 2011, Modeling 5 years of subglacial lake activity in the

MacAyeal Ice Stream (Antarctica) catchment through assimilation of ICESat laser altimetry: Journal of Glaciology, v. 57, no. 206, p. 1098-1112.
Carter, S. P., Fricker, H. A., and Siegfried, M. R., 2013, Evidence of rapid subglacial water piracy under Whillans Ice Stream, West Antarctica: Journal of Glaciology, v. 59, no. 218, p. 1147-1162.
Childs, H., Brugger, E., Whitlock, B., Meredith, J., Ahern, S., Pugmire, D., Biagas, K., Miller, M., Harrison, C., Weber, G. H., Krishnan, H., Fogal, T., Sanderson, A., Garth, C., Bethel, E. W., Camp, D., Rubel, O., Durant, M., Favre, J. M., and Navratil, P., 2012, VisIt: An end-user tool for visualizing and analyzing very large data, High Performance Visualization--Enabling Extreme-Scale Scientific Insight.
Cornford, S. L., Martin, D., Payne, A., Ng, E., Le Brocq, A., Gladstone, R., Edwards, T. L., Shannon, S., Agosta, C., and Van Den Broeke, M., 2015, Century-scale simulations of the response of the West Antarctic Ice Sheet to a warming climate: Cryosphere (The), v. 9, p. 1579-1600.
Cornford, S. L., Martin, D. F., Graves, D. T., Ranken, D. F., Le Brocq, A. M., Gladstone, R. M., Payne, A. J., Ng, E. G., and Lipscomb, W. H., 2013, Adaptive mesh, finite volume modeling of marine ice sheets: Journal of Computational Physics, v. 232, no. 1, p. 529-549.
Creyts, T. T., and Schoof, C. G., 2009, Drainage through subglacial water sheets: Journal of Geophysical Research: Earth Surface, v. 114, no. F4.
Cuffey, K. M., and Paterson, W. S. B., 2010, The physics of glaciers, Academic Press, 693 p.:
Dalziel, I. W. D., and Lawver, L. A., 2001, The lithospheric setting of the West Antarctic ice sheet, The West Antarctic ice sheet: behavior and environment, Volume 77, American Geophysical Union, p. 29-44.
Dinniman, M. S., Klinck, J. M., and Hofmann, E. E., 2012, Sensitivity of Circumpolar Deep Water transport and ice shelf basal melt along the west Antarctic Peninsula to changes in the winds: Journal of Climate, v. 25, no. 14, p. 4799-4816.
Dupont, T., and Alley, R., 2005, Assessment of the importance of ice-shelf buttressing to ice-sheet flow: Geophysical Research Letters, v. 32, no. 4.
Flowers, G. E., Modelling water flow under glaciers and ice sheets, *in* Proceedings Proc. R. Soc. A2015, Volume 471, The Royal Society, p. 20140907.
Flowers, G. E., and Clarke, G. K., 2002, A multicomponent coupled model of glacier hydrology 1. Theory and synthetic examples: Journal of Geophysical Research: Solid Earth, v. 107, no. B11.
Fretwell, P., Pritchard, H. D., Vaughan, D. G., Bamber, J. L., Barrand, N. E., Bell, R., Bianchi, C., Bingham, R. G., Blankenship, D. D., Casassa, G., Catania, G., Callens, D., Conway, H., Cook, A. J., Corr, H. F., Damaske, D., Damm, V., Ferraccioli, F., Forsberg, R., Fujita, S., Gim, Y., Gogineni, P., Griggs, J. A., Hindmarsh, R. C. A., Holmund, P., Holt, J. W., Jacobel, R. W., Jenkins, A., Jokat, W., Jordan, T., King, E. C., Kohler, J., Krabill, W., Riger-Kusk, M., Langley, K. A., Leitchenkov, G., Leuschen, C., Luyendyk, B. P., Matsuoka, K., Mouginot, J., Nitsche, F. O., Nogi, Y., Nost, O. A., Popov, S. V., Rignot, E., Rippin, D. M., Rivera, A., Roberts, J., Ross, N., Siegert, M. J., Smith, A. M., Steinhage, D.,

Studinger, M., Sun, B., Tinto, B. K., Welch, B. C., Wilson, D., Young, D. A., Xiangbin, C., and Zirrizzotti, A., 2013, Bedmap2: improved ice bed, surface and thickness datasets for Antarctica: The Cryosphere, v. 7, no. 1, p. 375-393.
Gille, S. T., 2014, Meridional displacement of the Antarctic Circumpolar Current: Philosophical Transactions of the Royal Society of London A: Mathematical, Physical and Engineering Sciences, v. 372, no. 2019, p. 20130273.
Goelzer, H., Huybrechts, P., Furst, J. J., Nick, F. M., Andersen, M. L., Edwards, T. L., Fettweis, X., Payne, A. J., and Shannon, S., 2013, Sensitivity of Greenland ice sheet projections to model formulations: Journal of Glaciology, v. 59, no. 216, p. 1.
Goff, J. A., Powell, E. M., Young, D. A., and Blankenship, D. D., 2014, Instruments and Methods--Conditional simulation of Thwaites Glacier (Antarctica) bed topography for flow models: incorporating inhomogeneous statistics and channelized morphology: Journal of Glaciology, v. 60, no. 222, p. 635.
Goldberg, D., Holland, D., and Schoof, C., 2009, Grounding line movement and ice shelf buttressing in marine ice sheets: Journal of Geophysical Research: Earth Surface, v. 114, no. F4.
Golledge, N. R., Fogwill, C. J., Mackintosh, A. N., and Buckley, K. M., 2012, Dynamics of the last glacial maximum Antarctic ice-sheet and its response to ocean forcing: Proceedings of the National Academy of Sciences, v. 109, no. 40, p. 16052-16056.
Golledge, N. R., Kowalewski, D. E., Naish, T. R., Levy, R. H., Fogwill, C. J., and Gasson, E. G. W., 2015, The multi-millennial Antarctic commitment to future sea-level rise: Nature, v. 526, no. 7573, p. 421-425.
Greve, R., and Blatter, H., 2009, Dynamics of ice sheets and glaciers, Springer Science & Business Media, 287 p.:
Gudmundsson, G., Krug, J., Durand, G., Favier, L., and Gagliardini, O., 2012, The stability of grounding lines on retrograde slopes: The Cryosphere, v. 6, p. 1497-1505.
Gudmundsson, G. H., 2003, Transmission of basal variability to a glacier surface: Journal of Geophysical Research: Solid Earth, v. 108, no. B5.
-, 2006, Fortnightly variations in the flow velocity of Rutford Ice Stream, West Antarctica: Nature, v. 444, no. 7122, p. 1063-1064.
Hiester, J., Sergienko, O., and Hulbe, C., 2016, Topographically mediated ice stream subglacial drainage networks: Journal of Geophysical Research: Earth Surface.
Hindmarsh, R., 1997, Deforming beds: viscous and plastic scales of deformation: Quaternary Science Reviews, v. 16, no. 9, p. 1039-1056.
Hindmarsh, R. C. A., 2004, A numerical comparison of approximations to the Stokes equations used in ice sheet and glacier modeling: Journal of Geophysical Research: Earth Surface (2003–2012), v. 109, no. F1.
Holt, J. W., Blankenship, D. D., Morse, D. L., Young, D. A., Peters, M. E., Kempf, S. D., Richter, T. G., Vaughan, D. G., and Corr, H. F. J., 2006, New boundary conditions for the West Antarctic Ice Sheet: Subglacial topography of the

Thwaites and Smith glacier catchments: Geophysical Research Letters, v. 33, no. 9.
Hulbe, C. L., Wang, W., Joughin, I. R., and Siegert, M. J., 2003, The role of lateral and vertical shear in tributary flow toward a West Antarctic ice stream: Annals of Glaciology, v. 36, no. 1, p. 244-250.
Hutter, K., 1983, Theoretical glaciology: material science of ice and the mechanics of glaciers and ice sheets, Springer.
Iverson, N. R., Hooyer, T. S., and Baker, R. V., 1998, Ring-shear studies of till deformation: Coulomb-plastic behavior and distributed strain in glacier beds: Journal of Glaciology, v. 44, no. 148, p. 634-642.
Joughin, I., Smith, B. E., and Medley, B., 2014, Marine ice sheet collapse potentially under way for the Thwaites Glacier Basin, West Antarctica: Science, v. 344, no. 6185, p. 735-738.
Joughin, I., and Tulaczyk, S., 2002, Positive mass balance of the Ross ice streams, West Antarctica: Science, v. 295, no. 5554, p. 476-480.
King, J. C., and Turner, J., 2007, Antarctic meteorology and climatology, Cambridge University Press, Cambridge Atmospheric and Space Science Series.
Llubes, M., Lanseau, C., and Rémy, F., 2006, Relations between basal condition, subglacial hydrological networks and geothermal flux in Antarctica: Earth and Planetary Science Letters, v. 241, no. 3, p. 655-662.
Lythe, M. B., Vaughan, D. G., and BEDMAP Consortium, 2001, BEDMAP: A new ice thickness and subglacial topographic model of Antarctica: Journal of Geophysical Research: Solid Earth (1978–2012), v. 106, no. B6, p. 11335-11351.
MacAyeal, D. R., 1989, Large-scale ice flow over a viscous basal sediment: Theory and application to ice stream B, Antarctica: Journal of Geophysical Research: Solid Earth (1978–2012), v. 94, no. B4, p. 4071-4087.
MacAyeal, D. R., 1993, A tutorial on the use of control methods in ice-sheet modeling: Journal of Glaciology, v. 39, no. 131.
Martin, D., 2014, Discussion of ice flow velocities on Thwaites Tongue, *in* Waibel, M. S., ed.
Mayewski, P. A., Meredith, M. P., Summerhayes, C. P., Turner, J., Worby, A., Barrett, P. J., Casassa, G., Bertler, N. A. N., Bracegirdle, T., Naveira Garabato, A. C., Bromwich, D., Campbell, H., Hamilton, G. S., Lyons, W. B., Maasch, K. A., Aoki, S., Xiao, C., and van Ommen, T., 2009, State of the Antarctic and Southern Ocean climate system: Reviews of Geophysics, v. 47, no. 1, p. RG1003.
Mercer, J. H., 1978, West Antarctic ice sheet and CO2 greenhouse effect: a threat of disaster: Nature, v. 27, p. 26.
Morland, L. W., 1984, Thermomechanical balances of ice sheet flows: Geophysical & Astrophysical Fluid Dynamics, v. 29, no. 1-4, p. 237-266.
-, Unconfined ice shelf flow, *in* Proceedings Dynamics of the West Antarctic Ice Sheet, University of Utrecht, 1985, Reidel, p. 99-116.
Morlighem, M., Rignot, E., Seroussi, H., Larour, E., Ben Dhia, H., and Aubry, D., 2010, Spatial patterns of basal drag inferred using control methods from a full-Stokes

and simpler models for Pine Island Glacier, West Antarctica: Geophysical Research Letters, v. 37, no. 14.
Mukasa, S. B., and Dalziel, I. W., 2000, Marie Byrd Land, West Antarctica: Evolution of Gondwana's Pacific margin constrained by zircon U-Pb geochronology and feldspar common-Pb isotopic compositions: Geological Society of America Bulletin, v. 112, no. 4, p. 611-627.
Naish, T., Powell, R., Levy, R., Wilson, G., Scherer, R., Talarico, F., Krissek, L., Niessen, F., Pompilio, M., Wilson, T., Carter, L., DeConto, R., Huybers, P., McKay, R., Pollard, D., Ross, J., Winter, D., Barrett, P., Browne, G., Cody, R., Cowan, E., Crampton, J., Dunbar, G., Dunbar, N., Florindo, F., Gebhardt, C., Graham, I., Hannah, M., Hansaraj, D., Harwood, D., Helling, D., Henrys, S., Hinnov, L., Kuhn, G., Kyle, P., Laufer, A., Maffioli, P., Magens, D., Mandernack, K., McIntosh, W., Millan, C., Morin, R., Ohneiser, C., Paulsen, T., Persico, D., Raine, I., Reed, J., Riesselman, C., Sagnotti, L., Schmitt, D., Sjunneskog, C., Strong, P., Taviani, M., Vogel, S., Wilch, T., and Williams, T., 2009, Obliquity-paced Pliocene West Antarctic ice sheet oscillations: Nature, v. 458, no. 7236, p. 322-328.
Nitsche, F. O., Jacobs, S. S., Larter, R. D., and Gohl, K., 2007, Bathymetry of the Amundsen Sea continental shelf: implications for geology, oceanography, and glaciology: Geochemistry, Geophysics, Geosystems, v. 8, no. 10.
Nowicki, S., Bindschadler, R. A., Abe-Ouchi, A., Aschwanden, A., Bueler, E., Choi, H., Fastook, J., Granzow, G., Greve, R., and Gutowski, G., 2013, Insights into spatial sensitivities of ice mass response to environmental change from the SeaRISE ice sheet modeling project I: Antarctica: Journal of Geophysical Research: Earth Surface, p. 1-23.
Parizek, B. R., Christianson, K., Anandakrishnan, S., Alley, R. B., Walker, R. T., Edwards, R. A., Wolfe, D. S., Bertini, G. T., Rinehart, S. K., and Bindschadler, R. A., 2013, Dynamic (in) stability of Thwaites Glacier, West Antarctica: Journal of Geophysical Research: Earth Surface, v. 118, no. 2, p. 638-655.
Patankar, S., 1980, Numerical heat transfer and fluid flow, CRC press.
Pattyn, F., 2003, A new three-dimensional higher-order thermomechanical ice sheet model: Basic sensitivity, ice stream development, and ice flow across subglacial lakes: Journal of Geophysical Research: Solid Earth (1978–2012), v. 108, no. B8.
-, 2010, Antarctic subglacial conditions inferred from a hybrid ice sheet/ice stream model: Earth and Planetary Science Letters, v. 295, no. 3, p. 451-461.
Pattyn, F., Schoof, C., Perichon, L., Hindmarsh, R., Bueler, E., Fleurian, B. d., Durand, G., Gagliardini, O., Gladstone, R., and Goldberg, D., 2012, Results of the marine ice sheet model intercomparison project, MISMIP: The Cryosphere, v. 6, no. 3, p. 573-588.
Pollard, D., and DeConto, R. M., 2009, Modelling West Antarctic ice sheet growth and collapse through the past five million years: Nature, v. 458, no. 7236, p. 329-332.
Price, S., Waddington, E., and Conway, H., 2007, A full-stress, thermomechanical flow band model using the finite volume method: Journal of Geophysical Research: Earth Surface, v. 112, no. F3.

Pritchard, H. D., Arthern, R. J., Vaughan, D. G., and Edwards, L. A., 2009, Extensive dynamic thinning on the margins of the Greenland and Antarctic ice sheets: Nature, v. 461, no. 7266, p. 971-975.
Rémy, F., and Legresy, B., 2004, Subglacial hydrological networks in Antarctica and their impact on ice flow: Annals of Glaciology, v. 39, no. 1, p. 67-72.
Rignot, E., 2001, Evidence for rapid retreat and mass loss of Thwaites Glacier, West Antarctica: Journal of Glaciology, v. 47, no. 157, p. 213-222.
-, 2008, Changes in West Antarctic ice stream dynamics observed with ALOS PALSAR data: Geophysical Research Letters, v. 35, no. 12.
Rignot, E., Mouginot, J., Morlighem, M., Seroussi, H., and Scheuchl, B., 2014, Widespread, rapid grounding line retreat of Pine Island, Thwaites, Smith, and Kohler glaciers, West Antarctica, from 1992 to 2011: Geophysical Research Letters, v. 41, no. 10, p. 3502-3509.
Rignot, E., Vaughan, D. G., Schmeltz, M., Dupont, T., and MacAyeal, D., 2002, Acceleration of pine island and thwaites glaciers, west antarctica: Annals of Glaciology, v. 34, no. 1, p. 189-194.
Ross, N., Bingham, R. G., Corr, H. F., Ferraccioli, F., Jordan, T. A., Le Brocq, A., Rippin, D. M., Young, D., Blankenship, D. D., and Siegert, M. J., 2012, Steep reverse bed slope at the grounding line of the Weddell Sea sector in West Antarctica: Nature Geoscience, v. 5, no. 6, p. 393-396.
Rydt, J. D., Gudmundsson, G. H., Corr, H., and Christoffersen, P., 2013, Surface undulations of Antarctic ice streams tightly controlled by bedrock topography: The Cryosphere, v. 7, no. 2, p. 407-417.
Schoof, C., 2002, Basal perturbations under ice streams: form drag and surface expression: Journal of Glaciology, v. 48, no. 162, p. 407-416.
-, 2007, Ice sheet grounding line dynamics: Steady states, stability, and hysteresis: Journal of Geophysical Research: Earth Surface, v. 112, no. F3.
Sergienko, O., 2013, Basal channels on ice shelves: Journal of Geophysical Research: Earth Surface, v. 118, no. 3, p. 1342-1355.
Sergienko, O., Creyts, T. T., and Hindmarsh, R., 2014, Similarity of organized patterns in driving and basal stresses of Antarctic and Greenland ice sheets beneath extensive areas of basal sliding: Geophysical Research Letters, v. 41, no. 11, p. 3925-3932.
Shepherd, A., Ivins, E. R., Geruo, A., Barletta, V. R., Bentley, M. J., Bettadpur, S., Briggs, K. H., Bromwich, D. H., Forsberg, R., and Galin, N., 2012, A reconciled estimate of ice-sheet mass balance: Science, v. 338, no. 6111, p. 1183-1189.
Shepherd, A., and Wingham, D., 2007, Recent sea-level contributions of the Antarctic and Greenland ice sheets: science, v. 315, no. 5818, p. 1529-1532.
Shepherd, A., Wingham, D., and Rignot, E., 2004, Warm ocean is eroding West Antarctic ice sheet: Geophysical Research Letters, v. 31, no. 23.
Shepherd, A., Wingham, D. J., and Mansley, J. A. D., 2002, Inland thinning of the Amundsen Sea sector, West Antarctica: Geophysical Research Letters, v. 29, no. 10, p. 2-1-2-4.

Smith, R. C., Ainley, D., Baker, K., Domack, E., Emslie, S., Fraser, B., Kennett, J., Leventer, A., Mosley-Thompson, E., Sharon, S., and Vernet, M., 1999, Marine Ecosystem Sensitivity to Climate Change: BioScience, v. 49, no. 5, p. 393-404.

Sun, S., Cornford, S., Liu, Y., and Moore, J. C., 2014, Dynamic response of Antarctic ice shelves to bedrock uncertainty: The Cryosphere, v. 8, no. 4, p. 1561-1576.

Thoma, M., Jenkins, A., Holland, D., and Jacobs, S., 2008, Modelling circumpolar deep water intrusions on the Amundsen Sea continental shelf, Antarctica: Geophysical Research Letters, v. 35, no. 18.

Thomas, R., Rignot, E., Casassa, G., Kanagaratnam, P., Acuña, C., Akins, T., Brecher, H., Frederick, E., Gogineni, P., and Krabill, W., 2004, Accelerated sea-level rise from West Antarctica: Science, v. 306, no. 5694, p. 255-258.

Trathan, P. N., Forcada, J., and Murphy, E. J., 2007, Environmental forcing and Southern Ocean marine predator populations: effects of climate change and variability: Philosophical Transactions of the Royal Society B: Biological Sciences, v. 362, no. 1488, p. 2351-2365.

Truffer, M., and Echelmeyer, K. A., 2003, Of isbrae and ice streams: Annals of Glaciology, v. 36, no. 1, p. 66-72.

Tulaczyk, S., 2006, Scale independence of till rheology: Journal of Glaciology, v. 52, no. 178, p. 377-380.

Versteeg, H. K., and Malalasekera, W., 2007, An introduction to computational fluid dynamics: the finite volume method, Pearson Education.

Vieli, A., and Payne, A., 2005, Assessing the ability of numerical ice sheet models to simulate grounding line migration: Journal of Geophysical Research: Earth Surface, v. 110, no. F1.

Wåhlin, A., Yuan, X., Björk, G., and Nohr, C., 2010, Inflow of Warm Circumpolar Deep Water in the Central Amundsen Shelf*: Journal of physical oceanography, v. 40, no. 6, p. 1427-1434.

Weertman, J., 1974, Stability of the junction of an ice sheet and an ice shelf: Journal of Glaciology, v. 13, no. 67, p. 3-11.

Appendix A Experiment 1 Summary Table

Driving stress and flux across the grounding line summarized for each co-located observation in experiment 1. Column1 is the observation number. Column 2 is the transect (T) used to determine co-location for the given observation. Column 3 is the year of the B260 simulation that corresponds to the observation. Column 4 is the mean driving stress of the B260 simulation's ROI with units of kPa. Column 5 is the flux across the grounding line for the B260 simulation in units of km^3a^{-1}. Columns 6 through 8 are the B270 simulation equivalents of columns 3 through 5. Column 9 is the difference in driving stress calculated as B270 minus B260 with units of kPa. Column 10 is the difference in flux across the grounding line in units of km^3a^{-1} and calculated as B270 minus B260.

obs	T	B260 year	driving stress (kPa)	flux (km^3a^{-1})	B270 year	driving stress (kPa)	flux (km^3a^{-1})	Δdriving stress (kPa)	Δflux (km^3a^{-1})
1	3	422	96.86	127.82	271	90.89	224.79	-5.97	96.97
2	3	424	96.93	128.13	272	91.12	212.35	-5.81	84.22
3	3	425	96.97	128.86	273	91.25	205.06	-5.72	76.19
4	3	426	97.00	127.57	274	91.40	199.03	-5.61	71.46
5	3	427	97.06	128.84	275	91.53	189.93	-5.52	61.09
6	3	420	96.78	127.58	276	91.63	178.35	-5.15	50.77
7	3	414	96.58	126.03	277	91.75	174.87	-4.83	48.84
8	3	415	96.61	125.88	278	91.80	173.30	-4.81	47.42
9	3	416	96.64	125.44	279	91.84	169.50	-4.80	44.06
10	3	410	96.42	125.27	280	91.95	168.06	-4.47	42.79
11	3	411	96.46	127.37	281	92.06	167.90	-4.40	40.53
12	3	412	96.51	126.31	282	92.19	167.32	-4.32	41.01
13	3	413	96.53	126.39	283	92.28	166.78	-4.26	40.39
14	3	417	96.67	126.59	284	92.39	165.98	-4.28	39.39
15	3	418	96.71	126.21	285	92.46	164.24	-4.24	38.03
16	3	409	96.37	126.21	286	92.50	163.65	-3.86	37.44
17	3	407	96.27	124.85	287	92.62	162.55	-3.65	37.70
18	3	457	98.22	129.20	322	95.88	166.13	-2.34	36.92
19	3	458	98.27	130.69	323	96.00	165.28	-2.27	34.58
20	3	459	98.34	132.16	324	96.12	164.51	-2.22	32.36
21	3	460	98.39	130.74	325	96.17	164.69	-2.22	33.95
22	3	465	98.58	133.40	326	96.23	165.10	-2.35	31.70
23	3	461	98.41	129.99	327	96.37	163.61	-2.04	33.63

obs	T	B260 year	driving stress (kPa)	flux (km^3a^{-1})	B270 year	driving stress (kPa)	flux (km^3a^{-1})	Δdriving stress (kPa)	Δflux (km^3a^{-1})
24	3	462	98.45	129.85	328	96.46	162.97	-1.99	33.12
25	3	463	98.50	129.04	329	96.58	162.30	-1.92	33.26
26	3	464	98.55	130.53	330	96.71	161.91	-1.84	31.38
27	3	478	99.22	130.69	335	97.09	159.78	-2.13	29.09
28	3	470	98.84	132.87	336	97.25	160.73	-1.59	27.86
29	3	471	98.89	133.55	337	97.34	161.42	-1.55	27.87
30	3	472	98.96	135.05	338	97.35	160.92	-1.61	25.87
31	3	473	99.01	133.63	339	97.47	160.37	-1.54	26.74
32	3	474	99.05	132.13	340	97.57	161.65	-1.49	29.52
33	3	477	99.17	129.64	341	97.65	160.87	-1.52	31.22
34	3	476	99.11	133.01	342	97.76	160.89	-1.35	27.88
35	3	479	99.27	132.44	343	97.82	160.84	-1.44	28.40
36	3	481	99.34	130.05	345	98.01	160.03	-1.32	29.98
37	3	486	99.49	130.47	347	98.13	160.70	-1.36	30.23
38	3	484	99.44	131.69	348	98.23	161.27	-1.21	29.58
39	3	489	99.65	130.64	349	98.35	160.59	-1.30	29.95
40	3	490	99.66	129.17	350	98.41	159.82	-1.25	30.65
41	3	497	99.99	128.84	351	98.46	160.09	-1.53	31.25
42	3	498	100.04	127.91	352	98.53	161.46	-1.52	33.56
43	3	500	100.10	128.41	353	98.62	159.95	-1.48	31.54
44	3	501	100.13	128.21	354	98.68	159.59	-1.45	31.38
45	3	502	100.17	128.07	355	98.77	160.03	-1.39	31.96
46	3	507	100.31	126.84	356	98.92	160.21	-1.38	33.36
47	3	510	100.43	128.19	357	99.00	160.81	-1.43	32.62
48	3	512	100.53	128.73	358	99.08	160.73	-1.46	31.99
49	3	513	100.57	128.30	359	99.17	160.30	-1.41	32.00
50	3	514	100.60	128.35	360	99.22	161.06	-1.38	32.72
51	3	515	100.65	129.23	361	99.27	159.34	-1.38	30.11
52	3	516	100.67	129.38	362	99.32	159.30	-1.35	29.92
53	3	517	100.71	129.96	363	99.41	159.59	-1.30	29.63
54	3	518	100.76	130.27	364	99.51	159.99	-1.24	29.71
55	3	519	100.79	129.95	365	99.60	158.28	-1.19	28.33
56	3	520	100.86	130.26	366	99.65	157.50	-1.21	27.24
57	3	521	100.92	130.40	367	99.76	159.02	-1.16	28.62
58	3	523	101.00	130.39	368	99.88	160.28	-1.12	29.89
59	3	525	101.08	130.14	369	99.98	161.47	-1.10	31.32
60	3	526	101.12	130.65	370	100.06	161.72	-1.06	31.07
61	3	529	101.23	130.41	371	100.11	162.70	-1.12	32.29
62	3	530	101.29	130.73	372	100.23	161.29	-1.06	30.57
63	3	531	101.32	129.95	373	100.31	162.55	-1.01	32.61

obs	T	B260 year	driving stress (kPa)	flux (km^3a^{-1})	B270 year	driving stress (kPa)	flux (km^3a^{-1})	Δdriving stress (kPa)	Δflux (km^3a^{-1})
64	3	534	101.44	129.72	374	100.42	164.90	-1.02	35.18
65	3	535	101.45	129.81	375	100.50	165.43	-0.96	35.62
66	3	537	101.54	130.41	376	100.58	167.01	-0.96	36.60
67	3	540	101.68	129.79	377	100.66	166.79	-1.02	37.00
68	3	541	101.72	129.11	378	100.78	166.66	-0.93	37.55
69	3	550	102.07	129.33	379	100.83	168.83	-1.24	39.50
70	3	552	102.10	129.86	380	100.96	170.66	-1.14	40.80
71	3	555	102.21	129.36	381	101.08	172.79	-1.13	43.43
72	3	558	102.33	130.00	382	101.23	173.66	-1.10	43.66
73	3	561	102.45	129.34	383	101.29	174.30	-1.16	44.96
74	3	567	102.67	130.52	384	101.37	174.80	-1.30	44.29
75	3	569	102.74	129.87	385	101.50	173.09	-1.25	43.22
76	3	571	102.80	130.76	386	101.56	175.16	-1.24	44.40
77	3	575	102.97	130.08	387	101.63	176.18	-1.34	46.10
78	3	577	103.06	131.89	388	101.78	175.93	-1.28	44.04
79	3	579	103.16	133.37	389	101.92	175.77	-1.24	42.40
80	3	580	103.20	133.21	390	102.00	175.29	-1.20	42.09
81	3	583	103.30	136.31	391	102.12	175.74	-1.18	39.43
82	3	584	103.39	138.72	392	102.25	178.40	-1.14	39.68
83	3	586	103.54	139.84	393	102.31	181.59	-1.23	41.75
84	3	587	103.60	140.31	394	102.46	183.60	-1.14	43.29
85	3	591	103.87	138.95	396	102.69	183.59	-1.18	44.64
86	3	593	103.98	140.36	397	102.79	182.78	-1.19	42.42
87	3	594	104.07	141.14	398	102.92	182.64	-1.15	41.49
88	3	595	104.13	140.59	399	103.04	181.43	-1.09	40.84
89	3	598	104.34	139.92	400	103.16	182.60	-1.18	42.68
90	3	600	104.40	138.65	401	103.24	181.84	-1.17	43.19
91	3	602	104.52	139.79	402	103.29	180.88	-1.24	41.09
92	3	605	104.65	138.24	403	103.41	180.84	-1.24	42.60
93	3	607	104.78	139.76	404	103.53	181.07	-1.25	41.31
94	3	608	104.83	139.89	405	103.64	179.55	-1.19	39.66
95	3	609	104.89	139.66	406	103.66	178.58	-1.23	38.92
96	3	610	104.95	139.79	407	103.78	177.68	-1.17	37.90
97	3	611	105.02	139.32	408	103.90	176.35	-1.13	37.03
98	3	612	105.10	137.85	409	104.04	177.01	-1.07	39.17
99	3	616	105.34	138.13	410	104.16	177.80	-1.18	39.67
100	3	617	105.42	138.34	411	104.23	179.97	-1.20	41.62
101	3	620	105.55	139.94	412	104.29	180.41	-1.25	40.47
102	3	621	105.61	140.84	413	104.40	178.75	-1.21	37.91
103	3	622	105.65	141.93	414	104.54	178.62	-1.11	36.70

obs	T	B260 year	driving stress (kPa)	flux (km^3a^{-1})	B270 year	driving stress (kPa)	flux (km^3a^{-1})	Δdriving stress (kPa)	Δflux (km^3a^{-1})
104	3	623	105.70	142.33	415	104.67	180.05	-1.03	37.72
105	3	625	105.86	143.24	416	104.79	178.33	-1.08	35.09
106	3	626	105.90	143.69	417	104.92	180.67	-0.98	36.98
107	3	627	105.98	144.48	418	105.01	181.01	-0.98	36.53
108	3	628	106.05	145.05	419	105.15	181.17	-0.90	36.12
109	3	629	106.13	146.55	420	105.25	181.09	-0.89	34.54
110	3	630	106.22	147.34	421	105.38	179.64	-0.84	32.30
111	3	635	106.68	149.14	426	106.06	181.56	-0.62	32.42
112	3	636	106.75	149.73	427	106.18	179.37	-0.57	29.64
113	3	643	107.35	150.47	434	106.95	182.69	-0.40	32.22
114	3	645	107.48	152.79	436	107.19	180.47	-0.29	27.69
115	3	646	107.60	151.89	437	107.31	182.27	-0.28	30.38
116	3	647	107.68	151.19	438	107.48	183.77	-0.20	32.58
117	3	648	107.80	152.47	439	107.58	184.18	-0.22	31.71
118	3	650	108.00	154.99	440	107.72	185.91	-0.27	30.91
119	3	651	108.10	154.26	441	107.89	184.23	-0.22	29.97
120	3	652	108.19	153.86	442	107.97	182.86	-0.22	29.00
121	3	653	108.30	152.89	443	108.15	183.42	-0.15	30.53
122	3	654	108.37	153.66	444	108.28	186.22	-0.09	32.56
123	3	655	108.47	154.94	445	108.44	187.72	-0.03	32.78
124	3	656	108.54	155.78	446	108.58	187.11	0.04	31.33
125	3	657	108.63	155.89	447	108.68	186.69	0.05	30.80
126	3	658	108.71	157.12	448	108.83	186.58	0.12	29.46
127	3	660	108.89	155.27	449	108.96	186.63	0.07	31.36
128	3	662	109.04	154.21	450	109.14	187.17	0.10	32.96
129	3	663	109.08	154.67	451	109.29	187.00	0.21	32.33
130	3	665	109.26	154.52	452	109.41	184.80	0.15	30.28
131	3	666	109.35	152.92	453	109.54	183.56	0.19	30.64
132	3	668	109.49	151.43	454	109.67	181.48	0.18	30.05
133	3	669	109.59	150.69	455	109.78	181.07	0.19	30.38
134	3	670	109.65	151.18	456	109.90	180.73	0.24	29.55
135	3	671	109.71	150.57	457	109.92	181.39	0.21	30.82
136	3	672	109.78	149.81	458	110.03	179.55	0.25	29.75
137	3	673	109.87	150.14	459	110.13	179.75	0.27	29.60
138	3	675	110.03	151.53	460	110.24	180.16	0.21	28.63
139	3	676	110.06	149.79	461	110.33	180.81	0.27	31.02
140	3	677	110.12	149.80	462	110.45	180.10	0.33	30.30
141	3	678	110.19	149.66	463	110.55	179.09	0.36	29.43
142	3	680	110.28	149.31	464	110.65	179.50	0.38	30.19
143	3	681	110.35	149.65	465	110.77	179.87	0.43	30.22

obs	T	B260 year	driving stress (kPa)	flux (km^3a^{-1})	B270 year	driving stress (kPa)	flux (km^3a^{-1})	Δdriving stress (kPa)	Δflux (km^3a^{-1})
144	3	682	110.39	149.76	466	110.84	181.42	0.46	31.66
145	3	685	110.59	149.50	467	111.00	182.25	0.41	32.75
146	3	687	110.73	151.10	468	111.15	181.01	0.42	29.91
147	3	688	110.83	149.83	469	111.27	181.41	0.43	31.58
148	3	689	110.89	150.59	470	111.34	181.73	0.45	31.14
149	3	690	110.94	150.90	471	111.46	181.31	0.52	30.41
150	3	691	111.01	151.60	472	111.56	180.55	0.55	28.95
151	3	692	111.05	151.54	473	111.70	181.63	0.66	30.08
152	3	695	111.30	150.62	474	111.86	182.29	0.56	31.67
153	3	696	111.36	150.67	475	112.00	181.52	0.64	30.85
154	3	698	111.48	149.66	476	112.16	181.56	0.68	31.90
155	3	699	111.53	148.81	477	112.30	181.90	0.76	33.08
156	3	700	111.60	149.22	478	112.39	181.83	0.80	32.61
157	3	702	111.74	150.11	479	112.54	181.28	0.80	31.17
158	3	703	111.79	149.05	480	112.68	181.17	0.89	32.12
159	3	704	111.85	149.07	481	112.76	180.21	0.91	31.14
160	3	706	111.99	148.96	482	112.91	179.96	0.92	31.00
161	3	707	112.05	148.20	483	113.02	180.16	0.97	31.96
162	3	708	112.10	147.95	484	113.17	180.35	1.07	32.40
163	3	712	112.35	147.13	486	113.38	179.67	1.03	32.54
164	3	713	112.44	146.78	487	113.50	179.22	1.06	32.44
165	3	717	112.65	145.96	488	113.64	177.56	0.99	31.60
166	3	711	112.30	147.41	489	113.73	177.61	1.43	30.21
167	3	722	112.97	145.33	490	113.85	176.30	0.88	30.97
168	3	719	112.74	145.32	491	113.92	175.87	1.18	30.55
169	3	723	113.05	145.49	492	114.03	176.29	0.98	30.79
170	3	724	113.10	145.80	493	114.20	177.99	1.10	32.19
171	3	727	113.37	147.46	494	114.33	179.85	0.96	32.39
172	3	728	113.43	148.36	495	114.50	182.58	1.07	34.22
173	3	729	113.49	149.60	496	114.67	184.22	1.18	34.62
174	3	731	113.65	150.46	497	114.81	186.02	1.16	35.56
175	3	732	113.76	151.11	498	114.97	187.43	1.21	36.32
176	3	733	113.83	151.43	499	115.08	187.66	1.25	36.23
177	3	735	114.01	153.33	500	115.26	188.23	1.25	34.90
178	3	737	114.20	155.59	501	115.42	189.01	1.21	33.42
179	3	738	114.32	155.50	502	115.53	190.48	1.21	34.98
180	3	739	114.43	155.26	503	115.68	191.11	1.25	35.85
181	3	740	114.54	155.06	504	115.85	192.06	1.31	37.00
182	3	744	114.87	155.07	505	115.98	192.30	1.11	37.23
183	3	745	114.97	154.65	506	116.12	193.53	1.15	38.88

obs	T	B260 year	driving stress (kPa)	flux (km^3a^{-1})	B270 year	driving stress (kPa)	flux (km^3a^{-1})	Δdriving stress (kPa)	Δflux (km^3a^{-1})
184	3	746	115.02	155.39	507	116.26	193.74	1.24	38.35
185	3	748	115.29	156.23	508	116.39	194.10	1.10	37.87
186	3	749	115.40	156.75	509	116.47	193.88	1.07	37.13
187	3	750	115.52	156.47	510	116.64	193.49	1.12	37.02
188	3	751	115.63	156.77	511	116.79	191.88	1.16	35.12
189	3	752	115.70	156.56	512	116.90	191.48	1.21	34.92
190	3	753	115.77	156.26	513	117.00	190.72	1.23	34.46
191	3	754	115.86	156.31	514	117.13	190.11	1.27	33.81
192	3	755	115.91	156.13	515	117.26	188.85	1.35	32.72
193	3	756	115.99	156.60	516	117.40	188.16	1.41	31.56
194	3	757	116.06	156.82	517	117.51	187.81	1.45	30.99
195	3	758	116.14	157.02	518	117.63	187.49	1.49	30.47
196	3	759	116.24	156.93	519	117.72	187.86	1.48	30.93
197	3	761	116.41	157.08	521	117.90	187.69	1.49	30.61
198	3	762	116.50	157.25	522	117.96	187.37	1.46	30.12
199	3	763	116.57	156.50	523	118.12	187.12	1.55	30.63
200	3	764	116.62	156.92	524	118.20	186.43	1.58	29.50
201	3	765	116.74	157.13	525	118.31	186.35	1.57	29.21
202	3	767	116.95	156.69	526	118.41	185.66	1.46	28.97
203	3	768	116.99	156.48	527	118.49	185.88	1.50	29.40
204	3	769	117.12	156.46	528	118.61	186.04	1.49	29.58
205	3	770	117.19	156.28	529	118.75	185.90	1.55	29.62
206	3	773	117.43	156.08	530	118.85	185.77	1.42	29.69
207	3	774	117.46	156.03	531	119.01	185.23	1.55	29.20
208	3	776	117.65	155.82	532	119.12	185.40	1.47	29.59
209	3	777	117.73	155.08	533	119.23	185.25	1.50	30.17
210	3	778	117.80	154.99	534	119.37	185.60	1.57	30.61
211	3	779	117.87	154.89	535	119.48	185.65	1.61	30.76
212	3	782	118.07	154.35	536	119.58	185.47	1.51	31.12
213	3	783	118.13	154.78	537	119.70	185.40	1.57	30.62
214	3	784	118.17	154.50	538	119.81	185.43	1.64	30.93
215	3	785	118.23	154.16	539	119.90	185.05	1.67	30.89
216	3	786	118.32	154.07	540	120.03	184.07	1.70	30.00
217	3	787	118.37	153.67	541	120.11	183.23	1.74	29.56
218	3	788	118.43	153.37	542	120.16	183.07	1.72	29.70
219	3	789	118.49	152.65	543	120.26	182.94	1.77	30.29
220	3	792	118.68	151.64	544	120.33	182.89	1.65	31.24
221	3	793	118.73	151.41	545	120.46	182.98	1.73	31.56
222	3	794	118.82	151.21	546	120.55	182.72	1.74	31.50
223	3	796	118.99	150.96	547	120.64	182.68	1.65	31.72

obs	T	B260 year	driving stress (kPa)	flux (km^3a^{-1})	B270 year	driving stress (kPa)	flux (km^3a^{-1})	Δdriving stress (kPa)	Δflux (km^3a^{-1})
224	3	797	119.05	150.98	548	120.65	182.87	1.60	31.89
225	3	798	119.11	150.93	549	120.78	183.15	1.67	32.23
226	3	801	119.30	150.37	550	120.90	183.07	1.60	32.70
227	3	802	119.40	150.91	552	121.09	182.64	1.69	31.73
228	3	804	119.55	150.63	553	121.19	182.38	1.64	31.76
229	3	805	119.63	150.21	554	121.29	182.20	1.67	31.98
230	3	807	119.74	149.57	555	121.41	182.01	1.66	32.44
231	3	808	119.85	149.38	556	121.52	181.71	1.67	32.33
232	3	809	119.91	149.11	557	121.60	181.88	1.70	32.77
233	3	810	120.00	149.09	558	121.73	181.46	1.73	32.38
234	3	811	120.04	148.80	559	121.83	181.19	1.78	32.38
235	3	812	120.11	148.33	560	122.00	181.40	1.88	33.07
236	3	813	120.17	148.06	561	122.10	180.96	1.93	32.90
237	3	818	120.43	147.59	562	122.21	180.46	1.78	32.87
238	3	819	120.46	147.59	563	122.26	180.49	1.80	32.90
239	3	820	120.54	147.82	565	122.46	180.81	1.92	32.99
240	3	821	120.61	147.90	566	122.56	180.50	1.95	32.60
241	3	822	120.65	148.50	567	122.61	180.20	1.95	31.70
242	3	824	120.79	149.14	568	122.76	180.93	1.97	31.79
243	3	827	120.99	149.90	569	122.89	181.43	1.90	31.53
244	3	825	120.85	149.18	570	122.98	181.89	2.13	32.71
245	3	826	120.96	149.38	571	123.03	181.83	2.07	32.45
246	3	828	121.07	150.32	572	123.15	181.82	2.08	31.50
247	3	829	121.14	150.34	573	123.25	181.88	2.11	31.54
248	3	830	121.19	150.74	574	123.34	181.76	2.16	31.02
249	3	831	121.24	151.12	575	123.48	181.52	2.24	30.40
250	3	836	121.56	153.17	576	123.50	181.60	1.94	28.44
251	3	833	121.38	152.04	577	123.52	181.90	2.14	29.86
252	3	834	121.42	152.48	578	123.59	181.55	2.17	29.07
253	3	835	121.51	152.73	579	123.71	181.10	2.20	28.37
254	3	837	121.65	153.42	580	123.77	180.94	2.12	27.53
255	3	838	121.73	153.20	581	123.87	180.53	2.14	27.32
256	3	839	121.81	152.91	582	123.98	180.03	2.17	27.12
257	3	840	121.89	152.93	583	124.08	179.24	2.19	26.31
258	3	841	121.97	152.73	584	124.18	178.50	2.21	25.77
259	3	842	122.04	152.76	585	124.27	178.47	2.22	25.71
260	3	823	120.71	148.89	586	124.33	178.54	3.63	29.65
261	3	844	122.18	152.45	588	124.55	178.30	2.37	25.85
262	3	845	122.21	152.72	589	124.65	177.61	2.44	24.89
263	3	850	122.52	151.98	590	124.60	177.18	2.08	25.19

obs	T	B260 year	driving stress (kPa)	flux (km^3a^{-1})	B270 year	driving stress (kPa)	flux (km^3a^{-1})	Δdriving stress (kPa)	Δflux (km^3a^{-1})
264	3	852	122.66	151.21	591	124.68	177.19	2.01	25.98
265	3	853	122.77	151.12	592	124.80	176.96	2.03	25.83
266	3	854	122.85	151.03	593	124.87	176.72	2.03	25.68
267	3	855	122.91	151.06	594	125.00	176.57	2.08	25.51
268	3	856	122.98	150.82	595	125.09	176.31	2.11	25.49
269	3	857	123.00	150.65	596	125.11	176.03	2.12	25.38
270	3	858	123.06	150.60	597	125.19	175.91	2.13	25.31
271	3	859	123.11	150.50	598	125.28	175.67	2.18	25.18
272	3	860	123.23	150.36	599	125.39	175.37	2.15	25.01
273	3	861	123.32	150.38	600	125.50	175.49	2.18	25.11
274	3	862	123.39	150.18	601	125.58	175.54	2.19	25.36
275	3	865	123.58	149.49	602	125.68	175.27	2.10	25.78
276	3	866	123.64	149.26	603	125.75	175.12	2.12	25.87
277	3	867	123.65	149.47	604	125.86	174.76	2.21	25.28
278	3	868	123.71	148.84	605	125.96	174.25	2.25	25.41
279	3	870	123.83	148.04	606	126.07	173.71	2.24	25.67
280	3	873	124.01	147.50	610	126.41	173.06	2.40	25.56
281	3	875	124.10	146.95	611	126.48	173.17	2.38	26.22
282	3	876	124.08	147.30	612	126.53	173.03	2.45	25.73
283	3	877	124.14	146.82	613	126.58	172.80	2.44	25.98
284	3	878	124.21	146.38	614	126.65	171.56	2.44	25.18
285	3	879	124.33	146.32	615	126.70	171.44	2.37	25.12
286	3	880	124.40	145.98	616	126.79	171.18	2.39	25.20
287	3	882	124.53	146.35	617	126.93	171.14	2.40	24.78
288	3	885	124.71	145.89	620	127.20	170.81	2.49	24.92
289	3	886	124.75	145.26	621	127.34	170.81	2.59	25.56
290	3	887	124.81	145.39	622	127.39	171.40	2.58	26.01
291	3	888	124.84	144.87	623	127.44	170.98	2.60	26.10
292	3	889	124.86	144.67	624	127.46	170.54	2.60	25.87
293	3	890	124.83	144.14	625	127.54	169.99	2.70	25.84
294	3	893	125.02	143.60	626	127.62	170.26	2.60	26.66
295	3	894	125.04	143.75	628	127.77	170.11	2.73	26.37
296	3	897	125.16	143.49	629	127.87	169.34	2.71	25.85
297	3	898	125.23	143.14	630	127.94	168.97	2.72	25.83
298	3	899	125.30	142.89	631	127.99	168.68	2.69	25.79
299	3	901	125.37	143.19	632	128.05	168.46	2.68	25.28
300	3	902	125.43	143.30	633	128.13	169.07	2.70	25.77
301	3	903	125.48	142.98	634	128.18	169.28	2.70	26.30
302	3	904	125.54	142.90	635	128.26	168.68	2.72	25.78
303	3	906	125.65	142.99	636	128.26	168.64	2.61	25.66

obs	T	B260 year	driving stress (kPa)	flux (km^3a^{-1})	B270 year	driving stress (kPa)	flux (km^3a^{-1})	Δdriving stress (kPa)	Δflux (km^3a^{-1})
304	3	907	125.71	143.38	637	128.35	168.26	2.64	24.88
305	3	908	125.76	143.38	638	128.42	168.65	2.66	25.27
306	3	909	125.82	143.16	639	128.50	169.27	2.68	26.11
307	3	910	125.87	142.72	640	128.60	169.39	2.72	26.67
308	3	912	126.03	142.99	641	128.68	170.43	2.65	27.43
309	3	913	126.06	142.75	642	128.73	170.84	2.67	28.09
310	3	914	126.12	142.75	643	128.82	170.24	2.70	27.49
311	3	917	126.30	143.02	644	128.92	169.62	2.62	26.60
312	3	918	126.36	143.41	645	129.01	170.11	2.65	26.70
313	3	920	126.51	143.91	646	129.01	170.21	2.51	26.31
314	3	921	126.57	143.94	647	129.11	170.16	2.54	26.23
315	3	923	126.69	144.19	648	129.20	169.34	2.52	25.14
316	3	925	126.76	144.41	649	129.32	168.71	2.56	24.30
317	3	926	126.83	143.82	650	129.39	168.63	2.56	24.81
318	3	927	126.90	144.22	651	129.47	169.15	2.57	24.93
319	3	931	127.24	144.65	654	129.73	170.97	2.49	26.32
320	3	933	127.34	145.32	655	129.82	171.31	2.48	25.99
321	3	934	127.40	146.06	656	129.91	172.17	2.51	26.11
322	3	935	127.47	144.80	657	129.94	170.90	2.48	26.10
323	3	936	127.52	145.04	658	130.05	171.18	2.53	26.14
324	3	937	127.62	145.22	659	130.12	171.13	2.49	25.91
325	3	938	127.67	145.70	660	130.21	170.81	2.55	25.11
326	3	939	127.73	146.19	661	130.32	171.00	2.58	24.81
327	3	941	127.98	145.80	662	130.40	170.25	2.42	24.45
328	3	942	128.05	145.89	663	130.50	170.01	2.45	24.12
329	3	943	128.18	146.04	664	130.60	170.26	2.42	24.22
330	3	944	128.17	145.88	665	130.71	169.93	2.54	24.05
331	3	945	128.25	145.67	666	130.81	169.15	2.55	23.48
332	3	946	128.38	145.62	667	130.86	169.80	2.49	24.18
333	3	948	128.54	145.03	668	130.86	169.55	2.32	24.53
334	3	949	128.62	144.81	669	130.96	169.84	2.34	25.03
335	3	950	128.72	145.12	670	131.05	170.05	2.33	24.93
336	3	951	128.78	144.95	671	131.11	169.90	2.32	24.95
337	3	952	128.82	145.03	672	131.17	169.45	2.35	24.43
338	3	953	128.87	145.23	673	131.21	168.99	2.34	23.76
339	3	955	129.03	145.50	674	131.29	169.40	2.25	23.90
340	3	956	129.10	145.94	675	131.39	169.90	2.28	23.96
341	3	957	129.16	145.73	676	131.49	171.00	2.33	25.27
342	3	958	129.23	145.28	677	131.59	170.88	2.35	25.60
343	3	959	129.32	144.92	678	131.69	170.49	2.37	25.56

obs	T	B260 year	driving stress (kPa)	flux (km^3a^{-1})	B270 year	driving stress (kPa)	flux (km^3a^{-1})	Δdriving stress (kPa)	Δflux (km^3a^{-1})
344	3	962	129.48	144.89	679	131.80	170.80	2.32	25.91
345	3	963	129.55	145.02	680	131.88	170.59	2.33	25.57
346	3	964	129.61	144.87	681	131.96	170.11	2.35	25.24
347	3	965	129.67	144.60	682	131.99	169.74	2.32	25.14
348	3	967	129.78	144.79	683	132.06	169.49	2.28	24.70
349	3	968	129.85	144.58	684	132.16	169.52	2.31	24.94
350	3	969	129.94	144.65	685	132.26	169.41	2.32	24.76
351	3	971	130.06	145.08	687	132.42	170.39	2.36	25.31
352	3	972	130.12	145.07	688	132.51	170.93	2.40	25.85
353	3	974	130.24	144.15	689	132.60	170.46	2.36	26.31
354	3	976	130.35	143.90	690	132.80	169.83	2.46	25.93
355	3	977	130.41	144.20	691	132.92	169.48	2.51	25.28
356	3	979	130.49	144.14	692	132.97	169.37	2.48	25.23
357	3	980	130.49	143.86	693	133.10	168.63	2.61	24.77
358	3	982	130.64	143.40	694	133.17	168.31	2.54	24.91
359	3	983	130.68	143.37	695	133.25	168.28	2.57	24.91
360	3	984	130.75	143.67	696	133.34	169.12	2.59	25.45
361	3	987	130.96	143.76	697	133.46	169.33	2.50	25.57
362	3	988	131.04	143.48	698	133.58	169.43	2.54	25.95
363	3	989	131.10	143.21	699	133.66	169.15	2.56	25.95
364	3	990	131.19	142.86	700	133.83	169.03	2.64	26.17
365	3	991	131.26	143.03	701	133.92	169.26	2.66	26.22
366	3	993	131.44	143.56	702	134.02	169.07	2.58	25.51
367	3	994	131.53	143.22	703	134.12	168.67	2.59	25.45
368	3	997	131.68	143.20	704	134.17	168.51	2.49	25.30
369	3	998	131.74	143.44	705	134.27	168.54	2.53	25.10
370	3	999	131.80	143.63	706	134.32	168.60	2.51	24.97
371	3	1000	131.86	143.92	707	134.38	168.65	2.52	24.74
372	3	1001	131.95	144.03	708	134.55	169.48	2.60	25.45
373	3	1002	132.05	145.04	709	134.64	169.60	2.59	24.56
374	3	1004	132.26	146.11	710	134.73	170.54	2.48	24.43
375	3	1005	132.36	146.66	711	134.79	172.42	2.43	25.75
376	3	1006	132.42	146.95	712	134.79	173.93	2.37	26.99
377	3	1008	132.58	146.99	713	134.89	173.71	2.31	26.72
378	3	1009	132.66	146.97	714	135.03	172.70	2.37	25.73
379	3	1016	133.08	143.45	720	135.62	169.69	2.54	26.23
380	3	1017	133.21	142.74	721	135.69	169.43	2.48	26.69
381	3	1019	133.37	142.42	722	135.82	168.92	2.45	26.50
382	3	1021	133.46	142.32	723	135.91	169.06	2.45	26.74
383	3	1022	133.57	142.19	724	136.05	168.79	2.48	26.60

obs	T	B260 year	driving stress (kPa)	flux (km^3a^{-1})	B270 year	driving stress (kPa)	flux (km^3a^{-1})	Δdriving stress (kPa)	Δflux (km^3a^{-1})
384	3	1023	133.53	142.04	725	136.18	168.73	2.65	26.69
385	3	1025	133.65	141.79	726	136.31	168.75	2.66	26.96
386	3	1026	133.67	141.62	727	136.40	168.65	2.74	27.03
387	3	1027	133.71	141.33	728	136.46	168.91	2.75	27.58
388	3	1030	133.90	140.43	729	136.59	168.76	2.69	28.33
389	3	1031	133.96	140.34	730	136.73	168.48	2.77	28.14
390	3	1032	134.08	140.32	731	136.80	168.14	2.72	27.82
391	3	1034	134.20	140.04	732	136.93	168.39	2.73	28.35
392	3	1035	134.29	139.80	733	137.03	168.09	2.74	28.29
393	3	1037	134.43	139.64	734	137.17	167.76	2.74	28.12
394	3	1039	134.60	139.58	735	137.29	167.46	2.69	27.88
395	3	1041	134.73	139.63	736	137.42	166.80	2.69	27.17
396	3	1042	134.80	139.84	737	137.49	166.97	2.69	27.13
397	3	1044	134.94	140.24	738	137.58	166.93	2.64	26.69
398	3	1045	135.03	140.58	739	137.70	166.73	2.67	26.15
399	3	1047	135.21	140.58	740	137.79	167.16	2.59	26.58
400	3	1048	135.28	140.32	741	137.95	166.71	2.66	26.40
401	3	1049	135.35	140.34	742	138.02	166.69	2.67	26.35
402	3	1051	135.51	139.92	743	138.14	167.42	2.63	27.51
403	3	1052	135.59	139.89	744	138.22	167.18	2.63	27.29
404	3	1054	135.74	139.72	745	138.33	166.92	2.59	27.19
405	3	1056	135.87	139.54	746	138.45	166.41	2.58	26.86
406	3	1057	135.94	139.64	750	138.88	166.04	2.94	26.40
407	3	1058	136.01	139.71	751	138.89	165.47	2.88	25.76
408	3	1063	136.37	138.73	754	139.26	165.69	2.89	26.97
409	3	1064	136.43	139.03	755	139.42	165.90	2.99	26.86
410	3	1066	136.56	138.62	756	139.50	165.23	2.94	26.61
411	3	1067	136.63	138.83	757	139.64	165.02	3.01	26.18
412	3	1069	136.75	138.85	758	139.78	164.59	3.02	25.74
413	3	1070	136.83	138.53	759	139.89	164.88	3.06	26.34
414	3	1072	136.96	138.68	760	139.99	165.06	3.03	26.38
415	3	1073	137.00	138.74	761	140.08	164.84	3.08	26.11
416	3	1075	137.18	139.24	762	140.17	164.58	2.99	25.34
417	3	1076	137.25	139.28	763	140.26	164.97	3.00	25.70
418	3	1077	137.32	138.95	764	140.39	164.67	3.07	25.72
419	3	1079	137.52	139.01	765	140.50	164.80	2.97	25.79
420	3	1078	137.44	138.83	766	140.60	165.00	3.16	26.16
421	3	1080	137.61	139.11	767	140.73	165.49	3.13	26.38
422	3	1082	137.75	139.39	768	140.82	166.61	3.07	27.22
423	3	1084	137.87	139.04	769	140.98	167.51	3.11	28.47

obs	T	B260 year	driving stress (kPa)	flux (km^3a^{-1})	B270 year	driving stress (kPa)	flux (km^3a^{-1})	Δdriving stress (kPa)	Δflux (km^3a^{-1})
424	3	1085	137.95	139.27	770	141.08	167.67	3.13	28.40
425	3	1086	138.09	139.50	771	141.18	168.49	3.09	28.99
426	3	1088	138.20	139.96	772	141.35	169.03	3.15	29.07
427	3	1089	138.27	140.01	773	141.45	169.49	3.18	29.48
428	3	1090	138.34	140.36	774	141.60	170.70	3.25	30.34
429	3	1094	138.69	143.14	775	141.83	171.19	3.14	28.04
430	3	1095	138.81	142.86	776	141.99	171.34	3.18	28.48
431	3	1096	138.89	142.81	777	142.11	171.42	3.22	28.61
432	3	1099	139.09	143.17	778	142.22	171.05	3.13	27.88
433	3	1100	139.20	142.95	779	142.35	171.06	3.15	28.12
434	3	1101	139.34	142.91	780	142.51	170.77	3.17	27.86
435	3	1104	139.62	143.00	781	142.63	170.58	3.01	27.58
436	3	1105	139.73	143.19	782	142.66	170.14	2.93	26.95
437	3	1106	139.86	143.21	783	142.81	170.42	2.95	27.21
438	3	1107	139.88	143.36	784	142.94	171.09	3.06	27.73
439	3	1110	140.23	143.21	785	143.09	170.89	2.86	27.67
440	3	1111	140.28	143.22	786	143.26	171.00	2.98	27.78
441	3	1112	140.34	142.99	787	143.38	170.64	3.04	27.65
442	3	1114	140.52	143.03	788	143.53	170.42	3.01	27.39
443	3	1115	140.63	143.02	789	143.63	170.30	3.01	27.27
444	3	1116	140.73	142.81	790	143.75	170.79	3.02	27.97
445	3	1117	140.83	142.67	791	143.94	170.76	3.11	28.09
446	3	1119	141.02	142.55	792	144.06	170.74	3.04	28.19
447	3	1120	141.13	142.27	793	144.17	171.18	3.05	28.91
448	3	1121	141.20	142.30	794	144.25	171.25	3.04	28.94
449	3	1125	141.54	142.76	795	144.44	171.20	2.90	28.44
450	3	1126	141.65	143.15	796	144.48	171.65	2.82	28.50
451	3	1127	141.74	143.37	797	144.63	171.59	2.89	28.22
452	3	1129	141.91	143.20	798	144.78	171.73	2.87	28.53
453	3	1130	142.01	143.09	799	144.90	171.73	2.90	28.64
454	3	1131	142.07	142.83	800	144.98	171.41	2.91	28.59
455	3	1132	142.15	142.68	801	145.11	170.87	2.96	28.20
456	3	1133	142.23	142.27	802	145.18	170.48	2.95	28.21
457	3	1134	142.30	142.10	803	145.31	169.75	3.01	27.66
458	3	1137	142.57	141.45	804	145.49	169.74	2.92	28.29
459	3	1138	142.70	141.31	805	145.58	169.80	2.87	28.50
460	3	1139	142.73	140.76	806	145.82	169.53	3.08	28.77
461	3	1141	142.87	140.24	807	145.84	168.82	2.98	28.58
462	3	1142	142.93	140.16	808	145.96	168.02	3.04	27.86
463	3	1143	143.04	139.94	809	146.07	167.46	3.03	27.52

obs	T	B260 year	driving stress (kPa)	flux (km^3a^{-1})	B270 year	driving stress (kPa)	flux (km^3a^{-1})	Δdriving stress (kPa)	Δflux (km^3a^{-1})
464	3	1144	143.10	139.93	810	146.24	167.26	3.14	27.34
465	3	1147	143.36	139.29	811	146.31	166.89	2.95	27.60
466	3	1149	143.44	138.65	812	146.41	166.11	2.97	27.46
467	3	1150	143.48	138.55	813	146.49	165.62	3.01	27.06
468	3	1151	143.56	138.44	814	146.54	164.85	2.98	26.42
469	3	1152	143.65	138.37	815	146.64	163.94	2.99	25.56
470	3	1148	143.40	139.02	816	146.70	163.67	3.30	24.65
471	3	1153	143.68	138.14	817	146.85	163.30	3.16	25.15
472	3	1154	143.76	137.82	818	146.88	163.10	3.11	25.29
473	3	1156	143.87	137.83	819	147.01	162.99	3.14	25.16
474	3	1157	143.94	137.70	820	147.07	162.69	3.13	25.00
475	3	1158	144.05	137.45	821	147.22	162.89	3.17	25.43
476	3	1159	144.10	137.29	822	147.28	162.84	3.18	25.55
477	3	1160	144.14	136.91	823	147.43	163.18	3.28	26.27
478	3	1161	144.21	136.70	824	147.52	162.88	3.32	26.18
479	3	1165	144.48	136.30	825	147.61	163.17	3.13	26.87
480	3	1166	144.54	136.22	826	147.74	163.06	3.21	26.85
481	3	1167	144.58	136.26	827	147.82	162.99	3.24	26.73
482	3	1168	144.63	136.00	828	147.99	162.51	3.36	26.52
483	3	1169	144.68	135.80	829	148.05	162.17	3.36	26.36
484	3	1173	145.03	136.39	830	148.17	162.16	3.14	25.77
485	3	1174	145.06	136.30	831	148.26	162.18	3.20	25.88
486	3	1175	145.15	136.38	832	148.40	161.70	3.25	25.32
487	3	1176	145.20	136.34	833	148.51	161.27	3.31	24.93
488	3	1177	145.29	136.16	834	148.60	161.21	3.31	25.05
489	3	1178	145.39	136.15	835	148.71	161.15	3.32	25.01
490	3	1179	145.48	136.09	836	148.81	161.13	3.33	25.04
491	3	1183	145.84	135.59	837	148.87	161.30	3.02	25.70
492	3	1184	145.92	135.26	838	149.05	161.17	3.12	25.92
493	3	1185	145.98	135.04	839	149.14	161.52	3.15	26.48
494	3	1186	146.05	135.04	840	149.31	161.08	3.25	26.04
495	3	1187	146.09	135.18	841	149.42	160.88	3.34	25.71
496	3	1190	146.34	135.15	842	149.47	161.02	3.13	25.86
497	1	1210	148.27	133.09	868	152.58	155.95	4.31	22.86
498	1	1211	148.40	132.81	869	152.70	154.98	4.30	22.17
499	1	1213	148.58	132.60	871	152.90	154.55	4.32	21.95
500	1	1216	148.87	131.98	873	153.19	154.06	4.32	22.08
501	1	1217	148.96	132.10	874	153.41	153.80	4.45	21.70
502	1	1218	149.03	131.97	875	153.58	153.71	4.55	21.74
503	1	1219	149.11	131.41	876	153.63	153.40	4.53	21.99

obs	T	B260 year	driving stress (kPa)	flux (km^3a^{-1})	B270 year	driving stress (kPa)	flux (km^3a^{-1})	Δdriving stress (kPa)	Δflux (km^3a^{-1})
504	1	1221	149.29	130.55	877	153.74	153.04	4.44	22.50
505	1	1222	149.36	130.61	878	153.85	152.67	4.50	22.06
506	1	1223	149.43	130.63	879	153.97	152.57	4.54	21.94
507	1	1225	149.60	130.21	880	154.10	152.61	4.50	22.40
508	1	1226	149.75	129.94	881	154.18	152.31	4.43	22.37
509	1	1228	149.88	130.49	882	154.33	152.36	4.46	21.87
510	1	1229	149.94	130.00	883	154.50	151.88	4.56	21.88
511	1	1230	150.04	129.87	884	154.53	151.79	4.49	21.92
512	1	1231	150.14	129.80	885	154.61	152.14	4.47	22.34
513	1	1232	150.20	129.81	886	154.74	152.05	4.54	22.24
514	1	1233	150.26	129.75	887	154.87	151.62	4.61	21.87
515	1	1235	150.43	129.66	888	155.04	151.13	4.61	21.46
516	1	1236	150.47	129.85	889	155.16	151.53	4.69	21.68
517	1	1238	150.67	129.40	891	155.36	150.93	4.69	21.53
518	1	1239	150.72	129.21	892	155.49	150.83	4.77	21.62
519	1	1241	150.87	128.95	893	155.55	151.07	4.68	22.12
520	1	1242	150.95	128.94	894	155.71	150.76	4.77	21.82
521	1	1243	151.07	129.06	895	155.80	150.74	4.74	21.68
522	1	1245	151.23	129.23	896	155.97	150.76	4.74	21.53
523	1	1247	151.38	129.15	898	156.13	151.06	4.75	21.92
524	1	1249	151.60	129.19	899	156.30	151.54	4.70	22.35
525	1	1251	151.76	129.38	901	156.59	151.09	4.84	21.71
526	1	1252	151.85	129.13	902	156.74	150.90	4.89	21.78
527	1	1254	152.00	129.14	903	156.76	151.01	4.76	21.86
528	1	1255	152.07	129.16	904	156.92	150.79	4.84	21.63
529	1	1256	152.15	129.35	905	157.11	150.14	4.96	20.79
530	1	1258	152.37	129.53	906	157.24	150.66	4.87	21.13
531	1	1259	152.48	129.56	907	157.40	150.57	4.92	21.01
532	1	1261	152.61	129.53	909	157.61	150.90	5.00	21.36
533	1	1263	152.76	129.08	910	157.75	150.87	4.99	21.79
534	1	1264	152.85	129.22	911	157.85	149.98	5.00	20.76
535	1	1265	152.93	129.18	912	157.90	150.09	4.97	20.91
536	1	1266	153.00	129.02	913	157.95	150.12	4.95	21.10
537	1	1267	153.06	129.09	914	158.14	149.57	5.08	20.48
538	1	1268	153.16	128.87	915	158.32	149.19	5.16	20.32
539	1	1272	153.51	127.51	916	158.44	148.95	4.93	21.44
540	1	1273	153.60	127.38	917	158.50	148.15	4.90	20.77
541	1	1274	153.66	126.95	918	158.58	147.94	4.93	20.99
542	1	1275	153.72	126.98	919	158.72	147.74	5.00	20.76
543	1	1276	153.86	126.75	920	158.84	147.53	4.99	20.78

obs	T	B260 year	driving stress (kPa)	flux (km^3a^{-1})	B270 year	driving stress (kPa)	flux (km^3a^{-1})	Δdriving stress (kPa)	Δflux (km^3a^{-1})
544	1	1278	154.00	126.53	921	159.10	147.84	5.10	21.31
545	1	1280	154.08	126.37	922	159.20	147.08	5.13	20.71
546	1	1281	154.18	125.96	923	159.27	146.76	5.09	20.81
547	1	1282	154.29	126.25	924	159.42	146.80	5.12	20.55
548	1	1283	154.33	126.44	925	159.57	146.56	5.23	20.11
549	1	1284	154.37	125.84	927	159.79	146.80	5.42	20.96
550	1	1285	154.39	126.11	928	159.93	146.31	5.54	20.20
551	1	1289	154.81	126.88	930	160.07	146.61	5.27	19.73
552	1	1290	154.87	126.59	931	160.19	145.92	5.32	19.33
553	1	1291	154.90	127.05	932	160.25	146.13	5.35	19.08
554	1	1292	154.99	126.76	933	160.39	146.14	5.40	19.38
555	1	1294	155.16	126.32	934	160.48	146.41	5.32	20.09
556	1	1295	155.21	126.48	935	160.54	145.91	5.33	19.43
557	1	1297	155.38	126.37	937	160.74	145.98	5.37	19.61
558	1	1298	155.48	126.38	939	161.05	145.72	5.57	19.34
559	1	1299	155.58	126.14	940	161.10	146.68	5.52	20.54
560	1	1300	155.62	126.28	941	161.19	146.23	5.57	19.96
561	1	1301	155.73	126.09	942	161.38	145.89	5.65	19.80
562	1	1302	155.74	126.03	943	161.40	145.87	5.66	19.84
563	1	1303	155.83	125.51	944	161.54	145.49	5.70	19.98
564	1	1304	155.91	125.67	945	161.66	145.03	5.75	19.36
565	1	1311	156.60	124.95	946	161.75	145.12	5.15	20.17
566	1	1318	157.07	123.55	954	162.74	143.96	5.67	20.41
567	1	1320	157.18	123.76	956	162.96	144.27	5.78	20.51
568	1	1321	157.25	123.48	957	163.07	143.63	5.83	20.16
569	1	1322	157.30	123.28	958	163.19	143.50	5.90	20.22
570	1	1323	157.41	123.23	959	163.30	143.29	5.89	20.06
571	1	1325	157.60	123.39	960	163.37	143.11	5.77	19.72
572	1	1326	157.65	123.22	961	163.49	143.43	5.85	20.21
573	1	1327	157.72	123.44	962	163.59	143.16	5.86	19.72
574	1	1329	157.84	123.36	963	163.54	143.34	5.69	19.99
575	1	1331	158.03	122.80	965	163.81	142.87	5.78	20.06
576	1	1332	158.15	123.07	966	163.91	142.48	5.76	19.41
577	1	1333	158.20	122.70	969	164.29	141.92	6.09	19.22
578	1	1341	158.96	122.18	973	164.78	141.78	5.82	19.60
579	1	1342	159.07	122.38	974	164.88	142.40	5.81	20.02
580	1	1344	159.21	122.29	975	165.00	142.09	5.79	19.80
581	1	1345	159.24	121.69	976	165.13	142.27	5.89	20.58
582	1	1347	159.36	121.87	977	165.27	141.55	5.91	19.68
583	1	1348	159.43	121.35	978	165.38	141.86	5.95	20.51

obs	T	B260 year	driving stress (kPa)	flux (km^3a^{-1})	B270 year	driving stress (kPa)	flux (km^3a^{-1})	Δdriving stress (kPa)	Δflux (km^3a^{-1})
584	1	1350	159.59	121.22	979	165.54	140.90	5.95	19.68
585	1	1351	159.69	120.88	980	165.59	141.30	5.91	20.41
586	1	1356	160.15	121.33	984	166.09	141.54	5.94	20.20
587	1	1357	160.20	121.21	985	166.21	141.39	6.01	20.18
588	1	1359	160.35	121.40	986	166.29	141.40	5.94	19.99
589	1	1360	160.43	120.92	987	166.44	141.86	6.02	20.93
590	1	1362	160.58	121.78	988	166.58	141.39	6.00	19.61
591	1	1363	160.66	121.85	989	166.69	141.84	6.03	19.99
592	1	1364	160.74	122.12	990	166.82	141.31	6.08	19.19
593	1	1365	160.88	122.05	991	166.96	141.25	6.07	19.20
594	1	1367	161.04	122.36	992	167.06	141.19	6.02	18.83
595	1	1369	161.19	122.38	994	167.24	141.10	6.06	18.72
596	1	1370	161.28	122.25	995	167.36	141.16	6.08	18.90
597	1	1375	161.89	122.25	996	167.41	140.56	5.53	18.31
598	1	1376	162.02	121.80	997	167.51	140.60	5.48	18.79
599	1	1372	161.50	122.49	999	167.75	140.19	6.25	17.70
600	1	1373	161.61	122.00	1000	167.91	139.68	6.30	17.69
601	1	1374	161.78	121.99	1001	168.03	139.53	6.25	17.54
602	1	1378	162.25	121.96	1003	168.27	138.90	6.01	16.94
603	1	1379	162.34	121.15	1004	168.34	138.29	6.00	17.13
604	1	1380	162.42	120.79	1005	168.47	138.89	6.06	18.10
605	1	1381	162.51	121.00	1006	168.61	138.35	6.10	17.35
606	1	1382	162.58	120.65	1007	168.70	138.39	6.13	17.74
607	1	1383	162.68	120.29	1008	168.77	138.20	6.10	17.92
608	1	1385	162.87	119.97	1009	168.93	137.55	6.05	17.58
609	1	1386	162.96	119.57	1010	169.05	137.37	6.09	17.79
610	1	1388	163.14	119.35	1011	169.13	137.13	5.99	17.78
611	1	1389	163.20	119.27	1012	169.23	137.21	6.03	17.94
612	1	1390	163.28	119.22	1013	169.27	137.34	5.99	18.12
613	1	1391	163.34	119.05	1014	169.36	137.09	6.01	18.04
614	1	1393	163.51	118.53	1015	169.50	137.04	5.99	18.51
615	1	1395	163.61	118.72	1016	169.58	136.27	5.97	17.54
616	1	1396	163.69	118.50	1017	169.64	136.24	5.95	17.75
617	1	1397	163.73	118.20	1018	169.79	135.45	6.05	17.24
618	1	1399	163.93	118.29	1019	169.86	135.58	5.94	17.29
619	1	1400	164.00	118.35	1020	169.93	135.58	5.92	17.23
620	1	1401	164.05	118.28	1021	170.11	135.19	6.06	16.91
621	1	1402	164.27	117.86	1022	170.16	135.60	5.88	17.75
622	1	1404	164.38	117.73	1023	170.18	135.28	5.80	17.55
623	1	1405	164.44	117.75	1024	170.19	135.09	5.75	17.33

obs	T	B260 year	driving stress (kPa)	flux (km^3a^{-1})	B270 year	driving stress (kPa)	flux (km^3a^{-1})	Δdriving stress (kPa)	Δflux (km^3a^{-1})
624	1	1407	164.54	117.45	1025	170.28	135.28	5.74	17.83
625	1	1406	164.45	117.54	1026	170.39	135.14	5.94	17.60
626	1	1409	164.72	117.34	1027	170.57	135.49	5.85	18.14
627	1	1411	164.91	117.06	1028	170.71	135.27	5.80	18.21
628	1	1412	164.95	116.96	1029	170.80	134.74	5.85	17.78
629	1	1413	164.99	117.03	1030	170.87	134.60	5.88	17.58
630	1	1414	165.08	116.81	1031	171.01	134.86	5.93	18.05
631	1	1416	165.22	116.70	1032	171.25	134.57	6.03	17.87
632	1	1417	165.30	116.37	1033	171.34	134.52	6.05	18.15
633	1	1418	165.38	116.03	1034	171.39	134.37	6.02	18.33
634	1	1420	165.55	115.93	1035	171.55	134.26	6.00	18.34
635	1	1422	165.73	115.64	1036	171.48	134.18	5.75	18.54
636	1	1423	165.78	115.42	1037	171.57	133.69	5.79	18.27
637	1	1424	165.87	115.48	1038	171.68	133.76	5.81	18.28
638	1	1425	165.93	115.34	1039	171.80	133.88	5.86	18.53
639	1	1427	166.01	115.28	1040	171.94	133.10	5.93	17.81
640	1	1428	166.04	115.27	1041	172.05	133.34	6.01	18.06
641	1	1429	166.06	115.16	1042	172.18	133.81	6.12	18.65
642	1	1430	166.14	114.81	1043	172.26	133.25	6.12	18.44
643	1	1432	166.22	114.74	1044	172.36	133.21	6.14	18.47
644	1	1434	166.34	114.30	1045	172.58	132.73	6.24	18.42
645	1	1435	166.40	114.06	1046	172.74	132.09	6.34	18.04
646	1	1436	166.45	114.10	1047	172.85	131.83	6.41	17.73
647	1	1437	166.56	114.34	1048	173.02	131.87	6.46	17.52
648	1	1438	166.62	114.03	1049	173.16	131.38	6.55	17.35
649	1	1439	166.64	113.94	1050	173.22	131.21	6.58	17.26
650	1	1441	166.74	114.34	1051	173.43	131.13	6.68	16.79
651	1	1442	166.77	114.19	1052	173.46	131.26	6.69	17.08
652	1	1445	166.92	113.29	1053	173.53	131.38	6.61	18.10
653	1	1447	167.02	113.30	1054	173.63	131.57	6.61	18.27
654	1	1448	167.06	113.40	1055	173.71	131.20	6.65	17.81
655	1	1449	167.21	113.27	1056	173.81	131.11	6.59	17.83
656	1	1451	167.40	112.79	1057	173.89	131.24	6.49	18.45
657	1	1452	167.49	112.96	1058	173.99	131.14	6.49	18.18
658	1	1454	167.62	113.19	1059	174.10	130.86	6.47	17.67
659	1	1455	167.66	113.19	1060	174.09	130.72	6.42	17.54
660	1	1457	167.77	112.89	1061	174.27	130.19	6.49	17.30
661	1	1458	167.87	112.83	1062	174.21	130.15	6.34	17.32
662	1	1461	168.02	112.47	1063	174.21	130.03	6.20	17.57
663	1	1462	168.05	112.35	1064	174.30	129.54	6.25	17.20

obs	T	B260 year	driving stress (kPa)	flux (km^3a^{-1})	B270 year	driving stress (kPa)	flux (km^3a^{-1})	Δdriving stress (kPa)	Δflux (km^3a^{-1})
664	1	1463	168.08	111.93	1065	174.39	129.46	6.31	17.52
665	1	1464	168.15	112.08	1066	174.53	129.36	6.38	17.28
666	1	1465	168.25	112.02	1067	174.63	129.05	6.38	17.03
667	1	1466	168.43	111.76	1068	174.71	128.77	6.28	17.01
668	1	1467	168.46	111.69	1069	174.84	128.86	6.38	17.17
669	1	1468	168.52	111.83	1070	174.83	128.75	6.31	16.92
670	1	1469	168.58	111.97	1071	174.92	128.45	6.34	16.48
671	1	1471	168.70	111.46	1072	174.94	128.21	6.24	16.76
672	1	1472	168.82	111.71	1073	175.06	128.30	6.24	16.59
673	1	1475	169.03	111.63	1074	175.20	128.53	6.17	16.90
674	1	1476	169.21	111.60	1075	175.23	128.21	6.02	16.62
675	1	1477	169.24	111.25	1076	175.31	128.11	6.07	16.86
676	1	1478	169.27	111.21	1077	175.36	127.83	6.09	16.62
677	1	1480	169.41	111.40	1078	175.46	128.35	6.05	16.94
678	1	1481	169.45	111.16	1079	175.46	127.33	6.02	16.16
679	1	1482	169.53	110.90	1080	175.51	127.65	5.98	16.75
680	1	1485	169.77	110.56	1081	175.58	127.90	5.81	17.34
681	1	1486	169.81	110.49	1082	175.66	127.46	5.84	16.97
682	1	1487	169.81	110.49	1083	175.60	127.64	5.79	17.15
683	1	1488	169.85	110.47	1084	175.69	127.43	5.84	16.97
684	1	1492	169.95	110.93	1085	175.81	127.12	5.85	16.19
685	1	1493	170.03	110.40	1086	175.83	127.10	5.80	16.69
686	1	1490	169.87	110.59	1087	175.93	127.36	6.06	16.77
687	1	1494	170.06	110.53	1088	175.94	127.07	5.88	16.54
688	1	1495	170.15	110.73	1089	175.97	127.57	5.82	16.84
689	1	1496	170.14	110.77	1090	176.08	127.45	5.94	16.68
690	1	1497	170.13	110.97	1091	176.15	127.40	6.02	16.43
691	1	1499	170.26	110.95	1092	176.26	127.37	6.00	16.42
692	1	1501	170.41	111.05	1093	176.24	127.78	5.83	16.73
693	1	1502	170.51	111.24	1094	176.36	128.09	5.85	16.84
694	1	1505	170.65	111.01	1095	176.53	128.31	5.88	17.30
695	1	1507	170.90	110.85	1096	176.62	128.51	5.72	17.66
696	1	1508	170.96	110.52	1097	176.76	128.21	5.81	17.69
697	1	1509	170.98	110.63	1098	176.85	128.28	5.87	17.65
698	1	1510	171.08	110.59	1099	176.93	127.80	5.86	17.21
699	1	1512	171.20	110.48	1100	176.99	128.46	5.79	17.97
700	1	1513	171.27	110.43	1101	177.03	128.65	5.76	18.22
701	1	1517	171.59	111.15	1102	177.23	128.57	5.64	17.42
702	1	1519	171.79	111.35	1103	177.36	128.72	5.57	17.36
703	1	1520	171.86	111.48	1104	177.46	129.06	5.60	17.58

obs	T	B260 year	driving stress (kPa)	flux (km^3a^{-1})	B270 year	driving stress (kPa)	flux (km^3a^{-1})	Δdriving stress (kPa)	Δflux (km^3a^{-1})
704	1	1521	171.87	111.62	1105	177.52	129.33	5.65	17.72
705	1	1522	171.97	111.79	1106	177.68	129.48	5.71	17.69
706	1	1523	172.08	111.91	1107	177.77	129.47	5.69	17.55
707	1	1524	172.17	112.28	1108	177.92	129.73	5.75	17.45
708	1	1525	172.22	112.14	1109	177.99	129.77	5.77	17.63
709	1	1526	172.34	112.24	1110	178.16	129.68	5.82	17.44
710	1	1527	172.39	111.92	1111	178.31	129.74	5.92	17.81
711	1	1531	172.80	111.51	1112	178.43	129.85	5.63	18.33
712	1	1536	173.15	111.48	1113	178.62	129.93	5.47	18.45
713	1	1537	173.20	111.62	1114	178.74	130.61	5.54	18.99
714	1	1533	172.92	111.35	1115	178.91	130.78	5.99	19.43
715	1	1534	172.97	111.43	1116	179.08	130.38	6.10	18.96
716	1	1538	173.20	111.48	1117	179.26	130.11	6.06	18.63
717	1	1539	173.27	111.51	1118	179.39	129.77	6.12	18.27
718	1	1540	173.39	111.62	1119	179.49	129.49	6.09	17.87
719	1	1542	173.57	111.70	1121	179.56	129.36	5.99	17.66
720	1	1543	173.63	111.62	1122	179.68	129.31	6.04	17.69
721	1	1544	173.75	111.67	1123	179.81	129.39	6.07	17.72
722	1	1545	173.85	111.46	1124	179.85	129.29	6.00	17.83
723	1	1547	173.95	111.24	1125	179.99	129.15	6.04	17.92
724	1	1548	174.04	111.27	1126	180.04	128.64	6.00	17.38
725	1	1549	174.15	111.28	1127	180.15	128.60	6.00	17.32
726	1	1551	174.27	110.90	1128	180.32	128.68	6.05	17.79
727	1	1550	174.25	111.07	1129	180.47	128.62	6.22	17.55
728	1	1552	174.32	110.55	1130	180.54	129.43	6.21	18.88
729	1	1557	174.64	110.05	1131	180.71	129.31	6.07	19.26
730	1	1556	174.64	110.07	1132	180.81	129.06	6.17	18.99
731	1	1560	174.82	109.72	1133	180.90	129.42	6.08	19.70
732	1	1562	174.95	109.88	1134	180.97	129.23	6.02	19.35
733	1	1563	175.09	110.09	1135	180.90	129.48	5.81	19.39
734	1	1564	175.16	110.05	1136	180.93	129.32	5.77	19.27
735	1	1566	175.26	110.47	1137	181.11	129.21	5.85	18.73
736	1	1567	175.31	110.20	1138	181.22	129.08	5.90	18.88
737	1	1570	175.55	110.35	1139	181.36	129.05	5.80	18.70
738	1	1571	175.67	110.49	1140	181.46	128.94	5.79	18.45
739	1	1572	175.77	110.06	1141	181.50	128.62	5.72	18.56
740	1	1574	175.96	109.72	1142	181.68	128.96	5.71	19.25
741	1	1576	176.03	109.62	1144	181.68	128.13	5.66	18.51
742	3	1585	176.55	109.26	1145	181.77	128.26	5.22	19.00
743	3	1588	176.69	109.28	1146	181.88	128.44	5.19	19.16

obs	T	B260 year	driving stress (kPa)	flux (km^3a^{-1})	B270 year	driving stress (kPa)	flux (km^3a^{-1})	Δdriving stress (kPa)	Δflux (km^3a^{-1})
744	3	1589	176.68	109.21	1147	181.87	128.38	5.19	19.17
745	3	1590	176.73	109.03	1148	181.90	128.06	5.17	19.02
746	3	1591	176.88	109.03	1149	182.04	128.20	5.16	19.17
747	3	1592	176.90	108.87	1150	182.12	128.25	5.22	19.38
748	3	1593	176.95	108.89	1151	182.22	128.05	5.27	19.17
749	3	1599	177.21	108.23	1154	182.50	127.58	5.29	19.35
750	3	1597	177.14	108.78	1155	182.58	127.69	5.43	18.91
751	3	1598	177.18	108.47	1156	182.72	127.43	5.54	18.97
752	3	1600	177.27	108.82	1157	182.91	127.01	5.64	18.18
753	3	1601	177.29	108.90	1158	183.02	127.19	5.73	18.29
754	3	1602	177.36	108.51	1159	182.92	127.19	5.56	18.68
755	3	1603	177.40	108.14	1160	183.01	127.06	5.61	18.92
756	3	1604	177.47	108.14	1161	183.10	127.32	5.62	19.18
757	3	1607	177.62	108.08	1162	183.08	127.34	5.46	19.27
758	3	1608	177.66	107.98	1163	183.20	127.19	5.54	19.21
759	3	1609	177.72	108.09	1164	183.28	127.40	5.56	19.31
760	3	1610	177.77	108.02	1165	183.29	127.24	5.52	19.22
761	3	1611	177.80	108.21	1166	183.35	126.93	5.55	18.72
762	3	1614	177.96	107.66	1167	183.38	127.21	5.42	19.55
763	3	1615	178.01	107.40	1168	183.34	127.45	5.33	20.05
764	3	1616	178.03	107.31	1169	183.47	127.11	5.44	19.81
765	3	1618	178.11	107.41	1170	183.53	126.69	5.42	19.28
766	3	1619	178.17	107.16	1171	183.65	126.60	5.48	19.44
767	3	1623	178.32	107.77	1172	183.70	127.02	5.38	19.24
768	3	1624	178.36	106.97	1173	183.78	126.61	5.43	19.63
769	3	1631	178.73	107.39	1174	183.85	126.38	5.12	18.98
770	3	1632	178.74	107.10	1175	183.93	126.14	5.19	19.05
771	3	1635	178.88	106.90	1178	184.17	125.26	5.29	18.36
772	3	1636	178.95	106.74	1179	184.16	125.06	5.21	18.32
773	3	1639	179.05	106.84	1182	184.35	125.53	5.30	18.70
774	3	1640	179.13	106.83	1183	184.42	125.67	5.28	18.83
775	3	1641	179.19	106.69	1184	184.46	125.42	5.27	18.73
776	3	1642	179.20	107.24	1185	184.57	125.14	5.36	17.91
777	3	1647	179.47	106.85	1186	184.62	125.55	5.15	18.70
778	3	1648	179.56	106.84	1187	184.77	125.74	5.21	18.90
779	3	1649	179.66	107.15	1188	184.82	125.84	5.16	18.69
780	3	1650	179.74	107.54	1189	184.97	126.30	5.23	18.76
781	3	1652	179.99	107.29	1192	185.34	125.96	5.35	18.67
782	3	1653	180.03	107.21	1193	185.44	125.65	5.41	18.44
783	3	1654	180.10	106.93	1194	185.53	125.83	5.42	18.90

obs	T	B260 year	driving stress (kPa)	flux (km^3a^{-1})	B270 year	driving stress (kPa)	flux (km^3a^{-1})	Δdriving stress (kPa)	Δflux (km^3a^{-1})
784	3	1655	180.10	106.86	1195	185.74	126.29	5.64	19.43
785	3	1656	180.14	106.93	1196	185.87	126.32	5.74	19.39
786	3	1658	180.24	107.28	1197	185.96	125.87	5.72	18.58
787	3	1660	180.44	107.30	1198	186.04	125.85	5.60	18.56
788	3	1661	180.44	107.26	1199	186.06	125.69	5.62	18.43
789	3	1664	180.61	107.28	1200	186.07	125.47	5.46	18.20
790	3	1665	180.68	107.41	1201	186.14	125.72	5.46	18.31
791	3	1666	180.75	107.71	1202	186.25	126.06	5.50	18.35
792	3	1667	180.88	107.81	1203	186.39	125.76	5.51	17.95
793	3	1669	180.99	107.84	1204	186.50	126.12	5.51	18.28
794	3	1671	181.02	107.97	1205	186.55	126.29	5.53	18.33
795	3	1672	181.12	108.36	1206	186.58	126.97	5.46	18.61
796	3	1673	181.16	108.50	1207	186.68	126.72	5.53	18.21
797	3	1674	181.24	108.42	1208	186.82	126.71	5.58	18.29
798	3	1675	181.25	108.34	1209	186.90	126.80	5.65	18.46
799	3	1678	181.37	108.89	1210	186.96	126.92	5.58	18.03
800	3	1679	181.48	108.66	1211	187.02	126.58	5.54	17.93
801	3	1680	181.56	107.94	1212	187.14	126.49	5.58	18.55
802	3	1682	181.68	107.42	1213	187.27	126.04	5.60	18.62
803	3	1683	181.73	107.28	1214	187.37	125.80	5.64	18.52
804	3	1686	181.82	107.30	1215	187.53	125.74	5.71	18.43
805	3	1687	181.89	107.13	1216	187.64	125.50	5.74	18.37
806	3	1689	182.05	106.79	1217	187.72	125.32	5.67	18.53
807	3	1690	182.13	106.97	1218	187.75	124.93	5.62	17.96
808	3	1691	182.14	106.89	1219	187.85	125.11	5.71	18.22
809	3	1693	182.27	107.03	1220	187.82	124.75	5.55	17.71
810	3	1694	182.32	106.86	1221	187.91	124.66	5.58	17.80
811	3	1696	182.45	106.22	1222	187.94	124.54	5.49	18.32
812	3	1697	182.55	106.08	1223	188.08	124.00	5.53	17.92
813	3	1698	182.62	106.13	1224	188.19	123.54	5.57	17.41
814	3	1700	182.73	105.96	1225	188.20	123.53	5.47	17.57
815	3	1701	182.81	105.76	1226	188.20	123.51	5.39	17.75
816	3	1702	182.86	105.51	1227	188.28	123.34	5.42	17.83
817	3	1703	182.92	105.42	1228	188.35	123.07	5.43	17.65
818	3	1706	182.98	105.13	1229	188.40	123.10	5.42	17.97
819	3	1707	183.02	105.11	1230	188.44	122.88	5.42	17.77
820	3	1708	183.09	104.75	1231	188.48	122.30	5.39	17.55
821	3	1709	183.09	104.52	1232	188.47	121.89	5.38	17.38
822	3	1710	183.12	104.39	1233	188.49	121.69	5.37	17.30
823	3	1711	183.16	104.40	1234	188.56	121.39	5.40	16.99

obs	T	B260 year	driving stress (kPa)	flux (km^3a^{-1})	B270 year	driving stress (kPa)	flux (km^3a^{-1})	Δdriving stress (kPa)	Δflux (km^3a^{-1})
824	3	1712	183.17	104.07	1235	188.65	121.37	5.48	17.30
825	3	1713	183.20	103.98	1236	188.72	121.04	5.51	17.06
826	3	1714	183.20	103.91	1237	188.82	121.08	5.61	17.17
827	3	1715	183.27	103.86	1238	188.85	120.56	5.58	16.71
828	3	1716	183.29	103.82	1239	188.84	120.38	5.54	16.56
829	3	1725	183.66	102.92	1240	188.93	120.30	5.27	17.38
830	3	1726	183.66	102.95	1241	189.07	120.13	5.40	17.19
831	3	1727	183.70	103.00	1242	189.13	120.63	5.43	17.63
832	3	1728	183.76	102.95	1243	189.25	120.75	5.49	17.80
833	3	1729	183.78	103.18	1244	189.28	120.06	5.50	16.88
834	3	1730	183.73	103.25	1245	189.28	120.39	5.55	17.15
835	3	1731	183.74	103.25	1246	189.32	120.35	5.58	17.10
836	3	1732	183.79	102.99	1247	189.36	120.16	5.57	17.16
837	3	1738	183.85	102.80	1248	189.43	120.28	5.58	17.48
838	3	1739	183.90	102.65	1249	189.47	120.02	5.57	17.37
839	3	1740	183.92	102.67	1250	189.50	120.11	5.58	17.43
840	3	1741	183.95	102.29	1251	189.57	119.71	5.62	17.42
841	3	1742	183.92	102.31	1252	189.61	119.45	5.69	17.14
842	3	1743	183.99	102.36	1253	189.67	119.53	5.68	17.17
843	3	1744	184.01	102.37	1254	189.73	119.68	5.72	17.31
844	3	1745	183.97	102.45	1255	189.81	119.58	5.84	17.13
845	3	1751	184.10	102.30	1256	189.82	119.63	5.73	17.33
846	3	1752	184.14	102.68	1257	189.91	119.79	5.77	17.10
847	3	1753	184.20	102.58	1258	189.98	119.92	5.78	17.34
848	3	1755	184.34	102.61	1259	189.99	119.46	5.65	16.85
849	3	1756	184.37	102.52	1260	190.03	119.69	5.65	17.18
850	3	1758	184.41	102.47	1261	190.04	119.57	5.62	17.10
851	3	1759	184.46	102.59	1262	190.09	119.68	5.63	17.09
852	3	1760	184.38	102.26	1263	190.13	119.76	5.76	17.50
853	3	1761	184.39	102.45	1264	190.21	119.72	5.82	17.28
854	3	1764	184.58	102.45	1265	190.22	119.39	5.64	16.94
855	3	1765	184.59	102.60	1266	190.31	119.58	5.71	16.98
856	3	1766	184.63	102.47	1267	190.35	119.09	5.72	16.62
857	3	1768	184.81	102.60	1268	190.42	118.74	5.61	16.14
858	3	1769	184.82	102.39	1269	190.54	119.08	5.73	16.69
859	3	1770	184.88	102.21	1270	190.59	118.96	5.70	16.75
860	3	1771	184.90	102.03	1271	190.70	118.36	5.80	16.34
861	3	1772	184.92	102.09	1272	190.61	118.60	5.70	16.52
862	3	1773	184.95	101.89	1273	190.68	118.45	5.73	16.56
863	3	1774	184.95	101.80	1274	190.72	118.68	5.77	16.89

obs	T	B260 year	driving stress (kPa)	flux (km^3a^{-1})	B270 year	driving stress (kPa)	flux (km^3a^{-1})	Δdriving stress (kPa)	Δflux (km^3a^{-1})
864	3	1779	185.02	101.22	1275	190.74	118.36	5.72	17.14
865	3	1780	184.98	101.43	1276	190.80	118.02	5.82	16.60
866	3	1781	185.09	101.47	1277	190.79	117.76	5.70	16.29
867	3	1782	185.10	101.51	1278	190.87	118.08	5.77	16.57
868	3	1783	185.14	101.82	1279	190.93	118.36	5.79	16.54
869	3	1784	185.17	101.68	1280	190.96	118.41	5.80	16.73
870	3	1785	185.19	101.80	1281	191.00	118.55	5.82	16.76
871	3	1786	185.31	101.88	1282	191.12	118.74	5.81	16.87
872	3	1787	185.29	101.80	1283	191.18	118.92	5.88	17.12
873	3	1788	185.35	101.88	1284	191.18	119.02	5.82	17.14
874	3	1793	185.55	101.89	1285	191.21	119.23	5.65	17.34
875	3	1794	185.56	102.07	1286	191.22	118.93	5.66	16.87
876	3	1799	185.77	101.91	1287	191.35	119.30	5.58	17.39
877	3	1800	185.78	101.75	1288	191.39	119.35	5.61	17.60
878	3	1801	185.84	102.00	1289	191.48	119.07	5.64	17.07
879	3	1802	185.90	102.04	1290	191.55	119.43	5.65	17.39
880	3	1803	185.92	102.11	1291	191.67	119.43	5.76	17.31
881	3	1804	185.93	101.84	1292	191.68	118.98	5.75	17.14
882	3	1805	185.94	102.00	1293	191.66	118.95	5.72	16.95
883	3	1806	185.97	101.71	1294	191.78	118.93	5.82	17.23
884	3	1807	186.06	101.83	1295	191.89	118.70	5.83	16.87
885	3	1811	186.27	102.03	1296	191.96	118.92	5.69	16.89
886	3	1812	186.25	102.08	1297	191.88	119.18	5.62	17.11
887	3	1813	186.26	102.49	1298	191.99	119.08	5.73	16.58
888	3	1814	186.27	102.09	1299	191.96	119.19	5.69	17.10
889	3	1815	186.36	102.14	1300	191.99	119.39	5.63	17.24
890	3	1816	186.38	101.61	1301	192.00	119.12	5.62	17.52
891	3	1817	186.42	101.38	1302	192.06	119.34	5.63	17.96
892	3	1818	186.50	101.39	1303	192.01	119.20	5.51	17.82
893	3	1821	186.61	101.47	1304	192.10	118.93	5.50	17.46
894	3	1822	186.60	101.35	1305	192.19	118.22	5.59	16.87
895	3	1839	187.06	101.21	1306	192.30	118.39	5.24	17.17
896	3	1823	186.59	101.54	1307	192.35	118.49	5.76	16.95
897	3	1824	186.61	101.38	1308	192.39	118.34	5.78	16.96
898	3	1840	187.10	101.28	1309	192.46	118.58	5.36	17.30
899	3	1841	187.14	101.42	1310	192.55	118.38	5.42	16.95
900	3	1842	187.10	101.26	1311	192.64	118.31	5.53	17.05
901	3	1843	187.14	101.43	1312	192.68	118.51	5.54	17.08
902	3	1844	187.16	101.73	1313	192.72	118.02	5.56	16.29
903	3	1845	187.24	101.60	1314	192.68	118.19	5.44	16.59

obs	T	B260 year	driving stress (kPa)	flux (km^3a^{-1})	B270 year	driving stress (kPa)	flux (km^3a^{-1})	Δdriving stress (kPa)	Δflux (km^3a^{-1})
904	3	1846	187.32	101.17	1315	192.74	117.96	5.42	16.79
905	3	1847	187.32	101.27	1316	192.82	118.16	5.50	16.89
906	3	1848	187.40	101.01	1317	192.88	118.14	5.48	17.13
907	3	1859	187.83	101.83	1318	192.94	118.14	5.11	16.30
908	3	1860	187.92	101.74	1319	192.97	118.30	5.04	16.56
909	3	1861	187.99	101.64	1320	193.01	118.54	5.02	16.90
910	3	1862	188.05	101.33	1321	193.09	118.28	5.04	16.94
911	3	1863	188.06	101.64	1322	193.20	117.95	5.14	16.31
912	3	1864	188.13	101.21	1323	193.24	118.31	5.10	17.11
913	3	1865	188.12	101.14	1324	193.30	118.29	5.18	17.15
914	3	1849	187.46	101.18	1325	193.38	117.97	5.93	16.79
915	3	1850	187.56	101.02	1326	193.41	117.79	5.84	16.77
916	3	1851	187.60	101.00	1327	193.49	117.96	5.88	16.96
917	3	1852	187.61	101.15	1328	193.51	118.18	5.90	17.03
918	3	1853	187.62	101.11	1329	193.53	118.30	5.91	17.19
919	3	1866	188.14	101.05	1330	193.63	118.86	5.49	17.81
920	3	1867	188.21	100.85	1331	193.68	118.11	5.47	17.26
921	1	1869	188.26	100.54	1340	194.10	116.91	5.84	16.37
922	1	1871	188.28	100.62	1341	194.18	116.65	5.90	16.03
923	1	1872	188.31	100.42	1342	194.20	116.27	5.89	15.86
924	1	1873	188.27	100.67	1343	194.32	116.02	6.04	15.35
925	1	1874	188.23	100.73	1344	194.39	115.89	6.16	15.16
926	1	1876	188.26	100.44	1345	194.39	115.84	6.13	15.40
927	1	1877	188.34	99.97	1346	194.53	115.68	6.19	15.72
928	1	1879	188.43	99.92	1347	194.53	115.24	6.10	15.32
929	1	1880	188.51	100.11	1348	194.59	115.01	6.09	14.90
930	1	1882	188.56	99.81	1349	194.68	115.20	6.12	15.39
931	1	1883	188.56	99.66	1350	194.72	115.22	6.16	15.56
932	1	1885	188.57	99.54	1351	194.77	114.90	6.20	15.36
933	1	1886	188.57	99.44	1352	194.76	115.12	6.19	15.69
934	1	1887	188.55	99.36	1353	194.68	114.82	6.13	15.46
935	1	1888	188.59	99.31	1354	194.71	114.67	6.12	15.35
936	1	1889	188.64	99.61	1355	194.73	114.50	6.09	14.89
937	1	1890	188.65	99.42	1356	194.83	114.57	6.18	15.15
938	1	1892	188.79	99.14	1357	194.82	114.57	6.03	15.43
939	1	1893	188.77	98.91	1358	194.90	114.64	6.12	15.73
940	1	1894	188.72	98.91	1359	194.93	114.62	6.21	15.71
941	1	1897	188.83	98.92	1360	194.94	114.56	6.11	15.64
942	1	1898	188.83	98.86	1361	194.97	114.37	6.14	15.51
943	1	1900	188.94	98.31	1362	195.02	114.42	6.07	16.10

obs	T	B260 year	driving stress (kPa)	flux (km^3a^{-1})	B270 year	driving stress (kPa)	flux (km^3a^{-1})	Δdriving stress (kPa)	Δflux (km^3a^{-1})
944	1	1902	189.07	97.86	1363	195.04	114.14	5.97	16.28
945	1	1903	189.07	98.45	1364	195.07	114.04	5.99	15.59
946	1	1906	189.20	99.23	1365	195.09	113.85	5.89	14.61
947	1	1907	189.19	98.91	1366	195.10	113.91	5.91	14.99
948	1	1908	189.30	99.02	1367	195.14	113.84	5.83	14.81
949	1	1909	189.32	99.12	1368	195.19	113.90	5.87	14.78
950	1	1910	189.39	98.97	1369	195.25	113.65	5.86	14.68
951	1	1911	189.45	99.11	1370	195.28	113.49	5.83	14.38
952	1	1912	189.42	99.18	1371	195.22	113.81	5.80	14.63
953	1	1915	189.59	98.76	1372	195.24	113.98	5.65	15.23
954	1	1916	189.69	98.78	1373	195.31	114.01	5.62	15.23
955	1	1918	189.76	98.61	1374	195.37	113.78	5.61	15.17
956	1	1919	189.93	98.59	1375	195.40	113.97	5.48	15.38
957	1	1923	189.86	98.10	1376	195.38	113.97	5.52	15.87
958	1	1924	189.83	98.19	1377	195.28	114.08	5.45	15.89
959	1	1925	189.86	98.37	1378	195.38	113.96	5.51	15.59
960	1	1928	189.97	98.49	1380	195.49	113.77	5.52	15.28
961	1	1927	189.92	98.79	1382	195.56	113.60	5.64	14.81
962	1	1929	190.02	98.62	1383	195.67	113.58	5.65	14.96
963	1	1930	190.01	98.51	1384	195.69	113.34	5.68	14.83
964	1	1933	190.08	98.41	1385	195.74	113.28	5.65	14.87
965	1	1934	190.09	98.33	1386	195.78	113.15	5.69	14.82
966	1	1937	190.09	98.13	1387	195.87	113.05	5.78	14.92
967	1	1938	190.14	98.13	1388	195.89	112.99	5.75	14.87
968	1	1939	190.20	97.99	1389	195.94	112.99	5.74	15.00
969	1	1940	190.22	97.79	1390	196.04	112.83	5.82	15.04
970	1	1941	190.23	97.62	1391	196.07	112.25	5.84	14.62
971	1	1942	190.25	97.47	1392	196.15	112.37	5.90	14.90
972	1	1945	190.31	97.58	1393	196.16	112.27	5.85	14.69
973	1	1947	190.38	97.37	1394	196.18	112.88	5.79	15.50
974	1	1948	190.39	97.63	1395	196.29	112.33	5.90	14.70
975	1	1950	190.45	97.50	1396	196.32	112.52	5.87	15.01
976	1	1953	190.61	97.66	1397	196.43	112.32	5.82	14.66
977	1	1954	190.60	97.76	1398	196.45	112.25	5.85	14.49
978	1	1955	190.59	97.81	1399	196.39	112.11	5.80	14.30
979	1	1956	190.60	97.88	1400	196.43	112.17	5.82	14.29
980	1	1957	190.61	97.74	1401	196.51	112.13	5.90	14.40
981	1	1958	190.63	97.78	1402	196.50	112.53	5.88	14.75
982	1	1959	190.61	97.83	1403	196.53	112.20	5.92	14.37
983	1	1960	190.68	97.76	1404	196.60	112.28	5.92	14.52

obs	T	B260 year	driving stress (kPa)	flux (km^3a^{-1})	B270 year	driving stress (kPa)	flux (km^3a^{-1})	Δdriving stress (kPa)	Δflux (km^3a^{-1})
984	1	1961	190.65	98.08	1405	196.66	112.14	6.01	14.06
985	1	1962	190.77	98.24	1406	196.78	112.73	6.01	14.49
986	1	1967	191.06	97.42	1407	196.74	112.77	5.68	15.35
987	1	1969	191.01	97.39	1408	196.78	112.73	5.77	15.34
988	1	1970	191.06	97.66	1409	196.85	112.73	5.79	15.07
989	1	1971	191.10	97.69	1410	196.91	112.80	5.81	15.12
990	1	1972	191.08	97.51	1411	196.94	112.84	5.85	15.33
991	1	1973	191.13	97.77	1412	196.96	112.58	5.84	14.81
992	1	1974	191.20	98.00	1413	197.00	112.63	5.79	14.64
993	1	1976	191.28	97.53	1414	197.08	112.68	5.80	15.15
994	1	1975	191.25	97.79	1415	197.18	112.72	5.93	14.93
995	1	1977	191.35	97.49	1416	197.18	113.08	5.83	15.60
996	1	1978	191.38	97.95	1417	197.20	113.17	5.82	15.22
997	1	1980	191.41	97.47	1418	197.22	112.97	5.81	15.51
998	1	1981	191.43	97.73	1419	197.29	112.75	5.86	15.02
999	1	1982	191.49	97.74	1420	197.41	112.96	5.92	15.23
1000	1	1983	191.50	97.64	1421	197.38	112.89	5.88	15.25
1001	1	1984	191.57	97.64	1422	197.45	112.85	5.88	15.21
1002	1	1985	191.61	97.61	1423	197.55	112.91	5.95	15.30
1003	1	1986	191.63	97.43	1424	197.60	112.68	5.98	15.25
1004	1	1987	191.67	97.51	1425	197.67	112.63	6.01	15.12
1005	1	1996	191.98	97.31	1426	197.77	112.78	5.79	15.46
1006	1	1997	191.99	97.40	1427	197.80	113.28	5.81	15.88
1007	1	1999	192.15	98.02	1428	197.84	113.36	5.69	15.33
1008	1	2000	192.10	98.07	1429	197.88	113.60	5.78	15.53
1009	1	2001	192.18	97.78	1430	197.92	113.13	5.75	15.35
1010	1	2002	192.20	98.08	1431	197.95	114.09	5.75	16.01
1011	1	2003	192.20	98.20	1432	197.96	114.18	5.76	15.98
1012	1	2004	192.20	98.45	1433	198.03	114.32	5.83	15.87
1013	1	2005	192.26	98.58	1434	198.13	114.56	5.87	15.98
1014	1	2007	192.32	98.89	1435	198.27	114.90	5.95	16.01
1015	1	2008	192.29	99.05	1436	198.21	115.16	5.93	16.11
1016	1	2010	192.38	99.11	1437	198.27	115.73	5.90	16.62
1017	1	2011	192.42	98.99	1438	198.42	115.89	6.00	16.91
1018	1	2012	192.46	99.45	1439	198.43	115.99	5.97	16.54
1019	1	2013	192.39	99.32	1440	198.49	116.07	6.10	16.75
1020	1	2015	192.46	99.69	1441	198.53	116.06	6.07	16.37
1021	1	2016	192.38	100.01	1442	198.55	116.27	6.17	16.27
1022	1	2017	192.40	100.02	1443	198.63	116.68	6.24	16.65
1023	1	2018	192.48	100.30	1444	198.77	116.69	6.29	16.39

obs	T	B260 year	driving stress (kPa)	flux (km^3a^{-1})	B270 year	driving stress (kPa)	flux (km^3a^{-1})	Δdriving stress (kPa)	Δflux (km^3a^{-1})
1024	1	2020	192.66	100.44	1445	198.84	117.13	6.18	16.69
1025	1	2022	192.81	100.51	1446	198.95	117.17	6.14	16.66
1026	1	2023	192.87	100.66	1447	199.00	117.52	6.13	16.86
1027	1	2024	192.86	100.28	1448	198.94	117.49	6.08	17.21
1028	1	2027	192.94	100.08	1449	198.99	116.96	6.06	16.88
1029	1	2030	193.05	99.40	1450	199.20	115.66	6.15	16.26
1030	1	2031	193.07	99.48	1451	199.26	115.54	6.19	16.06
1031	1	2029	193.00	99.59	1452	199.27	115.69	6.27	16.10
1032	1	2033	193.16	99.04	1453	199.25	115.38	6.09	16.33
1033	1	2035	193.29	99.50	1454	199.38	115.93	6.09	16.43
1034	1	2036	193.28	99.72	1455	199.40	116.29	6.13	16.58
1035	1	2037	193.30	99.86	1456	199.52	115.57	6.22	15.71
1036	1	2038	193.37	99.16	1457	199.47	115.74	6.10	16.57
1037	1	2040	193.47	99.18	1458	199.64	115.89	6.17	16.71
1038	1	2041	193.53	98.71	1459	199.73	115.11	6.20	16.40
1039	1	2042	193.52	98.50	1460	199.70	115.35	6.18	16.86
1040	1	2044	193.66	98.80	1461	199.81	115.34	6.15	16.53
1041	1	2046	193.78	98.84	1462	199.93	115.15	6.15	16.31
1042	1	2047	193.89	98.40	1463	200.04	115.89	6.15	17.49
1043	1	2049	194.01	99.35	1464	200.14	115.96	6.13	16.61
1044	1	2050	194.04	98.33	1465	200.22	115.98	6.18	17.65
1045	1	2053	194.18	98.05	1466	200.28	116.45	6.10	18.40
1046	1	2054	194.24	98.81	1467	200.32	116.24	6.08	17.43
1047	1	2057	194.36	98.74	1468	200.38	117.39	6.02	18.65
1048	1	2059	194.46	98.22	1469	200.46	117.22	6.00	19.00
1049	1	2062	194.59	99.29	1470	200.64	117.09	6.04	17.80
1050	1	2064	194.70	99.67	1471	200.78	116.90	6.08	17.23
1051	1	2065	194.73	99.69	1472	200.91	116.74	6.19	17.05
1052	1	2067	194.81	99.12	1473	200.91	117.84	6.10	18.72
1053	1	2070	194.94	99.16	1474	201.05	117.36	6.11	18.20
1054	1	2068	194.81	99.48	1475	200.97	117.30	6.16	17.82
1055	1	2071	195.04	98.98	1476	201.01	117.37	5.97	18.39
1056	1	2074	195.15	100.11	1477	201.15	117.91	6.00	17.80
1057	1	2075	195.11	99.63	1478	201.35	118.16	6.24	18.53
1058	1	2077	195.22	99.70	1479	201.47	118.04	6.25	18.34
1059	1	2079	195.36	99.43	1480	201.55	118.34	6.19	18.90
1060	1	2080	195.35	99.85	1481	201.68	118.32	6.33	18.47
1061	1	2083	195.50	99.99	1482	201.89	118.36	6.39	18.37
1062	1	2084	195.54	99.92	1483	202.05	118.30	6.51	18.38
1063	1	2085	195.56	100.14	1484	202.14	118.54	6.58	18.40

obs	T	B260 year	driving stress (kPa)	flux (km^3a^{-1})	B270 year	driving stress (kPa)	flux (km^3a^{-1})	Δdriving stress (kPa)	Δflux (km^3a^{-1})
1064	1	2087	195.60	100.33	1485	202.29	118.72	6.69	18.40
1065	1	2088	195.65	100.22	1486	202.35	118.96	6.70	18.74
1066	1	2091	195.74	99.97	1487	202.47	119.16	6.74	19.19
1067	1	2092	195.73	100.10	1488	202.60	119.41	6.86	19.31
1068	1	2093	195.73	100.33	1489	202.72	119.26	6.99	18.93
1069	1	2095	195.92	100.21	1490	202.85	119.74	6.93	19.53
1070	1	2096	195.76	100.45	1491	203.02	119.20	7.26	18.75
1071	1	2098	195.82	100.19	1492	203.14	119.02	7.32	18.83
1072	1	2100	195.97	99.83	1493	203.26	118.15	7.29	18.33
1073	1	2101	196.06	99.82	1494	203.32	118.62	7.26	18.80
1074	1	2104	196.25	99.76	1495	203.38	118.22	7.13	18.47
1075	1	2105	196.19	100.10	1496	203.49	119.00	7.30	18.90
1076	1	2106	196.29	100.14	1497	203.57	119.32	7.28	19.18
1077	1	2110	196.46	99.97	1498	203.62	119.41	7.15	19.44
1078	1	2112	196.45	99.71	1499	203.71	119.73	7.26	20.02
1079	1	2113	196.42	99.72	1500	203.88	119.54	7.46	19.82
1080	1	2114	196.40	99.78	1501	203.97	119.36	7.57	19.57
1081	1	2117	196.60	99.82	1502	204.13	119.65	7.53	19.84
1082	1	2118	196.63	99.84	1503	204.15	119.79	7.52	19.95
1083	1	2119	196.63	99.78	1504	204.14	119.82	7.52	20.04
1084	1	2123	196.95	99.97	1505	204.27	119.97	7.33	20.00
1085	1	2124	197.01	99.91	1506	204.34	119.91	7.33	20.00
1086	1	2126	197.09	100.39	1507	204.45	119.99	7.36	19.60
1087	1	2128	197.13	100.75	1508	204.56	120.24	7.43	19.49
1088	1	2130	197.30	100.85	1509	204.63	120.05	7.33	19.20
1089	1	2131	197.45	100.90	1510	204.80	120.60	7.35	19.69
1090	1	2134	197.65	101.11	1511	205.01	120.44	7.36	19.33
1091	1	2135	197.61	101.21	1512	205.04	120.71	7.43	19.50
1092	1	2136	197.74	101.25	1513	205.11	120.90	7.37	19.65
1093	1	2139	197.97	101.42	1514	205.18	120.55	7.22	19.13
1094	1	2140	198.01	101.36	1515	205.26	120.67	7.25	19.31
1095	1	2142	198.08	101.80	1516	205.30	120.55	7.21	18.75
1096	1	2146	198.30	101.60	1517	205.38	120.23	7.08	18.63
1097	1	2144	198.26	101.79	1518	205.57	120.82	7.31	19.03
1098	1	2148	198.41	101.57	1519	205.30	121.22	6.88	19.65
1099	1	2151	198.59	101.79	1520	205.40	121.42	6.80	19.62
1100	1	2152	198.54	101.76	1521	205.70	121.23	7.16	19.46
1101	1	2154	198.64	102.07	1522	205.71	121.58	7.07	19.51
1102	1	2155	198.71	102.18	1523	205.84	122.23	7.13	20.05
1103	1	2156	198.81	102.24	1524	206.04	122.48	7.23	20.24

obs	T	B260 year	driving stress (kPa)	flux (km^3a^{-1})	B270 year	driving stress (kPa)	flux (km^3a^{-1})	Δdriving stress (kPa)	Δflux (km^3a^{-1})
1104	1	2160	198.99	102.27	1525	206.27	122.51	7.28	20.24
1105	1	2161	199.05	102.17	1526	206.48	122.52	7.43	20.35
1106	1	2164	199.18	102.73	1527	206.45	122.30	7.28	19.57
1107	1	2166	199.26	103.18	1528	206.53	122.45	7.27	19.26
1108	1	2167	199.32	103.29	1529	206.67	122.58	7.35	19.29
1109	1	2168	199.36	103.24	1530	206.71	122.64	7.34	19.40
1110	1	2170	199.60	103.06	1531	206.93	122.40	7.32	19.33
1111	1	2171	199.60	103.19	1532	206.96	123.39	7.36	20.20
1112	1	2174	199.91	103.33	1533	207.18	122.53	7.27	19.20
1113	1	2175	200.00	103.46	1534	207.35	122.66	7.34	19.20
1114	1	2176	200.14	103.49	1535	207.44	122.57	7.31	19.09
1115	1	2178	200.19	103.51	1536	207.60	122.77	7.41	19.26
1116	1	2180	200.30	103.77	1537	207.61	122.43	7.32	18.67
1117	1	2181	200.25	103.79	1538	207.67	122.47	7.42	18.68
1118	1	2183	200.41	103.60	1539	207.77	122.70	7.36	19.10
1119	1	2185	200.55	103.67	1540	207.94	123.35	7.40	19.68
1120	1	2187	200.68	103.25	1541	208.05	123.30	7.37	20.05
1121	1	2188	200.67	103.30	1542	208.04	122.66	7.37	19.36
1122	1	2190	200.89	103.52	1543	208.15	123.14	7.26	19.63
1123	1	2191	200.88	103.41	1544	208.33	122.25	7.45	18.84
1124	1	2192	200.96	103.49	1545	208.51	121.88	7.55	18.39
1125	1	2193	200.93	103.64	1546	208.53	121.97	7.59	18.33
1126	1	2194	201.03	103.90	1547	208.67	121.91	7.64	18.01
1127	1	2196	201.08	103.57	1548	208.53	122.28	7.45	18.71
1128	1	2200	201.15	103.92	1549	208.67	122.62	7.52	18.70
1129	1	2201	201.19	104.09	1550	208.77	122.83	7.58	18.74
1130	1	2202	201.27	104.14	1551	208.66	122.64	7.39	18.50
1131	1	2204	201.49	104.04	1552	208.77	122.43	7.28	18.39
1132	1	2205	201.53	103.96	1553	208.78	122.15	7.25	18.19
1133	1	2206	201.65	103.99	1554	208.93	122.88	7.28	18.88
1134	1	2208	201.71	104.01	1555	209.01	122.33	7.30	18.31
1135	1	2209	201.73	104.21	1556	209.16	122.32	7.43	18.11
1136	1	2211	201.82	104.53	1558	209.26	121.99	7.45	17.47
1137	1	2212	201.93	104.54	1559	209.36	122.63	7.44	18.09
1138	1	2213	201.92	104.38	1560	209.41	122.65	7.50	18.27
1139	1	2216	202.18	104.95	1561	209.56	123.34	7.38	18.39
1140	1	2217	202.26	104.99	1562	209.71	122.78	7.44	17.79
1141	1	2220	202.45	105.26	1563	209.69	122.86	7.23	17.60
1142	1	2221	202.52	105.44	1564	209.52	123.32	7.00	17.89
1143	1	2223	202.59	105.69	1565	209.79	123.20	7.20	17.52

obs	T	B260 year	driving stress (kPa)	flux (km^3a^{-1})	B270 year	driving stress (kPa)	flux (km^3a^{-1})	Δdriving stress (kPa)	Δflux (km^3a^{-1})
1144	1	2224	202.53	105.33	1566	209.67	123.06	7.14	17.73
1145	1	2225	202.64	105.73	1567	209.80	122.84	7.16	17.11
1146	1	2226	202.66	105.30	1568	209.93	122.64	7.27	17.34
1147	1	2228	202.88	105.34	1569	210.08	123.02	7.19	17.67
1148	1	2229	202.86	105.00	1570	210.31	122.99	7.46	17.98
1149	1	2230	202.91	105.02	1571	210.46	123.01	7.55	17.99
1150	1	2231	203.05	104.85	1572	210.43	122.79	7.38	17.93
1151	1	2233	203.10	105.27	1573	210.42	122.80	7.31	17.53
1152	1	2234	203.14	105.35	1574	210.48	122.66	7.34	17.31
1153	1	2237	203.25	105.57	1575	210.68	123.03	7.43	17.46
1154	1	2238	203.35	105.13	1576	210.80	123.34	7.45	18.21
1155	1	2242	203.54	105.20	1578	211.01	123.03	7.47	17.83
1156	1	2244	203.71	105.05	1580	211.15	122.85	7.44	17.80
1157	1	2246	203.60	105.42	1581	211.06	122.59	7.46	17.17
1158	1	2248	203.69	105.28	1582	211.23	122.60	7.54	17.32
1159	1	2249	203.78	105.37	1583	211.33	122.63	7.55	17.25
1160	1	2250	203.86	105.52	1584	211.38	122.67	7.52	17.15
1161	1	2251	203.95	105.27	1585	211.47	122.39	7.52	17.12
1162	1	2252	204.03	105.70	1586	211.65	122.22	7.62	16.52
1163	1	2254	204.17	105.20	1587	211.70	122.32	7.54	17.12
1164	1	2256	204.40	104.76	1588	211.83	121.95	7.43	17.19
1165	1	2257	204.39	104.65	1589	211.82	121.54	7.43	16.89
1166	1	2259	204.56	104.77	1590	211.91	121.57	7.35	16.80
1167	1	2260	204.52	104.85	1591	211.83	121.10	7.31	16.25
1168	1	2261	204.47	104.74	1592	211.88	121.35	7.41	16.61
1169	1	2262	204.59	104.80	1593	211.98	121.83	7.39	17.03
1170	1	2266	204.76	105.13	1594	212.04	121.37	7.28	16.24
1171	1	2267	204.82	104.99	1595	212.03	121.47	7.21	16.48
1172	1	2270	204.91	104.46	1596	212.04	121.26	7.13	16.80
1173	1	2271	205.04	104.16	1597	212.16	121.13	7.13	16.97
1174	1	2272	205.07	104.39	1598	212.24	121.07	7.17	16.68
1175	1	2273	205.15	104.28	1599	212.34	120.95	7.19	16.67
1176	1	2277	205.24	103.79	1600	212.35	121.00	7.11	17.20
1177	1	2278	205.20	103.61	1601	212.36	120.76	7.16	17.15
1178	1	2279	205.16	103.51	1602	212.37	120.67	7.21	17.16
1179	1	2280	205.20	103.68	1603	212.36	120.76	7.15	17.09
1180	1	2282	205.36	103.96	1604	212.37	120.65	7.00	16.69
1181	1	2284	205.36	104.06	1605	212.44	120.47	7.08	16.41
1182	1	2285	205.36	104.18	1606	212.46	120.52	7.11	16.35
1183	1	2286	205.36	103.70	1607	212.60	120.64	7.23	16.94

obs	T	B260 year	driving stress (kPa)	flux (km^3a^{-1})	B270 year	driving stress (kPa)	flux (km^3a^{-1})	Δdriving stress (kPa)	Δflux (km^3a^{-1})
1184	1	2289	205.51	104.09	1608	212.54	120.51	7.03	16.42
1185	1	2291	205.59	103.70	1609	212.56	120.78	6.97	17.08
1186	1	2294	205.63	104.01	1610	212.59	121.01	6.95	17.00
1187	1	2295	205.62	103.94	1611	212.64	120.63	7.02	16.69
1188	1	2296	205.53	103.88	1612	212.68	120.33	7.16	16.45
1189	1	2297	205.74	103.50	1613	212.76	120.40	7.02	16.91
1190	1	2298	205.78	103.45	1614	212.95	120.68	7.18	17.22
1191	1	2302	205.99	103.57	1615	212.96	120.30	6.97	16.73
1192	1	2303	206.03	103.34	1616	213.09	120.63	7.05	17.29
1193	1	2304	206.08	103.15	1617	213.08	120.17	7.01	17.02
1194	1	2305	206.09	103.46	1618	213.08	120.22	7.00	16.76
1195	1	2308	206.14	103.03	1619	213.21	119.74	7.07	16.71
1196	1	2309	206.25	103.05	1620	213.23	119.74	6.99	16.69
1197	1	2311	206.38	103.21	1621	213.30	119.43	6.92	16.23
1198	1	2312	206.44	103.33	1622	213.37	119.45	6.93	16.12
1199	1	2313	206.53	102.63	1623	213.44	119.52	6.91	16.89
1200	1	2314	206.53	102.89	1624	213.49	119.25	6.96	16.36
1201	1	2315	206.48	102.56	1625	213.55	119.82	7.07	17.26
1202	1	2319	206.60	102.39	1626	213.79	119.41	7.19	17.02
1203	1	2321	206.76	102.09	1627	213.88	119.53	7.12	17.45
1204	1	2323	206.82	102.88	1628	213.97	119.53	7.15	16.65
1205	1	2324	206.82	102.46	1629	214.06	119.32	7.24	16.86
1206	1	2326	206.99	102.81	1630	214.12	119.44	7.13	16.62
1207	1	2327	207.04	102.42	1631	214.25	119.47	7.22	17.05
1208	1	2328	207.04	102.43	1632	214.37	119.08	7.33	16.65
1209	1	2332	207.19	102.77	1633	214.45	119.12	7.26	16.35
1210	1	2333	207.24	103.17	1634	214.42	119.07	7.19	15.90
1211	1	2335	207.31	102.74	1635	214.53	119.10	7.22	16.36
1212	1	2336	207.46	102.46	1636	214.49	119.43	7.03	16.97
1213	1	2337	207.41	102.56	1637	214.49	119.36	7.08	16.80
1214	1	2338	207.47	102.48	1638	214.45	118.91	6.98	16.43
1215	1	2341	207.66	102.72	1639	214.57	118.71	6.91	15.99
1216	1	2342	207.67	102.48	1640	214.69	118.74	7.01	16.27
1217	1	2343	207.67	103.08	1641	214.62	118.89	6.95	15.81
1218	1	2344	207.65	102.86	1642	214.64	118.92	7.00	16.06
1219	1	2349	208.01	102.35	1643	214.65	118.95	6.64	16.59
1220	1	2350	208.03	102.26	1644	214.86	118.27	6.83	16.01
1221	1	2351	208.01	102.09	1645	214.91	118.54	6.91	16.45
1222	1	2352	208.10	101.86	1646	214.90	117.85	6.79	15.99
1223	1	2353	208.11	101.97	1647	214.94	118.12	6.83	16.15

obs	T	B260 year	driving stress (kPa)	flux (km^3a^{-1})	B270 year	driving stress (kPa)	flux (km^3a^{-1})	Δdriving stress (kPa)	Δflux (km^3a^{-1})
1224	1	2354	208.09	101.79	1648	215.10	117.87	7.01	16.08
1225	1	2355	208.15	101.74	1649	214.91	118.11	6.76	16.37
1226	1	2360	208.20	101.23	1650	214.81	118.00	6.62	16.77
1227	1	2361	208.21	101.03	1651	215.02	118.16	6.82	17.13
1228	1	2362	208.25	101.08	1652	214.99	117.90	6.75	16.82
1229	1	2363	208.22	100.99	1653	214.92	117.92	6.70	16.93
1230	1	2370	208.16	101.46	1654	214.99	117.99	6.84	16.54
1231	1	2371	208.25	101.77	1655	214.99	117.96	6.74	16.20
1232	1	2372	208.30	101.53	1656	214.97	118.04	6.67	16.50
1233	1	2373	208.43	101.63	1657	215.07	118.48	6.64	16.85
1234	1	2374	208.51	101.53	1658	215.19	117.69	6.68	16.17
1235	1	2375	208.49	101.11	1659	215.31	117.26	6.82	16.15
1236	1	2376	208.50	101.77	1660	215.33	117.71	6.83	15.94
1237	1	2377	208.53	101.54	1661	215.46	117.50	6.93	15.96
1238	1	2378	208.48	101.99	1662	215.55	117.84	7.07	15.85
1239	1	2379	208.50	101.83	1663	215.52	117.88	7.02	16.04
1240	1	2380	208.49	101.43	1664	215.35	117.69	6.86	16.26
1241	1	2381	208.53	101.89	1665	215.39	117.45	6.86	15.56
1242	1	2383	208.64	102.02	1666	215.50	117.63	6.85	15.60
1243	1	2384	208.79	101.68	1667	215.42	117.50	6.64	15.82
1244	1	2385	208.75	101.54	1668	215.41	118.00	6.66	16.47
1245	1	2387	208.89	101.25	1669	215.44	117.96	6.55	16.71
1246	1	2388	208.90	101.45	1670	215.41	117.52	6.50	16.07
1247	1	2392	208.88	101.25	1671	215.48	117.87	6.60	16.62
1248	1	2393	209.05	101.12	1672	215.53	117.56	6.48	16.44
1249	1	2394	209.07	101.31	1673	215.68	117.06	6.61	15.75
1250	1	2395	208.93	101.06	1674	215.75	116.50	6.82	15.44
1251	1	2396	209.08	100.78	1675	215.74	116.65	6.66	15.86
1252	1	2397	208.94	100.77	1676	215.93	116.83	6.99	16.06
1253	1	2401	209.14	100.38	1677	215.85	116.70	6.72	16.32
1254	1	2402	209.06	100.73	1678	215.95	116.89	6.89	16.16
1255	1	2403	209.22	100.80	1679	216.07	116.73	6.85	15.93
1256	1	2404	209.06	100.77	1680	216.13	116.88	7.07	16.11
1257	1	2398	209.07	100.83	1681	216.16	116.89	7.09	16.05
1258	1	2405	209.19	100.72	1682	216.05	116.41	6.86	15.69
1259	1	2409	209.23	100.96	1683	216.13	115.90	6.90	14.95
1260	1	2410	209.20	101.00	1684	216.22	116.18	7.02	15.18
1261	1	2415	209.07	100.32	1685	216.27	116.16	7.20	15.84
1262	1	2416	209.11	100.35	1686	216.25	116.50	7.14	16.15
1263	1	2417	209.10	100.95	1687	216.22	116.16	7.12	15.21

obs	T	B260 year	driving stress (kPa)	flux (km^3a^{-1})	B270 year	driving stress (kPa)	flux (km^3a^{-1})	Δdriving stress (kPa)	Δflux (km^3a^{-1})
1264	1	2418	209.12	100.72	1688	216.20	116.43	7.08	15.71
1265	1	2419	209.35	100.68	1689	216.32	115.93	6.97	15.25
1266	1	2420	209.22	100.54	1690	216.38	115.82	7.15	15.28
1267	1	2421	209.21	100.62	1691	216.18	115.96	6.96	15.34
1268	1	2422	209.27	100.57	1692	216.27	115.81	7.00	15.23
1269	1	2423	209.26	100.54	1693	216.33	115.56	7.08	15.02
1270	1	2429	209.30	101.25	1694	216.39	115.53	7.09	14.28
1271	1	2430	209.26	100.90	1695	216.47	115.55	7.21	14.64
1272	1	2431	209.33	101.10	1696	216.53	115.69	7.20	14.60
1273	1	2432	209.42	100.99	1697	216.63	115.64	7.21	14.65
1274	1	2433	209.49	101.00	1698	216.67	115.68	7.17	14.68
1275	1	2434	209.44	100.86	1699	216.66	115.40	7.22	14.54
1276	1	2435	209.49	100.94	1700	216.72	115.08	7.23	14.14
1277	1	2436	209.59	100.59	1701	216.72	115.21	7.13	14.62
1278	1	2437	209.58	100.47	1702	216.76	115.07	7.18	14.59
1279	1	2438	209.60	100.12	1703	216.91	114.83	7.31	14.71
1280	1	2439	209.62	100.16	1704	216.89	114.64	7.27	14.48
1281	1	2440	209.62	100.22	1705	216.86	114.78	7.24	14.57
1282	1	2442	209.68	100.43	1706	217.09	114.65	7.40	14.22
1283	1	2443	209.63	100.53	1707	217.02	114.52	7.39	13.98
1284	1	2444	209.69	100.43	1708	216.94	114.41	7.25	13.98
1285	1	2445	209.74	100.30	1709	216.96	114.67	7.22	14.37
1286	1	2446	209.77	100.18	1710	217.07	114.72	7.30	14.54
1287	1	2447	209.82	100.14	1711	217.09	114.61	7.27	14.47
1288	1	2448	209.82	100.12	1712	217.16	114.77	7.33	14.66
1289	1	2454	209.83	99.80	1713	217.23	114.57	7.39	14.76
1290	1	2455	209.83	100.13	1714	217.18	114.78	7.35	14.64
1291	1	2456	209.88	100.00	1715	217.22	114.53	7.34	14.53
1292	1	2458	209.90	99.51	1716	217.15	114.93	7.25	15.41
1293	1	2459	209.93	99.21	1717	217.28	115.03	7.35	15.82
1294	1	2460	209.89	99.80	1718	217.13	115.03	7.24	15.23
1295	1	2461	209.92	99.70	1719	217.17	114.29	7.26	14.59
1296	1	2462	209.98	99.59	1720	217.28	114.38	7.31	14.79
1297	1	2463	209.95	99.64	1721	217.31	114.55	7.35	14.91
1298	1	2464	209.95	99.68	1722	217.31	114.41	7.37	14.73
1299	1	2465	209.86	99.72	1723	217.35	114.05	7.49	14.33
1300	1	2471	209.99	99.31	1724	217.37	113.71	7.38	14.40
1301	1	2466	209.87	100.07	1725	217.55	113.62	7.68	13.55
1302	1	2472	210.08	99.53	1726	217.33	113.56	7.25	14.03
1303	1	2476	210.12	98.93	1727	217.37	113.88	7.24	14.95

obs	T	B260 year	driving stress (kPa)	flux (km^3a^{-1})	B270 year	driving stress (kPa)	flux (km^3a^{-1})	Δdriving stress (kPa)	Δflux (km^3a^{-1})
1304	1	2477	210.20	98.90	1728	217.50	114.86	7.29	15.95
1305	1	2483	210.01	98.74	1729	217.56	114.20	7.56	15.46
1306	1	2484	209.95	98.80	1730	217.59	114.27	7.64	15.46
1307	1	2485	209.95	98.43	1731	217.61	113.88	7.66	15.46
1308	1	2486	210.10	98.23	1732	217.62	113.46	7.52	15.24
1309	1	2487	209.96	98.39	1733	217.68	113.73	7.72	15.34
1310	1	2488	209.90	98.49	1734	217.64	113.70	7.74	15.21
1311	1	2492	210.00	98.52	1735	217.59	113.62	7.58	15.10
1312	1	2493	209.99	98.07	1736	217.71	113.79	7.72	15.73
1313	1	2494	209.98	98.05	1737	217.63	114.26	7.65	16.21
1314	1	2495	209.97	98.21	1738	217.67	114.24	7.71	16.03
1315	1	2502	210.05	98.84	1739	217.69	113.86	7.64	15.02
1316	1	2503	210.12	98.80	1740	217.69	113.76	7.57	14.96
1317	1	2504	210.20	98.65	1741	217.72	113.35	7.52	14.70
1318	1	2505	210.06	98.53	1742	217.79	113.10	7.74	14.57
1319	1	2506	210.15	98.63	1743	217.83	113.19	7.68	14.56
1320	1	2507	210.16	98.16	1744	217.85	113.00	7.68	14.85
1321	1	2508	210.10	98.14	1745	217.84	112.69	7.74	14.55
1322	1	2509	210.05	98.25	1746	217.95	113.03	7.90	14.78
1323	1	2510	210.10	98.11	1747	217.95	113.49	7.85	15.38
1324	1	2512	210.10	98.11	1748	218.05	113.90	7.94	15.78
1325	1	2513	210.13	97.97	1749	218.01	113.84	7.88	15.86
1326	1	2514	210.17	98.00	1750	218.06	113.89	7.89	15.89
1327	1	2515	210.23	97.77	1751	218.18	113.26	7.95	15.49
1328	1	2516	210.17	98.13	1752	218.02	113.04	7.85	14.91
1329	1	2517	210.25	97.90	1753	218.02	112.97	7.77	15.07
1330	1	2518	210.27	97.94	1754	218.14	112.18	7.87	14.24
1331	1	2522	210.32	97.94	1755	218.04	112.66	7.71	14.73
1332	1	2523	210.17	98.06	1756	218.07	112.76	7.89	14.71
1333	1	2524	210.08	97.86	1757	218.11	112.91	8.03	15.06
1334	1	2525	210.06	98.00	1758	218.23	113.24	8.17	15.24
1335	1	2526	210.11	97.86	1759	218.24	113.21	8.13	15.35
1336	1	2533	210.18	97.55	1760	218.13	112.99	7.95	15.43
1337	1	2534	210.21	97.68	1761	218.20	112.70	7.99	15.02
1338	1	2535	210.28	97.60	1762	218.13	112.52	7.85	14.92
1339	1	2536	210.25	97.39	1763	218.29	112.30	8.04	14.91
1340	1	2537	210.27	97.24	1764	218.34	112.26	8.07	15.01
1341	1	2538	210.20	97.49	1765	218.38	112.35	8.17	14.86
1342	1	2539	210.23	97.73	1766	218.35	112.62	8.12	14.88
1343	1	2544	210.38	97.31	1767	218.17	112.26	7.79	14.95

obs	T	B260 year	driving stress (kPa)	flux (km^3a^{-1})	B270 year	driving stress (kPa)	flux (km^3a^{-1})	Δdriving stress (kPa)	Δflux (km^3a^{-1})
1344	1	2545	210.43	97.50	1768	218.12	112.56	7.69	15.06
1345	1	2546	210.37	96.97	1769	218.30	111.97	7.93	14.99
1346	1	2547	210.41	96.99	1770	218.37	112.17	7.95	15.18
1347	1	2548	210.44	96.89	1771	218.42	111.96	7.98	15.07
1348	1	2549	210.42	96.86	1772	218.36	112.15	7.94	15.29
1349	1	2550	210.44	97.05	1773	218.44	112.27	7.99	15.22
1350	1	2551	210.44	96.81	1774	218.47	112.14	8.03	15.33
1351	1	2552	210.43	97.23	1775	218.53	112.15	8.10	14.93
1352	1	2540	210.33	97.35	1776	218.45	111.92	8.12	14.57
1353	1	2553	210.48	97.25	1777	218.31	112.07	7.82	14.82
1354	1	2554	210.62	97.08	1778	218.29	111.91	7.67	14.84
1355	1	2555	210.52	97.06	1779	218.35	111.46	7.83	14.40
1356	1	2556	210.55	97.13	1780	218.40	111.59	7.85	14.46
1357	1	2557	210.47	97.17	1781	217.93	112.08	7.46	14.91
1358	1	2558	210.51	97.18	1782	218.00	111.86	7.49	14.67
1359	1	2559	210.55	97.13	1783	217.90	112.09	7.35	14.96
1360	1	2563	210.20	97.46	1784	217.84	112.14	7.63	14.68
1361	1	2564	210.07	97.25	1785	217.97	111.75	7.89	14.50
1362	1	2565	210.11	96.93	1786	218.02	111.67	7.91	14.74
1363	1	2566	210.06	97.02	1787	217.96	111.67	7.91	14.65
1364	1	2567	209.98	96.82	1788	217.97	111.23	7.99	14.41
1365	1	2568	210.09	96.87	1789	217.86	111.37	7.77	14.50
1366	1	2569	209.91	97.12	1790	217.67	111.13	7.76	14.00
1367	1	2570	209.93	96.73	1791	217.76	111.54	7.83	14.81
1368	1	2573	209.87	97.49	1792	217.70	111.83	7.83	14.34
1369	1	2574	209.91	97.28	1793	217.71	112.24	7.80	14.96
1370	1	2575	209.96	97.31	1794	217.74	111.80	7.78	14.50
1371	1	2576	209.96	97.17	1795	217.82	111.71	7.85	14.54
1372	1	2577	210.01	97.08	1796	217.83	111.88	7.82	14.81
1373	1	2578	210.00	97.42	1797	217.96	111.72	7.97	14.31
1374	1	2579	209.99	97.43	1798	217.94	111.52	7.95	14.09
1375	1	2580	210.08	97.47	1799	217.89	111.34	7.81	13.87
1376	1	2581	209.99	97.68	1800	217.87	111.87	7.89	14.19
1377	1	2585	209.85	97.18	1801	217.80	111.71	7.95	14.53
1378	1	2586	210.06	97.04	1802	217.89	111.27	7.83	14.23
1379	1	2587	209.96	97.11	1803	217.89	111.45	7.93	14.35
1380	1	2588	209.99	97.05	1804	217.92	111.16	7.92	14.11
1381	1	2589	209.98	97.34	1805	217.95	110.98	7.97	13.63
1382	1	2590	210.07	97.24	1806	218.01	110.87	7.94	13.63
1383	1	2591	210.07	97.00	1807	218.03	111.16	7.96	14.16

obs	T	B260 year	driving stress (kPa)	flux (km^3a^{-1})	B270 year	driving stress (kPa)	flux (km^3a^{-1})	Δdriving stress (kPa)	Δflux (km^3a^{-1})
1384	1	2592	210.12	97.11	1808	217.88	111.57	7.76	14.46
1385	1	2599	210.06	97.04	1809	217.97	111.15	7.91	14.11
1386	1	2600	210.05	96.97	1810	218.12	111.19	8.06	14.21
1387	1	2601	210.04	96.61	1811	218.03	111.27	7.99	14.66
1388	1	2602	210.00	96.94	1812	218.03	110.75	8.03	13.81
1389	1	2603	210.13	96.84	1813	218.22	110.75	8.09	13.90
1390	1	2604	210.17	96.79	1814	218.25	111.04	8.08	14.25
1391	1	2605	210.12	96.71	1815	218.17	110.88	8.04	14.17
1392	1	2606	209.98	97.32	1816	218.25	110.64	8.27	13.32
1393	1	2607	210.05	97.07	1817	218.28	110.84	8.24	13.77
1394	1	2612	209.93	96.84	1818	218.31	110.55	8.38	13.71
1395	1	2613	210.01	96.96	1819	218.38	110.68	8.37	13.72
1396	1	2614	210.01	97.01	1820	218.42	110.59	8.42	13.59
1397	1	2615	209.91	97.03	1821	218.42	110.38	8.51	13.35
1398	1	2616	209.98	97.00	1822	218.47	110.24	8.49	13.24
1399	1	2617	209.97	96.91	1823	218.37	110.26	8.40	13.35
1400	1	2618	210.02	96.81	1824	218.25	110.73	8.24	13.91
1401	1	2619	210.04	96.67	1825	218.27	110.89	8.23	14.21
1402	1	2625	210.12	97.13	1826	218.32	110.38	8.20	13.24
1403	1	2626	210.16	96.61	1827	218.33	110.32	8.17	13.71
1404	1	2627	210.16	96.61	1828	218.37	110.01	8.21	13.40
1405	1	2628	210.08	96.50	1829	218.34	110.09	8.26	13.58
1406	1	2629	210.17	96.42	1830	218.34	109.92	8.18	13.49
1407	3	2631	210.14	96.86	1855	218.59	109.67	8.45	12.81
1408	3	2632	210.16	97.07	1856	218.60	109.52	8.44	12.45
1409	3	2633	210.19	96.80	1857	218.66	109.17	8.47	12.37
1410	3	2635	210.14	96.86	1858	218.72	109.02	8.58	12.16
1411	3	2636	210.10	96.80	1859	218.67	109.02	8.57	12.22
1412	3	2637	210.13	96.48	1860	218.69	109.46	8.56	12.98
1413	3	2638	209.89	96.88	1861	218.68	109.80	8.79	12.92
1414	3	2639	209.89	96.75	1862	218.65	110.16	8.76	13.41
1415	3	2640	209.95	97.11	1863	218.75	110.07	8.80	12.97
1416	3	2643	210.19	96.58	1864	218.72	110.23	8.53	13.65
1417	3	2644	210.26	96.41	1865	218.82	109.79	8.56	13.38
1418	3	2645	210.30	96.36	1866	218.62	109.60	8.32	13.24
1419	3	2646	210.24	96.28	1867	218.71	109.72	8.47	13.44
1420	3	2647	210.41	96.22	1868	218.48	110.10	8.07	13.88
1421	3	2648	210.10	96.74	1869	218.58	109.87	8.48	13.13
1422	3	2653	210.24	96.34	1870	218.65	109.66	8.41	13.32
1423	3	2654	210.21	96.59	1871	218.66	109.46	8.45	12.87

obs	T	B260 year	driving stress (kPa)	flux (km^3a^{-1})	B270 year	driving stress (kPa)	flux (km^3a^{-1})	Δdriving stress (kPa)	Δflux (km^3a^{-1})
1424	3	2655	210.25	96.40	1872	218.69	109.45	8.45	13.06
1425	3	2656	210.32	96.41	1873	218.75	109.41	8.43	13.00
1426	3	2657	210.23	96.50	1874	218.77	109.36	8.53	12.86
1427	3	2658	210.07	96.56	1875	218.73	109.45	8.66	12.89
1428	3	2664	210.35	96.14	1876	218.73	109.37	8.38	13.23
1429	3	2665	210.26	96.20	1877	218.94	109.43	8.68	13.24
1430	3	2666	210.16	96.19	1878	218.95	109.69	8.79	13.49
1431	3	2667	210.20	96.21	1879	218.96	109.84	8.76	13.63
1432	3	2668	210.22	96.44	1880	219.07	109.86	8.85	13.42
1433	3	2669	210.13	96.49	1881	219.01	110.08	8.89	13.58
1434	3	2670	210.14	96.36	1882	218.83	109.84	8.69	13.48
1435	3	2671	210.19	96.14	1883	218.75	109.70	8.56	13.56
1436	3	2672	210.11	95.83	1884	218.71	109.66	8.60	13.83
1437	3	2684	210.41	95.78	1885	218.79	109.56	8.39	13.78
1438	3	2685	210.39	96.09	1886	218.71	109.63	8.31	13.55
1439	3	2686	210.46	95.52	1887	218.71	109.68	8.25	14.15
1440	3	2687	210.49	95.83	1888	218.88	109.71	8.39	13.88
1441	3	2688	210.30	96.21	1889	219.10	109.68	8.80	13.47
1442	3	2689	210.38	96.31	1890	218.97	109.65	8.59	13.34
1443	3	2690	210.36	95.79	1891	219.08	108.95	8.73	13.16
1444	3	2691	210.40	95.98	1892	219.04	108.98	8.63	13.00
1445	3	2692	210.36	95.89	1893	219.16	108.23	8.80	12.35
1446	3	2693	210.43	95.97	1894	219.00	108.68	8.57	12.71
1447	3	2704	210.56	95.29	1895	219.03	108.64	8.47	13.34
1448	3	2705	210.52	95.51	1896	218.96	108.66	8.44	13.14
1449	3	2706	210.59	95.73	1897	219.04	108.55	8.45	12.83
1450	3	2707	210.69	95.48	1898	219.05	108.40	8.36	12.92
1451	3	2708	210.68	95.48	1899	218.95	108.66	8.28	13.17
1452	3	2709	210.65	95.34	1900	218.96	108.95	8.30	13.60
1453	3	2710	210.50	95.47	1901	219.05	108.66	8.55	13.19
1454	3	2711	210.49	95.34	1902	219.01	108.30	8.52	12.95
1455	3	2712	210.62	95.25	1903	219.11	108.61	8.50	13.36
1456	3	2713	210.55	95.44	1904	219.16	108.56	8.61	13.12
1457	3	2714	210.57	95.27	1905	219.02	108.45	8.45	13.18
1458	3	2715	210.54	95.28	1906	219.16	108.22	8.62	12.94
1459	3	2716	210.50	95.93	1907	218.86	108.32	8.36	12.40
1460	3	2717	210.51	95.87	1908	218.95	108.49	8.44	12.61
1461	3	2718	210.67	96.14	1909	219.08	108.36	8.41	12.22
1462	3	2719	210.61	96.04	1910	219.05	108.69	8.45	12.65
1463	3	2720	210.57	96.14	1911	219.09	109.02	8.52	12.88

obs	T	B260 year	driving stress (kPa)	flux (km^3a^{-1})	B270 year	driving stress (kPa)	flux (km^3a^{-1})	Δdriving stress (kPa)	Δflux (km^3a^{-1})
1464	3	2721	210.58	95.88	1912	218.83	108.08	8.25	12.19
1465	3	2730	210.78	95.99	1913	218.80	108.31	8.03	12.32
1466	3	2739	210.77	95.23	1914	218.69	108.69	7.92	13.46
1467	3	2738	210.81	95.74	1917	218.86	108.47	8.05	12.73
1468	3	2733	210.90	95.84	1918	218.83	108.50	7.93	12.66
1469	3	2734	210.75	96.05	1919	218.84	108.38	8.09	12.34
1470	3	2735	210.86	95.97	1920	218.93	108.32	8.07	12.35
1471	3	2742	210.93	95.28	1921	218.88	108.71	7.95	13.42
1472	3	2743	210.93	95.19	1922	218.87	108.28	7.94	13.08
1473	3	2746	210.96	95.59	1923	218.77	108.75	7.81	13.16
1474	3	2747	210.99	95.65	1924	218.90	108.64	7.91	12.99
1475	3	2748	211.00	95.67	1925	218.96	108.76	7.96	13.10
1476	3	2749	211.03	95.66	1926	218.91	108.59	7.88	12.93
1477	3	2750	211.04	95.68	1927	219.05	108.10	8.01	12.42
1478	3	2751	210.95	95.91	1928	219.04	108.26	8.09	12.35
1479	3	2757	211.07	95.43	1929	218.90	108.66	7.83	13.23
1480	3	2759	210.96	95.53	1930	218.88	108.42	7.92	12.90
1481	3	2762	210.81	95.62	1936	218.77	108.70	7.96	13.08
1482	3	2770	210.92	95.23	1937	218.88	108.76	7.97	13.52
1483	3	2771	210.94	95.32	1938	218.79	108.01	7.84	12.69
1484	3	2772	210.93	95.65	1939	219.02	108.62	8.09	12.97
1485	3	2773	211.02	95.40	1940	218.97	108.79	7.95	13.39
1486	3	2778	211.14	95.69	1941	218.85	108.82	7.71	13.13
1487	3	2779	210.90	95.59	1942	218.91	108.94	8.01	13.35
1488	3	2780	210.87	95.65	1943	218.95	108.65	8.08	13.00
1489	3	2781	211.07	95.27	1944	218.87	108.81	7.80	13.54
1490	3	2782	211.08	95.31	1945	218.95	108.94	7.87	13.63
1491	3	2783	211.05	95.17	1946	218.92	109.09	7.88	13.92
1492	3	2784	211.14	95.09	1947	218.99	109.40	7.85	14.31
1493	3	2785	211.07	95.29	1948	219.01	109.37	7.94	14.09
1494	3	2793	210.90	94.93	1949	218.95	109.62	8.05	14.69
1495	3	2794	211.05	94.70	1950	218.97	108.98	7.92	14.28
1496	3	2795	210.98	95.15	1951	218.99	109.04	8.01	13.89
1497	3	2796	210.86	95.06	1952	218.89	108.73	8.04	13.67
1498	3	2797	210.89	95.22	1953	219.00	109.14	8.11	13.92
1499	3	2798	210.85	94.99	1954	219.03	109.47	8.18	14.48
1500	3	2799	210.64	94.91	1955	219.14	109.18	8.50	14.26
1501	3	2800	210.75	94.84	1956	219.07	109.50	8.32	14.66
1502	3	2810	210.80	94.67	1957	219.17	109.46	8.36	14.79
1503	3	2811	210.88	94.50	1958	219.22	109.26	8.35	14.75

obs	T	B260 year	driving stress (kPa)	flux (km^3a^{-1})	B270 year	driving stress (kPa)	flux (km^3a^{-1})	Δdriving stress (kPa)	Δflux (km^3a^{-1})
1504	3	2812	210.91	94.61	1959	219.19	109.54	8.28	14.93
1505	3	2813	210.84	94.53	1960	219.21	109.27	8.37	14.74
1506	3	2814	210.84	94.36	1961	219.38	108.98	8.55	14.62
1507	3	2815	210.96	94.24	1962	219.35	108.96	8.39	14.73
1508	3	2816	210.87	94.62	1963	219.28	109.18	8.41	14.56
1509	3	2817	210.83	94.70	1964	219.36	109.14	8.53	14.44
1510	3	2818	210.91	94.22	1965	219.37	109.19	8.45	14.97
1511	3	2819	210.99	94.40	1966	219.44	108.80	8.44	14.40
1512	3	2833	210.68	94.00	1967	219.44	109.07	8.76	15.07
1513	3	2834	210.62	94.32	1968	219.43	109.17	8.81	14.85
1514	3	2835	210.83	93.83	1969	219.46	108.88	8.63	15.05
1515	3	2836	210.72	94.21	1970	219.46	108.70	8.74	14.50
1516	3	2837	210.71	94.34	1971	219.46	108.83	8.75	14.49
1517	3	2838	210.70	94.00	1972	219.49	108.52	8.79	14.52
1518	3	2839	210.65	93.93	1973	219.53	108.50	8.88	14.57
1519	3	2840	210.66	94.18	1974	219.33	108.72	8.68	14.54
1520	3	2841	210.56	93.83	1975	219.38	109.05	8.82	15.22
1521	3	2842	210.53	93.82	1976	219.32	108.87	8.78	15.06
1522	3	2850	210.46	93.80	1977	219.48	108.96	9.02	15.16
1523	3	2851	210.47	94.05	1978	219.54	108.59	9.06	14.54
1524	3	2852	210.48	94.39	1979	219.54	108.06	9.06	13.68
1525	3	2853	210.54	94.06	1980	219.52	107.99	8.99	13.92
1526	3	2854	210.51	94.04	1981	219.62	108.53	9.11	14.50
1527	3	2855	210.50	94.08	1982	219.56	108.71	9.06	14.63
1528	3	2861	210.55	94.26	1983	219.37	108.22	8.82	13.96
1529	3	2862	210.56	93.59	1984	219.22	108.50	8.66	14.90
1530	3	2863	210.53	93.58	1985	219.38	108.50	8.85	14.92
1531	3	2864	210.53	93.76	1986	219.40	108.10	8.86	14.33
1532	3	2865	210.64	94.01	1987	219.48	107.84	8.84	13.82
1533	3	2866	210.64	93.98	1988	219.51	107.76	8.87	13.78
1534	3	2870	210.60	93.85	1989	219.58	107.64	8.98	13.79
1535	3	2871	210.65	94.13	1990	219.52	108.11	8.87	13.98
1536	3	2872	210.61	94.20	1991	219.50	107.99	8.90	13.79
1537	3	2873	210.63	94.34	1992	219.48	107.92	8.85	13.59
1538	3	2874	210.72	94.54	1993	219.71	107.32	8.99	12.78
1539	3	2875	210.65	94.67	1994	219.64	107.36	8.99	12.69
1540	3	2876	210.76	94.73	1995	219.77	107.30	9.01	12.57
1541	3	2877	210.76	94.51	1996	219.57	107.09	8.81	12.58
1542	3	2878	210.73	94.36	1997	219.65	107.00	8.92	12.64
1543	3	2879	210.68	94.45	1998	219.73	106.77	9.05	12.32

obs	T	B260 year	driving stress (kPa)	flux (km^3a^{-1})	B270 year	driving stress (kPa)	flux (km^3a^{-1})	Δdriving stress (kPa)	Δflux (km^3a^{-1})
1544	3	2880	210.73	93.98	1999	219.66	106.61	8.93	12.63
1545	3	2881	210.82	94.38	2000	219.63	106.71	8.81	12.33
1546	3	2882	210.85	94.32	2001	219.61	107.02	8.77	12.71
1547	3	2897	210.78	93.86	2002	219.58	106.86	8.80	13.01
1548	3	2898	210.72	93.44	2003	219.72	106.91	9.00	13.47
1549	3	2899	210.81	93.31	2004	219.65	106.46	8.84	13.15
1550	3	2900	210.71	93.94	2005	219.69	106.55	8.97	12.61
1551	3	2901	210.77	93.54	2006	219.73	106.76	8.96	13.22
1552	3	2902	210.86	93.46	2007	219.73	106.92	8.86	13.47
1553	3	2903	210.81	93.45	2008	219.68	106.62	8.87	13.16
1554	3	2904	210.74	93.59	2009	219.73	106.55	8.99	12.96
1555	3	2905	210.71	93.34	2010	219.67	106.59	8.96	13.25
1556	3	2906	210.74	93.37	2011	219.67	106.79	8.93	13.42
1557	3	2907	210.81	93.61	2012	219.67	106.53	8.86	12.92
1558	3	2923	210.63	93.32	2013	219.70	106.39	9.07	13.07
1559	3	2927	210.45	93.24	2014	219.69	106.40	9.24	13.16
1560	3	2928	210.64	93.08	2015	219.65	106.61	9.01	13.54
1561	3	2929	210.37	93.19	2016	219.69	106.63	9.32	13.45
1562	3	2930	210.36	93.20	2017	219.70	106.14	9.34	12.94
1563	3	2931	210.55	93.39	2018	219.73	106.62	9.18	13.22
1564	3	2932	210.35	93.41	2019	219.73	105.92	9.38	12.51
1565	3	2933	210.36	92.62	2020	219.56	105.87	9.20	13.26
1566	3	2934	210.53	92.94	2021	219.59	106.57	9.06	13.62
1567	3	2935	210.36	92.66	2022	219.63	106.30	9.27	13.64
1568	3	2936	210.26	92.49	2023	219.60	105.84	9.35	13.35
1569	3	2937	210.52	92.81	2024	219.41	106.01	8.89	13.20
1570	3	2946	210.38	92.40	2025	219.60	105.77	9.21	13.37
1571	3	2947	210.31	92.82	2026	219.55	105.64	9.24	12.83
1572	3	2948	210.57	92.50	2027	219.55	105.48	8.98	12.98
1573	3	2949	210.64	92.58	2028	219.60	105.44	8.96	12.86
1574	3	2950	210.40	92.88	2029	219.46	105.45	9.06	12.57
1575	3	2951	210.52	93.10	2030	219.58	105.82	9.06	12.72
1576	3	2952	210.40	92.88	2031	219.64	105.95	9.24	13.07
1577	3	2953	210.25	92.56	2032	219.53	105.94	9.28	13.39
1578	3	2956	210.31	92.35	2033	219.73	106.29	9.41	13.94
1579	3	2957	210.49	92.51	2034	219.67	105.89	9.18	13.38
1580	3	2958	210.35	92.48	2035	219.70	105.96	9.35	13.48
1581	3	2959	210.42	92.63	2036	219.53	105.39	9.12	12.75
1582	3	2960	210.30	92.58	2037	219.44	105.91	9.14	13.33
1583	3	2962	210.20	93.08	2038	219.43	106.35	9.23	13.27

obs	T	B260 year	driving stress (kPa)	flux (km^3a^{-1})	B270 year	driving stress (kPa)	flux (km^3a^{-1})	Δdriving stress (kPa)	Δflux (km^3a^{-1})
1584	3	2963	210.32	92.80	2039	219.22	106.21	8.90	13.41
1585	3	2964	210.18	92.92	2040	219.35	105.76	9.17	12.85
1586	3	2966	210.25	92.64	2041	219.22	106.07	8.97	13.43
1587	3	2968	210.37	92.80	2042	219.34	105.82	8.97	13.02
1588	3	2969	210.29	93.02	2043	219.28	105.65	8.99	12.63
1589	3	2972	210.37	93.49	2045	219.33	106.12	8.96	12.63
1590	3	2973	210.35	92.74	2046	219.33	106.20	8.98	13.45
1591	3	2971	210.26	93.31	2047	219.34	105.97	9.07	12.66
1592	3	2976	210.22	92.78	2048	219.35	105.90	9.12	13.12
1593	3	2977	210.21	92.87	2049	219.36	105.85	9.15	12.98
1594	3	2979	210.25	92.79	2050	219.28	105.84	9.03	13.05
1595	3	2980	210.25	92.86	2051	219.25	105.81	8.99	12.95
1596	3	2982	210.17	92.49	2052	219.33	105.91	9.15	13.42
1597	3	2983	210.16	92.71	2053	219.33	106.01	9.17	13.30
1598	3	2984	210.27	92.91	2054	219.28	105.97	9.01	13.07
1599	3	2987	210.24	93.20	2055	219.44	106.02	9.20	12.82
1600	3	2988	210.24	93.04	2056	219.38	105.63	9.13	12.60
1601	3	2989	210.28	93.16	2057	219.44	106.09	9.16	12.93
1602	3	2990	210.28	93.19	2058	219.43	105.97	9.15	12.78
1603	3	2991	210.29	93.22	2059	219.47	105.73	9.18	12.52
1604	3	2992	210.21	93.19	2060	219.46	105.77	9.25	12.58
1605	3	2993	210.36	93.17	2061	219.42	105.36	9.06	12.19
1606	3	2994	210.31	93.13	2062	219.47	105.79	9.16	12.66
1607	3	2996	210.27	92.97	2063	219.42	106.11	9.16	13.15
1608	3	2997	210.27	92.98	2064	219.45	106.00	9.18	13.02
1609	3	2995	210.32	93.09	2065	219.38	105.73	9.06	12.64
1610	3	2999	210.31	92.69	2066	219.42	105.83	9.11	13.14
1611	3	3001	210.36	93.12	2067	219.34	105.78	8.98	12.67
1612	3	3003	210.30	92.60	2068	219.32	105.69	9.02	13.09
1613	3	3004	210.20	92.75	2069	219.25	105.99	9.04	13.23
1614	3	3006	210.26	92.94	2070	219.24	105.80	8.99	12.86
1615	3	3008	210.08	92.98	2071	219.36	105.96	9.28	12.98
1616	3	3009	210.01	92.67	2072	219.41	105.93	9.40	13.27
1617	3	3010	210.04	92.70	2073	219.33	105.40	9.30	12.70
1618	3	3011	210.06	92.95	2074	219.39	105.40	9.33	12.45
1619	3	3014	210.09	93.02	2075	219.50	105.59	9.40	12.57
1620	3	3015	210.07	92.78	2076	219.36	105.16	9.29	12.38
1621	3	3016	210.13	92.68	2077	219.43	105.64	9.30	12.96
1622	3	3018	210.04	92.85	2078	219.36	105.61	9.33	12.76
1623	3	3020	210.13	92.76	2079	219.39	105.68	9.26	12.92

obs	T	B260 year	driving stress (kPa)	flux (km^3a^{-1})	B270 year	driving stress (kPa)	flux (km^3a^{-1})	Δdriving stress (kPa)	Δflux (km^3a^{-1})
1624	3	3021	210.13	92.50	2080	219.41	105.31	9.28	12.81
1625	3	3017	210.07	92.88	2081	219.40	105.14	9.33	12.25
1626	3	3025	210.16	92.26	2082	219.27	105.11	9.11	12.85
1627	3	3026	210.12	92.04	2083	219.32	105.26	9.20	13.22
1628	3	3027	210.14	91.80	2084	219.27	104.93	9.12	13.12
1629	3	3028	210.18	91.78	2085	219.30	104.68	9.11	12.90
1630	3	3032	210.06	91.92	2087	219.23	104.66	9.17	12.73
1631	3	3033	210.11	91.90	2088	219.28	104.56	9.17	12.66
1632	3	3037	209.85	92.08	2091	219.33	104.06	9.47	11.97
1633	3	3038	209.86	91.81	2092	219.31	104.03	9.45	12.22
1634	3	3040	209.83	91.82	2093	219.33	104.56	9.50	12.75
1635	3	3041	209.93	91.87	2094	219.35	104.36	9.42	12.49
1636	3	3045	210.01	92.20	2096	219.30	104.31	9.29	12.11
1637	3	3047	209.98	92.33	2097	219.31	104.58	9.33	12.25
1638	3	3049	210.06	92.19	2098	219.37	104.56	9.30	12.37
1639	3	3050	210.04	91.82	2099	219.30	104.66	9.26	12.84
1640	3	3051	209.94	92.09	2100	219.29	104.60	9.35	12.50
1641	3	3054	209.95	91.84	2101	219.34	104.32	9.39	12.49
1642	3	3055	209.89	91.97	2102	219.26	104.37	9.37	12.41
1643	3	3057	209.80	91.88	2103	219.24	104.25	9.43	12.38
1644	3	3062	209.75	91.57	2105	219.13	104.45	9.38	12.88
1645	3	3060	209.75	91.75	2106	219.28	104.75	9.53	13.00
1646	3	3061	209.76	91.47	2107	219.19	104.43	9.42	12.97
1647	3	3065	209.78	91.26	2109	219.25	104.38	9.47	13.12
1648	3	3066	209.83	91.60	2110	219.22	104.43	9.38	12.83
1649	3	3069	209.85	91.53	2111	219.25	104.27	9.39	12.74
1650	3	3073	209.90	91.04	2112	219.34	104.58	9.45	13.54
1651	3	3074	209.91	91.22	2113	219.22	104.39	9.31	13.17
1652	3	3080	209.89	91.34	2114	219.18	104.45	9.29	13.10
1653	3	3075	209.92	91.52	2115	219.14	104.44	9.22	12.92
1654	3	3076	209.95	91.71	2116	219.17	104.16	9.22	12.45
1655	3	3077	209.93	91.60	2117	219.12	103.99	9.18	12.39
1656	3	3078	209.95	91.35	2118	219.19	103.96	9.24	12.61
1657	3	3081	209.89	91.15	2119	218.99	103.93	9.11	12.78
1658	3	3082	209.87	91.18	2120	218.97	104.22	9.11	13.05
1659	3	3085	209.94	91.29	2121	218.96	104.09	9.02	12.80
1660	3	3086	209.88	91.35	2123	218.89	104.13	9.01	12.78
1661	3	3087	209.77	91.41	2124	219.03	104.04	9.26	12.62
1662	3	3092	209.73	91.24	2125	219.17	103.95	9.44	12.70
1663	3	3093	209.71	91.13	2126	219.10	104.25	9.39	13.12

obs	T	B260 year	driving stress (kPa)	flux (km^3a^{-1})	B270 year	driving stress (kPa)	flux (km^3a^{-1})	Δdriving stress (kPa)	Δflux (km^3a^{-1})
1664	3	3094	209.74	91.12	2127	219.26	104.35	9.52	13.23
1665	3	3096	209.65	90.84	2128	219.06	104.64	9.40	13.81
1666	3	3097	209.67	90.95	2129	219.09	104.41	9.42	13.46
1667	3	3098	209.64	90.84	2130	219.01	104.51	9.37	13.66
1668	3	3099	209.65	90.71	2131	219.06	104.21	9.41	13.50
1669	3	3100	209.65	90.65	2132	219.05	103.83	9.40	13.19
1670	3	3101	209.54	90.43	2133	219.05	103.77	9.52	13.34
1671	3	3102	209.58	90.43	2134	219.10	103.80	9.53	13.37
1672	3	3108	209.59	90.10	2135	218.84	103.70	9.25	13.61
1673	3	3109	209.56	90.21	2136	218.76	103.28	9.20	13.07
1674	3	3110	209.55	90.30	2137	218.77	103.32	9.22	13.02
1675	3	3111	209.57	90.17	2138	219.04	103.39	9.48	13.22
1676	3	3112	209.56	90.27	2139	218.98	103.50	9.42	13.24
1677	3	3122	209.46	90.07	2143	218.91	103.60	9.44	13.53
1678	3	3125	209.49	90.22	2144	218.80	103.49	9.31	13.28
1679	3	3126	209.51	89.99	2145	218.75	104.12	9.24	14.13
1680	3	3127	209.50	89.88	2146	218.75	103.77	9.25	13.89
1681	3	3128	209.49	89.97	2147	218.79	103.77	9.30	13.79
1682	3	3132	209.55	90.19	2148	218.61	103.95	9.07	13.76
1683	3	3135	209.48	90.66	2150	218.55	103.97	9.08	13.31
1684	3	3152	209.11	90.56	2151	218.57	103.94	9.46	13.38
1685	3	3153	209.18	90.53	2152	218.56	103.79	9.38	13.26
1686	3	3154	209.20	90.43	2153	218.51	103.96	9.31	13.53
1687	3	3155	209.16	90.50	2154	218.64	103.88	9.48	13.37
1688	3	3141	209.44	90.50	2155	218.54	104.08	9.10	13.58
1689	3	3148	209.15	91.03	2156	218.52	103.60	9.37	12.56
1690	3	3149	209.33	90.44	2157	218.62	103.91	9.28	13.47
1691	3	3150	209.27	90.30	2158	218.55	103.52	9.29	13.22
1692	3	3151	209.17	90.54	2159	218.57	103.62	9.40	13.08
1693	3	3156	209.16	90.20	2165	218.54	103.57	9.38	13.37
1694	3	3157	209.13	90.28	2166	218.57	103.65	9.44	13.37
1695	3	3158	209.14	90.39	2167	218.53	103.67	9.39	13.28
1696	3	3161	209.09	90.67	2170	218.49	103.91	9.40	13.24
1697	3	3162	209.18	90.58	2171	218.54	103.44	9.36	12.86
1698	3	3181	208.94	90.16	2172	218.47	103.53	9.53	13.36
1699	3	3166	209.15	90.75	2174	218.31	103.31	9.16	12.56
1700	3	3167	209.03	90.64	2175	218.44	103.26	9.41	12.62
1701	3	3168	209.13	90.90	2176	218.54	102.95	9.41	12.04
1702	3	3171	208.84	90.39	2177	218.36	103.01	9.52	12.62
1703	3	3180	208.89	90.43	2180	218.34	103.20	9.45	12.77

obs	T	B260 year	driving stress (kPa)	flux (km^3a^{-1})	B270 year	driving stress (kPa)	flux (km^3a^{-1})	Δdriving stress (kPa)	Δflux ($km^3a^{-1)}$
1704	3	3186	208.87	89.76	2181	218.31	102.94	9.44	13.18
1705	3	3177	208.84	90.66	2182	218.18	102.77	9.34	12.11
1706	3	3178	208.88	90.17	2183	218.33	102.67	9.45	12.50
1707	3	3187	208.89	89.40	2184	218.34	102.47	9.45	13.07
1708	3	3188	208.80	89.44	2185	218.29	102.74	9.49	13.30
1709	3	3189	208.80	89.45	2186	218.27	102.64	9.48	13.18
1710	3	3163	209.14	90.84	2187	218.26	102.60	9.12	11.76
1711	3	3205	208.79	89.61	2188	218.27	102.21	9.47	12.60
1712	3	3182	208.94	90.18	2189	218.27	102.31	9.33	12.13
1713	3	3172	208.83	90.48	2190	218.21	102.09	9.39	11.61
1714	3	3173	208.84	90.50	2191	218.19	102.39	9.35	11.90
1715	3	3174	208.81	90.35	2192	218.19	102.63	9.38	12.28
1716	3	3175	208.83	90.53	2193	218.10	102.73	9.27	12.20
1717	3	3137	209.50	90.60	2194	218.03	102.42	8.52	11.82

Appendix B Experiment 2 Summary Table

Driving stress and flux across the grounding line summarized for each co-located observation in experiment 2. Column1 is the observation number. Column 2 is the transect (T) used to determine co-location for the given observation. Column 3 is the year of the B270 simulation that corresponds to the observation. Column 4 is the mean driving stress of the B270 simulation's ROI with units of kPa. Column 5 is the flux across the grounding line for the B270 simulation in units of km^3a^{-1}. Columns 6 through 8 are the G425 simulation equivalents of columns 3 through 5. Column 9 is the difference in driving stress calculated as G425 minus B270 with units of kPa. Column 10 is the difference in flux across the grounding line in units of km^3a^{-1} and calculated as G425 minus G425.

obs	T	B270 year	driving stress (kPa)	flux (km^3a^{-1})	G425 year	driving stress (kPa)	flux (km^3a^{-1})	Δdriving stress (kPa)	Δflux (km^3a^{-1})
1	4	659	130.12	171.13	426	131.01	408.85	0.89	237.72
2	1	665	130.71	169.93	428	132.29	399.66	1.58	229.73
3	1	668	130.86	169.55	429	132.71	394.86	1.86	225.31
4	1	673	131.21	168.99	430	133.35	384.42	2.14	215.43
5	1	706	134.32	168.6	443	138.61	314.54	4.29	145.94
6	1	708	134.55	169.48	444	138.93	307.39	4.38	137.92
7	1	741	137.95	166.71	490	147.08	241.04	9.14	74.33
8	1	743	138.14	167.42	491	147.36	241.5	9.22	74.08
9	1	744	138.22	167.18	492	147.5	241.78	9.27	74.59
10	1	745	138.33	166.92	493	147.6	241.15	9.28	74.24
11	1	746	138.45	166.41	494	147.62	240.44	9.17	74.03
12	1	756	139.5	165.23	495	147.72	240.19	8.22	74.96
13	1	778	142.22	171.05	510	150.76	234.59	8.53	63.54
14	1	779	142.35	171.06	511	150.71	233.64	8.36	62.58
15	1	780	142.51	170.77	512	150.97	233.9	8.46	63.13
16	1	781	142.63	170.58	513	151.17	232.35	8.54	61.77
17	1	787	143.38	170.64	519	152.31	228.28	8.93	57.64
18	1	788	143.53	170.42	520	152.53	227.63	9.01	57.21
19	1	789	143.63	170.3	521	152.46	227.55	8.83	57.25
20	1	790	143.75	170.79	523	152.73	225.07	8.99	54.29
21	1	791	143.94	170.76	524	152.99	224.3	9.05	53.53
22	2	804	145.49	169.74	525	153.07	224.72	7.58	54.98
23	4	820	147.07	162.69	527	153.29	223.9	6.22	61.21

obs	T	B270 year	driving stress (kPa)	flux (km^3a^{-1})	G425 year	driving stress (kPa)	flux (km^3a^{-1})	Δdriving stress (kPa)	Δflux (km^3a^{-1})
24	4	823	147.43	163.18	530	153.75	220.46	6.33	57.28
25	2	827	147.82	162.99	538	154.57	215.64	6.75	52.65
26	2	828	147.99	162.51	539	154.73	216.89	6.74	54.37
27	2	829	148.05	162.17	540	154.87	215.92	6.83	53.75
28	2	831	148.26	162.18	543	155.4	215.94	7.14	53.77
29	2	832	148.4	161.7	544	155.5	215.36	7.1	53.66
30	2	833	148.51	161.27	545	155.6	214.14	7.1	52.87
31	2	837	148.87	161.3	549	156.06	212.64	7.19	51.34
32	2	854	150.58	157.21	564	158.49	203.72	7.9	46.51
33	2	855	150.74	156.92	565	158.76	202.46	8.03	45.55
34	2	858	151.13	157.6	569	159.37	200.18	8.24	42.58
35	2	859	151.26	157.31	572	159.72	196.84	8.47	39.53
36	2	860	151.34	157.11	573	159.84	196.34	8.5	39.24
37	2	861	151.48	156.55	574	159.94	196.12	8.46	39.57
38	2	877	153.74	153.04	575	160.05	195.32	6.32	42.27
39	2	878	153.85	152.67	577	160.2	194.24	6.35	41.57
40	2	879	153.97	152.57	578	160.25	193.71	6.28	41.14
41	2	880	154.1	152.61	579	160.35	192.95	6.25	40.34
42	2	881	154.18	152.31	580	160.52	193.28	6.34	40.97
43	2	882	154.33	152.36	581	160.71	192.71	6.38	40.34
44	2	1097	176.76	128.21	747	185.47	167.6	8.7	39.39
45	2	1130	180.54	129.43	760	188.1	166.77	7.57	37.33
46	2	1142	181.68	128.96	770	189.98	164.16	8.3	35.19
47	2	1143	181.75	128.8	771	190.19	164.3	8.44	35.5
48	2	1152	182.31	127.82	780	191.69	162.68	9.37	34.86
49	2	1153	182.43	127.63	781	191.9	162.63	9.47	35
50	2	1157	182.91	127.01	787	192.74	159.85	9.83	32.85
51	2	1158	183.02	127.19	788	192.94	159.81	9.92	32.62
52	2	1179	184.16	125.06	800	194.53	158.1	10.36	33.05
53	1	1179	184.16	125.06	819	197.5	158.85	13.34	33.8
54	1	1180	184.21	125.3	820	197.7	158.69	13.49	33.4
55	1	1181	184.25	125.36	821	197.73	158.42	13.48	33.06
56	1	1186	184.62	125.55	823	198.09	158.26	13.47	32.71
57	1	1187	184.77	125.74	824	198.22	158.31	13.45	32.57
58	1	1188	184.82	125.84	826	198.58	158.3	13.76	32.47
59	1	1189	184.97	126.3	827	198.75	158.19	13.78	31.88
60	1	1191	185.22	126	828	198.98	158.24	13.76	32.23
61	2	1226	188.2	123.51	829	199.16	158.1	10.96	34.59
62	1	1231	188.48	122.3	846	202.26	158.25	13.79	35.95
63	1	1241	189.07	120.13	847	202.28	158.86	13.22	38.73

obs	T	B270 year	driving stress (kPa)	flux (km^3a^{-1})	G425 year	driving stress (kPa)	flux (km^3a^{-1})	Δdriving stress (kPa)	Δflux (km^3a^{-1})
64	1	1242	189.13	120.63	848	202.44	158.46	13.31	37.83
65	1	1263	190.13	119.76	849	202.56	158.1	12.43	38.34
66	1	1264	190.21	119.72	850	202.61	158.15	12.4	38.43
67	1	1266	190.31	119.58	852	203.01	159.25	12.7	39.67
68	1	1284	191.18	119.02	853	203.24	159.27	12.06	40.25
69	1	1292	191.68	118.98	854	203.35	158.92	11.67	39.94
70	1	1293	191.66	118.95	855	203.69	158.2	12.03	39.25
71	1	1294	191.78	118.93	856	203.78	157.63	12	38.7
72	1	1295	191.89	118.7	857	204.05	157.52	12.16	38.83
73	1	1296	191.96	118.92	858	204.25	156.8	12.29	37.88
74	1	1297	191.88	119.18	859	204.46	156.59	12.59	37.4
75	1	1302	192.06	119.34	860	204.7	156.87	12.64	37.54
76	1	1303	192.01	119.2	861	204.65	155.53	12.64	36.32
77	1	1304	192.1	118.93	862	204.79	154.71	12.68	35.78
78	1	1305	192.19	118.22	863	204.85	155.68	12.67	37.46
79	2	1306	192.3	118.39	891	207.82	151.52	15.52	33.13
80	2	1308	192.39	118.34	892	208.05	151.59	15.66	33.24
81	2	1309	192.46	118.58	893	208.13	151.68	15.67	33.1
82	2	1310	192.55	118.38	895	208.44	152.01	15.89	33.64
83	2	1311	192.64	118.31	896	208.52	151.98	15.88	33.67
84	2	1312	192.68	118.51	897	208.75	152.39	16.06	33.88
85	2	1313	192.72	118.02	898	208.83	152.15	16.11	34.13
86	1	1357	194.82	114.57	919	211.42	149.08	16.6	34.51
87	1	1358	194.9	114.64	920	211.55	149.04	16.66	34.39
88	1	1359	194.93	114.62	921	211.73	149.06	16.79	34.44
89	1	1387	195.87	113.05	925	212.23	149.8	16.37	36.75
90	2	1388	195.89	112.99	929	213.01	149.14	17.12	36.15
91	2	1389	195.94	112.99	930	213.1	149.48	17.16	36.49
92	2	1390	196.04	112.83	931	213.2	149.66	17.16	36.83
93	2	1391	196.07	112.25	932	213.17	149.8	17.1	37.55
94	1	1412	196.96	112.58	935	213.75	148.85	16.79	36.27
95	1	1415	197.18	112.72	936	213.9	148.97	16.72	36.25
96	1	1418	197.22	112.97	937	213.97	148.94	16.74	35.97
97	1	1420	197.41	112.96	938	214.24	149.03	16.83	36.07
98	2	1425	197.67	112.63	940	214.57	149.74	16.9	37.11
99	2	1438	198.42	115.89	942	214.85	149.72	16.44	33.83
100	4	1444	198.77	116.69	945	215.09	149.06	16.32	32.37
101	4	1477	201.15	117.91	965	217.87	148.36	16.72	30.45
102	4	1479	201.47	118.04	966	217.85	149.14	16.38	31.11
103	4	1490	202.85	119.74	987	221.02	145.12	18.17	25.38

obs	T	B270 year	driving stress (kPa)	flux (km^3a^{-1})	G425 year	driving stress (kPa)	flux (km^3a^{-1})	Δdriving stress (kPa)	Δflux (km^3a^{-1})
104	4	1497	203.57	119.32	989	221.06	144.98	17.49	25.66
105	4	1498	203.62	119.41	992	221.66	145.21	18.04	25.8
106	1	1498	203.62	119.41	997	222.03	146.26	18.41	26.86
107	1	1500	203.88	119.54	998	222.24	145.91	18.37	26.37
108	1	1505	204.27	119.97	999	222.39	146.12	18.12	26.15
109	1	1508	204.56	120.24	1000	222.28	146.26	17.72	26.01
110	1	1510	204.8	120.6	1001	222.52	146.23	17.73	25.63
111	1	1511	205.01	120.44	1002	222.75	146.02	17.73	25.58
112	1	1515	205.26	120.67	1003	222.91	146.18	17.66	25.51
113	1	1517	205.38	120.23	1004	223.09	146.7	17.71	26.47
114	1	1519	205.3	121.22	1005	223.26	146.74	17.96	25.52
115	1	1521	205.7	121.23	1006	223.33	146.47	17.63	25.25
116	1	1522	205.71	121.58	1007	223.36	145.95	17.65	24.38
117	1	1523	205.84	122.23	1008	223.52	145.78	17.68	23.55
118	1	1525	206.27	122.51	1009	223.62	145.11	17.36	22.6
119	1	1527	206.45	122.3	1010	223.73	144.84	17.28	22.55
120	1	1528	206.53	122.45	1011	223.89	144.82	17.36	22.37
121	1	1529	206.67	122.58	1012	223.93	144.59	17.26	22.01
122	1	1530	206.71	122.64	1013	224.18	144.41	17.48	21.77
123	1	1531	206.93	122.4	1014	224.2	143.8	17.28	21.41
124	1	1532	206.96	123.39	1015	224.52	143.52	17.56	20.13
125	1	1538	207.67	122.47	1021	224.75	142.32	17.07	19.85
126	1	1539	207.77	122.7	1022	224.74	142.7	16.97	20
127	1	1541	208.05	123.3	1024	225.17	142.42	17.12	19.12
128	1	1545	208.51	121.88	1027	225.51	141.81	17.01	19.93
129	1	1547	208.67	121.91	1028	225.72	141.84	17.05	19.93
130	1	1548	208.53	122.28	1029	225.87	142.5	17.34	20.22
131	1	1549	208.67	122.62	1030	225.92	142.47	17.25	19.85
132	1	1552	208.77	122.43	1031	225.98	142.17	17.22	19.73
133	1	1553	208.78	122.15	1033	225.96	141.9	17.18	19.75
134	1	1554	208.93	122.88	1034	226.13	141.7	17.2	18.83
135	1	1555	209.01	122.33	1035	226.25	141.92	17.24	19.59
136	1	1556	209.16	122.32	1036	226.36	141.82	17.2	19.5
137	1	1558	209.26	121.99	1037	226.46	141.51	17.2	19.52
138	1	1559	209.36	122.63	1038	226.65	141.52	17.29	18.89
139	1	1560	209.41	122.65	1039	226.64	141.77	17.23	19.13
140	1	1561	209.56	123.34	1040	226.76	141.89	17.2	18.54
141	1	1562	209.71	122.78	1041	226.84	141.47	17.13	18.69
142	1	1563	209.69	122.86	1042	227.07	141.76	17.38	18.9
143	1	1564	209.52	123.32	1043	227.06	142.16	17.54	18.84

obs	T	B270 year	driving stress (kPa)	flux (km^3a^{-1})	G425 year	driving stress (kPa)	flux (km^3a^{-1})	Δdriving stress (kPa)	Δflux (km^3a^{-1})
144	1	1565	209.79	123.2	1044	227.05	141.91	17.25	18.71
145	1	1568	209.93	122.64	1045	227.06	141.39	17.13	18.76
146	1	1569	210.08	123.02	1046	227.08	141.23	17	18.21
147	1	1570	210.31	122.99	1047	227.02	141.2	16.7	18.22
148	4	1597	212.16	121.13	1049	226.98	140.79	14.82	19.66
149	1	1597	212.16	121.13	1071	228.51	138.1	16.34	16.97
150	1	1598	212.24	121.07	1072	228.47	137.84	16.22	16.78
151	1	1600	212.35	121	1073	228.39	137.54	16.04	16.54
152	1	1601	212.36	120.76	1074	228.7	138.37	16.34	17.61
153	1	1602	212.37	120.67	1075	228.51	138.29	16.14	17.62
154	1	1603	212.36	120.76	1076	228.54	139.01	16.19	18.25
155	1	1605	212.44	120.47	1077	228.57	138.77	16.13	18.3
156	1	1608	212.54	120.51	1078	228.73	138.35	16.18	17.85
157	1	1609	212.56	120.78	1079	228.85	138.38	16.29	17.6
158	1	1610	212.59	121.01	1080	228.82	138.03	16.24	17.02
159	1	1614	212.95	120.68	1081	228.87	137.74	15.92	17.07
160	1	1615	212.96	120.3	1082	228.91	137.46	15.95	17.15
161	1	1616	213.09	120.63	1083	228.84	137.22	15.75	16.59
162	1	1619	213.21	119.74	1084	228.86	137.61	15.65	17.87
163	1	1620	213.23	119.74	1085	228.9	137.58	15.67	17.84
164	1	1621	213.3	119.43	1086	229.17	137.53	15.87	18.09
165	1	1622	213.37	119.45	1087	228.76	137.21	15.39	17.76
166	1	1623	213.44	119.52	1088	229.06	137.71	15.62	18.2
167	1	1626	213.79	119.41	1089	228.95	137.15	15.15	17.75
168	1	1627	213.88	119.53	1090	229.18	136.69	15.3	17.15
169	1	1628	213.97	119.53	1091	229.38	136.95	15.41	17.41
170	1	1629	214.06	119.32	1092	229.52	136.73	15.46	17.41
171	1	1630	214.12	119.44	1093	229.48	137.38	15.36	17.94
172	1	1631	214.25	119.47	1094	229.53	136.84	15.27	17.37
173	1	1633	214.45	119.12	1095	229.59	136.32	15.14	17.2
174	1	1635	214.53	119.1	1096	229.61	135.7	15.08	16.61
175	1	1636	214.49	119.43	1097	229.72	135.95	15.22	16.51
176	1	1637	214.49	119.36	1098	229.62	135.44	15.14	16.08
177	1	1638	214.45	118.91	1099	229.58	135.85	15.13	16.94
178	1	1639	214.57	118.71	1100	229.73	135.99	15.15	17.28
179	1	1640	214.69	118.74	1101	229.77	136.07	15.08	17.32
180	1	1643	214.65	118.95	1102	229.96	135.89	15.32	16.95
181	1	1644	214.86	118.27	1103	230	136.35	15.14	18.08
182	1	1645	214.91	118.54	1104	229.97	136.12	15.05	17.58
183	1	1646	214.9	117.85	1105	230.15	135.4	15.25	17.56

obs	T	B270 year	driving stress (kPa)	flux (km^3a^{-1})	G425 year	driving stress (kPa)	flux (km^3a^{-1})	Δdriving stress (kPa)	Δflux (km^3a^{-1})
184	1	1647	214.94	118.12	1106	230.16	135.06	15.22	16.94
185	1	1650	214.81	118	1107	230.16	135.1	15.34	17.1
186	1	1651	215.02	118.16	1108	230.07	134.87	15.04	16.71
187	1	1652	214.99	117.9	1109	230.27	134.49	15.28	16.6
188	1	1653	214.92	117.92	1110	230.14	134.99	15.22	17.07
189	1	1654	214.99	117.99	1111	230.48	135.23	15.49	17.23
190	1	1655	214.99	117.96	1112	230.4	135.71	15.41	17.74
191	1	1658	215.19	117.69	1113	230.42	135.22	15.23	17.52
192	1	1659	215.31	117.26	1114	230.52	135.79	15.21	18.53
193	1	1661	215.46	117.5	1115	230.12	135.51	14.66	18.01
194	1	1664	215.35	117.69	1116	230.59	135.54	15.24	17.85
195	1	1665	215.39	117.45	1117	230.46	135.66	15.06	18.21
196	1	1666	215.5	117.63	1118	230.66	135.43	15.17	17.8
197	1	1667	215.42	117.5	1119	230.77	134.9	15.35	17.4
198	1	1668	215.41	118	1120	230.86	134.51	15.45	16.5
199	1	1669	215.44	117.96	1121	230.82	134.29	15.38	16.33
200	1	1670	215.41	117.52	1122	230.68	134.34	15.27	16.82
201	1	1671	215.48	117.87	1123	230.62	134.93	15.14	17.07
202	1	1672	215.53	117.56	1124	230.56	135.3	15.03	17.74
203	1	1673	215.68	117.06	1125	230.73	135.07	15.04	18.01
204	1	1682	216.05	116.41	1126	230.82	134.9	14.77	18.49
205	1	1683	216.13	115.9	1130	231.07	134.16	14.94	18.26
206	1	1684	216.22	116.18	1131	231.03	134.15	14.81	17.97
207	1	1686	216.25	116.5	1132	230.86	134.36	14.61	17.86
208	1	1688	216.2	116.43	1134	230.98	134.06	14.78	17.63
209	1	1689	216.32	115.93	1135	230.9	133.9	14.57	17.97
210	1	1690	216.38	115.82	1136	231.02	134.38	14.65	18.56
211	1	1691	216.18	115.96	1137	231.16	134.21	14.98	18.26
212	1	1692	216.27	115.81	1138	231.18	134.03	14.91	18.23
213	1	1693	216.33	115.56	1139	231.3	133.92	14.96	18.36
214	1	1694	216.39	115.53	1140	231.33	133.71	14.94	18.18
215	1	1697	216.63	115.64	1141	231.1	133.59	14.47	17.95
216	1	1698	216.67	115.68	1142	231.3	133.52	14.63	17.83
217	1	1706	217.09	114.65	1143	231.34	132.99	14.26	18.34
218	1	1707	217.02	114.52	1144	231.34	132.7	14.33	18.18
219	1	1708	216.94	114.41	1145	231.46	132.39	14.52	17.98
220	1	1709	216.96	114.67	1146	231.46	132.01	14.5	17.34
221	1	1710	217.07	114.72	1147	231.54	131.97	14.47	17.25
222	1	1711	217.09	114.61	1148	231.67	131.75	14.58	17.14
223	1	1712	217.16	114.77	1149	231.73	131.96	14.58	17.18

obs	T	B270 year	driving stress (kPa)	flux (km^3a^{-1})	G425 year	driving stress (kPa)	flux (km^3a^{-1})	Δdriving stress (kPa)	Δflux (km^3a^{-1})
224	1	1713	217.23	114.57	1150	231.91	131.69	14.68	17.12
225	1	1714	217.18	114.78	1151	231.91	131.61	14.73	16.84
226	1	1716	217.15	114.93	1152	231.67	131.04	14.52	16.12
227	1	1717	217.28	115.03	1153	231.71	130.9	14.43	15.87
228	1	1718	217.13	115.03	1154	231.71	130.86	14.58	15.83
229	1	1719	217.17	114.29	1155	231.82	130.5	14.64	16.21
230	1	1720	217.28	114.38	1156	231.71	130.84	14.43	16.46
231	1	1721	217.31	114.55	1157	231.68	130.73	14.37	16.18
232	1	1722	217.31	114.41	1158	231.79	131.02	14.48	16.61
233	1	1724	217.37	113.71	1159	231.69	131.32	14.32	17.61
234	1	1726	217.33	113.56	1160	231.85	130.86	14.52	17.31
235	1	1727	217.37	113.88	1161	231.91	130.9	14.54	17.02
236	1	1729	217.56	114.2	1162	231.91	130.66	14.34	16.46
237	1	1730	217.59	114.27	1163	231.99	130.52	14.4	16.26
238	1	1731	217.61	113.88	1164	232.03	130.66	14.42	16.77
239	1	1732	217.62	113.46	1165	232.12	130.65	14.5	17.18
240	1	1733	217.68	113.73	1166	231.89	130.97	14.2	17.23
241	1	1734	217.64	113.7	1167	231.91	130.96	14.27	17.26
242	1	1735	217.59	113.62	1168	232.03	131.31	14.45	17.69
243	1	1739	217.69	113.86	1169	231.99	131.31	14.3	17.45
244	1	1740	217.69	113.76	1170	232.22	131.04	14.52	17.29
245	1	1741	217.72	113.35	1171	232.22	131.26	14.5	17.91
246	1	1742	217.79	113.1	1172	232.34	131	14.54	17.9
247	1	1743	217.83	113.19	1173	232.49	130.9	14.66	17.71
248	1	1748	218.05	113.9	1174	232.44	131.22	14.39	17.32
249	1	1749	218.01	113.84	1175	232.49	130.94	14.48	17.1
250	1	1755	218.04	112.66	1176	232.52	130.19	14.49	17.53
251	1	1756	218.07	112.76	1177	232.62	130.36	14.55	17.59
252	1	1757	218.11	112.91	1178	232.7	130.03	14.59	17.11
253	1	1758	218.23	113.24	1179	232.67	130.2	14.44	16.96
254	1	1759	218.24	113.21	1180	232.79	130.26	14.55	17.05
255	1	1760	218.13	112.99	1181	232.58	130.45	14.45	17.46
256	1	1761	218.2	112.7	1182	232.68	130.4	14.48	17.7
257	1	1762	218.13	112.52	1183	232.68	130.45	14.55	17.93
258	1	1763	218.29	112.3	1184	232.55	130.23	14.26	17.93
259	1	1764	218.34	112.26	1185	232.64	129.93	14.31	17.67
260	1	1767	218.17	112.26	1186	232.5	130.12	14.33	17.86
261	1	1768	218.12	112.56	1187	232.55	130.01	14.43	17.45
262	1	1769	218.3	111.97	1188	232.62	129.77	14.31	17.8
263	1	1770	218.37	112.17	1189	232.61	129.64	14.24	17.47

obs	T	B270 year	driving stress (kPa)	flux (km^3a^{-1})	G425 year	driving stress (kPa)	flux (km^3a^{-1})	Δdriving stress (kPa)	Δflux (km^3a^{-1})
264	1	1771	218.42	111.96	1190	232.83	129.91	14.41	17.95
265	1	1777	218.31	112.07	1191	232.88	129.74	14.57	17.67
266	1	1778	218.29	111.91	1192	232.87	129.1	14.58	17.19
267	1	1779	218.35	111.46	1193	232.74	129.36	14.38	17.9
268	1	1780	218.4	111.59	1194	232.94	128.84	14.54	17.25
269	1	1781	217.93	112.08	1195	232.75	128.6	14.81	16.52
270	1	1782	218	111.86	1196	232.97	128.57	14.97	16.71
271	1	1783	217.9	112.09	1197	232.78	129.58	14.88	17.49
272	1	1784	217.84	112.14	1198	232.83	129.05	15	16.91
273	1	1785	217.97	111.75	1199	232.6	128.65	14.64	16.9
274	1	1786	218.02	111.67	1200	232.56	128.22	14.54	16.55
275	1	1787	217.96	111.67	1201	232.72	128.11	14.75	16.45
276	1	1788	217.97	111.23	1202	232.74	128	14.77	16.77
277	1	1792	217.7	111.83	1203	232.63	127.44	14.93	15.61
278	1	1793	217.71	112.24	1204	232.73	127.66	15.02	15.42
279	1	1794	217.74	111.8	1205	232.72	127.45	14.98	15.64
280	1	1795	217.82	111.71	1206	232.84	127.41	15.02	15.7
281	1	1796	217.83	111.88	1207	232.79	127.19	14.96	15.31
282	1	1797	217.96	111.72	1208	232.62	126.94	14.65	15.22
283	1	1798	217.94	111.52	1209	232.81	126.65	14.87	15.13
284	1	1801	217.8	111.71	1210	232.8	126.77	15	15.06
285	1	1802	217.89	111.27	1211	232.59	126.45	14.71	15.18
286	1	1803	217.89	111.45	1212	232.3	127.38	14.42	15.93
287	1	1804	217.92	111.16	1213	232.21	127.08	14.3	15.92
288	1	1805	217.95	110.98	1214	232.4	126.71	14.45	15.74
289	1	1806	218.01	110.87	1215	232.49	126.32	14.48	15.46
290	1	1809	217.97	111.15	1216	232.5	126.27	14.53	15.12
291	1	1810	218.12	111.19	1217	232.49	126.9	14.38	15.71
292	1	1811	218.03	111.27	1218	232.32	127.5	14.29	16.23
293	1	1812	218.03	110.75	1219	232.21	127.46	14.18	16.72
294	1	1813	218.22	110.75	1220	232.67	126.96	14.45	16.22
295	1	1814	218.25	111.04	1221	232.42	126.75	14.17	15.71
296	1	1815	218.17	110.88	1222	232.4	126.81	14.24	15.93
297	1	1816	218.25	110.64	1223	232.33	126.48	14.08	15.85
298	1	1817	218.28	110.84	1224	232.4	126.55	14.12	15.71
299	1	1818	218.31	110.55	1225	232.17	126.03	13.86	15.48
300	1	1819	218.38	110.68	1226	232.34	126.63	13.96	15.94
301	1	1820	218.42	110.59	1227	232.34	126.54	13.92	15.94
302	1	1821	218.42	110.38	1228	232.46	125.83	14.05	15.44
303	1	1822	218.47	110.24	1229	232.46	125.05	13.99	14.81

obs	T	B270 year	driving stress (kPa)	flux (km^3a^{-1})	G425 year	driving stress (kPa)	flux (km^3a^{-1})	Δdriving stress (kPa)	Δflux (km^3a^{-1})
304	1	1823	218.37	110.26	1230	232.51	125.73	14.14	15.47
305	1	1824	218.25	110.73	1231	232.51	124.9	14.26	14.17
306	1	1825	218.27	110.89	1232	232.42	124.96	14.15	14.07
307	1	1826	218.32	110.38	1233	232.77	126.09	14.45	15.72
308	1	1827	218.33	110.32	1234	232.5	125.97	14.17	15.65
309	1	1828	218.37	110.01	1235	232.66	125.66	14.3	15.64
310	1	1829	218.34	110.09	1236	232.62	125.78	14.29	15.69
311	1	1830	218.34	109.92	1237	232.6	125.47	14.25	15.55
312	1	1831	218.34	110.02	1238	232.54	125.32	14.2	15.3
313	1	1832	218.41	110.38	1239	232.39	125.65	13.98	15.27
314	1	1833	218.44	110.35	1240	232.54	126.53	14.1	16.18
315	1	1838	218.51	110.16	1241	232.41	126.36	13.89	16.2
316	1	1839	218.38	110.71	1242	232.48	126.69	14.1	15.98
317	1	1840	218.42	110.88	1243	232.59	126.28	14.17	15.41
318	1	1841	218.46	110.23	1244	232.66	126.23	14.2	16.01
319	1	1842	218.48	110.04	1245	232.65	126.42	14.17	16.38
320	1	1843	218.51	110.11	1246	232.63	126.36	14.11	16.25
321	1	1844	218.54	109.86	1247	232.72	126.76	14.18	16.9
322	1	1857	218.66	109.17	1260	232.68	126.03	14.02	16.86
323	1	1862	218.65	110.16	1265	233.01	125.55	14.36	15.38
324	1	1878	218.95	109.69	1279	233.36	125	14.41	15.32
325	1	1879	218.96	109.84	1280	233.3	125.06	14.34	15.22
326	1	1880	219.07	109.86	1281	233.17	124.6	14.11	14.73
327	1	1881	219.01	110.08	1282	233.18	124.62	14.17	14.55
328	1	1882	218.83	109.84	1283	233.27	124.61	14.44	14.77
329	1	1883	218.75	109.7	1284	233.15	124.61	14.4	14.92
330	1	1884	218.71	109.66	1285	233.18	124.71	14.47	15.05
331	1	1890	218.97	109.65	1286	233.34	125.02	14.37	15.37
332	1	1891	219.08	108.95	1287	233.18	124.58	14.1	15.63
333	1	1892	219.04	108.98	1288	233.34	124.87	14.3	15.89
334	1	1893	219.16	108.23	1289	233.35	124.49	14.19	16.25
335	1	1894	219	108.68	1290	233.42	124.65	14.42	15.97
336	1	1895	219.03	108.64	1291	233.54	124.76	14.51	16.12
337	1	1896	218.96	108.66	1292	233.31	124.35	14.35	15.69
338	1	1897	219.04	108.55	1293	233.28	124.1	14.24	15.55
339	1	1898	219.05	108.4	1294	233.37	123.97	14.32	15.58
340	1	1899	218.95	108.66	1295	233.49	123.67	14.54	15.01
341	4	1901	219.05	108.66	1312	232.93	122.9	13.89	14.24
342	4	1902	219.01	108.3	1313	233.01	122.68	14	14.38
343	1	1920	218.93	108.32	1314	233.11	122.4	14.18	14.08

obs	T	B270 year	driving stress (kPa)	flux (km^3a^{-1})	G425 year	driving stress (kPa)	flux (km^3a^{-1})	Δdriving stress (kPa)	Δflux (km^3a^{-1})
344	1	1932	218.91	108.43	1328	233.27	121.14	14.36	12.71
345	1	1940	218.97	108.79	1336	233.08	121.08	14.11	12.29
346	4	1940	218.97	108.79	1341	232.94	120.68	13.96	11.89
347	4	1941	218.85	108.82	1342	232.98	120.63	14.14	11.82
348	4	1942	218.91	108.94	1343	233.12	120.3	14.21	11.36
349	4	1945	218.95	108.94	1346	233.12	120.26	14.17	11.33
350	4	1946	218.92	109.09	1347	233.01	119.96	14.09	10.87
351	4	1947	218.99	109.4	1348	233.01	120.14	14.03	10.75
352	4	1948	219.01	109.37	1349	233.19	120.82	14.18	11.45
353	4	1949	218.95	109.62	1350	233.03	120.58	14.08	10.96
354	4	1950	218.97	108.98	1351	233.04	120.31	14.07	11.33
355	4	1952	218.89	108.73	1352	233.16	120.3	14.27	11.57
356	4	1953	219	109.14	1353	233.16	120.07	14.15	10.93
357	4	1961	219.38	108.98	1354	233.16	119.56	13.78	10.58
358	4	1962	219.35	108.96	1355	233.18	119.47	13.83	10.5
359	4	1963	219.28	109.18	1356	233.17	119.6	13.89	10.42
360	4	1966	219.44	108.8	1357	233.17	119.41	13.73	10.61
361	4	1967	219.44	109.07	1358	233.26	119.11	13.82	10.04
362	4	1968	219.43	109.17	1359	233.24	119.62	13.81	10.46
363	4	1969	219.46	108.88	1360	233.2	119.59	13.73	10.71
364	1	1973	219.53	108.5	1361	233.25	119.4	13.72	10.91
365	1	1975	219.38	109.05	1363	232.99	118.94	13.61	9.89
366	1	1976	219.32	108.87	1364	233.07	118.9	13.75	10.03
367	1	1977	219.48	108.96	1365	233.17	118.63	13.68	9.67
368	1	1978	219.54	108.59	1366	233.2	118.72	13.66	10.13
369	4	1981	219.62	108.53	1367	233.24	118.79	13.62	10.26
370	1	1983	219.37	108.22	1369	233.17	119.05	13.8	10.84
371	1	1984	219.22	108.5	1370	233.1	118.66	13.88	10.16
372	1	1985	219.38	108.5	1371	232.98	118.73	13.6	10.23
373	1	1986	219.4	108.1	1372	233.03	118.73	13.63	10.64
374	1	1987	219.48	107.84	1373	233.01	118.5	13.53	10.67
375	1	1988	219.51	107.76	1374	233.11	119.53	13.6	11.77
376	1	1989	219.58	107.64	1375	233.2	119.78	13.62	12.14
377	1	1990	219.52	108.11	1376	233.15	119.55	13.63	11.44
378	1	1991	219.5	107.99	1377	233.14	119.04	13.63	11.05
379	1	1992	219.48	107.92	1378	233.15	119.18	13.68	11.26
380	1	1993	219.71	107.32	1379	233.14	119.14	13.43	11.82
381	1	1994	219.64	107.36	1380	233.19	118.96	13.55	11.6
382	1	1995	219.77	107.3	1381	233.15	118.37	13.38	11.07
383	1	2003	219.72	106.91	1382	233.15	118.38	13.43	11.47

obs	T	B270 year	driving stress (kPa)	flux (km^3a^{-1})	G425 year	driving stress (kPa)	flux (km^3a^{-1})	Δdriving stress (kPa)	Δflux (km^3a^{-1})
384	1	2004	219.65	106.46	1383	233.27	118.35	13.62	11.9
385	1	2005	219.69	106.55	1384	233.11	118.37	13.43	11.82
386	1	2006	219.73	106.76	1385	233.21	118.05	13.49	11.3
387	1	2007	219.73	106.92	1386	233.1	118.34	13.37	11.41
388	1	2008	219.68	106.62	1387	233.17	118.2	13.5	11.58
389	1	2009	219.73	106.55	1388	233.15	118.07	13.42	11.52
390	1	2010	219.67	106.59	1389	233.16	118.2	13.49	11.62
391	1	2011	219.67	106.79	1390	233.08	118.21	13.41	11.42
392	1	2012	219.67	106.53	1391	233.16	118.21	13.49	11.69
393	1	2013	219.7	106.39	1392	233.09	117.91	13.39	11.52
394	1	2014	219.69	106.4	1393	233	117.97	13.31	11.57
395	1	2015	219.65	106.61	1394	232.99	117.78	13.34	11.17
396	1	2016	219.69	106.63	1395	233.01	117.79	13.32	11.15
397	1	2019	219.73	105.92	1396	233.17	116.92	13.44	11
398	1	2020	219.56	105.87	1397	233.13	117.27	13.57	11.4
399	1	2021	219.59	106.57	1398	233.12	117.35	13.53	10.78
400	1	2022	219.63	106.3	1399	233.03	117.56	13.4	11.26
401	1	2023	219.6	105.84	1400	233.12	117.26	13.52	11.42
402	1	2024	219.41	106.01	1401	232.96	117.11	13.55	11.1
403	1	2025	219.6	105.77	1402	233.1	117.23	13.5	11.47
404	1	2026	219.55	105.64	1403	233.19	117.27	13.64	11.62
405	1	2027	219.55	105.48	1404	233.24	117.18	13.69	11.71
406	1	2028	219.6	105.44	1405	233	117.14	13.4	11.71
407	1	2029	219.46	105.45	1406	233.18	117.77	13.72	12.32
408	1	2030	219.58	105.82	1407	233.1	117.73	13.52	11.9
409	1	2031	219.64	105.95	1408	232.91	117.51	13.27	11.55
410	1	2032	219.53	105.94	1409	232.84	116.96	13.31	11.02
411	1	2033	219.73	106.29	1410	232.95	116.93	13.22	10.65
412	4	2034	219.67	105.89	1411	232.84	117.16	13.17	11.27
413	4	2035	219.7	105.96	1412	232.77	117.02	13.07	11.05
414	4	2036	219.53	105.39	1413	232.93	117.43	13.39	12.04
415	4	2037	219.44	105.91	1414	232.93	117.28	13.49	11.38
416	4	2038	219.43	106.35	1415	232.76	117.32	13.33	10.97
417	4	2039	219.22	106.21	1416	232.67	116.94	13.45	10.72
418	1	2043	219.28	105.65	1417	232.75	116.66	13.47	11.02
419	1	2044	219.31	106.04	1418	232.76	116.62	13.45	10.58
420	1	2045	219.33	106.12	1419	232.4	116.66	13.07	10.54
421	1	2046	219.33	106.2	1420	232.51	117.24	13.18	11.04
422	1	2047	219.34	105.97	1421	232.52	116.55	13.18	10.59
423	1	2048	219.35	105.9	1422	232.56	116.4	13.21	10.5

obs	T	B270 year	driving stress (kPa)	flux (km^3a^{-1})	G425 year	driving stress (kPa)	flux (km^3a^{-1})	Δdriving stress (kPa)	Δflux (km^3a^{-1})
424	1	2049	219.36	105.85	1423	232.58	116.77	13.22	10.92
425	1	2050	219.28	105.84	1424	232.56	116.39	13.28	10.55
426	1	2051	219.25	105.81	1425	232.54	116.73	13.29	10.91
427	1	2052	219.33	105.91	1426	232.7	116.51	13.37	10.6
428	1	2069	219.25	105.99	1427	232.6	116.78	13.36	10.8
429	1	2070	219.24	105.8	1428	232.66	116.65	13.41	10.84
430	1	2071	219.36	105.96	1429	232.68	116.89	13.32	10.93
431	1	2072	219.41	105.93	1430	232.85	116.96	13.43	11.03
432	1	2073	219.33	105.4	1431	232.63	116.71	13.3	11.31
433	1	2074	219.39	105.4	1432	232.87	116.86	13.48	11.46
434	1	2075	219.5	105.59	1433	232.8	116.26	13.31	10.66
435	1	2076	219.36	105.16	1434	232.57	116.34	13.2	11.18
436	1	2077	219.43	105.64	1435	232.58	115.91	13.14	10.27
437	1	2078	219.36	105.61	1436	232.54	116.63	13.17	11.02
438	1	2099	219.3	104.66	1437	232.63	117.53	13.33	12.87
439	1	2100	219.29	104.6	1438	232.62	117.36	13.33	12.76
440	1	2101	219.34	104.32	1439	232.68	116.74	13.34	12.42
441	1	2102	219.26	104.37	1440	232.86	117.04	13.6	12.66
442	1	2103	219.24	104.25	1441	232.43	116.98	13.2	12.73
443	1	2125	219.17	103.95	1451	232.42	116.88	13.25	12.93
444	1	2126	219.1	104.25	1452	232.46	116.47	13.36	12.22
445	1	2127	219.26	104.35	1453	232.4	116.54	13.14	12.19
446	1	2128	219.06	104.64	1454	232.36	116.59	13.3	11.94
447	1	2129	219.09	104.41	1455	232.41	116.41	13.32	12.01
448	1	2130	219.01	104.51	1456	232.35	116.38	13.33	11.88
449	1	2131	219.06	104.21	1457	232.36	115.96	13.3	11.75
450	1	2132	219.05	103.83	1458	232.31	115.49	13.26	11.66
451	1	2133	219.05	103.77	1459	232.24	115.85	13.18	12.08
452	1	2134	219.1	103.8	1460	232.19	116.18	13.09	12.39
453	1	2135	218.84	103.7	1461	232.19	115.8	13.36	12.1
454	1	2136	218.76	103.28	1462	232.3	116.1	13.54	12.82
455	1	2137	218.77	103.32	1463	232.35	115.78	13.58	12.46
456	1	2138	219.04	103.39	1464	232.2	116.37	13.16	12.98
457	1	2139	218.98	103.5	1465	232.25	116.75	13.27	13.25
458	1	2140	218.93	103.44	1466	232.18	116.25	13.25	12.82
459	1	2152	218.56	103.79	1467	232.09	116.05	13.53	12.26
460	1	2153	218.51	103.96	1468	232	116.36	13.49	12.4
461	1	2154	218.64	103.88	1469	231.9	115.95	13.26	12.07
462	1	2155	218.54	104.08	1470	231.82	115.88	13.28	11.79
463	1	2156	218.52	103.6	1471	231.76	115.64	13.24	12.04

obs	T	B270 year	driving stress (kPa)	flux (km^3a^{-1})	G425 year	driving stress (kPa)	flux (km^3a^{-1})	Δdriving stress (kPa)	Δflux (km^3a^{-1})
464	1	2157	218.62	103.91	1472	231.86	116.01	13.24	12.1
465	1	2158	218.55	103.52	1473	231.9	116.19	13.34	12.67
466	1	2159	218.57	103.62	1474	231.87	115.59	13.3	11.97
467	1	2160	218.61	103.59	1475	231.9	115.46	13.29	11.87
468	1	2161	218.57	103.21	1476	231.88	115.51	13.31	12.31
469	1	2162	218.6	103.28	1477	231.94	115.28	13.33	12.01
470	1	2163	218.61	103.63	1478	231.92	115.12	13.31	11.49
471	1	2164	218.52	103.59	1479	232.06	115.44	13.53	11.85
472	1	2165	218.54	103.57	1480	231.98	115.15	13.43	11.58
473	1	2166	218.57	103.65	1481	231.93	115.14	13.36	11.49
474	1	2167	218.53	103.67	1482	231.99	115.52	13.46	11.85
475	1	2177	218.36	103.01	1483	231.82	115.46	13.46	12.44
476	1	2178	218.44	102.99	1484	231.78	115.83	13.34	12.84
477	1	2180	218.34	103.2	1485	231.72	115.82	13.37	12.62
478	1	2194	218.03	102.42	1487	231.57	115.85	13.54	13.43

APPENDIX C Grounding Line Retreat Over Beds

Animations showing grounding line retreat over the beds for each simulation. A gray transparency indicates the locations of floating ice and the grounding line is located generally on the landward side between the floating and grounded ice. Each frame is one year and animations show 40 frames per second. Resolution is variable from 4 km to 250 m.

file name	file type	size
B260_FloatBed_40fps.avi	AVI	55.8 MB
B270_FloatBed_40fps.avi	AVI	37.3 MB
G425_FloatBed_40fps.avi	AVI	27.8 MB

in supplemental files

APPENDIX D Ice Thickness Evolution

Animations showing temporal evolution of the thickness field from the last year of forced retreat until the end of the simulations. The grounding line positions and Thwaites domain boundary are contoured in black. Each frame is one year and animations show 40 frames per second. Resolution is variable from 4 km to 250 m with all grounded ice being at least 2 km resolution.

file name	file type	size
B260_Thk_40fps.avi	AVI	81 MB
B270_Thk_40fps.avi	AVI	58.2 MB
G425_Thk_40fps.avi	AVI	44.2 MB

in supplemental files

APPENDIX E Ice Velocity

Animations showing temporal evolution of the velocity field from the last year of forced retreat until the end of the simulations. The grounding line positions and Thwaites domain boundary are contoured in black. Each frame is one year and animations show 40 frames per second. Resolution is variable from 4 km to 250 m with velocities of grounded ice being at least 2 km resolution.

file name	file type	size
B260_Vel_40fps.avi	AVI	102.5 MB
B270_Vel_40fps.avi	AVI	74 MB
G425_Vel_40fps.avi	AVI	49 MB

in supplemental files

APPENDIX F Effective Strain Rate

Animations showing temporal evolution of the effective strain rate field (second invariant of strain tensor) from the last year of forced retreat until the end of the simulations. The Thwaites domain boundary is contoured in white. Each frame is one year and animations show 40 frames per second. Resolution is variable from 4 km to 250 m with the effective strain rate of grounded ice being at least 2 km resolution.

file name	file type	size
B260_EffStr_40fps.avi	AVI	133.4 MB
B270_EffStr_40fps.avi	AVI	89 MB
G425_EffStr_40fps.avi	AVI	102.4 MB

in supplemental files

APPENDIX G Transect 1

Vertical profile animations of unforced grounding line retreat and surface deflation along T1 (uppermost transect). Each frame is one year and animations display 25 frames per second.

file name	file type	size
IceProfileT1_B260_25fps.avi	AVI	28 MB
IceProfileT1_B270_25fps.avi	AVI	14 MB
IceProfileT1_G425_25fps.avi	AVI	12 MB

in supplemental files

APPENDIX H Transect 2

Vertical profile animations of unforced grounding line retreat and surface deflation along T2. Each frame is one year and animations display 25 frames per second.

file name	file type	size
IceProfileT2_B260_25fps.avi	AVI	14 MB
IceProfileT2_B270_25fps.avi	AVI	14 MB
IceProfileT2_G425_25fps.avi	AVI	11 MB

in supplemental files

APPENDIX I Transect 3

Vertical profile animations of unforced grounding line retreat and surface deflation along T3 (approximate geographic centerline). Each frame is one year and animations display 25 frames per second.

file name	file type	size
IceProfileT3_B260_25fps.avi	AVI	14 MB
IceProfileT3_B270_25fps.avi	AVI	14 MB
IceProfileT3_G425_25fps.avi	AVI	11 MB

in supplemental files

APPENDIX J Transect 4

Vertical profile animations of unforced grounding line retreat and surface deflation along T4. Each frame is one year and animations display 25 frames per second.

file name	file type	size
IceProfileT4_B260_25fps.avi	AVI	15 MB
IceProfileT4_B270_25fps.avi	AVI	15 MB
IceProfileT4_G425_25fps.avi	AVI	12.5 MB

in supplemental files

APPENDIX K Transect 5

Vertical profile animations of unforced grounding line retreat and surface deflation along T5 (lowest transect). Each frame is one year and animations display 25 frames per second.

file name	file type	size
IceProfileT5_B260_25fps.avi	AVI	13 MB
IceProfileT5_B270_25fps.avi	AVI	13 MB
IceProfileT5_G425_25fps.avi	AVI	11 MB

in supplemental files

APPENDIX L Experiment 1 Co-location

Field differences at co-located grounding line positions for experiment 1. The scalar fields include differences in thickness (m), differences in surface gradient, and differences in driving stress (kPa).

Also included is an animation showing how the ROIs differ for the simulations in experiment 1. For this animation, a value of 1 indicated the B260 ROI area, a value of 2 indicates the B270 ROI, and a value of 3 indicates their union (overlapping area).

The resolution is 4 km for these files.

file name	file type	size
Experiment1_Thkdiff_40fps.avi	AVI	26 MB
Experiment1_GradSdiff_40fps.avi	AVI	26 MB
Experiment1_Dsdiff_40fps.avi	AVI	26 MB
Experiment1_AreaDiff_60fps.avi	AVI	19 MB

in supplemental files

APPENDIX M Experiment 2 Co-location

Field differences at co-located grounding line positions for experiment 2. The scalar fields include differences in thickness (m), differences in surface gradient, and differences in driving stress (kPa).

Also included is an animation showing how the ROIs differ for the simulations in experiment 1. For this animation, a value of 1 indicated the B270 ROI area, a value of 2 indicates the G425 ROI, and a value of 3 indicates their union.

The resolution is 4 km for these files.

file name	file type	size
Experiment2_Thkdiff_40fps.avi	AVI	11 MB
Experiment2_GradSdiff_40fps.avi	AVI	12 MB
Experiment2_Dsdiff_40fps.avi	AVI	12 MB
Experiment2_AreaDiff_60fps.avi	AVI	6.4 MB

in supplemental files